DTU Mechanical Engineering
Department of Mechanical Engineering

Design of steam generator systems for concentrating solar power plants

Davide Ferruzza

PhD Thesis

Davide Ferruzza

Design of steam generator systems for concentrating solar power plants

Ph.D. Thesis

Supervisors:
Fredrik Haglind - Technical University of Denmark
Martin Ryhl Kærn - Technical University of Denmark
Björn Laumert - Royal Institute of Technology

DTU - Technical University of Denmark, Kgs. Lyngby - 2018

DTU Mechanical Engineering
Section of Thermal Energy Systems
Technical University of Denmark

Nils Koppels Allé, Bld. 403
DK-2800 Kgs. Lyngby
Denmark
Phone (+45) 4525 1360
Fax (+45) 4588 4325

www.mek.dtu.dk

Preface

This thesis is submitted in partial fulfilment of the requirements for the degree of Doctor of Philosophy in Mechanical Engineering at the Technical University of Denmark (DTU).

The research was conducted at the Section of Thermal Energy, Department of Mechanical Engineering. This work was carried out between the 1st of November 2015 and the 31st of October 2018 under the supervision of Associate Professor Fredrik Haglind and Senior Researcher Martin Ryhl Kærn from DTU and Professor Björn Laumert from Royal Institute of Technology (KTH), Sweden.

The project was funded by DTU and EuroTech fund. Financial support was also received from the Otto Mønsted A/S Fond in the frame of the SolarPACES 2016 and 2017 conferences. The work included attending one semester of Ph.D. level courses (30 ECTS) and co-supervision of 2 master thesis and 3 bachelor thesis.

Kongens Lyngby, October 31st 2018

Davide Ferruzza

Acknowledgements

Three years ago I started the journey that brought me to write this Ph.D. thesis. New country, new university and new challenges. Nothing of this would have been possible without those people who supported me during my professional and personal life in Copenhagen.

First and most importantly I would like to thank my supervisor Fredrik Haglind, for giving me the opportunity to be here at the Thermal Energy Section at DTU. Thank you for all the discussions, feedback and for making my Ph.D. a learning experience through constant improvement. I also would like to thank Martin Rhyl Kærn, for the many times you helped when I thought I was stuck with the models. Your help was always invaluable.

I would also like to thank Björn Laumert, my supervisor at KTH, for the discussion, feedback and support whenever was needed. My stay and collaboration with KTH would have not been the same without Monika Topel. I really am grateful for having you as my mentor, guide and friend throughout these three years. To Rafael Guédez goes my gratitude for inspiring me in pursuing my studies and making me so passionate about the concentrating solar power field. Thanks also to Monica and Alex, friends from so many years who make me always feel home when I am back in Stockholm.

I have changed many offices in the last years, but sharing my workplace with Enrico, Giacomo, Jesper, Matthias and Andrea brought always the laughter to alleviate the toughest work days. Thank you for having created such a nice work environment. I can say the same to Gennaro, Riccardo and René. Even though in a different office, I always felt we were actually sharing one. A special thanks goes to Simone. Colleague, office mate, flatmate and above all, a friend without whom my experience of these last three years would have been completely different. Lastly thanks to all the colleagues and friends in DTU for the valuable discussions, team-building events and dinners together.

Lastly my family, to whom I want to express my deepest gratitude. To my father Angelo, my mother Maria and my sister Valeria for supporting me even if my choices meant being far away from them. Thank you for being always there when I needed.

Abstract

Concentrating solar power plants employ reflecting mirrors to concentrate the incident solar irradiation, firstly converting it into high temperature heat and secondly into electric energy. The stochastic and fluctuating nature of the solar irradiation requires more operating flexibility as compared to traditional systems. The rate of response to frequent load changes and start-up procedures is however constrained by the use of conventional components, designed to operate under steady-state conditions. In particular, steam generator systems were designed for baseload applications and therefore their responsiveness to load changes is limited by thermo-mechanical stress, which might affect the components lifetime or cause failure.

This thesis work has two main objectives. The first one is to quantify the impact of the heating rate constraints on the economy of parabolic trough power plants to assess the prospects for improvement using more responsive steam generators. This is carried out by modelling the transient performance of such power plants and implement control strategies, which account for these constraints. The second objective is to define a method to design the steam generator system considering maximum allowable heating rates and their impact on the performance of the power plant. This is achieved by evaluating the significance of implementing such constraints in the sizing procedure and assessing the transient performance of the new designs. The models are validated against either data available in literature or provided by power plant operators.

The results from this thesis indicate that it is of significant importance to account for the steam generator thermo-mechanical limitations. The use of suitable designs to reach heating rates in the order of 7-10 K/min could increase the electric energy production of the power plant, while at the same time allowing for operating decision flexibility throughout the year. Designing the steam generator systems for such constraints results in different optimal configurations as compared to traditional sizing methods. However, the derived increase in the steam generator cost can be compensated by the gain in electric energy production and associated revenues.

Keywords: Concentrating solar power, parabolic trough, steam generator, start-up, operation strategy, flexibility, optimization

Resumé

Koncentrerende solkraftværker anvender reflekterende spejle til at koncentrere solens stråler, som først konverteres til høj-temperaturvarme og derefter til elektrisk energi. Solenergiens stokastiske og fluktuerende karakter kræver større driftsfleksibilitet i sammenligning med traditionelle systemer. Responstiden ved hyppige lastændringer og opstartsprocedurer er begrænset, da konventionelt udstyr er designet til stationær drift. Dampkedler var typisk designet til grundlastanvendelser og derfor er deres responstid begrænset af termiske materialespændinger, hvilket kan reducere udstyrets holdbar eller forårsage fejl.

Denne afhandling har to hovedformål. Det første formål er at kvantificere hvorledes økonomien for solkraftværker der bruger parabolske trug influeres af begrænsninger for opvarmningshastigheden, hvorved potentialet for at bruge hurtigt responderende dampkedler vurderes. Dette gøres ved at modellere de transiente egenskaber for disse solkraftværker og ved at implementere styrestrategier der tager højde for disse begrænsninger. Det andet formål er at definere en metode til at designe dampkedelsystemet, som tager højde for maksimale opvarmningshastigheder og deres indflydelse på solkraftværkets performance. Dette opnås ved at evaluere betydningen af at implementere disse begrænsninger i dimensioneringsproceduren og vurdere den transiente performance for de nye design. Modellerne er valideret ved brug af data fra litteraturen eller data leveret af operatører af solkraftværker.

Resultaterne fra denne afhandling indikerer at det er væsentligt at tage højde for begrænsninger for termiske materialespændinger i dampkedler. Brugen af passende design for at opnå opvarmningshastigheder i omegnen af 7-10 K/min kan øge solkraftværkets el-produktion og samtidig muliggøre fleksibilitet i driftsbeslutninger året rundt. Ved at tage højde for disse begrænsninger i designprocessen for dampkedelsystemer opnås anderledes optimale designkonfigurationer sammenlignet med traditionelle designmetoder. Den afledte forøgelse af dampkedelomkostninger kan dog kompenseres af øget el-produktion og dertilhørende indtægter.

Nøgleord: Koncentreret solkraftværk, parabolske trug, dampgenerator, opstart, driftsstrategi, fleksibilitet, optimering

Publications

The publications which are based on the work presented in this thesis are listed below and are presented in order of acceptance and relevance. Some of them refer to studies, which are not directly linked to the work presented in this thesis. Nonetheless, they were carried during the last three years and for this reason, they are listed under "Other publications". Chapter 4 is based on the work presented in the journal paper 1 and 2 and conference paper 1. Chapter 5 is based on the work presented in journal paper 3 and 4. The above mentioned papers are presented in the Appendix C.

Peer-reviewed journal papers

1. **Ferruzza, D.**, Topel, M., Laumert, B., Haglind, F. (2018). Impact of steam generator start-up limitations on the performance of a parabolic trough solar power plant. Solar Energy, 169, 255-263.

2. **Ferruzza, D.**, Topel, M., Laumert, B., Haglind, F. (2018). Optimal start-up operating strategies for gas-boosted parabolic trough solar power plants. Solar Energy, 176, 589-603.

3. **Ferruzza, D.**, Kærn, M.R., Haglind, F. (2019). Design of header and coil steam generators for concentrating solar power applications accounting for low-cycle fatigue requirements. Applied Energy, 236, 793-803.

4. **Ferruzza, D.**, Kærn, M.R., Haglind, F. (2018). Design of header and coil steam generators for parabolic trough concentrating solar power plants accounting for dynamic performance requirements. To be submitted (Under internal review).

5. González-Gómez, P. A., Gómez-Hernández, J., **Ferruzza, D.**, Haglind, F., Santana, D. (2019). Dynamic performance and stress analysis of the steam generator of parabolic trough solar power plants. Applied Thermal Engineering, 147, 804-818.

Peer-reviewed conference proceedings

1. **Ferruzza, D.**, Topel, M., Basaran, I., Laumert, B., Haglind, F. (2017). Start-up performance of parabolic trough concentrating solar power plants. In AIP Conference Proceedings (Vol. 1850, No. 1, p. 160008). AIP Publishing.

Other publications

1. Topel, M., **Ferruzza, D.**, Seeger, F., Laumert, B. (2018). Analysis of Plant Performance with Improved Turbine Flexibility: Test Case on a Parabolic Trough Configuration. In AIP Conference Proceedings (Vol. 2033, No. 1, p. 070002). AIP Publishing.

2. Backen, M., **Ferruzza, D.**, Larsen, L. K., Haglind, F. (2018). Hybridization of Concentrated Solar Power and Biomass Combustion for Combined Heat and Power Generation in Northern Europe. Accepted for publication. In AIP Conference Proceedings (Vol. 2033, No. 1, p. 180001). AIP Publishing.

3. Pan, C. A., **Ferruzza, D.**, Guédez, R., Dinter, F., Laumert, B., Haglind, F. (2018). Identification of Optimum Molten Salts for Use as Heat Transfer Fluids in Parabolic Trough Plants. A Techno-Economic Comparative Optimization. Accepted for publication. In AIP Conference Proceedings (Vol. 2033, No. 1, p. 030012). AIP Publishing.

Contents

List of figures

List of tables

Nomenclature

Abbreviations

ACC	air cooled condenser
BH	booster heater
BPVC	boiler pressure vessel code
C	controller
CSP	concentrating solar power
CT	cold tank
D	deaerator
DNA	Dynamic Network Analysis
DNI	direct normal irradiation
DYESOPT	Dynamic Energy Systems Optimizer
ECO	economizer
EVA	evaporator
FW	feedwater
HP	high pressure
HT	hot tank
HTFH	heat transfer fluid heater
HTRI	Heat Transfer Research, Inc.
IHX	intermediate heat exchanger
IRE	integral relative error
ITD	inlet temperature difference

LCF	low cycle fatigue
LP	low pressure
NRMSE	normalized root mean squared error
NTU	number of transfer units
OM	operating mode
OTSG	once-through steam generator
PB	power block
PID	proportional integral derivative
PSA	plataforma solar de Almeria
PTPP	parabolic trough power plant
PV	photovoltaic/process variable
QMOO	queueing multi-objective optimizer
RD	ramp delay
RH	re-heater
RMSE	root mean squared error
SAM	system advisor model
SCA	solar collector assembly
SD	synchronization delay
SF	solar field
SGS	steam generator system
SH	superheater
SM	solar multiple
ST	steam turbine
TEMA	tubular exchangers manufacturers association
TES	thermal energy storage
UTS	ultimate tensile strength
WCC	water-cooled condenser

Subscripts

amb	ambient
ap	approach
avg	average
b	bend
c	cross section
dc	downcomer
dp	driving pressure
e	parallel to the economizer
end	end losses
F	frictional
f	fluid
f	frictional per unit length
fm	friction and momentum
hx	heat exchanger
i	inside
in	inlet
L	length
l	liquid
M	mechanical
m	metal
max	maximum
min	minimum
o	outside
out	outlet
r	riser
ref	reference

s	parallel to the super-heater
sca,loops	sca for each loop
sha	shadowing
spa	spacing
T	thermal
t	total
tl	tube layer
txl	tube for each layer
v	vapour
w	water

Greek symbols

α	stress concentration factor	[-]
β	thermal expansion coefficient	[K $^{-1}$]
Δ	difference	
δ	declination angle	[rad]
η	efficiency	[-]
γ	UA scaling coefficient in part-load	[-]
λ	thermal conductivity	[W/(m K)]
ν	Poisson ratio	[-]
ω	hour angle (Chapter 4)	[-]
ω	outer to inner diameter ratio (Chapter 5)	[-]
Φ_w	non-dimensional geometrical coefficient	[-]
ρ	density	[kg/m^3]
σ	stress	[Pa]
θ	incident angle (Chapter 4)	[rad]
θ	tube coil angle of bend (Chapter 5)	[rad]
θ_z	zenith angle (Chapter 4)	[rad]

Roman symbols

A	area	[m^2]
a	heat exchanger baseline cost modifier (Chapter B	[-]
a	incident angle modifier coefficient	[-]
A_{pt}	solar field efficiency coefficient	[-]
b	heat exchanger specific cost (Chapter 5)	[USD/m^2]
b	incident angle modifier coefficient (Chapter 4)	[-]
B_{pt}	solar field efficiency coefficient	[-]
c	heat exchanger specific cost correction factor	[-]
C_{pt}	solar field efficiency coefficient	[-]
c_p	specific heat at constant pressure	[kJ/(kg K)]
$CAPEX$	capital expenditure	[USD]
CRF	capital recovery factor	[-]
D_{pt}	solar field efficiency coefficient	[-]
E	Young's modulus	[Pa]
F	LMTD correction factor (Chapter 5.2)	[-]
F	focus length (Chapter 4)	[m]
F	force (Chapter 5.3.2)	[N]
f	heat exchanger specific cost front head correction factor	[-]
f_D	Darcy's friction factor	[-]
f_{hx}	indirect TES volume coefficient	[m]
FR	flow rate	[kg/s]
g	Earth's gravitation constant	[m/s^2]
h	heat transfer coefficient	[W/(m^2 K)]
h	specific enthalpy	[J/kg]
HPI	historical price index	[-]

i	interest rate	[-]
IAM	incident angle modifier	[-]
ID	internal diameter	[m]
ITD	inlet temperature difference	[K]
k	bend loss coefficient (Chapter 5)	[-]
k	insurance rate (Chapter 4)	[-]
L	length	[m]
$LCOE$	levelized cost of electricity	[USD/kWh]
$LMTD$	mean logarithmic temperature difference	[K] / [°C]
M	mass	[kg]
$\dot{m}$	mass flow rate	[kg/s]
NTP	number of tube passes	[-]
$OPEX$	operational expenditure	[USD]
p	pressure	[bar]
p_{OD}	heat exchanger specific cost outer diameter correction factor	[-]
PEC	purchased equipment cost	[USD]
Q	thermal energy	[J] / [GWh]
$\dot{Q}$	heat rate	[W]
r	heat exchanger specific cost rear head correction factor	[-]
r	radius	[m]
S	maximum allowable stress	[Pa]
S_{l}	longitudinal pitch	[m]
S_{t}	transversal pitch	[m]
T	temperature	[K] / [°C]
t	thickness	[m]
U	overall heat transfer coefficient	[W/(m^{2}K)]

u	specific internal energy	[J/kg]
V	volume	[m^3]
v	velocity	[m/s]
v_T	heating rate	[K/min]
W	electric energy (Chapter 4.3.3)	[J] / [GWh]
W	width (Chapter 4.1)	[m]
x	spatial coordinate	[m]
y	safety coefficient	[-]
y_n	CAPEX scaling exponent	[-]
z	vertical coordinate	[m]

Chapter 1

Introduction

This chapter presents a general context for the thesis work, a review regarding the previous research in the field, the overall motivation, objectives and methods and an outline of the thesis.

1.1 Context

The increasing energy demand and the underlining risk of increasing climatic adversities due to the growing consumption of fossil fuels are establishing a rising pressure towards the deployment of renewable energy sources. The European Union has the goal of achieving 32 % of renewable generation in the energy mix [1], while some more ambitious countries like Denmark aim at being completely independent of fossil fuel by 2050 [2]. As solar energy is the most abundant energy source available, any technology utilizing it will play a vital role in this transition [3]. Photovoltaic and concentrating solar power (CSP) are the two most common technologies to convert the solar input to useful energy [4, 5]. The former converts directly the solar irradiation by means of a physical process. The latter employs a two-step conversion chain, by first converting the solar radiation into useful heat and later into electric energy. This aspect makes it an interesting solution as it allows for storing thermal energy in a relatively cheap way [6]. This enables it to decouple the solar input from the electric energy production, thus making it an attractive player in the growing fluctuating electricity market.

In 2014, the International Energy Agency expected the CSP technology to play an important role by having an 11 % share in the power production by 2050 [7]. However current trends are lowering these predictions, as in the IRENA Renewable Energy Roadmap [8], forecasts on CSP instalment by 2030

saw a 15 % reduction in power to be installed as compared to the previous projection. Due to the steep falling of photovoltaic and battery costs, the competition is growing stronger and some fundings are moving towards the photovoltaic sector. Secondly, the moratorium of the feed-in tariffs in Spain [9] and of the loan guarantee in USA [10] are creating a difficult economic environment. Nonetheless, the power installed is predicted to increase by 40 GW in the next 10 years in a conservative scenario [8]. In addition to this, big projects like the Ouarzazate facility in Morocco [11] or the Solar Park [12] near Dubai are being completed or under development, proving the interest in the technology and in its ability to dispatch electricity at will.

Parabolic trough power plants (PTPP) represent the most technically and economically mature technology among CSP plants. They account for around 80 % of both the currently installed and planned to be constructed power plants [13–15]. In such systems, the conventional fossil fuel fired boiler is replaced by a series of parabolic mirrors to concentrate direct solar radiation onto the receiver tubes and convert it into useful high-temperature heat and in a successive step into electricity by a Rankine cycle. The main link between the solar field (SF) and the power block (PB) is the steam generator system (SGS). It consists of a train of heat exchangers which transfer the useful high-temperature heat from the heat transfer fluid (HTF) to the water coming from the condensing line of the Rankine cycle. The temperature of the liquid water is raised until reaching superheated steam conditions at the inlet of the turbine [14].

In order to guarantee the development and competitiveness different technical and economic challenges need to be addressed. From a technical perspective, the fluctuating and stochastic nature of the solar irradiation causes operating challenges such as frequent variations in load and daily start-up and shut-down procedures. A way to overcome these challenges is to improve the operating performance by maximizing the responsiveness of the components towards fluctuating loads. By doing so, it is possible to utilize the solar irradiation as effectively as possible, therefore maximizing the electric energy production and profitability [16]. In order to maximize the flexibility (i.e. to increase the responsiveness of the power plant to a change in the power load or in irradiation), and both the peak and the baseline rate of electric power production, it is essential that all the components are able to start as quickly as possible and enable the CSP plants to readily start harvesting the incoming solar irradiation. On the other hand, there might be limiting factors for one component, which might reduce the required heating rate for another. For example, if the receiver or solar field are the limiting factors, there is no need for the SGS to be able to start up at a faster rate than that of the solar field. On the other hand, in order to preserve the lifetime of certain components, the maximum gradient of temperature (heating rate) is constrained by the induced

thermo-mechanical stresses which might affect the lifetime of the components or cause failure. These are calculated according to low-cycle fatigue (LCF) theories and norms for the component considered. CSP plants currently in operation have SGSs which were designed as conventional heat exchangers, not optimized for transient operation [17]. Improving the design of such components is one of the ways to enhance the flexibility and performance of such power plants.

1.2 Previous research

The dynamic performance of PTPPs was previously analysed, although some of the models available in literature dealt mainly with the validation of the detailed modelling of the solar field [18–21]. Blanco et al. [19] presented a model of a parabolic trough power plant (PTPP) and validated it against experimental data, but in this case, the model of the power block was developed with a simplified correlation. Another approach was presented by Abed et al. [22], in which a detailed dynamic model in APROS (Advanced Process Simulation Software) was validated against the operational data of Andasol II. The focus of the study was to develop a detailed control strategy of the power plant by means of PI (Proportional-Integral) controllers. The model presented focused mainly on daily control. A similar approach was undertaken by Montanes et al. [23] but by developing a physical model in Modelica language. Research was also performed on modelling and evaluating the performance of PTPPs with both oil and molten salts as heat transfer fluid, with and without gas-fired backup. For instance, Boukelia et al. [24, 25] investigated this by modelling specifically the power block in Ebsilon professional [26] and evaluated the optimal levelised cost of electricity (LCOE) by means of artificial neural network algorithms implemented in Matlab. Biencinto et al. [27] performed modelling of PTPPs both with nitrogen and Therminol-VP as heat transfer fluids. The model of the solar field was validated in detail against real plant data, while the overall model was compared with SAM (System advisor model) [28]. In this case, the model was used to compare the annual yield of the two configurations.

Bonilla and Jose [29] modelled a direct solar steam generator PTPP using object-oriented modelling and calibrated it by comparing the model results with plant data from CIEMAT-PSA (Centro de Investigaciones Energéticas, Medioambientales y Tecnológicas Plataforma Solar de Almería) by means of a genetic algorithm based multi-objective optimization. The study focused mainly on the solar field detailed modelling and not on the overall power plant. Blanco et al. [19] developed a model in the Wolfram mathematical

software and compared the results to available power plant data. In this case, the power block was not modelled in detail, but thermal efficiency correlations as a function of the thermal input were used. Another example can be found in the work performed by Al-Hanaei et al. [30], in which the authors developed a model of the Shams I power plant. Overall many simulation tools are available to perform the design and performance evaluations of a CSP plant. System Model Advisor (SAM) from NREL [31–34], Greenius from DLR (Deutschen Zentrums für Luft und Raumfahrt) and Solergy from Sandia National laboratories [35] are commonly known tools in the CSP community. Nonetheless, it needs to be stressed that none of the aforementioned models, research work or numerical tools did account for thermo-mechanical constraints of the steam generator system.

Regarding the study of the impact of thermo-mechanical constraints on the performance of CSP plants, attention was given towards the steam turbine limitations and start-up schedules [36–39]. In particular, Topel et al. [37–39] studied the potential for power plant performance improvement through the increase of steam turbine flexibility considering different operational enhancements for start-up time reduction. Similar research work is not found in the literature regarding the steam generator system. One of the closest approaches was performed by Pelagotti et al. [40] but their calculations did not take into account start-up schedules of steam turbines or rates of heat availability, nor yearly performance evaluation of such power plants. The main focus was given to the detailed dynamic model of the steam generator and low cycle fatigue analysis. From a broader perspective, constraints from both steam turbine and steam generator were never considered at the same time, during the evaluation of the power plant performance.

Concerning the research regarding the steam generator at the component level, one of the most recent works was performed by Gonzalez-Gomez et al. [41–44]. The authors developed a method to design TEMA (tubular exchanger manufacturer association) type heat exchangers for CSP applications and evaluated the thermo-mechanical stress evolution during the start-up phase for assumed heating rate constraints. Lastly, they also evaluated the lifetime of the components with low-cycle fatigue (LCF) theories. The authors focused mostly on the component perspective and did not include any system consideration to determine optimal heating rate constraints. Previously, methodologies have been developed and refined to determine the heating rate constraints for conventional steam generator systems [45–47]. The authors determined a method to develop optimal start-up curves in order to minimize the induced stresses to the components and speed-up the start-up procedure.

Regarding the steam generator field of research abundant material can be found and traced back up to two centuries ago, as the technology is relatively old,

but great number of work has been performed since the development of nuclear power [48]. In addition, with the advent of modern computers, more focus was given towards the dynamic performance modelling of steam boilers in the late '90s and early 2000s as there started to be a growing interest in the flexibility of the electricity market [49, 50]. Brian Elmegaard [49] developed a dynamic model in DNA (Dynamic Network Analysis) for a biomass based IGCC plant. Kim Sørensen [50] developed dynamic model into an optimization framework to account for both control problems and temperature gradients.

Recently, many papers dealt with the optimization of the design of conventional heat recovery steam generators. For instance, Duran et al. [51] applied a genetic algorithm to optimize the geometric design of heat recovery steam generators (HRSG). The focus was only on the geometrical design. A similar approach was presented by Franco et al. [52], and in this case, a two-step optimization approach was presented, by firstly minimizing pressure drops and secondly minimizing the dimension of the heat exchangers. As for the associated cost, for instance, Wildi-Tremblay and Gosselin [53] used a genetic algorithm to minimize both investment and operational costs. Gonzalez-Gomez et al. [42] applied a cost-based optimization methodology to find a trade-off between levelized cost of electricity and investment costs for the SGS, specifically for parabolic trough power plant applications.

In general, it can be said that many design methodologies are available and applied in literature, but none so far have taken into consideration the LCF limitations during the design phase. This is done as a performance check afterwards by calculating what is the maximum allowable heating rate for a specific given design. On a broader perspective, never before the transient requirements from a system point of view were integrated into the design approach.

1.3 Motivation and objectives

Even though the steam generator systems account for a small percentage in terms of the investment cost of CSP plants (1.83 % of the total cost according to Ref. [14]), they still represent the link between the solar field and the power block of the systems. Failure due to excessive thermo-mechanical loading could hinder the performance of the power plant both from a technical and economic perspective. However, many of the currently installed CSP plants are equipped with SGS, which were designed in a traditional way as they were previously targeted to baseload power plants. Furthermore, currently, the design of such components does not take into account LCF constraints, as these are meant to be a performance check for a given design.

The improvement of the thermo-mechanical performance could guarantee a safer operation to the entire power plant, but at the same time, it is important to determine which degree of responsiveness is necessary to reach to significantly improve the power plant performance. These points constituted the first main motivation and research question of the whole Ph.D. thesis. What is the impact of such constraints on the power plant performance and for which maximum constraints should we aim at? And once these criteria are found, the next question is: how can we properly design the steam generator to take these into account?

The objectives of the thesis can be considered split into two different perspectives. From a system level standpoint, hence power plant performance, the goal is to evaluate the impact of the heating rate constraints on the parabolic trough CSP plants electric energy production and flexibility towards operating strategy. Once these indicators and system constraints are obtained, the second aspect includes the component level perspective. The related main objective is to determine a method to properly design the SGS accounting for such constraints, while at the same time evaluating the significance of doing so as compared to more conventional approaches. These objectives can be translated into the following tasks.

i To develop and validate a parabolic trough power plant model which accounts for the steam generator thermo-mechanical constraints and start-up procedure strategy

ii To analyze the impact of the heating rates on the power plant performance and flexibility towards start-up operating strategies

iii To develop and validate a design tool and dynamic model for the steam generator system

iv To quantify the significance of including low cycle fatigue constraints in the design phase of the steam generators

v To design a steam generator for parabolic trough power plants accounting for dynamic performance, thermal stresses and impact on the system performance

Figure 1.1 illustrates the general approach to the thesis work. The result from the system and component level analysis are interdependent and the final optimization needs to integrate constraints and boundary conditions deriving from both aspects. Both modelling levels account for steady-state nominal design and dynamic performance evaluation. The CSP plant modeling was carried out using DYESOPT [54] (Dynamic energy system optimizer), a techno-economic tool developed and validated at KTH, Royal Institute of Technology in Sweden. The steady-state nominal design was implemented in Matlab [55], while the transient performance evaluation in TRNSYS [56]. All the new components and power plant layouts were implemented in the tool. The SGS nominal design was performed in Matlab, while the dynamic simulations in Dymola, which employs the Modelica language [57]. The thermodynamic properties were calculated using REFPROP 9.1 [58]. Table 1.1 presents an overview of the system and component modeling and the development for each section.

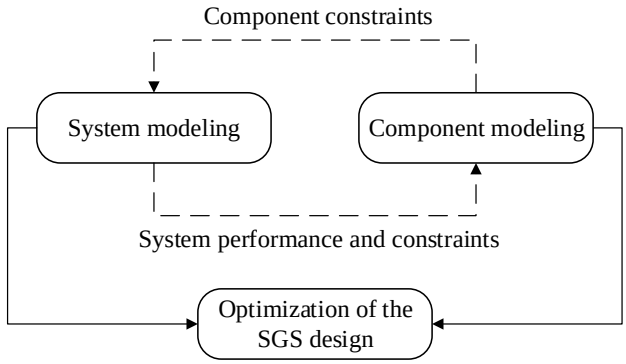

Figure 1.1: Overall method approach to the thesis work.

Table 1.1: Overview of the model frameworks and development.

	CSP models	SGS models
Chapter 4.2	Development and validation of a PTPP model. Implementation of the SGS control strategy. Analysis of the impact of the heating rate constraints.	Determination of the optimal heating rate constraints.
Chapter 4.3	Development and validation of a gas-boosted PTPP model. Further development of a start-up procedure control strategy. Optimization of the start-up procedure.	
Chapter 5.2		Development and validation of the steady-state sizing model. Optimization of the design.
Chapter 5.3	Development of the two split re-heater configuration for the PTPP model. Analysis of the power plant performance with different SGS configurations.	Development and validation of the transient thermo-mechanical models. Optimization routine accounting for dynamic performance.

1.4 Thesis outline

The thesis is structured as follows.

Chapter 2 presents a general background on CSP systems and the main sub-systems are briefly described. The operation of the power plants is described with a particular focus on the start-up procedure and its constraints.

Chapter 3 presents a general background on steam generator systems, their classification and heat exchanger arrangement. An overview of the operation of such component is also presented, with a particular focus on the controlling strategies during the start-up procedures.

Chapter 4 presents the framework of the CSP modelling tool and a general description of how the underlying algorithms work. It presents the results on the study of the impact of the heating rates on parabolic trough plants performance and their influence on the operating strategy flexibility.

Chapter 5 presents the framework of the SGS modelling tool developed during the thesis both for the design procedure and the transient response analysis. It presents the results of the steady-state nominal sizing and the significance of including LCF constraints during this phase. It also presents a method on how to account for thermo-mechanical stresses and the impact of the different designs on the power plant techno-economic performance during the design phase.

Chapter 6 concludes the thesis and summarizes the modelling approach key findings and suggestions for future works.

The thesis is ended with a list of references and appendices which comprises additional results and parameters used during the research work. Appendix C presents the main papers on which the thesis work is based on.

Chapter 2

Concentrating solar power

This chapter provides an overview of the CSP technology and the different plant configurations available. It describes the main components such as the solar field, thermal energy storage and power cycles. Lastly, a typical morning start-up operation is described.

2.1 Concentrating solar power technology

The CSP technology experienced its first development between 1982 and 1991 during the oil shock of the 80s [59], however, no further research or commercial development occurred until 2006 [60]. A rebirth happened with the commissioning of Andasol, a 150 MWe PTPP project developed in Spain, which then became the main reference for the parabolic trough power plants [60]. Since then, the technology developed and currently, 5.13 GWe are installed throughout the world, especially in locations such as Spain, USA, Chile, Morocco and UAE [61].

CSP can be explained as a two-step conversion by which a combination of mirrors and lenses are used to concentrate the direct solar irradiation and convert it into useful high temperature heat. This energy can be either directly used for process heat or converted into electricity by means of conventional thermodynamic cycles [5]. In CSP plants, the concentration is needed to increase the temperature of the useful heat, therefore, for the same heat sink temperature, higher thermal efficiencies are reached. Concentration is achieved by focusing the incoming direct irradiation on a large optical system (reflector) onto a smaller surface receiver [62]. Due to this, and unlike its photovoltaic counterpart, CSP systems are best suited only to areas with

high percentage of clear sky and high direct normal irradiation (DNI), making regions with at least 1700 kWh/m^2/year the most attractive locations [14].

Generating high temperature heat as an intermediate step allows a CSP plant to incorporate relatively cheap ways of storing energy in the form of thermal energy storage systems (TES), that enable the plant to convert it for later use. On the same note, having conventional power generation cycles to convert the energy, allows for the integration of more conventional fossil fuel based heat sources (hybridization). Figure 2.1 summarizes all the above considerations. By analyzing the conversion chain, three main sub-systems can be identified: the solar field block which comprises both the reflector and receiver, the thermal energy storage block and the power cycle block. The next sections will give a brief overview of all the three of them.

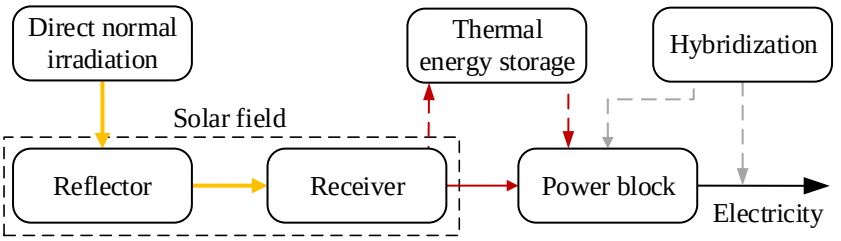

Figure 2.1: Schematic conversion flow in a concentrating solar power plant.

2.2 Solar field

The solar field is the responsible block for concentrating the direct solar irradiation. In order to collect as much irradiation as possible, the technology needs to be equipped with a tracking mechanism, which allows following the position of the sun throughout the day. Regardless of the particular collector configuration (receiver plus reflector), the heat absorbed by the receiver is transferred to a heat transfer fluid (HTF), which is responsible to exchange the energy with the working fluid of the power cycle block [5].

The size of the solar field is specified in terms of mirror aperture area or in terms of solar multiple (SM), which indicates the ratio of the power delivered at nominal conditions over the nominal thermal power required by the power block. In the case of solar multiples higher than 1, the solar field is oversized. This is required when the power plant is integrated with TES, in order to deliver enough heat to both charge the storage and operate the power cycle at design

conditions [63]. In case the storage is absent, it is still of economic interest to oversize the solar field to improve the electricity production of the power plant.

The different solar field technologies are generally classified according to the collector configuration. In case of fixed type collector, the receiver remains stationary and the focusing device needs to track the sun to always reflect the light to the same position. In moving type collectors, the receiver follows the mirror mechanisms, allowing easier tracking at the expense of more difficult transport mechanism for the HTF. The receiver can then be a linear or point focusing device allowing for a one-axis or a two-axis tracking mechanism. Up to now, four main technologies have emerged and they can be classified according to the receiver and tracking mechanism as summarized in Table 2.1.

Table 2.1: Concentrating solar power collector technologies.

Receiver / Focus	Line	Point
Fixed	Linear Fresnel	Central tower
Mobile	Parabolic trough	Parabolic dishes

2.2.1 Parabolic trough collectors

Parabolic trough collectors are mobile systems with parabolic shaped reflectors focusing on a linear tubular receiver [64]. Figure 2.2 illustrates a PT scheme on the left, and under real operation on the right. It is the most mature technology and saw development since the 1870s when it was used to run a 375 W engine [65]. Since the 1980s it developed into the modern concept in which the parabolic trough collectors concentrate the solar radiation to heat up the HTF (usually thermal oil), which is pumped through a vacuumed tubular receiver, that guarantees low convective thermal losses. Due to the properties of thermal oil, 393 °C is the maximum achievable temperature in order to prevent fluid degradation. There is however research regarding the feasibility study of employing other heat transfer fluids (such as molten salts) to increase this temperature up to 550 °C [66]. In some cases, the molten salt can also be used as a storage media to increase the energy output of the power plants.

2.2.2 Linear Fresnel collectors

Linear Fresnel is the fixed receiver type analogous of the PT collectors. They comprise many long row segments with a focus on a linear fixed receiver. The

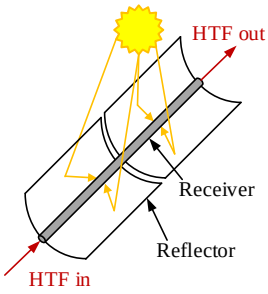

(a) Schematic.

(b) Parabolic trough test loop [67].

Figure 2.2: Parabolic trough collector.

mirrors rotate together to maintain the focus fixed on the receiver, giving considerable freedom of design [68]. Figure 2.3 shows a schematic concept (left) and an application of this technology (right).

Lower wind load and lower risk of oil leakage are the main advantages of a low profile fixed structure, as contrary to large parabolic reflectors that might become unwieldy. Moreover, they allow for easier cleaning systems, as taller vehicles are required for the parabolic troughs. However, this kind of arrangements introduces more losses and is less commercially mature making it more expensive than the mobile counterpart. Its characteristic makes it more suitable for relatively low-temperature applications because of higher thermal loss coefficients and for hybridization with photovoltaic plants [70].

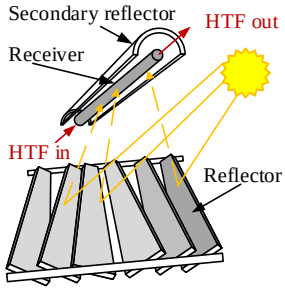

(a) Schematic.

(b) Plant in Liddell, Australia [69].

Figure 2.3: Linear Fresnel collector.

2.2.3 Dish stirling

Parabolic dish systems employ paraboloidal mirrors which track the sun and focus solar energy into a point focus receiver where the heat is either used locally in a thermal engine or transferred to a ground based plant. The most common use of this technology is the adoption of Stirling engines to produce electricity [71]. This technology has shown the highest efficiency (up to 30 %), yet the high cost makes it not commercially viable. Nowadays applications up to 10 MWe are present in the market, but its high efficiency makes it an interesting option for future development. Figure 2.4 illustrates a schematic and a current application of a dish Stirling engine.

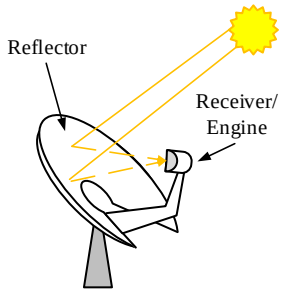

(a) Schematic.

(b) Dish Stirling engine facility [72].

Figure 2.4: Parabolic dish collector.

2.2.4 Solar tower

Solar tower central receiver systems consist of an array of tracking mirrors (heliostats) which reflect the direct irradiation to a central receiver placed on top of an elevated support (tower). Figure 2.5 illustrates a schematic (on the left) and an overview of the Gemasolar power plant in Spain (on the right). The mirrors are properly spaced to avoid shadowing and interference. The receiver is designed to effectively absorb the incoming radiation and absorb the heat at very high temperatures (up to 1000 °C) [73]. This configuration has the advantage of converting the solar energy in a fixed region allowing more cost-effective conversion processes. Secondly, as it is not characterized by kilometers of receiver tubes like in the PTPP case, it is possible to use the molten salt as both HTF and storage material increasing its yearly thermal efficiency. The main disadvantage of such configuration is that the heliostats

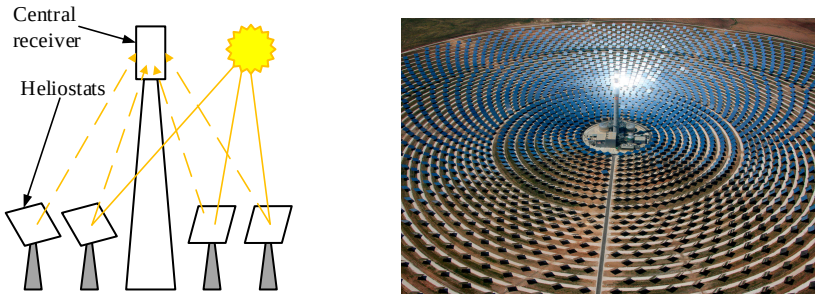

(a) Schematic. **(b)** Gemasolar power plant [74].

Figure 2.5: Solar tower.

generally do not point towards the sun, thus reducing the collected radiation as compared to the dish collectors [73]. Furthermore, having a single receiver point, makes the plant more susceptible to failure of such component, as a shut down procedure would be required. Currently, solar tower central systems represent 15 % of the installed power and they are experiencing an increasing trend in interest.

2.3 Thermal energy storage

Energy storage is defined as the storing of a form of energy which can be drawn upon at later time to perform some useful operation [75]. In the case of TES, heat is the useful energy which can be later converted. This concept is summarized in Figure 2.6. Depending on the storage medium, the TESs can be classified as sensible, latent or thermochemical systems [75].

Sensible TES consists of a medium which stores energy in the form of temperature change. In such systems, the heat will be transferred to the storage medium by raising its temperature, while it will be extracted by cooling it down. Sensible storage media are sub-grouped into liquid and solid. The latter are mainly preferred for building applications, but they found applicability also for high-temperature applications. The reduced risk of leakage and low specific costs are the main advantages of such systems, however, they manifest low heat storage density and high thermal losses. Concrete is the most used material in this sub-category for CSP applications. Liquid media have been the preferred choice, as they allow for either having

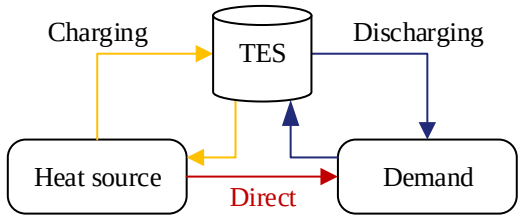

Figure 2.6: Thermal energy storage work principle.

two different tanks at two set temperatures (cold and hot), or for stratification enhancing the stored energy density. In CSP plants, molten salt is the prevalent material, which becomes also the HTF in the case of solar towers [76]. The most common salt is the SolarSalt, which is a 60/40 % mixture of $NaNO_3$ and KNO_3 [77].

Latent media store the energy in the form of phase change of the medium. In the solid-liquid transition, the heat is transferred to the medium by melting it, while it is extracted through solidification. High energy density, thermal stability, non-corrosiveness and cost decrease potential are the main advantages of such materials [76]. However, they are characterized by low thermal conductivity, slowing down the process of charging and discharging [78]. Promising materials are $NaNO_3$ and LiBr, as they present melting points around the molten salts operating temperatures [79].

Thermochemical solutions store thermal energy by exploiting the enthalpy of reaction of reversible chemical reactions. During the charging phase, a compound is split by an endothermic process into two or more simpler compounds which are stored separately. When the heat is needed, these are allowed to react again in an exothermic reaction, thus releasing the energy [75]. The most common reaction is the dissociation of ammonia [80]. These systems present the highest energy density, nonetheless, they are still at an early development stage, involving high costs [76].

TES systems can also classified according to their integration into the CSP plant [75, 77, 78]. They can be divided into active and passive systems. In the former category, the storage medium is directly circulating between the heat exchangers for transferring the energy either to the HTF or the power cycle working fluid. In the first case, they are sub-classified as indirect solutions, as an intermediate heat exchanger is needed. In the second case, they are sub-categorised as active systems as the TES medium is also the HTF medium of the solar field. Passive systems exploit a dual medium configuration in which

the HTF passes through the material for charging and discharging, therefore the storage medium itself does not circulate. These materials are mainly solid substances like concrete. They are an attractive solution as they present a very low specific cost, but challenges like low thermal conductivity or high thermal losses need to be overcome.

2.4 Power block

The Brayton cycle, the Rankine cycle and the combined cycle are the three mostly used thermodynamic cycles in CSP applications [81]. The Brayton cycle configuration consists of a volumetric air receiver atop and an adapted gas turbine, usually placed next to the solar collector in order to minimize thermal losses. This configuration is quite flexible and allows for hybridization with external fossil fuel fired combustors for higher production or efficiency [81]. Concerning the steam cycles, usually, a regenerative Rankine reheat cycle is employed. Reheat implies that the steam is expanded in a high and low-pressure turbine stage with a heat addition in between. Regeneration implies that fractions of the expanded steam are bypassed and used to pre-heat the water going to the steam generator.

When the steam generation happens directly in the solar field without using an intermediate HTF, the layout is defined as direct steam generation (DSG) [81]. Brayton and Rankine cycles can be used in two combined cycle configurations. In a first approach, the solar Brayton cycle is used as the top cycle to the bottoming Rankine cycle in a classic parallel configuration. In a second approach, the solar field input is used to provide heat to the evaporator, while the other SGS exchangers are in a heat recovery configuration from a conventional natural gas turbine. This is defined as an integrated solar combined cycle (ISCC). In the case of low temperature applications, the organic Rankine cycle can be applied. In this case, water is substituted by an organic substance (like R134a) as a working fluid [82].

Even though many configurations exist, Rankine cycle based power plants represent still the 90 % of the installed CSP capacity [8]. Nonetheless, it still presents drawbacks mainly related to the peculiarity of solar applications. As the plants are frequently located in desert regions, the amount of water required from the condenser might be limited by the scarce availability. Using air-cooled condensers is a way to overcome this issue at the cost of increased investment costs and electric parasitic consumption [83].

2.5 Parabolic trough power plants

Figure 2.7 illustrates a general layout of a PTPP, which is the main reference for this thesis work. The solar field comprises a large array of parabolic trough collectors. PTPP can be integrated with optional heater both for preheating the HTF (HTFH) during the morning start-up procedure or to boost the steam temperature at the outlet of the superheater (SH). The HTF is most commonly thermal oil (Therminol VP1 or Dowtherm A) and is indicated in the figure by the red lines. The thermal storage is integrated as indirect active system in form of a two-tank molten salt (yellow lines in Figure 2.7) storage which exchanges energy with the HTF by means of an intermediate heat exchanger (IHX). The HTF provides the required thermal input of the Rankine cycle to the SGS, which comprises an economizer (ECO), an evaporator (EVA), a superheater (SH) and a reheater (RH). The reference evaporator for this thesis work is a natural circulation configuration (Figure 2.7 does not illustrate the steam drum in order to avoid additional complexity to the layout). The blue cycle summarizes a simplified scheme of a regenerative Rankine reheat cycle with the high pressure (HP) and low pressure (LP) stages of the steam turbine (ST), deaerator (D) and air-cooled condenser (ACC). If the Rankine cycle is hybridized, there is the possibility to increase the steam temperature with a gas-fired booster heater (BH).

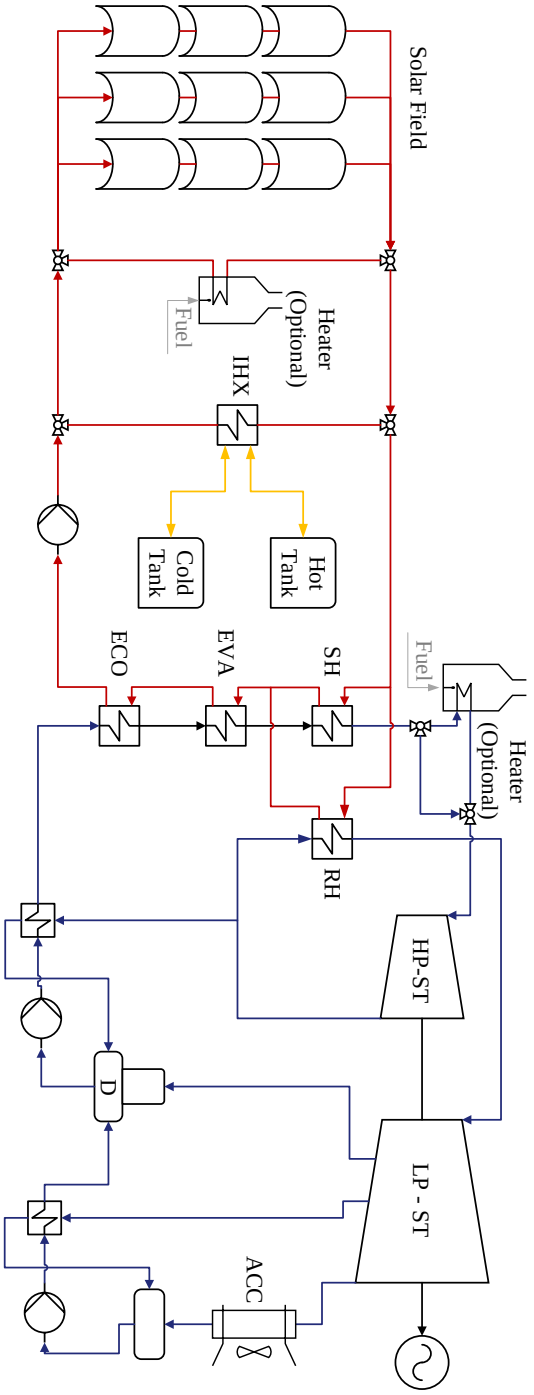

Figure 2.7: General parabolic trough power plant layout.

2.6 Start-up procedure of parabolic trough power plants

The start-up procedure of a CSP plant needs to take into account constraints from the three different blocks characterizing it. Regarding the power block, the process is rather similar to that of a conventional power plant and can be time-consuming due to the turbine and steam generator constraints. In addition, the high inertia of the parabolic trough field can cause delays from a solar field perspective. The start-up sequence comprises the following steps [84–86]:

1. **Initial power plant conditions**: Assuming that at the beginning of the day the power plant is shut down, no power is produced yet and the solar field is defocused in a position to minimize the wind loads. The HTF is recirculated in the receiver tube loop in order to maintain an even temperature distribution in the pipes and minimize potential thermal stresses [87]. If TES is available, the cold tank is monitored to avoid the molten salts temperature to fall below the freezing temperature [88]. The steam generator valves are closed and the drum water level is monitored. The steam turbine is in turning gear mode and rotated by a motor to allow for even cooling and avoid bending. There is no steam in the system.

2. **Tracking and focusing**: When the DNI is high enough and the wind is below the allowable threshold the mirrors start the tracking and focusing to the receiver and if needed a fine tuning of the focus mechanism can be done manually.

3. **HTF heating**: The recirculating HTF temperature is increased and the process can be aided before the first sun hour by an optional heater. The HTF keeps on recirculating in the receiver loop until it reaches an allowable temperature set by the steam generator system. At this point, the valves to the PB are opened and the first heat input is provided to the Rankine cycle. The HTF mass flow remains constant and any surplus of energy is dumped through defocusing.

4. **Steam generator start**: Steam mass flow is produced when the heat is provided to the evaporator. Until a minimum value of mass flow rate is produced, the valves are closed and the steam remains in the subsystem. Meanwhile, the condenser starts to evacuate air from the system and a vacuum pump is used as an initial source of vacuum during start-up. The turbine shaft steam sealing is operated to avoid air entering the turbine. The necessary steam is provided by either the steam generator itself or an auxiliary boiler.

5. **Preheating of the steam pipes**: Once a minimum mass flow rate is produced in the steam generator, the valves are opened and the steam is distributed to the system. At the beginning, the turbine is bypassed and the water flows to the condenser. In the meanwhile, the condenser pressure starts to decrease. Once the steam reaches a sufficient degree of superheat, the turbine start-up procedure takes place. The allowable steam temperature is determined in order to minimize the difference with the turbine metal temperature. The proper turbine start-up schedule is chosen in order to minimize thermal stresses. If an optional heater is used, this phase can be shortened by using booster heaters to increase the steam temperature and reach the allowable degree of superheat at an earlier stage.

6. **Steam turbine start**: When the steam is admitted to the turbine, the roll-up phase begins. The turbine is slowly turned up to its nominal speed and in this phase, the water pressure remains constant at the minimum allowable value. Once the nominal rotational speed is reached, the HTF mass flow rate starts to increase by checking the heating rate constraints of the SGS. The mass flow rate and pressure are increased.

7. **End of start-up procedure**: The end of the start-up procedure is reached when the nominal values of steam mass flow rate, pressure and power are obtained.

Chapter 3

Steam generator systems

This chapter presents an overview of the steam generator technologies and the different configurations available. It describes the main heat exchangers in the CSP industry, among which the header and coil configuration. It also presents the thermo-mechanical limitations and operation challenges during transient operation.

3.1 Technology

As previously mentioned, the steam generator system transfers the thermal energy (from combustion gases or other fluids) to the incoming liquid water, evaporating it and making it reach the design superheated conditions for the steam turbine inlet. The economizer, evaporator, superheater and re-heater are the four main heat exchangers, which constitute a steam generator system. In case of absence of re-heat in the Rankine cycle, the re-heater is avoided. It is common practice that these heat exchangers are placed in series with the re-heater in parallel to the superheater. However, there are some designs which include the economizer, evaporator and superheater in the same pressure vessel [89]. Figure 3.1 illustrates a typical temperature profile in a counter-current arrangement, summarizing the role of the three components.

The function of the economizer is to pre-heat the incoming subcooled water few degrees below saturation conditions (approach point) in order to avoid steaming as the vapour formation could lead to flow instabilities, vibrations and fouling. The superheater (and similarly the re-heater) role is to raise the steam temperature up to the designed superheated conditions at the inlet of the turbine. In the case of the superheater, the steam is at high pressure

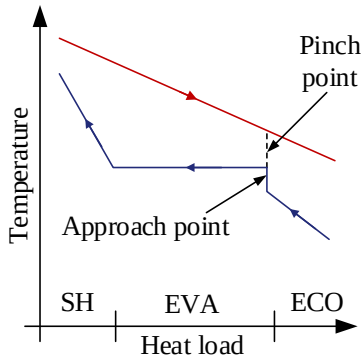

Figure 3.1: Typical temperature profile in a counter-current arranged steam generation process.

(around 100 bar), thus requiring tubes and shells to be designed with high thickness. In the re-heater case, the steam pressure is lower (around 20 bar), thus requiring lower thickness. However, lower heat transfer coefficients are achieved in the re-heater, thus requiring more heat transfer area. The evaporator is the main component of the SGS, both in terms of cost and heat load. The main purpose is to vaporise the liquid water and bring it to saturated vapour conditions.

Depending on the evaporator configuration, the steam generators can be categorised into those which include a steam separation point and those which do not, termed as once-through steam generators (OTSG). The most common separation system is the steam drum, which acts as both a water reservoir and a separation device, by means of cyclones. In these cases the liquid/vapour mixture is circulated and, if no pump is assisting this process, the configuration is termed as natural circulation. This process is driven by the density difference between the liquid water leaving the steam drum through the downcomer tubes and the vapour/liquid mixture going to the drum through the riser tubes.

If a circulation pump is present, the configuration is termed as assisted circulation. The natural circulation configuration provides the advantage of absent parasitic consumption and self-adaptability to possible changes in load. The assisted circulation can also be used at high pressures, as the difference in density lowers for higher pressure and allows manual control over the circulation (at the cost of parasitic consumption). In OTSG, there is no circulation and the water is pumped through a single circuit until it reaches superheated conditions. This configuration allows for pressure up to the

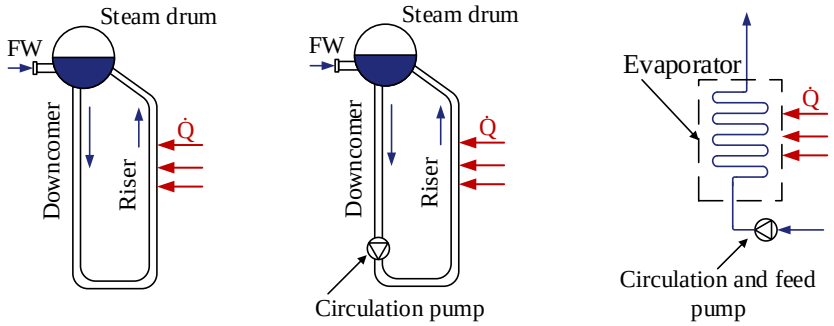

(a) Natural circulation **(b)** Assisted circulation **(c)** Once through

Figure 3.2: Evaporator circulation configurations.

supercritical design, lowering internal piping and valves, for faster starts due to lower volumes of water (hence lower thermal inertia). However, it is characterized by a higher sensibility to thermal input transients. Figure 3.2 illustrates the three evaporator configurations.

Considering the PTPP, the three main SGS heat exchangers (EVA, SH and ECO) are connected in series and the re-heater arrangement may be divided into two configurations. In the first case, the RH is parallel to the superheater and all the thermal load is transferred into one heat exchanger. In a second case, the RH is split into two heat exchangers, parallel to both the superheater and the economizer. The main advantage of the latter configuration is the lowering of the temperature difference between the HTF and the water side, thus minimizing thermal stresses. However, this arrangement introduces an additional component at the cost of more valves and pipings and an increased re-heater cost. Figure 3.3 illustrates the two configurations.

In the past, the tubular exchangers according to the TEMA (Tubular exchanger manufacturer association) standardization were the majority of the SGS heat exchangers used by the CSP industry. In particular, the evaporators were designed as a Kettle reboiler type, which is characterized by large diameter shells and thick tube plates, thus increasing associated thermal stresses and lowering their responsiveness to start-ups or changes in load. In this context, the header and coil configuration is a promising solution to overcome such a problem.

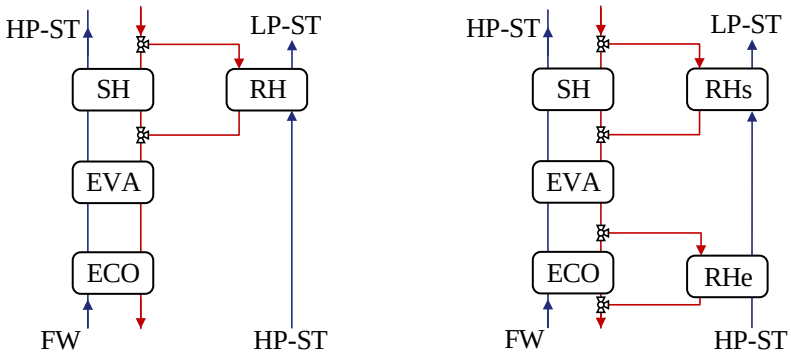

(a) Single re-heater **(b)** Two split re-heater

Figure 3.3: Re-heater configuration in concentrating solar power plants.

3.1.1 Conventional designs

Tubular heat exchangers are generally made of circular tubes and are quite flexible towards various design objectives as they can be constructed for high and low pressures in different applications [90]. In CSP applications, the shell and tube configuration is the most adopted [41]. They are built by a bundle of round tubes mounted in a cylindrical shell with the tube axis parallel to that of the shell. One fluid flows in the tubes, while the other in the shell across or along the tubes. Baffles can be used to deviate the flow of the shell fluid, while the tubes can be either straight or U-bended.

There are many configurations for the shell type (seven according to the TEMA standards), but in case of power production and CSP, the F and K type shells are the most common. The former employs a longitudinal baffle to enhance the exchanger effectiveness, resulting in a two shell passes and U tube configuration. The latter is a kettle reboiler used for pool boiling applications. Figure 3.4 illustrates a schematic for the Kettle reboiler (on the left) and TEMA F (on the right).

In Kettle reboilers, vapour and liquid are separated in the space above the bundle, and the vapour flows overhead to the riser, while the liquid is drawn to the downcomer. Low circulation rates, horizontal configuration, and all-vapour return flow make kettle reboilers relatively insensitive to system hydraulics [91]. As a result, they tend to be reliable in a wide range of operation. That explains why at the early stage of the CSP industry they were the chosen configuration for

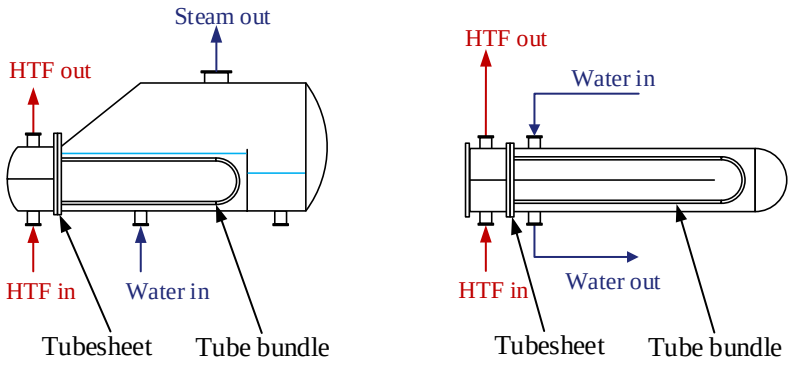

(a) Kettle reboiler **(b)** TEMA F

Figure 3.4: Conventional TEMA heat exchangers.

evaporators. However, low circulation ratios make them susceptible to fouling, while large K-shell makes them relatively expensive. Common to both TEMA K and F heat exchangers is the thick tube plate, which distributes the HTF flow to the tube bundle. Due to the flat shape, a high thickness is required to withstand pressure loads, making it susceptible to thermal stresses [41–43].

3.1.2 Header and coil design

In order to overcome the inherent higher stresses of the plane tubesheet of TEMA designs, it is possible to employ cylindrical manifolds (or headers) to redistribute the HTF flow to the tube bank [40, 92]. Moreover, having separated inlet and outlet manifolds allows for avoiding vertical gradient of temperature as compared to the tubesheet [43]. Lastly, in order to avoid long tube/shell configurations, the tubes can be coiled to have a compact design. In the case of single phase heat exchangers, the water flows in the tube side, while the HTF on the shell side. A simplified drawing of the geometry is presented in Figure 3.5.

In the case of the evaporator, the configuration is different. Firstly, the natural circulation is the chosen configuration as it suits pressure levels typical of CSP plants. Secondly, in this case, pool boiling is the chosen evaporating configuration, with the HTF flowing in the tube side. In order to improve the performance towards thermo-mechanical constraints, the evaporator heat exchanger is split in two. Hence, lower shell and header diameters can be

obtained. Figure 3.6 illustrates a simplified drawing of the evaporator geometry.

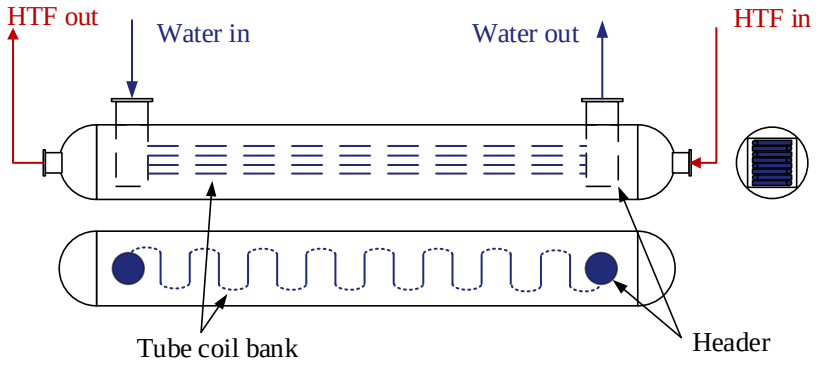

Figure 3.5: Header and coil shell single phase heat exchangers geometry. Front view (top), top view (bottom), side view (right).

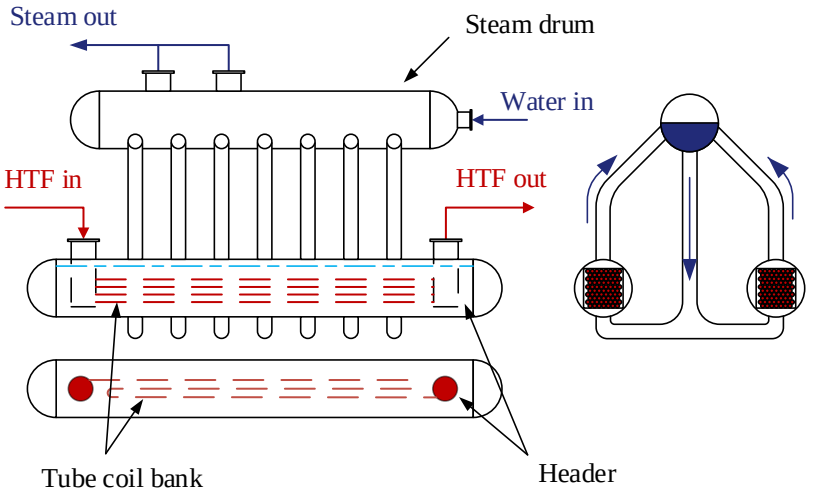

Figure 3.6: Header and coil shell recirculation evaporator geometry. Front view (top), top view of the shell (bottom), side view (right).

3.2 Limitations during the transient operation

Thick walled high pressure vessels, like steam drums and headers in circulating boilers or a water separator in OTSG, experience significant thermal stresses during start-up procedures [46]. Particular attention needs to be addressed towards geometric singularities such as the junctions between the main pressure vessel and the connecting pipes/tube. In the header and coil geometry, this is especially true for the steam drum/downcomer and tube/header junctions. The thickness calculations need to comply with the ASME Boiler Pressure Vessel Code (BPVC) [93], while the heating rate calculations are performed according to the EN (European norm) 12952-3 which defines the guidelines for the calculations of stress concentration factors at the pipes junctions [94].

The cyclic process of the start-up and shut-down procedures (being repeated a number of times throughout the lifetime of the pressure vessel) determines fatigue damage in terms of cracks [95]. Low cycle fatigue (LCF) refers to a process which involves a low number of cycles, with high stress values and plastic deformation. The involved stresses are close to the yield limit of the material causing plain strain, leading to the formation of cracks and their eventual propagation. LCF results are presented as a function of stress against a number of cycles to failure (S-N diagrams). These curves are dependent on material properties and temperature. Hence, the heating rates are calculated for a specific given lifetime and number of cycles and operating temperatures, which are characteristic to the plant operation [94].

Thermal stresses are directly proportional to the square of the wall thickness and linearly proportional to the heating rate. Figure 3.7a illustrates a schematic of the junction which is taken into consideration for thermo-mechanical stresses calculations. The point P_1 is the concentration point considered in the norm, hence the one considered in this thesis. The heating rates are dependent on both the inner and outer diameters (ID and OD) to the main vessel and the connecting pipe. Figure 3.7b illustrates an example of the results of the EN 12952-3 in terms of allowable heating rates. It gives minimum ($v_{T,\,min}$) and maximum ($v_{T,\,max}$) constraints for the respective minimum and maximum pressures (as for higher pressures higher heating rates are allowed).

The control and monitoring of the water level during dynamic operation of steam generators and, specifically, evaporators is another operational challenge [96]. Referred to as shrinking and swelling, these problems are related to the change in the load of the circulating steam generators. At steady state, the water level in the steam drum is around the centreline (or slightly below it), taking half of the drum internal volume. If the heat input increases, the steam production

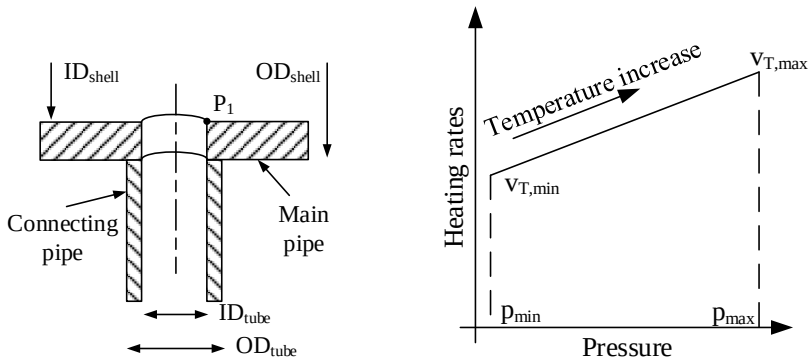

(a) Singularity for stress concentration. **(b)** Heating rate example.

Figure 3.7: Heatings rates on junction singularities.

in the evaporator will increase. As the vapour needs to take more space in the heat exchangers and circulating pipes, the excess of liquid will be delivered to the steam drum making the liquid level to rise (swelling). In opposite, if the heat input is decreased, the volume of vapour decreases, determining a decrease in liquid level in the drum. This transient operation poses a challenge from a controlling perspective. If the drum water level decreases, a feedwater controller would react by firstly increasing the inlet subcooled (hence with low enthalpy content) water mass flow rate, if the heat input is decreased. As the water is at the subcooled condition, some steam will condense and the vapour volume would lower even further, causing a decrease in the drum liquid level. Therefore, particular care needs to be addressed in calibrating and designing the feedwater controller.

The water pressure is the other variable which is controlled during transient operation. Two different strategies are available, i.e. fixed or sliding pressure [97]. In sliding pressure, the range of operation depends on the actual design of the system but in general, the evaporator is firstly operated at the lowest pressure and once the turbine constraints are met, the pressure can increase at the same time as the steam mass flow rate. One of the advantages of this operation strategy is that the volumetric flow of steam is almost constant in the sliding pressure range, which is beneficial for a steam turbine that can operate with fully open control valves, thus increasing the plant thermal efficiency [97].

Chapter 4

Evaluation of the power plant performance

This chapter presents the modelling framework of the parabolic trough concentrating solar power plants. It presents then a study on the impact of the steam generator system heating rate constraints on the plant performance. Lastly, a second study assessing how the flexibility towards operating strategy could influence the optimization the start-up strategies. Chapter 4.2 and 4.3 were based on the work presented in Refs. [98, 99] and Ref. [100], respectively.

4.1 Concentrating solar power plant modelling framework

Modelling was performed in DYESOPT, an in-house tool developed at KTH, Royal Institute of Technology, Stockholm, which was developed for techno-economic performance evaluation of CSP plants [101] . The tool was validated against Thermoflex, a commercially available software for power plant performance estimation [102], demonstrating a relative deviation between the results of two software below 10 % in the case considered. As may be seen in Figure 4.1, the tool allows for both steady-state nominal design and dynamic simulation and can perform techno-economic calculations for different assumed locations for the plant. The yellow and blue boxes represent the plant related and location related inputs, respectively. As the cost functions are both dependent on location and power plant specifications, they are represented as a green box. The black boxes indicate the tool output parameters.

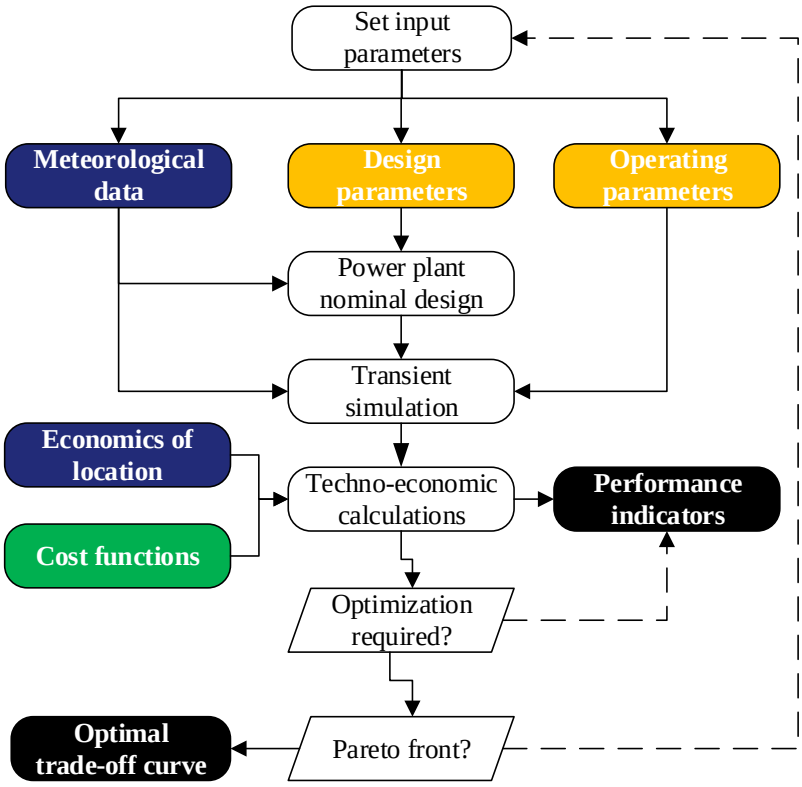

Figure 4.1: DYESOPT logic flow chart. Solid lines represent a YES logic, while dotted lines a NO logic.

The steady-state design and modelling of the power plant were developed and added to the tool. The sizing was performed in Matlab, while the transient modelling was carried out in TRNSYS. More details are provided in the following sections. DYESOPT incorporates a modified version of a queueing multi-objective optimizer (QMOO) based on a genetic algorithm developed at the Industrial Energy Systems Laboratory in Lausanne [103]. At the start of the optimization, it is possible to set conflicting objectives with regards to whether to maximize or minimize their quantities. Both design and operation parameters can be varied within the limits chosen for the study. The algorithm performs then as many iterations as needed to finalize the optimization and obtain an optimal trade-off curve or Pareto front.

4.1.1 Solar field

A parabolic trough solar field consists of a number of solar collector assemblies (SCA) connected in series or in parallel. Figure 4.2 illustrates a general configuration of a PTPP, with the SCA and SCA loops highlighted. The cold HTF (blue lines) enters one of the main loops and exits at demanded temperature. Every SCA is able to track independently the sun and each loop performs similarly, meaning that pressure drops and mass flow rates are the same. The overall solar field comprises a number of loops connected in parallel [87, 104].

The PT solar field sizing process takes into account this configuration and once the total required area is calculated according to Equation 4.1, the number of SCA and loops are determined. Lastly, the total mirror area is adjusted to account for the fixed area value of each SCA available in the market. The total area depends on the power block heat rate demand ($\dot{Q}_{\mathrm{PB}}$), the solar multiple chosen during the pre-design phase, the total efficiency of the solar field (η_{SF}), the incident angle (θ), the incident angle modifier (IAM), and the overall thermal losses ($\dot{Q}_{\mathrm{loss}}$). Depending on the chosen SCA area (A_{SCA}) and number of SCA for each loop ($N_{\mathrm{sca,loop}}$), the number of SCAs (N_{sca}) and loops (N_{loops}) is determined.

The solar field efficiency takes into account the efficiency curve calculated according to Equation 4.4, which depends on end loss efficiency (f_{end}), shadowing between each SCA row (η_{sha}) and cleanliness (f_{clean}) of the collectors. The efficiency curve is calculated according to Ref. [87], where A_{pt},

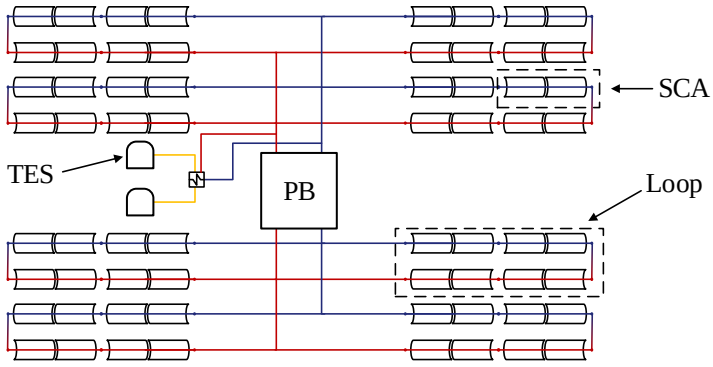

Figure 4.2: Schematic of a parabolic trough CSP plant with storage. Blue and red lines represent the HTF supply and return lines respectively.

B_{pt}, C_{pt}, D_{pt} are coefficients dependent of the type of the chosen solar collector. The efficiency depends also on wind speed v_{wind}, temperature difference ΔT at the inlet (i) and outlet (o) of the SF loop.

$$A_{\mathrm{PT}} = \frac{SM \cdot \dot{Q}_{\mathrm{PB}}}{\eta_{\mathrm{SF}} \cdot DNI \cdot IAM - \dot{Q}_{\mathrm{loss}}} \tag{4.1}$$

$$N_{\mathrm{sca}} = \frac{A_{\mathrm{PT}}}{A_{\mathrm{SCA}}} \tag{4.2}$$

$$N_{\mathrm{loops}} = \frac{A_{\mathrm{PT}}}{N_{\mathrm{sca,loop}}} \tag{4.3}$$

$$\begin{aligned}\eta_{\mathrm{SF}} = f_{\mathrm{end}} \cdot f_{\mathrm{clean}} \cdot \eta_{\mathrm{sha}} \cdot (A_{\mathrm{pt}} + B_{\mathrm{pt}} \cdot \frac{\Delta T_{\mathrm{i}} + \Delta T_{\mathrm{o}}}{2} + \\ + (C_{\mathrm{pt}} + C_{\mathrm{w}} v_{\mathrm{wind}}) \cdot \frac{\Delta T_{\mathrm{i}} + \Delta T_{\mathrm{o}}}{2 \cdot DNI} + \\ + D_{\mathrm{pt}} \cdot \frac{\Delta T_{\mathrm{i}} + \Delta T_{\mathrm{o}} + 1/3 \cdot (\Delta T_{\mathrm{i}} + \Delta T_{\mathrm{o}})^2}{DNI})\end{aligned} \tag{4.4}$$

During the design phase, a particular day and time are chosen as a reference and the incident angle depends on the the zenith angle (θ_{z}), declination angle (δ), and hour angle (ω) of the reference design point as calculated in Equation 4.5. The IAM is an angle dependent correction factor which considers the imperfection of a certain collector as described in Equation 4.6, with the parameters a and b depending on the chosen SCA. The shadowing effects depend on the spacing between each row (L_{spa}), the width (W) of the collectors as well as incident and zenith angle. Lastly, the end losses take into account the lower performance at the end of the length of the collector (L) and depends on the focal length (F) and incident angle. The heat losses depend on pipe and tank loss coefficients as expressed in Equation 4.9.

$$\cos\theta = \sqrt{\cos^2\theta_{\mathrm{z}} + \cos^2\delta \cdot \sin^2\omega} \tag{4.5}$$

$$IAM = \cos\theta + a \cdot \theta + b\theta^2 \tag{4.6}$$

$$\eta_{\mathrm{sha}} = \frac{L_{\mathrm{spa}}}{W} \cdot \frac{\cos\theta_{\mathrm{z}}}{\cos\theta} \tag{4.7}$$

$$f_{\mathrm{end}} = 1 - \frac{F \cdot \tan\theta}{L} \tag{4.8}$$

$$\dot{Q}_{\mathrm{loss}} = (f_{\mathrm{pipe}} + f_{\mathrm{tank}}) \cdot T_{\mathrm{avg}} \tag{4.9}$$

In part-load, the component is implemented in the TRNSYS models through a modified version of the component model available in the STEC library [105]. For a given required outlet temperature the mass flow rate is calculated as summarized in equation 4.10. The efficiency coefficients are calculated at each iteration depending on the position of the sun. The presented parameters depend on the collector type and are summarised in Table B.1 (see Appendix B.1).

$$\dot{m}_{\mathrm{HTF}}(t) = \frac{\dot{Q}_{\mathrm{net}}(t)}{h_{\mathrm{demand}}(t) - h_{\mathrm{in}}(t)} \tag{4.10}$$

$$\dot{Q}_{\mathrm{net}}(t) = A_{\mathrm{PT}} \cdot \eta_{\mathrm{SF}}(t) - \dot{Q}_{\mathrm{loss}}(t) \tag{4.11}$$

4.1.2 Thermal energy storage

The tank volume is calculated according to the required thermal input of the power block ($\dot{Q}_{\mathrm{PB}}$) and the number of storage hours. In PTPPs with thermal oil as HTF, an intermediate heat exchanger is required between the HTF and the storage media. This is taken into account in Equation 4.12 and 4.13 in which f_{hx} considers a lower temperature range for the two tanks accounting for the approach temperatures (ΔT_{ap}) at the cold and hot side. For the cold and hot tank, the density (ρ) and specific heat at constant pressure (c_{p}) are considered at respective average design temperatures.

$$V_{\mathrm{TES}} = \frac{\dot{Q}_{\mathrm{PB}} \cdot \Delta t_{\mathrm{TES}}}{\rho \cdot c_{\mathrm{p}} \cdot f_{\mathrm{hx}} \cdot (T_{\mathrm{SF,\,out}} - T_{\mathrm{SF,\,in}})} \tag{4.12}$$

$$f_{\mathrm{hx}} = 1 - \frac{\Delta T_{\mathrm{ap,\,cold}} + \Delta T_{\mathrm{ap,\,hot}}}{T_{\mathrm{SF,\,out}} - T_{\mathrm{SF,\,in}}} \tag{4.13}$$

$$\dot{Q}_{\mathrm{duty}} = (SM - 1) \cdot \dot{Q}_{\mathrm{PB}} \tag{4.14}$$

Secondly, the intermediate heat exchanger needs to be sized. In DYESOPT, this is performed by determining the UA value of the heat exchanger, as the TRNSYS models are zero-dimensional models. This is carried out with an $\epsilon - NTU$ method for a counterflow configuration [106]. The duty of the heat exchanger corresponds to the difference between the power cycle thermal power input and the power provided by the solar field as expressed in Equation 4.14.

The off-design of the thermal energy storage tanks is modelled as a variable volume tank by means of differential energy and mass conservation equations as expressed in Equations 4.15 and 4.16. The heat exchanger was modelled in quasi-steady state assumption by scaling the UA (overall heat transfer coefficient times area) value according to the instantaneous cold side mass flow rate as in Equation 4.17, where γ is a scaling coefficient which depends on the heat exchanger.

$$\frac{dM}{dt} = \dot{m}_{\text{in}} - \dot{m}_{\text{out}} \tag{4.15}$$

$$c_{\text{p,f}} \frac{d(MT)}{dt} = \dot{m}_{\text{in}} \cdot c_{\text{p,in}} T_{\text{in}} - \dot{m}_{\text{out}} \cdot c_{\text{p,f}} \cdot T - (UA)_{\text{tank}} \cdot (T - T_{\text{amb}}) \tag{4.16}$$

$$UA(t) = UA_{\text{design}} \cdot \left(\frac{\dot{m}_{\text{cold}}(t)}{\dot{m}_{\text{cold, design}}} \right)^{\gamma} \tag{4.17}$$

4.1.3 Power block

The power cycle sizing was already implemented in DYESOPT by means of an iterative process. The mass flow rate is assumed and assigned at the beginning of each iteration and each component is designed according to the correspondent power. The error is set on the net or gross electric power output. The condenser is defined by the pinch point of the heat exchanger and temperature difference either on the air o water flow depending on the condensing technology. The turbine performance is evaluated through the calculation of the isentropic efficiency and power output according to Pelster et al. [107]. The turbine high pressure and low pressure inlet conditions (pressure and temperature) are specified by the user based on the case study considered. The condensing pressure is also defined in order to determine the last stage of the turbine expansion. The steam generator boundaries are given in the form of pinch point, desired superheated and reheated steam conditions and the UA values of each heat exchanger is calculated.

Once the heat input for each SGS heat exchanger is known, the HTF thermodynamic conditions are calculated in order to size each heat exchanger. DYESOPT was implemented with the choice of the two different RH layouts as presented in Section 3.1, but the HTF cycle design routine is common to the two approaches. The evaporator pinch-point is set and the mass flow rate is iterated in order to have convergence on the set HTF outlet temperature. As described in the previous section, the UA values of each heat exchanger are determined with the $\epsilon - NTU$ method.

The off-design performance of all the heat exchangers was modelled as in the case of the intermediate heat exchanger by means of UA scaling functions as presented in Equation 4.17. The turbine off-design performance was modelled according to the Stodola ellipse law [108]. The complete Rankine cycle was modelled and analysed, by having models of each heat exchanger and turbine stage as described in this section.

4.1.4 Operational constraints

The TRNSYS PTPP models were integrated with the thermo-mechanical constraints of both steam turbine and steam generator. The steam turbine start-up procedure is limited by the permissible temperature difference between the metal surface and the steam. Different start-up schedules were defined according to the manufacturer design based on the initial temperature of the turbine metal (or stand still time). The turbine cool down was modelled according to a lumped capacitance method [106]. The start-up procedures are classified as cold, warm or hot. A hot start-up takes only 8-10 % of the time it takes for a cold start-up, while a warm start-up takes 45-50 % of that of a cold start-up [37]. Figure 4.3 illustrates the three different start-up curves. The start-up procedure involves two phases which are denoted for the cold case as the A-B and B-C lines which represent the rolling up and loading up of the turbine, respectively [37].

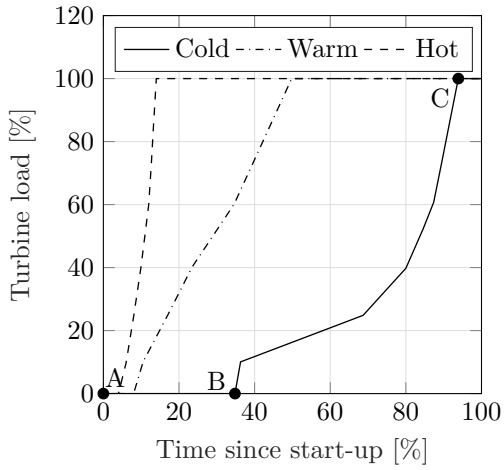

Figure 4.3: Turbine ramp curves for hot, warm and cold conditions.

The minimum allowable pressure was kept at the minimum allowable turbine pressure and the rate at which pressure, mass flow rate and temperature could rise were determined following Ref. [84]. During the rolling-up phase, the mass flow rate is kept at 5 % of the nominal value, while during the loading up the mass flow rate increases with a rate determined directly by the steam turbine start-up routine depending on the metal temperature at which the procedure begins. The different hot, warm and cold start-up curves presented in Figure 4.3 were introduced in the model, depending on the metal temperature [37].

The start-up procedure for a steam generator consists of bringing temperature, pressure and mass flow rate to nominal values in each component of the system. As previously mentioned, the rate at which this can be done is highly dependent on thermo-mechanical limitations that are determined by their materials and geometry. Previous studies have shown that the main limiting components during the SGS start-up are the evaporator and superheater, hence these two were considered in detail in this thesis work [47, 109]. Another constraint which must be addressed is the occurrence of thermal shocks that might happen if the HTF temperature is higher than the metal temperature by more than a critical amount, as the material could then experience cracking and ultimately failure [110]. A limit on the maximum allowable temperature difference was implemented in the control logic of the start-up operation. The heating rates used to calculate the permitted fluid temperature change were obtained using Equation 4.18 [47].

$$\frac{dT_{\mathrm{f}}}{dt} = \frac{p_2 \cdot v_{\mathrm{T}1} - p_1 \cdot v_{\mathrm{T}2}}{p_2 - p_1} + \frac{v_{\mathrm{T}2} - v_{\mathrm{T}1}}{p_2 - p_1} \cdot p(t) \tag{4.18}$$

These equations express the rate at which the fluid temperature (T_{f}) can change depending on the pressure of the fluid (minimum (p_1) and maximum (p_2)) and the minimum and maximum heating rates which are dependent on the geometry, material properties and operating temperature and pressure. In an evaporator, the water is at saturation point so the pressure and temperature are related. As a consequence, the temperature of the fluid will be dependent on the pressure, and Equation 4.18 can be solved using a Runge-Kutta method, assuming $T_{\mathrm{f}}(t = 0) = T_0$. In the case of the superheater, the fluid is not at saturation conditions, the pressure is a function of time and determined by the evaporator conditions.

During the shut-down procedure of the power plant, the thermo-mechanical limitations play a secondary role. In this case, the turbine has a pre-defined time to ramp down in order to maintain a proper synchronization with the electric generator. This was implemented in the models. During this phase, the steam generator will provide a lower mass flow rate and any excess will be bypassed and

condensed. Due to the subsequent reduction in boiler pressure, the allowable cooling rate increases and becomes very high (as for lower pressure drops, the cooling rates are higher). Therefore the cooling problem is less significant as the large mass of water provides high thermal inertia, which will not allow for the fast cooling of the drum [47]. That is why this problem was considered negligible in the economy of the power plant and not taken into consideration in the models.

4.1.5 Techno-economic performance indicators

In order to evaluate the techno-economic performance of the power plant, DYESOPT is implemented with the calculation of the levelized cost of electricity (LCOE) as expressed in Equation 4.19. The CRF is the capital recovery factor, which, as expressed in Equation 4.20, depends on the real interest rate (i), the considered plant lifetime and the annual insurance rate (k_{i}). The CAPEX refers to the capital expenditure, which takes into account direct (purchase and installation) and indirect (land, taxes and engineering) costs related to each component. The OPEX refers to the operational expenditures, which accounts for operation and maintenance costs such as labour, service costs, utility consumables and other additional costs. In the thesis work the plant lifetime was assumed to be 25 years, with a real debt interest rate of 6 % and an annual insurance rate of 0.25 % [54].

$$LCOE = \frac{CRF \cdot CAPEX + OPEX}{E_{\mathrm{gen,yr}}} \tag{4.19}$$

$$CRF = k_{\mathrm{i}} + \frac{i \cdot (1+i)^{N_{\mathrm{years}}}}{(1+i)^{N_{\mathrm{years}}} - 1} \tag{4.20}$$

$$CAPEX = CAPEX_{\mathrm{ref}} \cdot \left(\frac{X}{X_{\mathrm{ref,n}}} \right)^{y_{\mathrm{n}}} \tag{4.21}$$

Each component CAPEX estimation consists of taking costs that have been found in previous projects in the same location and scaling them to the desired plant capacity under study. This is summarized in Equation 4.21, where the X quantity refers to the quantity used for the scaling purpose. The exponent y_{n} of the equation represents a simplification used to approximate a non-linear behavior of the cost functions with respect to the plant size. In the CSP model, the exponent is changed according to the specific cost function. A similar approach is considered for the OPEX calculation. All the reference costs, sizes and scaling exponent were taken from Ref. [14, 54]. In the case of

the SGS, a more detailed approach is implemented as explained in section 5.2.2.5.

4.2 Impact of the heating rate constraints

4.2.1 Introduction

The number of start-ups and their typology (hot, warm or cold start-ups) is influenced by the operational strategy of the power plant [36, 54]. As an example, if a CSP plant is operated in a purely solar-driven mode without fuel back-up, its start-up procedures would occur in the morning when the sun is still rising and would be dependent on the solar thermal input availability. On the other hand, if peak-load is the chosen operating strategy, the plant would operate during a selected time of the day (e.g. during evening hours when the price of electricity is higher) and the start-up procedure would occur when the solar irradiation or thermal energy from the storage are readily available. From a start-up perspective (in the absence of back-up fuels), this would mean different availability of heat input, hence different start-up constraints.

The following sections present an analysis of the effects of the thermal stress limitations of the steam generator and steam turbine on the power plant start-up, and quantify their impact on the economy of the system, with the goal of determining an optimal range of heating rate constraints for the SGS. This was performed for both solar-driven and peak-load conditions to emphasize how different constraints on starting up a steam generator have different impacts on the electric power production and depend on how the plant is operated. It is also considered how differently sized solar fields (in terms of solar multiple) affect the impact of the steam generator constraints from an operational perspective.

Section 4.2.2 presents the power plant layout considered and modelling methods. Secondly, it summarizes the main limitation for the start-up of the steam generator and turbine and how such constraints were implemented in the control logic for the overall model. Section 4.2.3 presents the evaluation of the impact of the constraints of the steam generator on the electric power production both in peak-load and solar-driven operating strategies together with a discussion on the results.

4.2.2 Methods

Figure 4.4 shows the considered plant layout. The PTPP was designed for the location of Seville, Spain, with a power output of 55 MWe gross. The layout comprises an ACC, two-tank TES and a single re-heater.

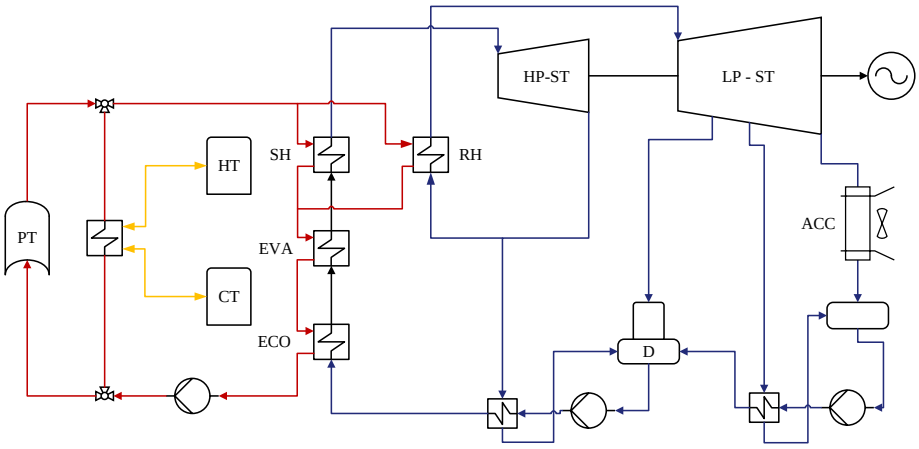

Figure 4.4: Layout of the considered parabolic trough power plant integrated with indirect thermal energy storage and air cooled condenser.

The sizing and dynamic model of the power plant system layout were developed and implemented in the context of the thesis work. This was added and adapted to DYESOPT. Each component block was available in the existing libraries [105], but when needed the components were adapted to modelling objectives. DYESOPT was already implemented with the Rankine cycle sizing routine, but this was adapted to the new configurations implemented.

A controller was implemented in the PTPP transient model in order to run the start-up procedure and check the constraints of the steam generator and turbine. A similar strategy was applied either for peak-load or solar-driven operating power plant strategies. In the latter, the start-up procedure will occur in the morning as soon as the solar heat is available. In this case, the required HTF temperature depends on the steam generator thermo-mechanical stress (in the form of heating rates) constraints. Eventually, the steam temperature rises accordingly until the minimum allowable superheated steam condition is reached. At this point, the steam turbine can initiate operation according to its start-up procedure which depends on the turbine metal temperature.

In a similar approach, for peak-load operation, the heating rate constraints

are calculated and the allowable thermal oil temperature is obtained. As the operation is set at specific times of the day, an optimal design is supposed to guarantee the availability of useful heat either from the thermal storage hot tank or the solar field [54]. In case the TES is used, the HTF temperature can be adjusted by regulating the salt mass flow rate. Nonetheless, if the HTF temperature is higher than the admissible SGS temperature, an attemperator may be used to reduce the temperature of the thermal oil or the HTF may be mixed (if possible) with oil at a lower temperature, either from the solar field loop or the SGS return line.

One of the main differences between the two modes is heat availability. During peak-load operation the thermal power is promptly available for the SGS and the component constraints become the limiting factor, while in solar-driven operation the heat availability depends on the sun position and the solar field size. Once both the steam generator and the turbine have reached nominal operating conditions, the start-up procedure is completed and the power plant enters daily operation. Table 4.1 summarizes the conditions for the two operational modes [54].

Table 4.1: Summary of operation modes.

Operation mode name	Condition
Solar-driven	Whenever radiation or TES are available
Peak-load	Only between 15-21 if heat input is available

Table 4.2 lists the main design parameters. It summarizes both the ones which were considered fixed and which were allowed to vary for the purpose of the analysis. The PTPP designed according to Table 4.2 served as a basis for the analysis of the impact of the constraints. The SM and TES size for the peak-load case were chosen following Ref. [54]. In the solar-driven case, the range of SM values was varied to account for the sensitivity to the solar field size, while the TES size was fixed at 10 h, as this was a size that would still imply warm turbine start-ups while allowing the plant to operate in the evening even in winter periods. The 15-21 time operation was chosen following Ref. [54]. However, in Ref. [54] the price of electricity in the suggested location was higher than zero even between 5 and 17. This study, hereby presented, considered only peak price hours, in order not to consider the influence of the solar field on the SGS. This means that the heat provided to the steam generator comes directly either only from the TES or from the combination of the TES and SF, in case it cannot come directly from the solar input. In case of high and regular DNI and weather conditions, the PT has already gone through its start-up procedure and could potentially provide nominal heat power input to the steam generator.

This makes it possible to focus on how the constraints of the evaporator and superheater influence the performance of the PTPP if electricity production was postponed to a particular time of the day.

Table 4.2: Summary of design parameters for the parabolic trough power plant.

	Units	Peakload	Solar-driven
SM	[-]	1.1	1.5-3
Gross Power	[MW]	55	55
TES capacity	[h]	5	10
Inlet HP/LP pressure	[bar]	100/16.7	100/16.7
Nominal condensing pressure	[bar]	0.06	0.06
SF HTF maximum temperature	[°C]	393	393
Nominal turbine inlet temperature	[°C]	378	378

For both operating conditions, the start-up constraints of the steam generator were analysed for the cases shown in Table 4.3. Simulations were carried out for different limitations on the evaporator and the superheater.

Considering the evaporator, two main start-up procedures can be identified. In the case of an evaporator with a drum configuration (natural or assisted circulation), the minimum admissible pressure of the steam turbine can be maintained overnight. This start-up routine will be termed a hot start-up. In the worst case scenario, the pressure is not kept overnight and the metal temperature is at ambient conditions. The evaporator will start-up from a much lower pressure and temperature. This will be termed as a cold start-up.

In order to analyse how different heating rate constraints will affect the start-up of the power plant, the study took into account both cold and hot start-up procedures, assuming the overnight heat losses from the steam drum to be negligible. Observations from existing power plants indicate that the overnight heat losses from the steam drum may be neglected due to the large mass of water with high thermal inertia and experiencing a limited temperature drop.

The lower bound for evaporator constraints was chosen as a reference, representing a slow start-up of the SGS system [40]. The higher threshold was assumed as a potential improvement over the designs already available in industry [111]. Lower and higher heating rates were also chosen for the superheater, indicated in the table in form of multipliers as compared to the evaporator values. The high threshold was considered as the maximum beneficial value for the power plant operation. If a hot start-up is available

(Case 1 and Case 3 respectively), it means that the minimum allowable pressure of the turbine is kept at the steam drum. The pressure starts from ambient conditions in case of a cold start-up (Case 2 and Case 4 respectively).

Table 4.3: Summary of the respective parameters for the four different cases analysed.

Case name	Units	1 a/b	2 a/b	3 a/b	4 a/b
Average EVA heating rate	[K/min]	3 - 12	3 - 12	3 - 12	3 - 12
SH heating rate multiplier	[-]	1.1/1.8	1.1/1.8	1.1/1.8	1.1/1.8
Start pressure	[bar]	35	1	35	1
Thermal shock ΔT	[K]	63	63	63	63
Operation strategy		peakload		solar-driven	

4.2.3 Results

4.2.3.1 Validation

The validation was carried out by comparing the yearly results with the available data in the literature. As the Andasol power plant is the main reference case, the ACC was substituted by a water-cooled condenser (WCC) in order to match the plant layout. Table 4.4 and Table 4.5 summarize the inputs and results of the validation, respectively. The comparison with the data of the reference model [112] indicates that the largest deviation occurs for the yearly electricity production, and in this case, the model predicts a value 8.9 % lower than that of the reference model. However if the comparison with Ref. [113] and Ref. [114] is considered, the deviation vary between +0.5 % and -3.7 %. In the reference model, the PTPP is integrated with an auxiliary burner to boost the production of electricity during start-ups or sudden losses in available thermal power [112], which was not considered in this specific model. These comparisons suggest that the models give results with sufficient accuracy for this thesis work.

Table 4.4: Main design parameters for the validation of the PTPP model.

Main Design Parameters	Units	Value
SM	[-]	1.75
Gross Power Output	[MWe]	55
TES Capacity	[h]	7.5
Inlet HP/LP-ST pressure	[bar]	100/16.5
SF Maximum outlet temperature	[°C]	393.3
Nominal WCC ITD	[°C]	11
# of HP/LP ST extractions	[-]	2/3
Operating strategy	[-]	Solar-driven

Table 4.5: Main performance indicators for the validation of the PTPP model [112–114].

Performance indicators	Units	Results	Reference	Deviation
Net power output	[MWe]	49.97	49.90	0.14%
Average efficiency	[%]	15.27	15.00	1.80%
Electricity production	[GWh/yr]	158.9	158/165/174.5[1]	0.5%/-3.7%/-8.9%
Land area	[ha]	202.2	200	1.10%

(1) The three values were taken from Ref. [113], Ref. [114] and Ref. [112], respectively.

4.2.3.2 Peak-load operating strategy

Figure 4.5 illustrates the results regarding the impact of the SGS heating rate constraints on the yearly electricity production for the cases presented in Table 4.8. Detailed results on the plant nominal design may be found in Table A.1 and Table A.2. The graph indicates that for a hot start-up, the potential improvement in Case 1a is 1.54 % (0.9 GWh_e). If only cold start-up procedures of the evaporator are considered, the potential raises up to 12.5 % (6.3 GWh_e). If lower SH heating rate multipliers are considered, the potential for improvement can reach values as high as 3.6 % and 25 % (Case 1b and Case 2b). In the first two cases, the evaporator was the main limiting component during the start-up, while in the latter the imposed limitations on the superheater delayed the starting phase of the turbine roll-up, making the impact of the procedure more significant in terms of electricity production.

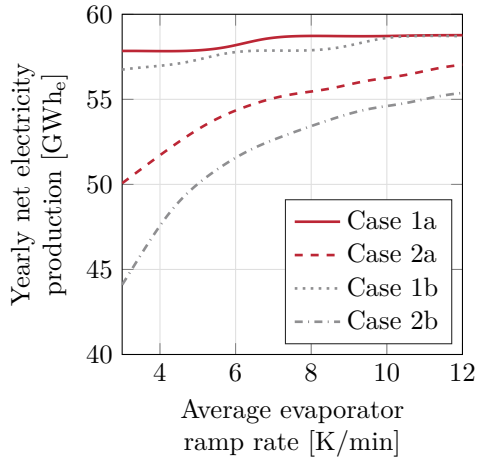

Figure 4.5: Impact of the evaporator heating rate constraints on the net electricity production for a peak-load operating strategy.

These considerations demonstrate the relevance of a properly designed and operated superheater while starting up the SGS. The results of Case 1a suggest that in the case of hot evaporator start-up procedures, it is possible to determine an optimal range of heating rate constraints range between 7 K/min and 10 K/min. Above this threshold, no considerable increase in electrical power production was observed, making going beyond this limit unnecessary. This is mainly related to the fact that even if the SH could attain nominal steam thermodynamic conditions at a faster rate, the turbine would still need to be properly operated in order to respect its thermal limitations. This

reinforces the consideration regarding how significant taking into account both components is, during the optimization of the total system design with respect to thermo-mechanical constraints. If a faster start-up rate was achievable for the steam turbine, then faster responsiveness would be required for the steam generator. Considering an evaporator cold start-up procedure, higher heating rates would always imply higher electricity production for both a fast and a slow superheater. As the starting pressure would be well below the minimum admissible steam turbine pressure, the SGS would need to cover a larger temperature gradient, in turn postponing the beginning of the steam turbine start-up procedure.

The results shown in Figure 4.5 may be better understood by looking at Figures 4.6 and 4.7. Figures 4.6a and 4.6b show the steam temperatures during a two day

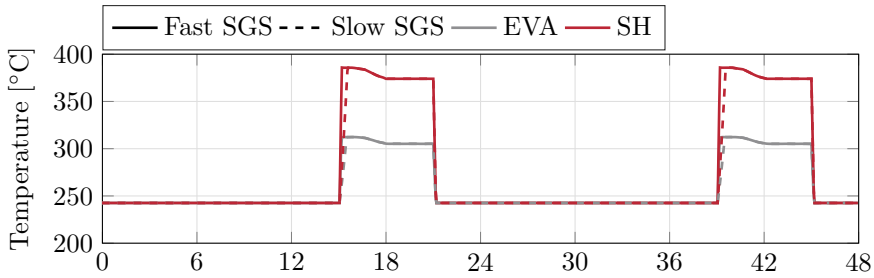

(a) Evaporator and superheater temperatures.

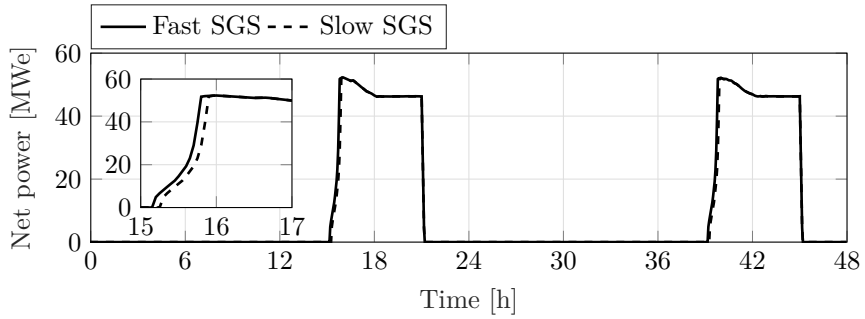

(b) Net power output.

Figure 4.6: Comparison of a two-day performance between a slow and a fast evaporator during a hot start-up for a peak-load operating strategy case.

period and the net electricity output for Case 1a, respectively. The dotted and solid lines refer to a slow (3 K/min) and a fast (12 K/min) SGS configuration, respectively. Figures 4.7a and 4.7b illustrate the same variables but for Case 2a. In the first two subfigures, it may be seen that even though the evaporator heating rate constraint is four times higher than in the slow case, the impact on the net power output is hardly noticeable (a close up is shown in the left part of the graph). More specifically, each day the beginning of the steam turbine start-up procedure is postponed by six minutes. Contrarily, in Case 2, if the steam pressure is not kept overnight, the delay is more noticeable and significant. In this case, the steam turbine would experience a delay of as much as 30 minutes, making the SGS a bottleneck for the start-up procedure. These considerations point out that maintaining the pressure overnight in the steam drum allows for starting up the power plant as efficiently as possible.

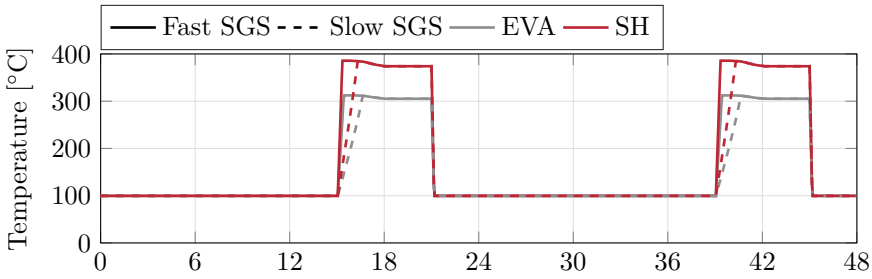

(a) Evaporator and superheater temperatures.

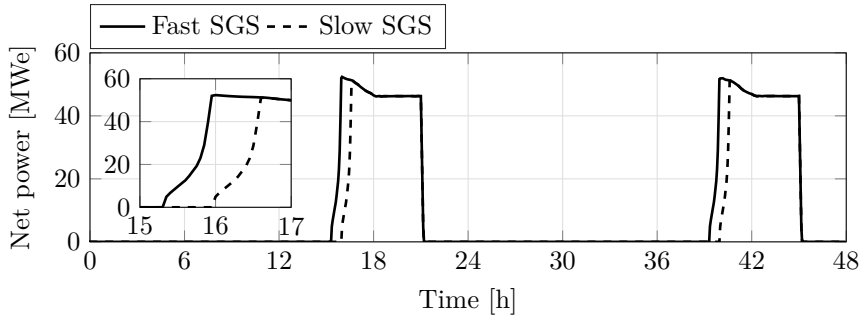

(b) Net power output.

Figure 4.7: Comparison of a two-day performance between a slow and a fast evaporator during a cold start-up for a peak-load operating strategy case.

4.2.3.3 Solar-driven operating strategy

An analogous analysis to the one described in the previous section, but for a solar-driven operational strategy is illustrated in Figure 4.8a. SM equal to 2 was the considered reference case, being a representative value for existing power plant configurations. Following a similar discussion as in the previous section, the results indicate that the potential for increase in net electricity production is as low as 0.27 % (0.56 GWh_e) if only hot evaporator start-up procedures are taken into account, while for cold ramp-up cases, this impact raises to a maximum value of 2.3 %. Similarly to the peak-load operation strategy, if the superheater is not operated or designed optimally, the maximum potential improvement increases up to 4.65 % for cold start-ups.

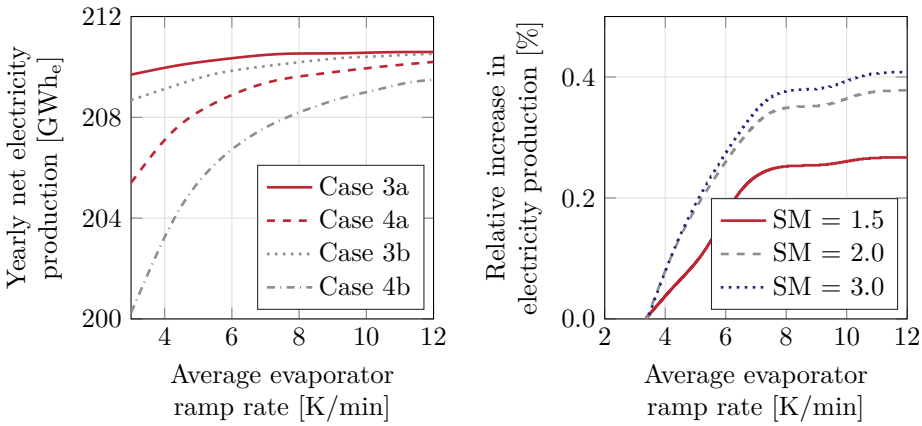

(a) Impact of the heating rate constraints considering a solar multiple equal to 2.

(b) Sensitivity to the solar field size.

Figure 4.8: Impact of the evaporator ramp rate on the net electricity production for a solar-driven operating strategy case.

The relative increase in electrical energy production for different Solar Multiple cases is shown in Figure 4.8b. The figure indicates that the influence of the heating rate constraints on the steam generator is significantly affected by the size of the solar field. It may be observed that by doubling the size of the solar field from a SM of 1.5 to 3.0, the relative increase can raise from a maximum of 0.28 % to 0.41 %. Nonetheless, the impact is not very significant in the economy of the power plant. Figure 4.9 shows the solar field thermal output and thermal input to the SGS and may indicate some reasons for this relatively low improvement. The figure illustrates that in the morning, the

heat input to the SGS follows the same trend as the solar field output, as no storage is available. This means that it takes roughly one hour to reach the nominal operating condition regarding the thermal power input to the SGS. The evaporator pressure follows a similar trend as it is proportional to the heat input. Therefore, the start-up procedure is no longer limited by its thermo-mechanical constraints but more by the heat available from the solar field. Figure 4.9b shows this consideration as it may be observed that in both the fast and slow cases, the evaporator temperature lines (and therefore the pressure, as it is at saturation point) are not separated but they overlap. The only limiting component from a thermo-mechanical standpoint is the superheater, resulting in only negligible differences in power production. In these cases the steam reaches the minimum allowable conditions at a later stage, delaying the start-up of the turbine.

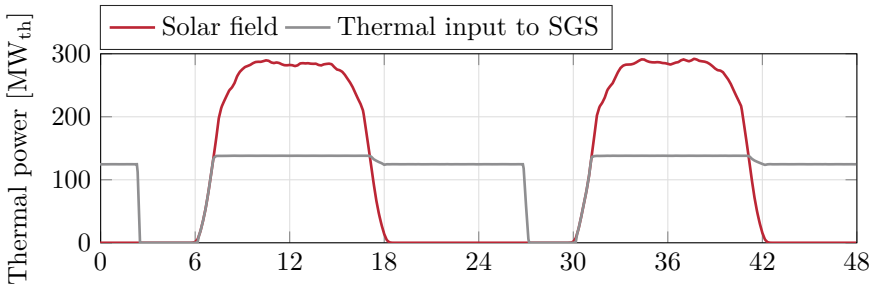

(a) Thermal power at solar field and input to the steam generator system.

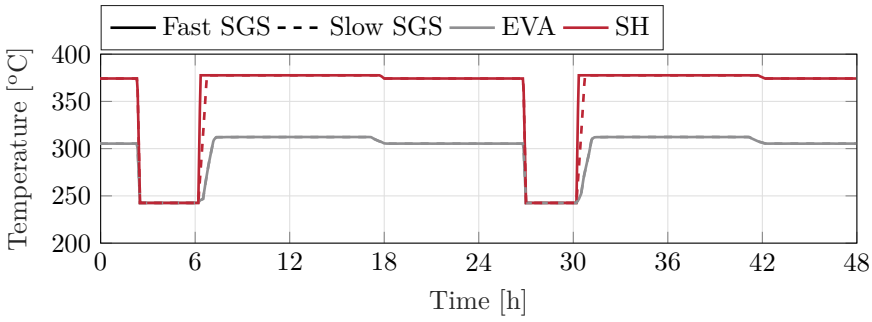

(b) Evaporator and superheater temperatures.

Figure 4.9: Comparison of a two-day performance between a slow and a fast evaporator during a hot start-up for a solar-driven operating strategy case.

4.3 Optimal start-up operating strategy

4.3.1 Introduction

From a yearly perspective, it might happen that low values of thermo-mechanical constraints are optimal solutions for the steam turbine or the SGS. On the other hand, having for instance components like the SGS exceeding such optimal point might allow for more flexibility in the operational strategies of the power plant. This point was not considered in the previous section and an analysis of the optimization of the start-up operating strategy is hereby presented.

A hybridized PTPP with a gas-fired booster heater (BH) located near Abu Dhabi is considered. The plant is also integrated with an additional heat transfer fluid heater (HTFH). The objective of this section is to define an optimal operational strategy for the power plant start-up procedure with the aim of minimizing its fuel consumption while at the same time maximizing its electric energy output, taking into account all the thermo-mechanical constraints involved in the procedure. This was done by considering the evaporator and booster heater heating rate constraints to verify how a dynamic performance oriented design for such components could lead to higher flexibility from an operational standpoint. In order to satisfy the aforementioned objectives, the optimal range for these constraints was determined. The numerical model was thoroughly validated considering the steady-state and transient performances using two sets of operational data of a power plant located near Abu Dhabi.

Section 4.3.2 presents the methods used to model the plant and validate it against operational data. It summarizes the constraints taken into account in the start-up strategy and dynamic operation and the implementation of the operation of the power plant in the control logic. Lastly, it presents the multi-objective optimization routine implemented. Section 4.3.3 presents the validation outcome, and afterward the results and discussion of the multi-objective optimization performed for two different weather conditions (spring and winter).

4.3.2 Methods

Figure 4.10 illustrates the layout considered, which is based on the configuration of a power plant located near Abu Dhabi [115]. It comprises an ACC, the hybridization in the form of a HTFH and a BH. The booster heater model was based on an efficiency map which depends on the steam inlet temperature according to the ASHRAE handbook [116]. Properties of the HTF were computed by linear interpolation in a data sheet from the oil manufacturer [117]. The inertia and response time of the components is taken into account by means of a lumped capacitance method [105, 106]. The Rankine cycle is a regenerative type without re-heating. Table 4.6 summarizes the main design parameters of the power plant.

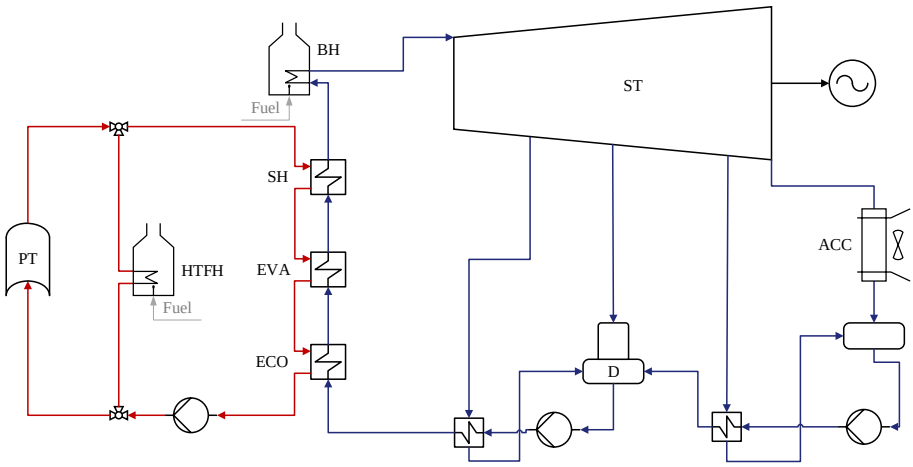

Figure 4.10: Layout of the considered parabolic trough power plant integrated with an oil heater and a booster heater.

The sizing and dynamic model of the power plant were developed and implemented in the context of the thesis work. This was added and adapted to DYESOPT. Similarly as explained in section 4.2.2, already available component models were adapted to the modelling purposes. The Rankine cycle sizing method was adapted to the difference in the layout of a gas-boosted power plant. The transient model was implemented with a logic controller which considers the morning start-up strategies and hybridization with the HTFH as well as the heating rate constraints. A summary of the morning start-up strategy is presented in Figure 4.12. Figure 4.11 illustrates a summary of the operating modes during the start-up procedure.

Table 4.6: Design parameters of the gas boosted parabolic trough power plant [115, 118].

Start-up parameter	Units	Value
Location	[-]	Abu Dhabi
Solar multiple	[-]	1
Gross power	[MWe]	124
Power block nominal efficiency	[-]	0.35
Solar field area	[m^2]	627840
Parabolic trough collector type	[-]	Astro
Solar field outlet temperature	[°C]	393
Superheater steam outlet temperature	[°C]	380
Turbine inlet pressure	[bar]	100
Condensing pressure	[bar]	0.17
Turbine inlet temperature	[°C]	540
Nominal condensing pressure	[bar]	0.13
Operating strategy	[-]	solar-driven

During the night the HTF is recirculated through the parabolic trough loop (as mentioned previously in section 2.6). In the morning the HTFH and the parabolic trough can start to operate not before a specific time set by the operation parameters (as indicated by (1) in Figure 4.12). These are choices usually set by the plant operators. In presence of sufficiently high DNI, the latter is allowed to operate after the time constraint and above all, if the wind speed is below the maximum allowable threshold. In a previous step, the thermal oil is heated up by the HTF and recirculated through the PT loop (OM1 in Figure 4.11).

The HTFH start time is a variable which can be set in the plant operating parameters. When the HTF temperature reaches the minimum allowable value for the SGS, the HTF mass flow rate is calculated and the start-up procedure takes place (as indicated by (2) in Figure 4.12 and OM2 in FIgure 4.11). The oil temperature is raised according to the SGS heating-rate constraints. As the last step, the required mass flow rate is pumped to the SGS. A similar strategy applies in case the DNI is high enough to start the solar field. The HTFH is turned off and the procedure can take place in solar only mode (as indicated by OM3 in Figure 4.11).

The superheated steam coming from the SGS is then heated up by the BH, which also needs to comply with thermal stress constraints. In the meanwhile, the steam turbine metal temperature is checked, and if the allowable conditions are reached, the turbine start-up procedure can take place, according to the

corresponding start-up curve, which is dependent on the metal temperature. The steam temperature is increased according to the heating rate constraints and the mass flow rate is kept at a constant value during the roll-up phase (5 % of the nominal value [84]) before the steam turbine can start to load up. The water mass flow rate and pressure are increased and the nominal values can be reached (as indicated by (3) in Figure 4.12 and OM4 in Figure 4.11). Once the procedure is completed the PTPP enters into daily operation, taking into consideration both steady state and part-load performance when the available heat power input is not high enough. During the daily transient operation, a similar control is carried out, by checking the governing thermal stress constraints.

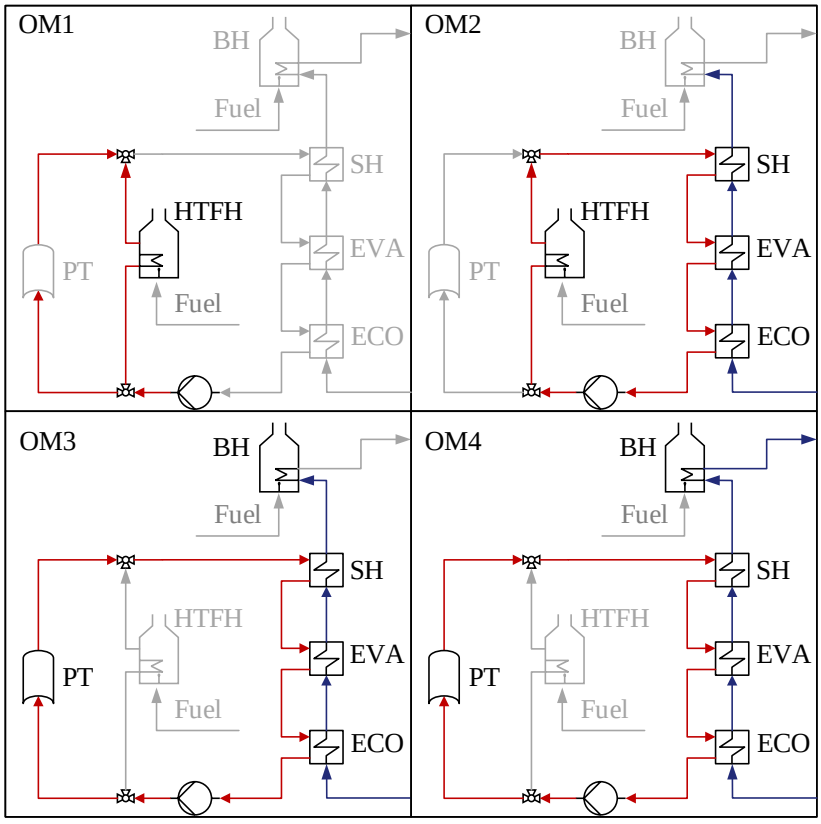

Figure 4.11: Operating modes (OM) during the start-up of the steam generator.

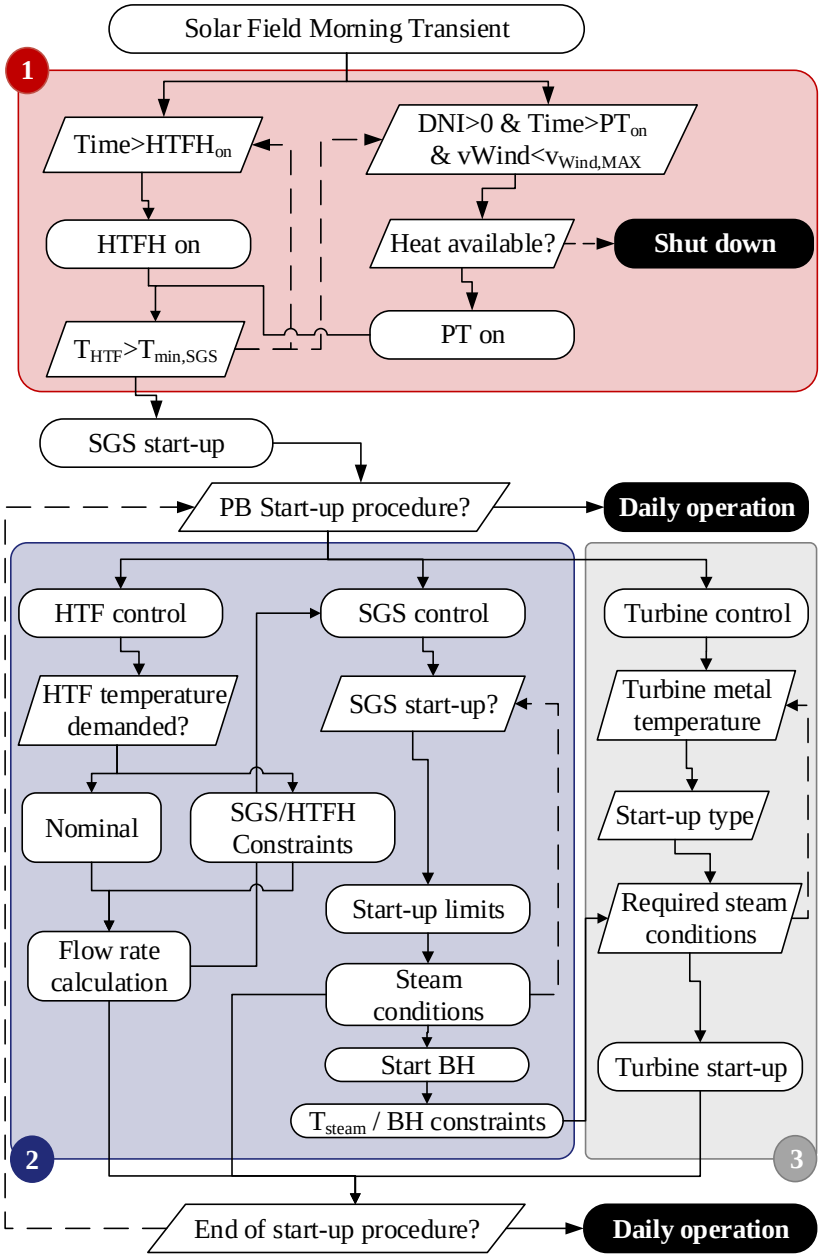

Figure 4.12: Layout of the considered parabolic trough power plant integrated with an oil heater and a booster heater.

4.3.2.1 Optimization

The minimization the fuel thermal energy consumption (Q_{fuel}) and maximization of the electric gross energy production (W_{gross}) were the two objectives of the optimization. Table 4.7 summarizes the chosen decision variables for the optimization studies. The optimization was carried out for two seasons, winter and spring weather conditions, illustrating the operational flexibility of the plant throughout the year. The selected two periods coincide to the data available for validation in order to illustrate how the operation of the plant can be improved with the proposed operating strategies. Using two different sets of weather conditions would allow analysing how the optimal operation strategy could change throughout the seasons considered.

The minimum and maximum values of the decision variables were chosen in order to allow the possibility of radically different operating strategies. Having a higher pre-heating temperature would put less strain on the steam generator as it would need to cover a lower temperature difference to reach the nominal condition, which may result in lower optimal heating rates. Minimum and maximum heating rate constraints values were chosen as the reference and potential improvements according to the available technology in the industry. Ramp rate in the range of 3 K/min to 9 K/min represents achievable design constraints available in the industry [111, 119]. An intermediate value of 6 K/min was chosen as the maximum value for the decision variables considered.

Table 4.7: Decision variables and constraints [18, 64].

Parameter	Unit	Minimum value	Maximum value
EVA heating rate	[K/min]	1	6
BH heating rate	[K/min]	1	6
HTFH operating time	[h]	0	2.5
HTFH temperature	[°C]	200	310

4.3.2.2 Validation

A validation was performed both for the steady-state design, nominal load conditions and for the transient simulation in order to analyse the accuracy of the developed model. The steady-state validation was carried out by comparing the rated thermal loads and mass flow rates with the available data of the power plant in Abu Dhabi. After the model was developed in TRNSYS, the transient simulation was validated against operational data of the power

plant. Data sets of 16^{th} 28^{th} February and 6^{th} 16^{th} May, representing winter and spring weather conditions, respectively, were used to evaluate the accuracy of the model. As the purpose of the model is to represent properly the power plant electric power production, the following six main parameters were chosen for the transient validation: turbine inlet temperature, evaporator steam inlet pressure, steam mass flow rate, HTF outlet temperature at the solar field, HTF mass flow rate and gross electric power.

In order to quantify the reliability and accuracy of the model the indicators presented in Equations 4.22-4.24 were used. The integral relative error (IRE) represents an overall measure throughout the simulation time considered of the accuracy of the model. It compares and estimates the deviation of the integral result over the time considered between the model results and the available data. For example, if the gross power is considered, it will estimate the deviation of the electric energy produced in the time considered. The root mean squared error (RMSE) and normalized RMSE (NRMSE) give a measure of the instantaneous accuracy of the model both in absolute and relative terms. They values refer to the model and data sets for a certain number of available data points (N).

$$IRE = \frac{\int_0^{\mathrm{time}} (y_{\mathrm{model}} - y_{\mathrm{data}})\ \mathrm{d}t}{\int_0^{\mathrm{time}} (y_{\mathrm{data}})\ \mathrm{d}t} \tag{4.22}$$

$$RMSE = \sqrt{\left(\frac{\sum_{\mathrm{i}=1}^{\mathrm{N}} (y_{\mathrm{model}} - y_{\mathrm{data}})^2}{N} \right)} \tag{4.23}$$

$$NRMSE = \frac{RMSE}{y_{\mathrm{max}} - y_{\mathrm{min}}} \tag{4.24}$$

4.3.3 Results

4.3.3.1 Validation

The steady state at design point/nominal load and for the dynamic simulation validation results are presented in this section. Detailed results on the plant nominal design may be found in Table A.3 and Table A.4. Table 4.8 and Table 4.9 present the results of the validation of the main power related results and mass flow rates, respectively, at the steady state nominal load. Due to the confidentiality nature of the plant operating data, the validation is presented in terms of normalized parameters. The mass flow rates and power were normalized with the nominal values of steam mass flow rate and gross power, respectively. In case of the transient validation, temperature and pressure values were normalized against the correspondent nominal steam parameters (see Table 4.6, section 4.3.2).

Table 4.8: Results of the validation of the main power related parameters. Normalized values.

	Model	Data	Deviation
SGS Nominal thermal load	207.30%	207.50%	-0.12%
BH nominal thermal load	45.60%	47.00%	-2.90%
Condenser nominal thermal load	152.90%	153.40%	-0.36%
Net electric power output	89.40%	89.10%	0.39%
Parasitic consumption	10.60%	11.20%	-5.13%
Solar + Fuel to Electricity efficiency	28.34%	28.57%	-0.81%

Table 4.9: Results of the validation of mass flow rates. Normalized values.

	Model	Data	Deviation
SGS HTF mass flow rate	869.66%	931.67%	-6.66%
SGS steam mass flow rate	98.62%	100.00%	-1.38%
BH exhaust gas mass flow rate	20.92%	21.38%	-2.13%
Condenser water mass flow rate	72.71%	72.67%	0.06%

The HTF mass flow rate at the inlet of the SGS presents the maximum deviation (-6.7 %) which is attributed to the approximations made in the property calculations of the HTF (see Section 4.3.2.2). The normalization parameter for all the mass flow rate values is the nominal steam mass flow rate. That is why the HTF related results present results higher than 100 %,

meaning that the required HTF mass flow rate is higher than the nominal turbine inlet mass flow rate. The other parameters results present lower deviations with a maximum value (in absolute) for the parasitic consumption, accounting for -5.1 %. This can be explained by the lower nominal HTF mass flow rate, which is required by the SGS in the model and which would influence the solar field parasitic consumption. Based on these results, it can be concluded that the PTPP sizing model provides reasonably accurate results in the context of this thesis work.

The model was also validated for transient operation; Figure 4.13 illustrates the DNI inputs for the two validation cases. Figures 4.14 and 4.15 illustrate the validation of the model for the data available between 16^{th} and 28^{th} of February and 6-16^{th} of May, respectively.

As depicted in the figures, the main thermodynamic parameters, mass flow rates and electric power are properly predicted. The most significant deviation for each quantity may be noticed at the end of the day (between 17.00-19.00), as in the plant real operation the mass flow rate of the HTF is recirculated through the PT even when there is no sufficient DNI in order to exploit the remaining

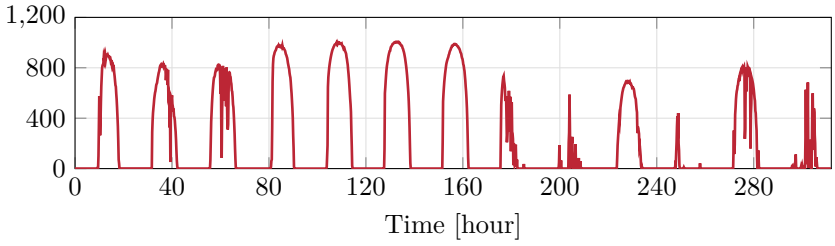

(a) Winter related DNI [W/m^2].

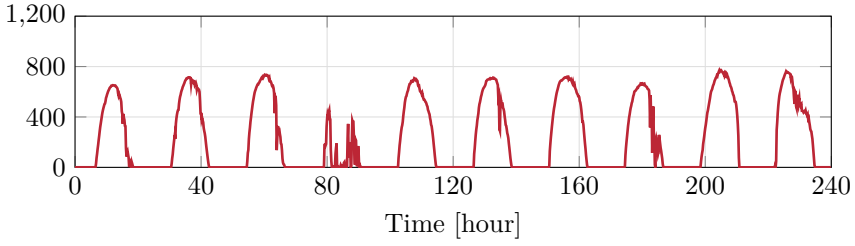

(b) Spring related DNI [W/m^2].

Figure 4.13: Validation direct normal irradiation inputs.

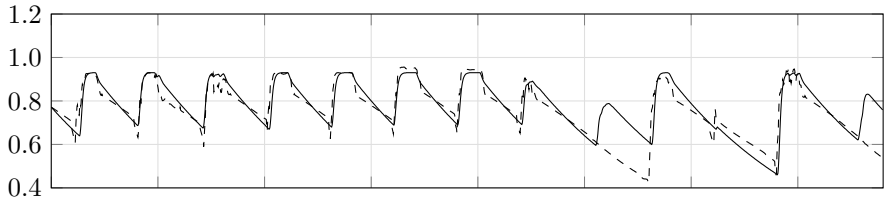

(a) Normalized turbine inlet steam temperature [-].

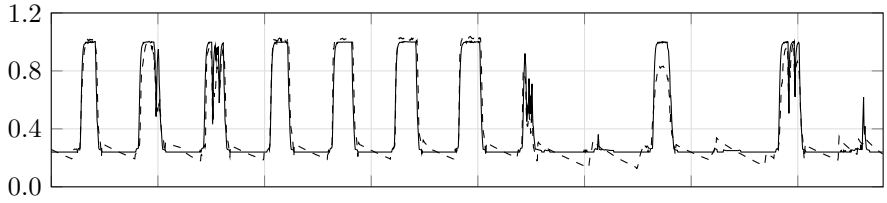

(b) Normalized evaporator inlet pressure [-].

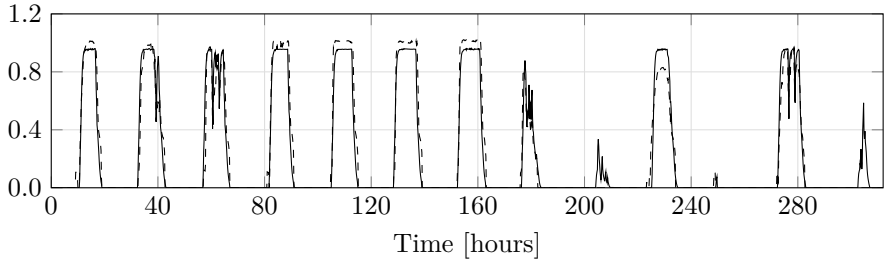

(c) Normalized turbine inlet steam mass flow rate [-].

Figure 4.14: Validation for the winter case. Water related results.

high thermal inertia of the PT solar field. This possibility is not fully captured in the model. Another significant deviation may be observed on day 9. In this case, the DNI is low but sufficiently high to allow for the operation of the solar field. Yet, due to a decision of the operators, the plant was not started up. A similar consideration can be applied to the last day of the simulation.

Relative deviation indicators as presented in section 4.3.2 and RMSE (which was normalized to the nominal reference value) are summarized in Table 4.10. Each row presents the normalized error for each of the six parameters considered. It illustrates that considering the integral result (over the days of the simulation) the model is accurate in predicting the power plant

performance, with the maximum relative deviation for the HTF mass flow rate at the SGS inlet accounting for 3.9 %. Even though at the nominal point the HTF mass flow rate is underestimated as noted in Table 4.9, its integral value is overestimated. This is mainly due to the days in which the power plant was not operated. The gross electrical energy production was overestimated by 2.4 % as compared to the operational data. When considering the instantaneous validation results, higher deviations were obtained. Specifically, the highest value of NRMSE is obtained for the HTF solar field outlet temperature, which accounts for +12 %.

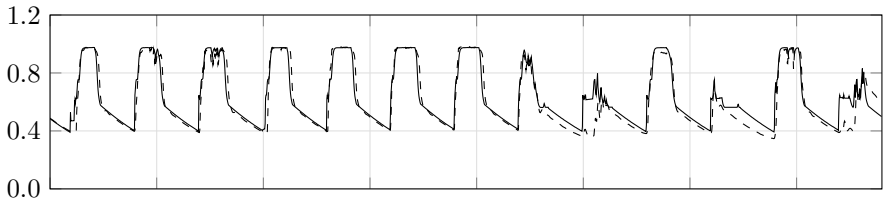

(a) Normalized solar field HTF outlet temperature [-].

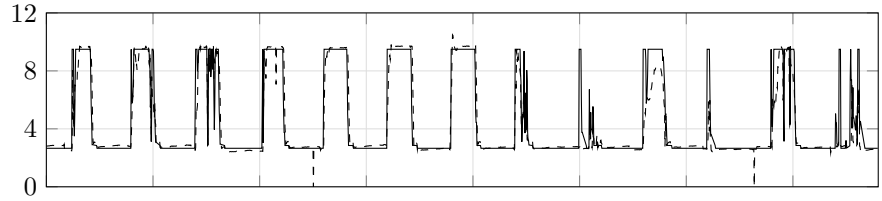

(b) Normalized solar field HTF mass flow rate [-].

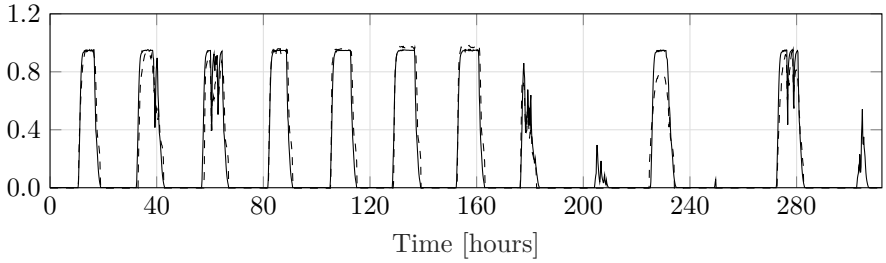

(c) Normalized electric gross power [-].

Figure 4.15: Validation for the spring case. Solar field related and electric gross power results.

Table 4.10: Validation results for the winter case.

Parameter	IRE [%]	RMSE [% of nominal reference values]	NRMSE [%]
TIT	2.25	7.35	9.66
$p_{in,EVA}$	2.11	7.74	8.49
FR_{steam}	-2.57	8.56	8.34
FR_{HTF}	3.19	7.62	12
T_{HTF}	3.86	119.49	11.39
Gross power	2.37	8.45	8.6

Table 4.11: Validation results for the spring case.

Parameter	IRE [%]	RMSE [% of nominal reference values]	NRMSE [%]
TIT	2.97	6.41	7.71
$p_{in,EVA}$	1.02	7.98	9.12
FR_{steam}	-4.12	9.93	9.72
FR_{HTF}	1.67	5.63	8.28
T_{HTF}	4.76	139.17	13.54
Gross power	4.32	10.23	10.32

In the case of gross electric power, the value corresponds to +8.6 %. These results can be correlated to a different operational decision of the operator.

The model was further validated against the available operation data corresponding to the period 6-16th May, which is characterized by a more regular DNI (even though with lower values), being a representative case for spring. The transient results are illustrated in Figure A.1 and A.2 (see Appendix A.1) and in Table 4.11 for the deviation estimation. By observing the figures and tables, comparable considerations as those of the winter case can be drawn for the spring case, resulting in deviations of similar magnitudes. However, in the spring case, a higher overestimation (+4.3 %) is obtained concerning the gross electric energy production, primarily because of day 4, when the plant was not operated due to a planned outage, whereas the model allowed for electric power production. In this case, the highest instantaneous error is observed for the HTF mass flow rate, both for the integral and instantaneous errors due to the same reasons as those of the winter validation.

Moreover, a validation of the time delay until reaching experimental power output was carried out. Table 4.12 illustrates the results for such validation on a daily basis for both weather conditions. An average value of the absolute term of the deviations is also presented. It may be noticed that a significant deviation is observed for day 10 in the winter case. This is mainly due to lower HTF mass flow rates caused by additional defocusing set by the plant operator, which is not reflected in the model. This is also why lower values are observable in Figure 4.15c. Days 9, 11 and 13 were excluded from the winter related calculations as in those days the plant was not operated. The same reasoning applies for day 4 in the spring data set. Excluding these outliers, the highest deviation (+11.1 %) in rising time is observed for day 7 for winter conditions, which is illustrated in Figure 4.16b. The lowest deviation is obtained in day 4 (-0.46 %) and the corresponding daily validation is depicted in Figure 4.16a. Higher deviations (in absolute terms) are observed for the spring case with values up to -15.6 % in the case of day 8 (represented in Figure 4.16d). A lower value, -8.7 %, is observed for day 7 (represented in Figure 4.16c). These deviations are mainly due to a more conservative approach employed by the operator in starting up the power plant during these periods. As an overall result, the absolute average deviation on the rise time is 7.9 % and 11.8 % for winter and spring weather conditions, respectively.

Table 4.12: Deviation results for rise time for gross power.

	Deviation on rise time	
Day	Winter	Spring
1	-6.8%	-13.2%
2	-13.2%	-11.9%
3	-10.2%	-11.7%
4	-0.5%	-
5	5.3%	-10.3%
6	5.0%	-8.8%
7	11.1%	-8.7%
8	10.0%	-15.6%
9	-	-15.4%
10	-25.9%	-10.5%
11	-	
12	-9.1%	
13	-	
Average (absolute value)	7.9%	11.8%

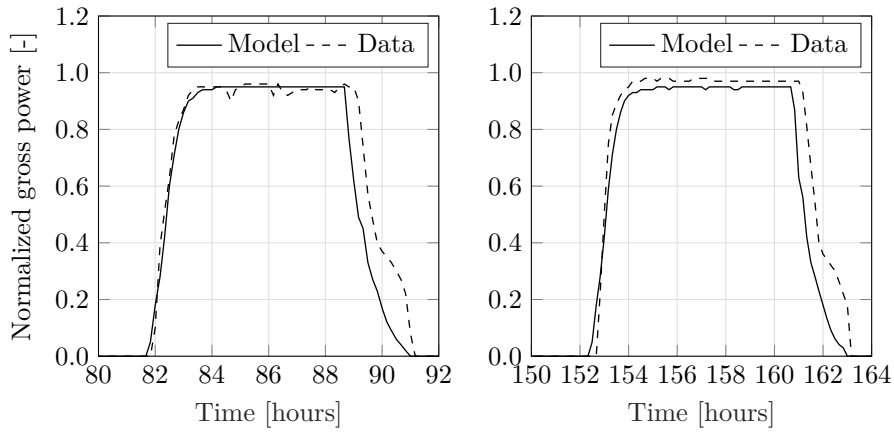

(a) Winter - Day 4.

(b) Winter - Day 7.

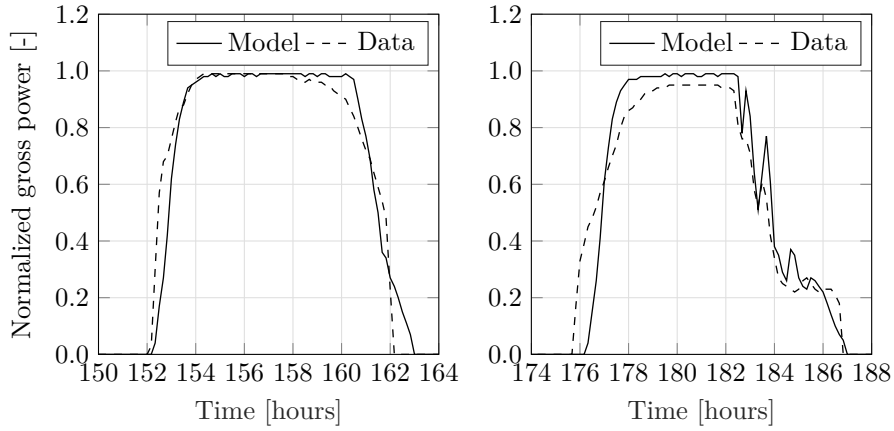

(c) Spring - Day 7.

(d) Spring - Day 8.

Figure 4.16: Close-ups on the transient daily validation results for the winter and spring data resulting in lowest (a, c) and highest deviations (b, d), respectively.

The last validation step was carried out by comparing the results of the model with the equivalent daily operational data for the gross electrical energy production. Such comparison is illustrated in Figure 4.17 (the data were normalized against the maximum integral value obtained from the operational data sets). Figures 4.17a and 4.17b refer to the winter and spring weather

conditions, respectively. The red dots represent the validation points, while the dashed lines represent the ±5 % and ±10 % deviation in the spring and winter cases, respectively. In the former case, the results indicate that 80 % of the values are within a 5 % deviation while the two least accurate days are overestimated. In the winter weather conditions, the deviation slopes raise to ±10 % and in this case, 85 % of the points are within this margin. In case of day 11 (on the (0,0) coordinate) both the plant and the model experience little to none electricity output and that is why even though the plant did not operate, no major discrepancies are observed. The other two points correspond to day 9 and 13 when the plant did not operate. These observations support the previous considerations on how the model differs more significantly only when the plant decision makers decided to change the normal operating routines.

The results of Figure 4.17 suggest that, from an integral perspective, the model is more accurate in spring conditions as the deviations are lower. On the other hand, the deviations for the winter case compensate for each other resulting in lower IRE, in this case. The validation results indicate that the model is able to predict the dynamic behaviour of a gas-boosted parabolic trough solar power plant with reasonable accuracy, which is sufficient for the purpose of this thesis work.

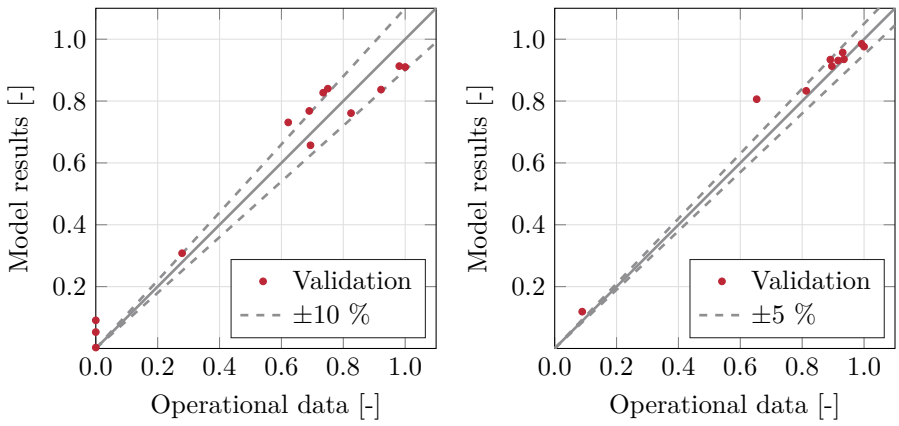

(a) Winter case. **(b)** Spring case.

Figure 4.17: Comparison of the model results in terms of daily electric energy production for the days available in the data sets (fraction of the maximum data value).

4.3.3.2 Optimization of the start-up strategy

The optimization studies for both the winter and spring weather conditions are presented in this section. The results for the former case are illustrated in Figure 4.18. The normalized objective variables (against the base case) are shown on the x-y-axes with one of the four decision variables (see Table 4.8) in each figure. Figure 4.18 highlights four different points, respectively:

i: Minimum fuel consumption

ii: Maximum electricity production

iii: Trade-off between the two objectives in the form of minimizing the fuel to electric energy ratio Q_{fuel}/W_{gross}.

bc: Base case: case used for the validation of the model.

Table 4.13 summarizes the obtained operational parameters and results. The results obtained in Figure 4.18 demonstrate that it is not possible to define a single optimal value for the heating rate constraints for both the booster heater and evaporator. Yet, a range of values can be defined to maximize the performance of the PTPP.

Table 4.13: Winter case optimization results.

Cases	EVA v_T [K/min]	BH v_T [K/min]	HTFH time [h]	HTFH T [°C]	W_{gross} [-]	Q_{fuel} [-]
bc	1	4	2.5	310	1	1
i	1	1	1.58	238	0.836	0.845
ii	4.4	5.2	2.6	310	1.229	1.654
iii	5.7	5.6	2.4	200	1.077	1.067

Concerning the evaporator, a range between 2.5 K/min and 4.5 K/min can be selected, as it comprises 47 % of the points in Figure 4.18, and an optimal value of 5.7 K/min is obtained in order to have a higher electricity production without at the same time increasing significantly the fuel consumption. Case (iii) shows that it is possible to significantly reduce the fuel consumption by having a high start-up constraint for both the evaporator and the superheater allowing for setting the temperature of the HTFH to a low value of 200 °C. In Case (ii), in order to maximize the electricity production, not only it is necessary to have higher v_T, but also it is required to set a higher set point for the HTFH

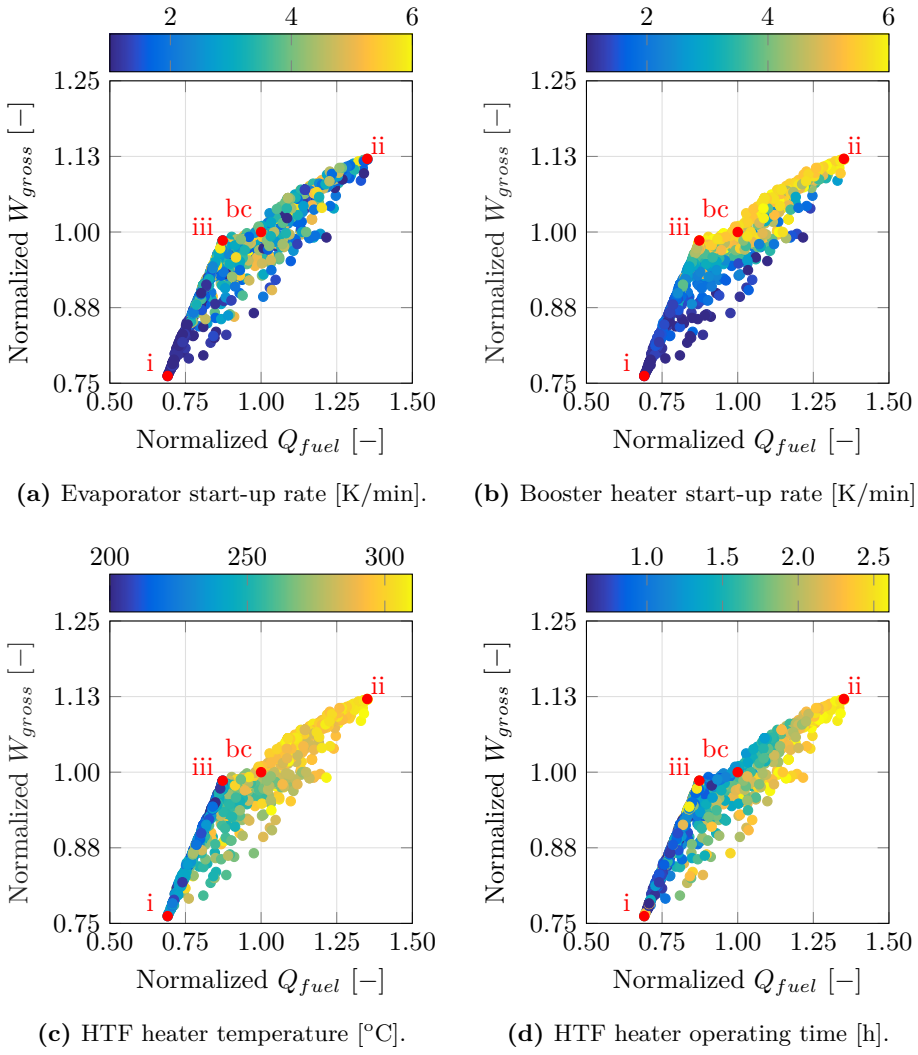

(a) Evaporator start-up rate [K/min].

(b) Booster heater start-up rate [K/min].

(c) HTF heater temperature [°C].

(d) HTF heater operating time [h].

Figure 4.18: Optimization results for the winter case considering the four decision variables.

temperature (with the maximum operating time). This is mainly correlated to the operating choices, which could allow for higher electricity production by maximizing the fuel consumption. Table 4.13 and Figure 4.18 also indicate that the base case (bc) has a slightly higher fuel/electricity ratio than the optimal

cases (i.e. cases close to point (iii)). By employing the start-up strategy depicted in case (iii) it is possible to increase the electricity production by 7.7 % and lower the fuel/electricity ratio by 1.5 % , compared with the base case.

As indicated by these results, it is not always needed to have a SGS designed with high values of thermo-mechanical constraints. However, having such a possibility could further increase the operational flexibility of the power plant. In this regard, an analysis of the fuel efficient solution is performed. A close-up on Case (iii) is presented in Figure 4.19, which shows the fuel/electricity ratio as a function of the evaporator heating rate constraint. On the z-axis colormap, the booster heater heating rate constraints are shown. Table 4.14 summarizes the decision variables and objective functions of Case (iii), Case (iv) and Case (v).

These cases present very similar results, yet they are characterized by different operating strategies. Table 4.14 and Figure 4.19 results suggest that it is possible to obtain a slightly higher (0.45 %) gross electricity production at the cost of increasing (by 0.22 %) the fuel consumption. However, increasing the set-point temperature of the HTFH and the constraint of the booster heater would be required in order to obtain lower constraints of the evaporator. It is then preferable to choose Case (iii), as the heater would only be used to pre-heat the oil to a maximum temperature of 200 °C in order to be less dependent on the fossil fuel source.

Table 4.14: Optimal efficiency points comparison.

Cases	EVA v_T [K/min]	BH v_T [K/min]	HTFH time [h]	HTFH T [°C]	W_{gross} [-]	Q_{fuel} [-]
iii	5.7	5.6	2.43	200	1.077	1.067
iv	2.6	6	2.12	220	1.082	1.069
v	1	1.8	0.9	242	0.932	0.921

In case it is not possible to employ a steam generator, which allows for such constraints as its design might not allow for it, it would still possible to operate the power plant in the optimal region at the cost of employing the HTF heater for more time and at a higher temperature. In terms of fuel to electricity ratio, a similar result can be obtained, see Case (v), which represents a limit case for a very slow evaporator in terms of heating rates. However, if the heating rates of the evaporator are constrained to the lower limit, in order to have a similar fuel to electricity ratio (0.522) a much lower (-13.5 %) electric energy production is achieved.

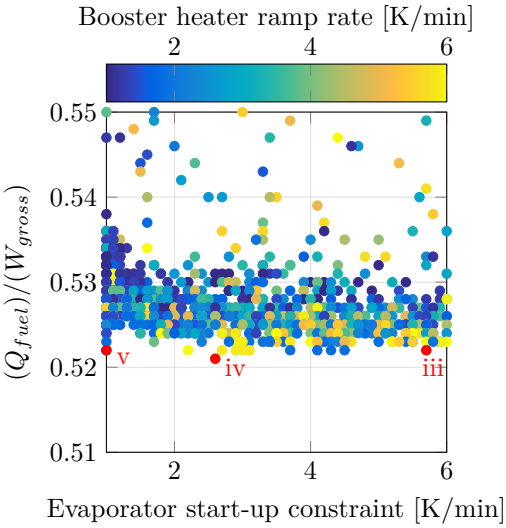

Figure 4.19: Analysis of evaporator constraints on the fuel/electricity ratio. Close-up on the optimal ratio Q_{fuel}/W_{gross}.

Figure A.3 (see Appendix A.1) summarizes the results of the multi-objective optimization for the spring season and also presents the aforementioned four cases. The base case is again below the Pareto front, meaning a non-optimal operating point. Table 4.15 presents the detailed results of the different cases.

Table 4.15: Spring case optimization results.

Cases	EVA v_T [K/min]	BH v_T [K/min]	HTFH time [h]	HTFH T [°C]	W_{gross} [-]	Q_{fuel} [-]
bc	1	1	2.5	310	1	1
i	1	1	0.62	263	0.947	0.93
ii	4.3	4.3	1.83	281	1.134	1.211
iii	6	6	0.78	290	1.062	1.057

In the spring case, higher optimal values for the evaporator heating rates (towards the upper boundary of the constraints) are obtained, especially for case (iii). As the heater is operated at a lower temperature, it is necessary to increase the start-up speed of the steam generator. Compared to the base case (bc), in case (iii), by increasing the fuel consumption (+5.6 %) it is possible to increase the electricity production by 6.2 %, decreasing the fuel to energy

ratio. The results indicate that if the fuel consumption is set as a constraint, a higher electricity production (+1.9 %) can be achieved by increasing the heating rates to the maximum limits and at the same time decreasing the HTF heater utilization.

The narrower range of solutions for the spring case as compared to the winter case is one of the main differences between Figure 4.18 and Figure A.3. This can be correlated with the lower number of fluctuations in the DNI values and as a consequence a lower impact of the heating rate constraints on the electricity production. This explains why a lower value for this constraint is obtained in Case (ii). This would mean that if anyway higher constraints are allowed, it would allow a higher degree of flexibility in operating the plant in worse seasons (in terms of regular DNI) like winter. The results suggest that there is no clear range of optimal values for the heating rates of the evaporator and booster heater. However, by being able to operate them at a faster rate it is possible to reduce the operating time of the HTF heater and maximize the electricity to fuel ratio.

4.4 Discussion and summary

Detailed models of parabolic trough power plants were developed, validated and implemented in an already existing tool for CSP plants performance evaluation (DYESOPT). Such models were integrated with control logics, which took into account the start-up constraints of the most sensitive components such as the steam generator, steam turbine and gas fired heaters. These models were used to analyse and evaluate the influence of such constraints on the annual power plant performance and start-up operating strategies. The two studies concluded that it is significant to account for the steam generator systems thermo-mechanical constraints during the yearly performance evaluation and that having high maximum allowable heating rates would allow for a higher degree in flexibility towards the operating strategy choices throughout the year. More details are summarized in the following sections.

4.4.1 Impact of steam generator heating rate constraints

A detailed analysis was presented to illustrate the impact of the steam generator system heating rate constraints during the start-up procedure of a parabolic trough power plant. To achieve this, a model of a parabolic trough power plant was developed to allow the simulation of two different operating strategies, namely peak-load and solar-driven operation. The results of the validation indicated that the model is able to predict the annual performance of a standard parabolic trough power plant with a deviation from the yearly electricity production ranging between +0.5 % to -8.9 % depending on the reference considered.

The results suggest that for peak-load operation, by changing the constraints of the steam generator from 3 K/min to 12 K/min, the potential improvement in total net electricity output is 1.5 %. It was shown that being able to maintain the minimum allowable turbine pressure overnight would be highly beneficial as it makes it possible to start the steam turbine in the most efficient way. The optimal range of maximum allowable heating rate for the evaporator was found to be about 7-10 K/min.

For solar-driven operation, the results indicate that for a solar field design with a solar multiple equal to 2, the potential improvement of electricity production is as low as 0.27 %. This figure increases if the solar field is further oversized, but only to 0.41 %. The main limiting factor during start-up procedures is the amount of heat available in the solar field. As the solar field can only

provide nominal operating power to the steam generator system after 1 hour, the pressure at the evaporator cannot achieve its nominal value before that time, so the heating rate will be slower than the maximum limits in most start-up procedures.

The results indicate that raising the maximum allowable evaporator constraints would not proportionally increase the yield of the power plant, as their effect is limited, either by other constraints at the steam turbine or at the solar field. It is therefore clear that the interaction among the three components is crucial when optimising the thermo-mechanical design of a SGS.

4.4.2 Optimal start-up operating strategy

A detailed model of a gas-boosted parabolic trough power plant was employed to obtain optimal start-up operational strategies by minimizing fuel consumption and maximizing electrical energy output. A validation was carried out both at steady-state and transient conditions and in a second step, a genetic algorithm based multi-objective optimizer was employed to perform the optimization study. Both analyses were carried out for two different time series corresponding to a winter and a spring case, respectively.

The results of the validation indicate that the model is able to predict with reasonable accuracy the behaviour of a gas-boosted parabolic trough solar power plant, both at steady state and dynamic operating conditions. The validation at steady-state condition showed a maximum relative error of -6.7 % for the steam generator system heat transfer fluid mass flow rate and -5.1 % for the total electric parasitic consumption. For dynamic operating conditions, the validation resulted in a maximum NRMSE of +13.5 % for the solar field heat transfer fluid mass flow rate, -11.8 % in rising time to reach experimental power and a maximum integral relative error of +4.3 % for gross electric energy production in the case of spring conditions. Considering the daily electric energy production, the validation indicated that 85 % of the values are within a ±10 % confidence range.

The results of the multi-objective optimization indicate that it is not possible to define a single optimal heating rate for evaporator constraints. However, different optimal start-up strategies can be identified. If minimum fuel consumption is desirable, the heating rates result optimal around the lower threshold of 1 K/min together with low utilization of the heat transfer fluid heater. An opposite conclusion can be drawn if maximum electric production is desirable, resulting in higher utilization of the heat transfer fluid heater both in terms of higher set point temperature and in time of activation. If however,

the operating strategy is to maximize the plant performance with regards to the electric energy production to fuel consumption ratio, higher evaporator heating rates are desirable, namely, 5.7 K/min and 6 K/min for the winter and spring cases, respectively.

It can be stated that even though an optimal value for the operation of the power plant can be lower than the maximum constraints stated by the manufacturer, it may be desirable to design the evaporator for higher constraints, enabling more flexibility regarding operating strategies. It is therefore clear that it is critical to take into consideration the heating rates constraints when finding the optimal start-up strategies of concentrating solar power plants.

Chapter 5

Design of the steam generator system

This chapter presents the modelling framework of the header and coil steam generator system. Firstly, it presents a study on how to design such heat exchangers and evaluates the impact of including low-cycle fatigue constraints during the design phase. In a second step, the methodology is expanded accounting for transient response, thermal stress evaluation and their impact on the power plant performance. Chapter 5.2 and 5.3 were based on the work presented in Ref. [100] and Ref. [120], respectively.

5.1 Steam generator modelling framework

Figure 5.1 illustrates the main steps of the SGS design routine. The grey and black boxes represent the inputs and outputs of the model, respectively. In order to perform the SGS design, power block data and operating constraints are the required inputs together with price data if economic calculations are performed. The results of the design provide the basis for the LCF analysis according to the EN12952-3 [94]. As long as the design does not comply with the regulation, geometric inputs are modified accordingly.

If needed, the model is coupled with a multi-objective optimizer available in the Matlab toolbox [55]. At the start of the optimization, conflicting objectives with regards to whether to maximize or minimize their quantities are set. Both design parameters and operation parameters can be set to allow for variations within the limits chosen for the study. The algorithm performs

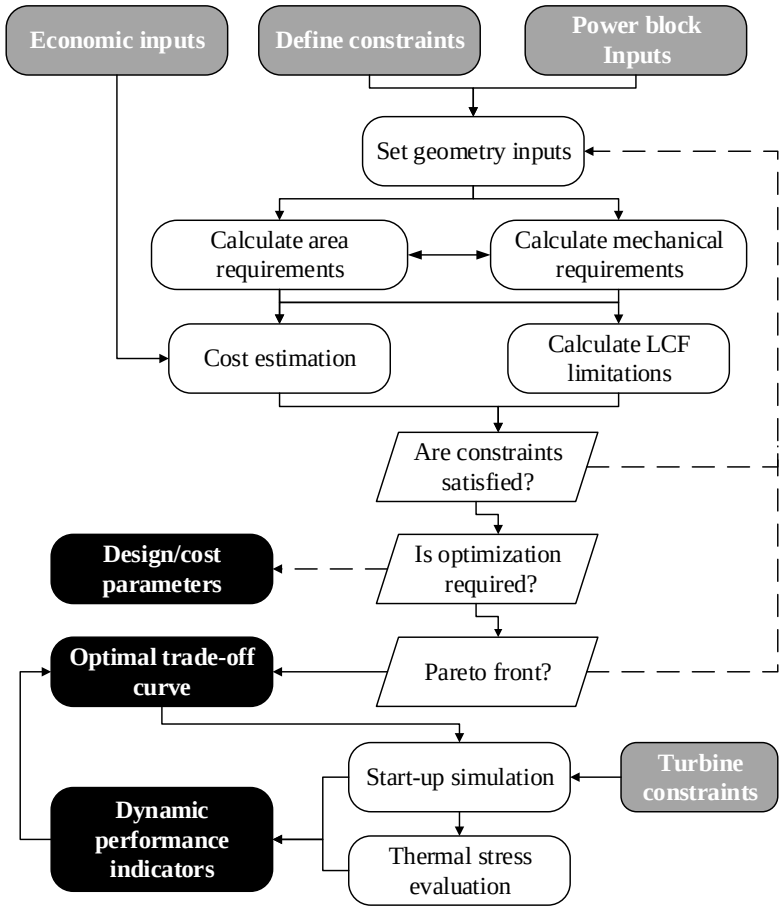

Figure 5.1: SGS design method workflow. Solid lines represent a YES logic while dashed lines represent a NO logic. Grey and black boxes represent the inputs and outputs of the model.

then as many iterations as needed to finalize the optimization and obtain an optimal trade-off curve or Pareto front [103]. Once the design routine is finished, the geometrical results are inputted in the dynamic simulation model. The start-up procedure is simulated in Dymola [57] and the results serve as a basis for the stress calculations. The impact of the SGS on the power plant performance was measured in terms of LCOE variations. As the power plant model considers zero-dimensional models for the heat exchangers, the detailed transient results were interpolated to determine the scaling power coefficients

for the TRNSYS model (see equation 4.17). The sizing routine and tool was developed and validated in the context of the thesis work. Regarding the dynamic model, the ThermoPower library has sub-components (already validated), which describe the transient conservation equations, but they were adapted and used for the context of the thesis work.

5.2 Design accounting for low-cycle fatigue constraints

5.2.1 Introduction

Based on the previous research works presented in Section 1.2, it can be stated that even though many design methodologies are available in the literature, so far none has included LCF limitations during the design phase. However, the results of the previous sections 4.2.3 and 4.3.3 demonstrated the significance of including the heating rate constraints in the power plant performance evaluation and operation strategy optimization. By accounting for this system constraint into the design phase, it is possible to guarantee optimal performance during the start-up phase and the flexibility to choose different operating strategies.

The objective of this section is therefore to present a SGS design method accounting for LCF constraints. The significance of the results is demonstrated by comparing the results with those of a design neglecting LCF constraints. The thermodynamic and economic calculations were coupled in a multi-objective optimization framework aiming at minimizing both pressure drops and purchased equipment costs (PEC). The header and coil design was chosen as it is a promising solution for CSP applications. The numerical models were validated with data provided by a manufacturer of a 55 MWe PTPP without storage.

Section 5.2.2, presents the methods used to calculate the required heat transfer parameters and pressure drops as well as the cost estimation and LCF heating rates calculations. Furthermore, it presents the multi-objective optimization method and required constraints to obtain feasible solutions. Section 5.2.3 presents and discusses the results of the validation and multi-objective optimization performed for two different cases to compare the results with the ones obtained without accounting for LCF constraints.

5.2.2 Methods

5.2.2.1 Case study

The reference power plant is based on the Andasol 1 configuration [121]. The absence of TES and the two split arrangement of the re-heaters (as presented in Section 3.1) are the main differences. Figure 5.2 illustrates a diagram of the PTPP. Table 5.1 summarizes the main inputs required for defining the boundary conditions of the SGS, necessary for its design.

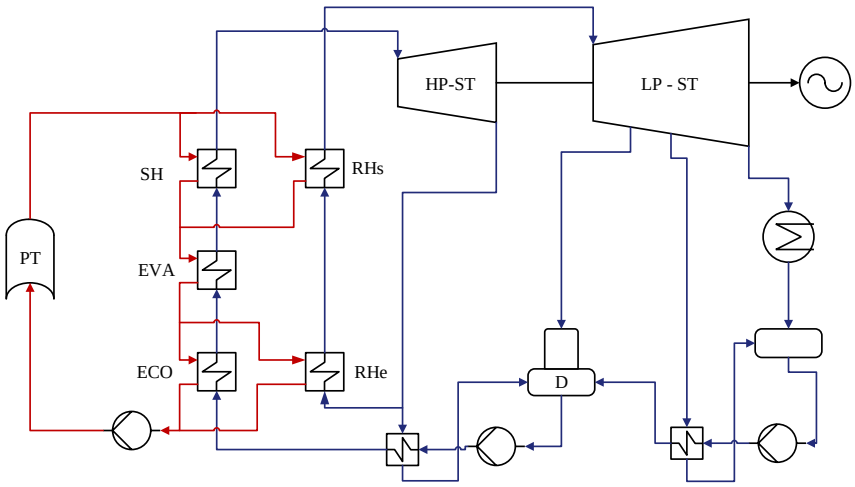

Figure 5.2: Parabolic trough power plant layout considered for the design of the steam generator system.

5.2.2.2 Heat transfer and pressure drops in the heat exchangers

The first step in the heat exchanger sizing is determining the required heat transfer area. The required heat duty ($\dot{Q}$) and temperature boundary conditions serve to calculate the mean logarithmic temperature difference ($LMTD$) according to Equation 5.1. Specifically, this depends on the inlet (i) and outlet (o) temperature of the cold and hot streams. F is a correction factor which depends on the flow configuration, which can be set to 1 in case the number of tube coils is higher than six, as the flow configuration can be approximated as a counter-current [122]. By calculating the overall heat

Table 5.1: Power block boundary conditions

Parameters	Units	Value
Turbine inlet temperature	[°C]	385.3
Turbine inlet pressure	[bar]	104
Reheat outlet temperature	[°C]	386.5
Inlet pressure at reheat	[bar]	20.3
Inlet temperature at reheat	[°C]	213
Feedwater temperature	[°C]	256.8
HTF inlet temperature	[°C]	393.3
HTF inlet pressure	[bar]	15
Heat load requirement	[MW]	166.2

transfer coefficient (U_o) as defined in Equation 5.4, the heat exchange is determined according to Equations 5.2 and 5.3.

$$\Delta T_{\mathrm{LMTD}} = F \cdot \frac{(T_{\mathrm{i,hot}} - T_{\mathrm{o,cold}}) - (T_{\mathrm{i,hot}} - T_{\mathrm{o,cold}})}{(\ln((T_{\mathrm{i,hot}} - T_{\mathrm{o,cold}})/(T_{\mathrm{i,hot}} - T_{\mathrm{o,cold}})))} \tag{5.1}$$

$$Q = U \cdot A \cdot \Delta T_{\mathrm{LMTD}} \tag{5.2}$$

$$A_o = N_{\mathrm{tl}} \cdot N_{\mathrm{txl}} \left(\pi \cdot \mathrm{OD} \cdot L_{\mathrm{tube}}\right) \tag{5.3}$$

$$\frac{1}{U_{\mathrm{o}}} = \frac{r_{\mathrm{o}}}{r_{\mathrm{i}} \cdot h_{\mathrm{i}}} + \frac{1}{h_{\mathrm{o}}} + \frac{r_{\mathrm{o}} \cdot ln\left(\frac{r_{\mathrm{o}}}{r_{\mathrm{i}}}\right)}{\lambda_{\mathrm{w}}} \tag{5.4}$$

The area depends on the number of tubes for each layer (txl) and tube layers, as well as on the single tube length (L), as illustrated in equation 5.3. The U value, as expressed in equation 5.4, is evaluated by calculating the heat transfer coefficients (h) of both shell and tube sides, the internal and outer radius (r), as well as on the thermal resistance posed by the tubes which depends on the wall (w) thermal conductivity (λ). The fouling factors were considered negligible. In fact, the manufacturer of such steam generator design guarantees no fouling [111].

The heat transfer coefficients were calculated according to the Gnielinski [106] and Zukauskas [123] correlations, respectively, in the case of single phase heat exchangers (ECO, SH, RH). The pool boiling heat transfer coefficient was

estimated using the Stephan-Abdelsalam correlation [124], for the evaporator. The convective effects on the evaporator water side heat transfer coefficient were considered negligible due to the low water velocities involved (lower than 0.1 m/s). This assumption is also supported by the fact that the heat transfer performance is governed primarily by the heat transfer coefficient on the oil side. The single-phase heat exchangers geometry was approximated as parallel tube banks as illustrated in Figure 5.3. S_l, S_t, N_{tl} represent the tube longitudinal and transversal pitch and the number of tube layers, respectively. The tubes are fixed in a horizontal position in order to avoid vibration and bending in the transversal direction.

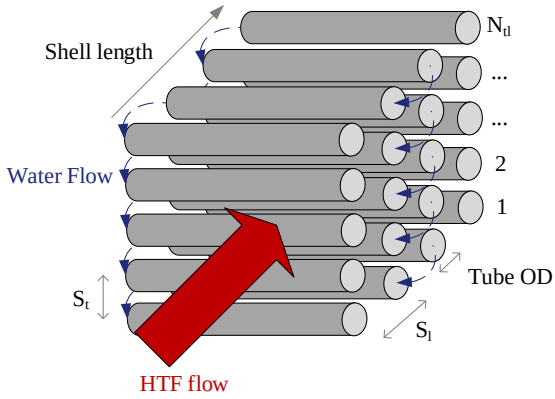

Figure 5.3: Tube bundle geometry approximation

Pressure drop on the shell side was estimated according to the Zukauskas correlation [123], which takes into account the effective fluid area flow inside the tube layer and it is dependent on the number of tube layers the fluid needs to cross. As expressed in Equation 5.5, the total tube pressure drop is calculated as the sum of the friction losses on an equivalent length accounting for the bend radius and the change in direction of the flow. The bend-loss coefficient (k_b) is obtained according to Idelchick et al. [125] and depends on the the curvature ratio $\left(\frac{R_b}{ID}\right)$ and the bend angle (θ). In Equation 5.5, u is velocity of the fluid and R_b is the bend radius. The Darcy friction factor (f_D) was calculated according to the Colebrook equation for the turbulent regime and to the Poiseuille equation for the laminar regime [106]. A summary of the used correlations is presented in Table 5.2.

The driving pressure of the natural circulation mechanism results from the density gradient between the two-phase mixture in the riser and the downcomer tubes [126]. For a given circulation ratio (CR) the tube height (H)

is obtained when the driving pressure (dp) equals the frictional and momentum (fm) pressure losses in the natural circulation circuit (downcomer (dc), riser (r) and heat exchangers (hx)). This is expressed in Equations 5.6 and 5.7. Each pressure drop term was calculated according to Ref. [127]. The CR was considered to be equal to 15 [111].

$$\Delta P_f = \frac{1}{2} f_{\mathrm{D}} \rho u^2 \left(\frac{\theta R_{\mathrm{b}} + L_{\mathrm{tube}}}{ID} \right) + \frac{1}{2} k_{\mathrm{b}} \rho u^2 \tag{5.5}$$

$$\Delta P_{\mathrm{dp}} = g \rho_{\mathrm{dc}} H_{\mathrm{dc}} - g(\rho_{\mathrm{hx}} H_{\mathrm{hx}} + \rho_{\mathrm{r}} H_{\mathrm{r}}) \tag{5.6}$$

$$\Delta P_{\mathrm{fm}} = \Delta P_{\mathrm{dc}} + \Delta P_{\mathrm{r}} + \Delta P_{\mathrm{hx}} + \Delta P_{\mathrm{nozzles}} + \Delta P_{\mathrm{b}} \tag{5.7}$$

Table 5.2: Correlations for heat transfer and pressure drop

Heat exchanger	Side	Pressure drop	Heat transfer coefficient
Single phase	Tube	Idelchick, Darcy (†)	Gnielinski
	Shell	Zukauskas	Zukauskas
Evaporator	Tube	Idelchick, Darcy (†)	Gnielinski
	Shell	Negligible	Stephan-Abdelsalam

(†) The Darcy coefficient was calculated according to the Colebrook and Poiseuille correlation for turbulent and laminar regime, respectively.

5.2.2.3 Mechanical and geometrical design

The thickness of the components such as shells, tubes, headers and pipes is calculated according to the ASME boiler pressure vessel code (BPVC) [93]. All the components are made of carbon steel. Table B.2 (see Appendix B.2) summarizes the materials used for each component, which are selected according to the regulations.

The chosen number of tube layers influences the shell diameter as in order to minimize the space required by the shell, the length of each coil was calculated to determine a square geometry which could be placed inside the shell with a low space waste. Based on the tube-side geometry, firstly the internal diameter was calculated and in a second step, according to the BPVC sec. VIII div. 2,

Equation 5.8 was used to calculate the thickness (t) of the shell.

$$t_{\text{shell}} = \frac{p \cdot ID/2}{S - (1 - y)p} + C \tag{5.8}$$

The thickness is dependent on the design pressure (p) (in barg), maximum allowable stress (S) of the chosen material at design temperature and a safety coefficient (y). The regulation takes into account a tolerance for allowable corrosion (C) which depends on the material and on the fluid as well as on the requirements of the power plant operator.

Similarly, each pipe (like the headers and risers/downcomers) thickness was calculated according to Equation 5.10, which, in this case, depends on the outer diameter (OD) of the pipes. In the case of the header, the diameter was calculated in order to align each tube equidistantly in each layer of the tube bundle geometry and provide sufficient spacing to avoid additional stress concentrations. Equation 5.9 refers to the tube thickness calculation.

$$t_{\text{Pipes}} = \frac{p \cdot OD}{2S + 2y \cdot p} + C \tag{5.9}$$

$$t_{\text{tubes}} = \frac{p \cdot OD}{2S + p} + 0.005 \cdot OD + C \tag{5.10}$$

A different approach needed to be applied to the evaporator tubes, as the highest pressure was on the shell side and not on the tube side, requiring higher thickness to withstand external pressure loads. The calculation procedure assumes a tube length and thickness, followed by a calculation of the maximum allowable pressure. The iteration stops when this value is higher than or equal to the design pressure considered. The operating pressure and required steam load by the evaporator determine the necessary steam drum volume. The steam volume chamber was determined according to chart that illustrates the minimum and maximum steam volumes as a function of the operating pressure[127]. The relation between chamber volume (in terms of m^3/s of produced steam for each m^3 of available volume) and working pressure is presented in Figure 5.4, with minimum and maximum suggested values. These charts were digitized and the data were obtained using linear interpolation during the optimization. The range is quite wide, but for high circulation ratio and efficient separation devices, values towards the higher limit can be chosen (hence lower required volumes).

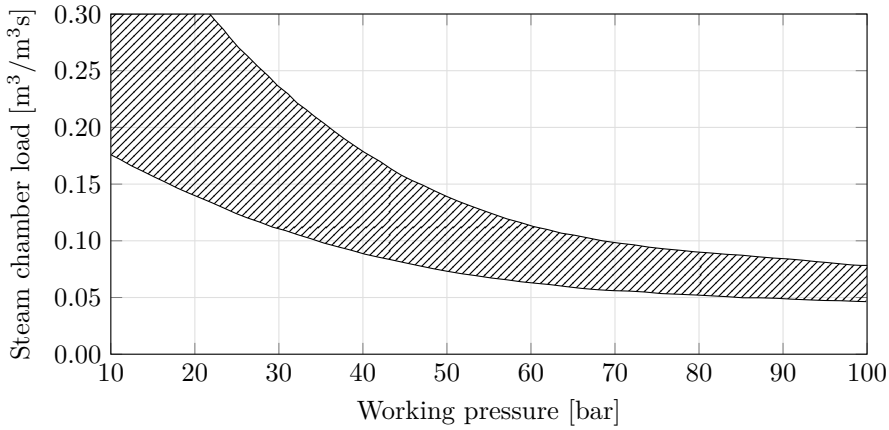

Figure 5.4: Relation between chamber volume and working pressure (adapted from Ref. [127]).

For this work, a value of 0.3 (in relative term) from the centerline was assumed as the reference curve. It is common practice that the water level corresponds with the center line of the drum, the drum volume becomes twice as large as the required steam drum chamber. According to industrial experience, the internal drum diameter was set to a minimum value of 1.5 m in order to allow for the correct placement of the separating devices and space requirement for internal inspection. The volume was determined to ensure that the maximum vapour velocity allowed avoiding gravitational settling of entrained liquid [127].

5.2.2.4 Heating rate calculation

The EN 12952-3 gives directions to determine the maximum allowable heating rates, to keep the induced stresses in the singularities (i.e. junction between downcomer and steam drum or header and tubes) below the allowable stress (σ_a) determined from a LCF diagram for a given number of cycles corresponding to the chosen lifetime of the component [94]. The norm can be applied to both steam drum/downcomer and header/tubes junctions [119, 128, 129]. Equation 5.11 summarizes the concept and illustrates how the resulting total stress calculated as the sum of the thermal stress and tensile stress. They depend on the thermal (T) and mechanical (m) stress concentration factors respectively (α), which were calculated according to the norm. E, β, ν are the Young's modulus, thermal expansion coefficient and Poisson's ratio, respectively. The main non-dimensional parameter is Φ_w which

depends on the outer to inner diameter ratio ω as shown in Equation 5.12.

$$\left|\alpha_{\mathrm{m}}(p-p_0)\frac{ID+t}{t}+\alpha_{\mathrm{T}}\cdot c\cdot\rho\frac{E\cdot\beta}{1-\nu}\frac{v_{\mathrm{T}}t^2}{\lambda}\Phi_{\mathrm{w}}\right|\leq|\sigma_{\mathrm{a}}| \tag{5.11}$$

$$\Phi_{\mathrm{w}}=\frac{1}{8}\frac{(\omega^2-1)(3\omega^2-1)-4\omega^4\cdot ln(\omega)}{(\omega^2-1)(\omega-1)^2} \tag{5.12}$$

The minimum and maximum values of allowable heating rates corresponding to the minimum and maximum pressure are calculated according to the norm for a specified start-up cycle. Once the two values are determined the heating rate can be calculated at each intermediate pressure by means of a linear interpolation according to Equation 4.18. In order to grasp the overall length of the start-up procedure, an average heating rate can be defined according to Equation 5.13. The considered start-up cycle, obtained from the parabolic trough model, corresponds to 25 years, 346 starts each year of which 21 cold, 234 warm and 91 hot start-up procedures which would correspond to starting pressure of 26 bar, 16 bar and 1 bar, respectively.

$$v_{\mathrm{Taverage}}=\frac{1}{t_{\mathrm{end}}-t_{\mathrm{start}}}\cdot\int_{t_{\mathrm{start}}}^{t_{\mathrm{end}}}\frac{dT_{\mathrm{f}}}{dt}\,\mathrm{d}t \tag{5.13}$$

5.2.2.5 Cost estimation

The costing method presented by Purohit et al. [130] was employed to estimate the purchased equipment cost (PEC) of the SGS. Firstly, the cost of a baseline exchanger is estimated according to Equation 5.14, where p_{OD}, f and r are cost multipliers for the outer diameter, front and rear head types, respectively. These parameters are chosen to match the considered configuration. The total single heat exchanger cost is then determined as a function of the heat exchange area as presented in Equation 5.15, where N_{s} indicates the number of shells and $c_{\mathrm{i,j}}$ represent a number of correction factors which take into account design pressure, length of the tubes and material selection. Each coefficient formulation or value is presented in Table B.3 (see Appendix B.2). The total SGS heat exchanger cost was then calculated as the sum of each heat exchanger cost and adjusted to 2017 as a reference year, according to the historical price index (HPI) reported

in Ref. [131]. The cost of the steam drum was calculated as a function of the drum metal mass [132] and carbon steel prices according to Ref. [133].

$$b = \left(\frac{6.6}{1 - e^{\left(\frac{7-ID}{27}\right)}} \right) \cdot p_{\mathrm{OD}} \cdot f \cdot r \tag{5.14}$$

$$PEC_{\mathrm{hx}} = b \cdot \left(1 + \sum_{i=1}^{n} c_{\mathrm{i}} \right) \cdot A \cdot N_{\mathrm{s}} \tag{5.15}$$

$$PEC_{\mathrm{SGS}} = \frac{HPI_{2017}}{HPI_{1983}} \cdot \sum_{\mathrm{j}=1}^{n_{\mathrm{hx}}} \left(b_{\mathrm{j}} \cdot \left(1 + \sum_{\mathrm{i}=1}^{\mathrm{n}} c_{\mathrm{i,j}} \right) \cdot A_{\mathrm{j}} \cdot N_{\mathrm{s,j}} \right) \tag{5.16}$$

5.2.2.6 Optimization and constraints

The optimization routine consisted of minimizing both the total water pressure drop and purchased equipment cost. The lower the pressure drop is, the lower the heat transfer coefficient will be as lower fluid velocities are required, implying higher heat transfer areas, hence cost. Therefore investment cost and pressure drops are conflicting parameters. From a system perspective, higher mass flow rates on the HTF side would imply higher parasitic consumptions and therefore lower profitability of the power plant. In addition to this, if storage systems are integrated, lower HTF temperature would be desirable as this would imply lower storage investment cost.

Previous research by Gonzalez-Gomez et al. [42] took into consideration all these aspects, yet the focus of this section was to analyse in a more detailed approach just the SGS, hence only the minimization of pressure drop and PEC was considered. This allows narrowing the influence of including the LCF constraints into the design routine, excluding external influences like power plant parameters. It is also common practice, in the industry, to select SGS by pressure drop in a given plant configuration. Hence having a trade-off curve between pressure drop and PEC, would allow choosing the most cost-effective design for a set of power plant constraints.

The optimization was carried with the genetic algorithm multi-objective optimization toolbox available in Matlab by varying the parameters in the

range presented in Table 5.3. It was decided to choose the same tube outer diameter for each heat exchanger, to favour an economy of scale. The diameter was chosen to be a discrete variable, with the possibility to decide from four different commonly available tube outer diameters according to Coulson et al. [134]. The four choices (referred as the index in Table 5.3) were 25 mm, 30 mm, 38 mm and 50 mm, respectively, with lower diameters excluded from the optimization since these designs gave rise to high pressure drops (above 10 bar). The tube pitch values were chosen to be fixed to the lowest value allowable by not drastically increasing the pressure drops. This resulted in a tube pitch ratio (distance/diameter) of 1.25 and a staggered alignment to allow for the lowest shell diameters, higher heat transfer coefficient and easier mechanical cleaning [135, 136]. These choices are also in agreement with the results presented by Gonzalez-Gomez et al. [42].

Table 5.3: Optimization decision variables.

Variables	Unit	Lower boundary	Upper boundary
Tube outer diameter index	[-]	1	4
RHe number of layers	[-]	20	40
RHs number of layers	[-]	20	40
EVA number of layers	[-]	20	40
SUP number of layers	[-]	20	40
ECO number of layers	[-]	20	40
Rhe number of tubes per layer	[-]	3	15
RHs number of tubes per layer	[-]	3	15
EVA number of tubes per layer	[-]	3	15
SUP number of tubes per layer	[-]	3	15
ECO number of tubes per layer	[-]	3	15
Riser outer diameter	[mm]	200	300
Number of risers	[-]	5	15

Constraints were set in order to obtain feasible designs from the optimization study. These are presented in Table 5.4. The minimum and maximum tube side velocities were set in order to reduce possible fouling and avoid excessive corrosion, respectively [134]. The maximum steam flow velocities were set according to the steam velocity diagram which is dependent on operational pressure as presented in Ref. [137].

Minimum values for maximum allowable heating rates were also considered for each component (header/tube junction for single-phase heat exchangers and drum/downcomer junction for the evaporator). According to the results presented in the previous section (see Section 4.2.3), a lower bound was set to

Table 5.4: Optimization constraints.

Parameter	Unit	Value
Tube minimum velocity	[m/s]	0.5
Tube maximum velocity	[m/s]	4
Shell minimum velocity	[m/s]	0.2
Shell maximum velocity	[m/s]	1.5
Steam maximum velocity	[m/s]	25
Oil maximum pressure drop	[bar]	2
Evaporator minimum heating rate	[K/min]	8.5
Super-heater minimum heating rate	[K/min]	15
Minimum drum internal diameter	[mm]	1500

the evaporator heating rate constraints as this component is the main limiting factor for the SGS start-up procedure. This value was chosen as an intermediate threshold as compared to the results previously presented (see section 4.2.3). All the other components were checked to have a lifetime higher than or equal to 25 years, while the superheater complied with a heating rate which was proportional to the evaporator heating rate (see Section 4.2.3). The optimization was carried for the following two cases:

1. No LCF constraints
2. LCF constraints, with a minimum heating rate for both the evaporator and superheater

The evaporator was also checked for specific constraints such as the critical heat flux for the tube bundle to avoid film boiling [138, 139] and assuring that the critical flow G_c in the water-steam mixture is not reached. Equation 5.17 was used to estimate this value, considering the reference (ref) properties at the upstream stagnation point (steam drum) and c_f as a choking correction factor [140].

$$G_c = \sqrt{2 \cdot [p_{ref} - c_f \cdot p_{sat} \cdot (T_{ref})] \cdot \rho_{l,ref}} \tag{5.17}$$

5.2.3 Results

5.2.3.1 Model validation

A validation on the design parameter results and steady-state results was carried out by comparing the most significant output of the model with the available data of the SGS of an existing and operating 55 MWe parabolic trough power plant employing a header and coil steam generator. Table 5.5 illustrates the validation of the key parameters results of the model. Due to the confidentiality nature of the detailed geometrical design, only the main results are presented in the table. The Purohit method used for the SGS cost estimation was developed specifically for the TEMA configuration, but in the case of the header and coil geometry, its applicability was demonstrated by comparing its results with cost figures provided by the boiler manufacturer. For the different sizes provided, the relative deviations between the results of the cost model and the manufacturer data were below 2 %, justifying the use of the method also for the header and coil geometry.

Table 5.5: Validation results for the steam generator steady state model.

Parameters	Units	Model	Data	Deviation
Total area required (HTF side)	[m^2]	2755	2688	2.50%
HTF SGS temperature drop	[K]	92.40	91.70	0.76%
Pressure drop (HTF side)	[bar]	1.663	1.640	1.40%
Pressure drop (Water side)	[bar]	1.850	1.852	-0.11%
Velocity SH steam outlet	[m/s]	10.81	10.95	-1.32%
Velocity ECO HTF outlet	[m/s]	0.912	0.900	1.33%
EVA maximum heating rate	[K/min]	8.830	9.000	-1.89%
Total weight	[ton]	231.8	240.4	-3.59%

A relative deviation of +2.5 % is obtained in case of the total heat exchange area estimation, meaning that the model properly predicts the heat transfer coefficients with a reasonable degree of accuracy. This is also supported by the total HTF inlet to outlet temperature difference deviation below 1 %. Small deviations are also found for the outlet water and HTF velocities indicating a good estimation for each fluid pressure drop, with a maximum deviation of +1.4 %. The table illustrates that even though the total area is overestimated, the opposite trend is observed for the weight estimation. This is explained by the fact that the thickness of the components is underestimated by 2.9 %, on average. This is related to the fact that a manufacturer would choose a tube with the closest dimensions in terms of thickness and diameter among those

available on the market. The results of the validation presented in Table 5.5 suggest that the models provide sufficiently accurate results for the purpose of this thesis work.

5.2.3.2 Optimization results

Figure 5.5 presents the multi-objective optimization results, comparing Case 1 and Case 2 (see Section 5.2.2.6) in Figure 5.5a and a total HTF pressure drop as colormap in Figure 5.5b. If only the thermodynamic constraints are considered (Case 1), the solution region corresponding to the 25 mm tube outer diameter is excluded due to exceeding velocities and pressure drops. Only the other three diameters (30 mm, 38 mm, and 50 mm) are the resulting feasible diameter options. If also the LCF constraints are included (Case 2), also the 30 mm solution region would be excluded due to two main reasons. If low tube numbers are considered (close to the lower bound), the pressure on the SH side significantly increases, determining higher steam pressure at the evaporator steam drum (considering constant inlet turbine pressure). This would require higher thickness for both the steam drum and downcomer pipes, increasing thermal stresses and reducing the maximum allowable heating rates. However, if the superheater tube number increases, the correspondent header design would result in larger diameters. This implies higher thickness requirements, hence inducing higher thermal stresses and therefore not meeting the LCF constraints on the superheater.

By comparing the grey and red plots in Figure 5.5a it may be observed that for the same desired total water pressure drop, the design could significantly change if LCF constraints are considered during the design procedure. For instance, if a 1 bar pressure drop is required, the PEC would rise by around 0.75 million USD, obtaining a design with 9.1 K/min of v_{T} for the evaporator. This value can be considered justifiable even though it corresponds to a 42 % increase in capital cost compared to the unconstrained design, which presents a maximum allowable evaporator heating rate of 6.2 K/min. If the economy of the plant is taken into consideration, as explained in the previous section (see Section 4.2.3), an evaporator v_{T} increase from 6.2 K/min to 7-10 K/min would result in an increase in electricity production ranging between 0.84 % and 3.31 %, depending if the superheater is optimally designed and operated considering the heating rate perspective. In a 25 years lifetime of the plant, and assuming the lowest bid for CSP power production of 94.5 USD/MWh [141], this could result in an increase in revenues between 1.17 million USD and 4.7 million USD. If different designs, which would only allow for low heating rate constraints (3 K/min), would be employed, these figures could rise to 2.1 million USD and 7.1 million USD, respectively.

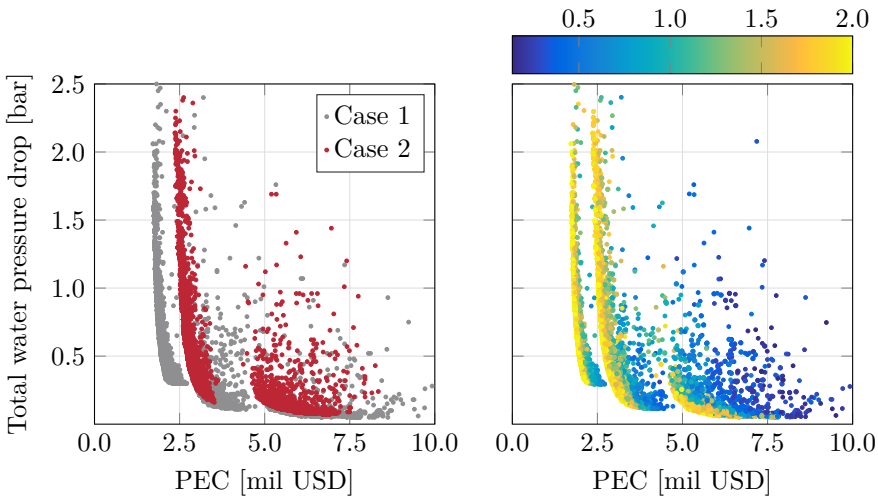

(a) Comparison between the three cases **(b)** HTF total pressure drop [bar]

Figure 5.5: Optimization results

Table 5.7 summarizes the optimal geometrical parameters for Case 2, for three different ranges of pressure drop. It lists the arithmetic mean average, relative standard deviation (RSD) around the mean and minimum and maximum values of the optimized variables at the Pareto front. The table is split between pressure drops higher and lower than 1 bar for the 38 mm outer diameter solution. A third column presents the results corresponding to the 50 mm solution corresponding to pressure drops lower than 0.225 bar. A low RSD and small difference between the minimum and maximum values imply that the correspondent variable does not vary significantly within the optimal configuration. The EVA, ECO, SH number of layers and EVA tubes per layer present the lowest RSD for pressure drops higher than 1 bar. A similar conclusion can be drawn for designs which would result in lower pressure drops. The results presented for the number of tube layers for the superheater support the aforementioned discussion regarding the necessity to increase such a parameter in case low pressure drops are required. The third column shows that, in this case, an increase of 28 % is necessary to satisfy this condition.

The riser/downcomer design (outer diameter and numbers) is characterized by a low RSD. The main reason is that a low number of risers would imply high pressure drops (as the mass flow rate would be divided in a lower number of tubes, hence resulting in higher velocities), therefore determining larger height

values. Larger diameter configurations would result in lower velocities, lower pressure drops, yet higher thickness requirements. The results presented in the three columns can be interpreted as the optimal configuration, considering the trade-off between the number of tubes and diameter to minimize thickness and height, hence the associated cost and the induced thermal stresses. The difference in operating pressure ranges between the three columns determines the slightly different design pressure between the three configurations.

The difference in optimal diameter for the high pressure drop designs is the most evident change between the two cases. Table 5.6 presents a comparison in terms of relative change in the number of tubes among the optimal designs for the pressure drop ranges as presented in Table 5.7. The average values for the whole Pareto front are presented in an additional column. Each column presents the relative variation of tube numbers in Case 2 as compared to Case 1. The variation stems from either an increase in the number of tube layers or the number of tubes for each layer. The main trend is an overall increase in the number of tubes for each heat exchanger. The superheater presents the highest relative increase in the number of tubes both for the high pressure drop designs and as an average considering the whole pressure drop range. By lowering the water pressure drop, the economizer presents the highest increase. In this case, in order to lower the water side pressure drop and at the same time keep high maximum allowable heating rates, the economizer pressure drop is decreased by increasing its number of tubes in equal proportion between the number of layers and number of tubes for each layer. Both Figure 5.5a and Table 5.6 suggest that by including LCF constraints during the design phase, different optimal designs are obtained in the whole cost range, with the cheaper designs being the most affected.

Table 5.6: Comparison of designs of the two optimization cases (Case 2 compared with Case 1) in terms of relative change in the number of tubes for each heat exchanger.

Component	$p > 1$ bar	0.225 bar $< p \leq 1$ bar	$p \leq 0.225$ bar	Average
RHe	145.0 %	134.1 %	105.6 %	128.2 %
RHs	141.5 %	132.8 %	110.4 %	127.9 %
EVA	105.0 %	134.8 %	127.6 %	122.1 %
SH	154.8 %	145.0 %	125.6 %	141.8 %
ECO	121.8 %	156.1 %	131.7 %	136.5 %

An example of the thermodynamic and geometric results for 1 bar total water pressure drop is illustrated in Table 5.8. Additional results concerning the thermodynamic states and heat loads may be found in Appendix, in Table A.6

and Table A.7. A low number of tubes is preferred in the high pressure heat exchangers, while large header diameters are preferred on the re-heater train side. On the cost side, the evaporator and the superheater are the two most expensive components, accounting for 34 % and 27 % of the total PEC, respectively. This determines a tendency towards a low number of tubes and high heat transfer coefficients for these components (in order to minimize heat transfer area). On the other hand, the re-heaters are less sensitive from an area/cost and heating rate perspective, accounting for 14 % and 12 % of the total PEC, respectively. This explains why in Table 5.7, the re-heater parameters experience high variations in the optimal solutions.

Observing Figure 5.5b may draw the additional consideration that the total HTF pressure drop converges towards the maximum allowable value of 2 bar in order to minimize the PEC. A decrease in the shell side velocity (i.e. heat transfer coefficient) would require a lower number of coils, hence a high number of tube layers. This would also cause a reduction in the water-side heat transfer rate, increasing the heat exchanger area requirements. In the case of the same 1 bar total water pressure drop, this would result in a PEC increase of 13 %, if a decrease in HTF total pressure drop from 2.0 bar to 1.5 bar is required.

It is important to denote that firstly these specific results are governed by the power plant design specifications and constraints. Therefore, if different specification or constraints are adopted, different SGS designs are obtained (for instance in the presence of thermal energy storage). Secondly, these results are specific to the parabolic trough power plant cases. As previously mentioned in Section 1.1, even though these plants are the most commercially mature, solar tower plants are experiencing an increasing trend in interest. If solar tower plants are considered instead, the methods presented in this section could be applied in a similar approach. The main difference would derive from the presence of molten salt as heat transfer fluid and the associated risk of freezing at relatively high temperature [88]. This would require a different design of the evaporator as the molten salt would be required on the shell-side in order to minimize the freezing risk and facilitate maintenance. Another difference would be the operating temperature. Typically, solar tower plants operate at around 565 °C. Having a higher temperature would require different materials and impose different stress cycles, hence the impact of the LCF constraints is expected to be more pronounced.

Table 5.7: Optimization results for Case 2. Minimum, mean, maximum and relative standard deviation of the optimized variables. The values are acquired from the Pareto front in Figure 5.5a.

		Higher than 1 bar				Between 0.225 and 1 bar				Lower or equal to 0.225 bar			
Variables	Units	min	mean	max	RSD	min	mean	max	RSD	min	mean	max	RSD
Tube outer diameter	[mm]	38	38	38	0%	38	38	38	0%	50	50	50	0%
RHe number of layers	[-]	28	29	30	3%	28	32	39	10%	27	34	38	9%
RHs number of layers	[-]	31	34	36	5%	34	35	35	1%	28	34	40	8%
EVA number of layers	[-]	29	30	33	4%	21	23	29	7%	20	20	22	3%
SH number of layers	[-]	20	22	24	6%	21	25	29	6%	25	32	39	13%
ECO number of layers	[-]	21	23	26	6%	21	22	29	6%	20	21	29	9%
RHe number of tubes per layer	[-]	7	8	10	14%	8	11	13	10%	14	15	15	3%
RHs number of tubes per layer	[-]	7	8	9	11%	8	11	15	18%	14	15	15	3%
EVA number of tubes per layer	[-]	4	4	4	0%	4	5	5	4%	3	3	5	21%
SH number of tubes per layer	[-]	4	6	7	18%	7	10	11	10%	8	8	11	12%
ECO number of tubes per layer	[-]	5	6	7	12%	5	6	8	13%	6	7	8	9%
Riser outer diameter	[mm]	253	280	296	5%	261	293	300	3%	294	298	300	1%
Number of risers	[-]	5	6	7	10%	5	6	8	9%	5	6	8	8%

Table 5.8: Result design for 1 bar pressure drop on water side

Parameter	Units	ECO	EVA (†)		SH	RHe	RHs
Shell diameter	[mm]	1636	1465	1658	1709	2246	2599
Shell length	[mm]	9.3	13.2	8.95	15.03	16.54	17.1
Shell thickness	[mm]	18	65	79	20	23	29
Number of shells	[-]	1	2	1	1	1	1
Tube outer diameter	[mm]	38	38		38	38	38
Tube thickness	[mm]	3.8	4.8		3.8	3.8	3.8
Tube layers	[-]	22	29		23	30	34
Tube per layers	[-]	6	4		7	9	9
Tube coils	[-]	23	3		34	10	12
Header diameter	[mm]	380.6	216.4		465.9	560.5	489.2
Header thickness	[mm]	27.0	22.6		37.0	19.0	16.0
Tube side average flow velocity	[m/s]	0.52	3.39		6.50	18.48	17.82
Shell side average flow velocity	[m/s]	1.01	-		1.04	0.59	0.52
Tube side heat transfer coefficient	[W/(m^{2}K)]	4567.0	5311.0		2024.3	735.5	578.3
Shell side heat transfer coefficient	[W/(m^{2}K)]	1993.1	23472.7		1866.1	1441.3	1218.1
Overall heat transfer coefficient	[W/(m^{2}K)]	1155.2	3245.6		1155.2	402.7	325.4
Oil side pressure drop	[bar]	0.289	1.133		0.445	0.078	0.294
Water side pressure drop	[bar]	0.031	0.017		0.472	0.294	0.206
Purchased equipment cost	[mil USD]	0.350	0.850		0.690	0.290	0.350
v_T average	[K/min]	68.7	9.1		31.7	246.1	153.7

(†) The shell parameters refer to the heat exchangers (on the left) and steam drum (on the right).

5.3 Design accounting for dynamic performance requirements

5.3.1 Introduction

Considering the previous research works presented in Section 1.2, it can be stated that even though there is availability in the literature of transient response modelling of heat exchangers and steam generators, this aspect is not taken into account during the design phase of all the components. However the results of the previous sections (4.2.3, 4.3.3) and 5.2 demonstrated the significance of including transient response analysis in the design process. More in details, even if a Pareto front with optimal SGS designs is obtained, little information is available on how to properly select the optimal design point. By accounting for the impact that such design would have on the power plant performance and by ensuring that the stresses are always below the maximum allowable threshold it would be possible to guarantee the optimal operation of the power plant.

The methods presented in this section build upon the design steps presented in the previous section (see Section 5.2) and expand it by adding the transient analysis during the start-up. The objective is to evaluate how different optimal designs (obtained with the method presented in section 5.2) influence the dynamic performance of the steam generator system. Stress sensitivity and impact on the power plant techno-economic performance are evaluated. These indicators are used to select the optimal design for the studied power plant. The design routine was applied to a reference power plant of 55 MWe integrated with thermal energy storage as the representative layout of the Andasol configuration.

Section 5.3.2 presents the methods used to optimize the SGS design, evaluate the power plant performance and address the SGS dynamic performance evaluation in terms of start-up procedure and stresses. Section 5.3.3 presents and discusses the results of the validation and multi-objective optimization and the impact of the different optimal designs on the LCOE and total stresses during start-up procedures.

5.3.2 Methods

5.3.2.1 Power plant modeling

Figure 5.6 presents the PTPP layout considered, which it is integrated with an ACC and a two tank TES system. The re-heater is divided into two heat exchangers and the power block is a regenerative Rankine-reheat cycle. The main inputs required for designing the PTPP are summarized in Table 5.9. Different storage sizes were analyzed to investigate the impact of the SGS dynamic performance on the LCOE calculations, as higher storage size would mean lower load changes and start-up procedures throughout the year. Table 5.10 presents the derived inputs for the SGS design.

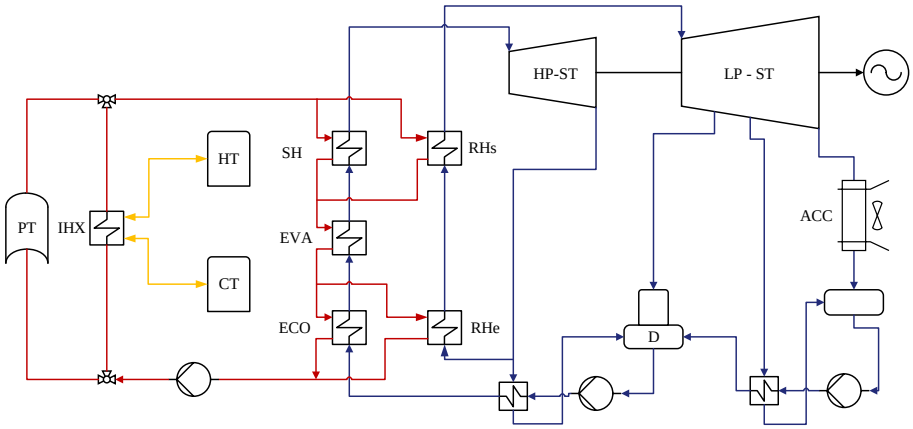

Figure 5.6: Parabolic trough power plant layout with two re-heaters and indirect thermal energy storage.

5.3.2.2 Steam generator transient modelling

The transient modelling was carried out in Modelica [57], which is an effective object-oriented language to develop models by using a modular approach. Existing and validated libraries of reusable models can be employed to carry out the specific modelling tasks as they can be modified and tailored to the needs of the particular case. In this work, the ThermoPower [142] library was chosen to carry out the transient modelling of the heat transfer for both the single phase heat exchangers and natural circulation evaporator.

Each control volume is based on mass, energy and momentum balances as shown in Equations 5.18, 5.19 and 5.20. In the equations, A_c is the cross section area, x the spatial coordinate, t the time, v the velocity. Equation 5.19 depends also on the internal energy u, thermal conductivity λ and temperature T and the frictional force per unit of length F_f. As for Equation 5.20, the additional parameters p, F_F, g and z are the pressure, frictional forces, constant of gravity and vertical coordinate, respectively. Additional information on the formulation of these equations in the ThermoPower library can be found in Refs. [142, 143]. In the case of two-phase flow regions, the equations are solved using the mean density method [144]. The equations are solved with the finite volume method (FVM) and a staggered alignment [145]. The modified Dassl [146] solver is used

Table 5.9: Parabolic trough power plant design parameters.

SGS design parameters	Units	Values
Solar multiple (SM)	[-]	2
Gross power	[MW]	55
TES capacity	[h]	5-7.5-10
Inlet HP/LP pressure	[bar]	100/16.7
Nominal condensing pressure	[bar]	0.06
SF HTF maximum temperature	[°C]	393
SF HTF outlet temperature	[°C]	293
Nominal turbine inlet temperature	[°C]	378

Table 5.10: Steam generator system design parameters

Parameters	Units	Value
EVA pinch point	[°C]	5
ECO approach point	[°C]	5
Turbine inlet temperature	[°C]	377.6
Turbine inlet pressure	[bar]	100
Reheat outlet temperature	[°C]	378.9
Inlet pressure at re-heat	[bar]	16.7
Inlet temperature at re-heat	[°C]	204.4
Feedwater temperature	[°C]	245.94
HTF inlet temperature	[°C]	393.3
HTF inlet pressure	[bar]	15
Steam mass flow rate	[kg/s]	60.988

to solve the algebraic system of equations.

$$\frac{d}{dt}(\rho A_c) + \frac{\partial}{\partial x}(\rho A_c v) = 0 \tag{5.18}$$

$$\begin{aligned}\frac{d}{dt}\left(\rho A_c\left(u+\frac{v^2}{2}\right)\right) + \frac{\partial}{\partial x}\left(\rho v\left(u+\frac{p}{\rho}+A_c\frac{v^2}{2}\right)\right) = \\ = -F_f - A_c\rho v g\frac{\partial z}{\partial x} + \frac{\partial}{\partial x}\left(\lambda A_c\frac{\partial T}{\partial x}\right)\end{aligned} \tag{5.19}$$

$$\frac{d}{dt}(\rho v A_c) + \frac{\partial}{\partial x}(\rho v^2 A_c) = -A\frac{\partial p}{\partial x} - F_F - A_c\rho g\frac{\partial z}{\partial x} \tag{5.20}$$

Each single-phase heat exchanger was modelled in a counter-current flow configuration, as the number of coils is higher than or equal to 6 [122]. On the other hand, the evaporator flow configuration was modelled according to Figure 5.7 based on a similar approach developed by Benato et al. [147]. Each water control volume (Nw) is associated with the corresponding tube control volume (Nt) in order to represent a 2D geometry. The total number of control volumes depends on the number of coils (Nc) as well as on the number of discretization volumes in the tube perpendicular direction (Nv). Pressure drop and heat transfer coefficients were calculated according to Section 5.2.2.2 as summarized in Table 5.2. The heat transfer correlation on the pool boiling side is calculated according to the simplified Jens and Lotte correlation [148] in order to save computational time. This is justifiable as the overall heat transfer performance is governed primarily by the heat transfer coefficient on the HTF side [149].

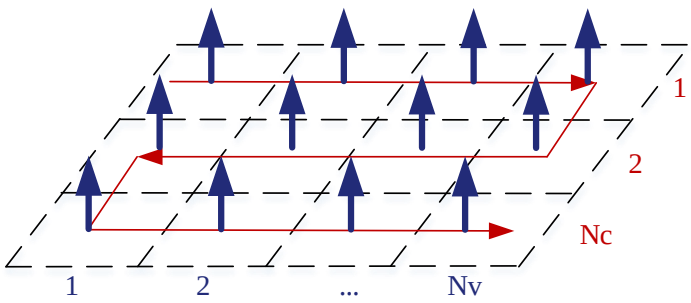

Figure 5.7: Two phase flow geometrical approach for the finite volume method.

The steam drum is modelled according to Åstrom and Bell [150] (as already implemented in ThermoPower) with energy and mass conservation equations as shown in Equation 5.21 and 5.22. The steam drum heat loss coefficient was calculated following the method presented by Churchill et al. [151] for natural convection against horizontal cylinders. The natural circulation loop between the heat exchanger and the steam drum is closed by the risers and downcomer, whose models take into account pressure drops. For a given tube number, height and diameter and the riser/downcomer mass flow rate is determined in order to balance the driving pressure force resulting from the density gradient between the two-phase mixture in the riser and liquid phase in the downcomer and the frictional pressure drop due to the length and singularities in the tubes [126] (see Section 5.2.2.2).

$$\frac{d}{dt}\left(\rho_{\mathrm{v}} V_{\mathrm{v}} + \rho_{\mathrm{l}} V_{\mathrm{l}}\right) = \dot{m}_{\mathrm{l}} - \dot{m}_{\mathrm{v}} \tag{5.21}$$

$$\frac{d}{dt}\left(\rho_{\mathrm{v}} V_{\mathrm{v}} h_{\mathrm{v}} + \rho_{\mathrm{l}} V_{\mathrm{l}} h_{\mathrm{l}} - p V_{\mathrm{t}} + m_{\mathrm{t}} C_{\mathrm{p}} T_{\mathrm{m}}\right) = \dot{m}_{\mathrm{l}} h_{\mathrm{l}} - \dot{m}_{\mathrm{v}} h_{\mathrm{v}} + \dot{Q} \tag{5.22}$$

5.3.2.3 Start-up constraints and control strategy

Figure 5.9 presents the SGS layout, with details including bypass valves and controllers configuration. The blue and red solid lines represent the water and HTF flows, respectively. The green and orange dashed lines follow the control signal of the two main controllers (C1 and C2), while the black dashed lines represent the process variable (PV) signals which are measured at the steam drum, superheater and re-heater.

Figure 5.8 presents the steam generator start-up procedure control logic which is mainly managed by the C2 controller illustrated in Figure 5.9. The presented control strategy is based on Refs. [39, 84] and adapted to the specific case considered. The process is initiated if the HTF reaches a sufficiently high temperature (280 °C) (as indicated by (1) in Figure 5.8). The HTF is then pumped to the SGS with a mass flow rate kept at 10 % of its nominal value in order to minimize heat losses [84]. By acting on the HP-ST opening valve, the pressure is kept at the minimum acceptable value of the steam turbine (26 bar). While the HTF and steam temperatures increase, the steam mass flow rate is bypassed and redirected to the condenser until the acceptable values for the turbine are achieved.

Once the minimum steam temperature is achieved the inlet HP-bypass valve is closed and the turbine can receive low mass flow rate (3-5 % of nominal value) to begin the roll-up phase and synchronization (as indicated by (2) in Figure 5.8). During this phase, whose duration depends on the turbine metal temperature, the excess steam mass flow rate is bypassed and sent to the feedwater system. When the roll-up is terminated the HP-ST valve is completely opened and both mass flow rate and pressure can be increased. The HTF mass flow rate is raised in a way to comply with the maximum allowable heating rate values of the steam drum (as indicated by (3) in Figure 5.8). Once the mass flow rate, temperature and pressure reach their nominal values, the SGS start-up phase is finished.

Another controller (as indicated by C1 in Figure 5.9) manages the water level in the drum around the center line by adjusting the feedwater mass flow rate, hence avoiding swelling and dry-out [48]. Both control strategies were integrated within proportional integral derivative (PID) controllers which were calibrated according to the Ziegler-Nichols method [152].

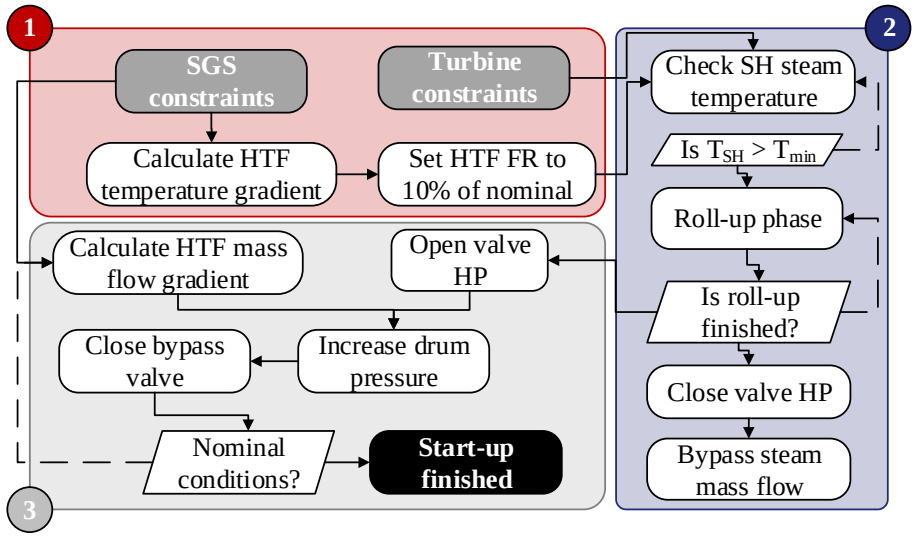

Figure 5.8: Steam generator system start-up logic. Solid lines represent a YES logic while dashed lines represent a NO logic. Grey and black boxes indicate input and outputs, respectively.

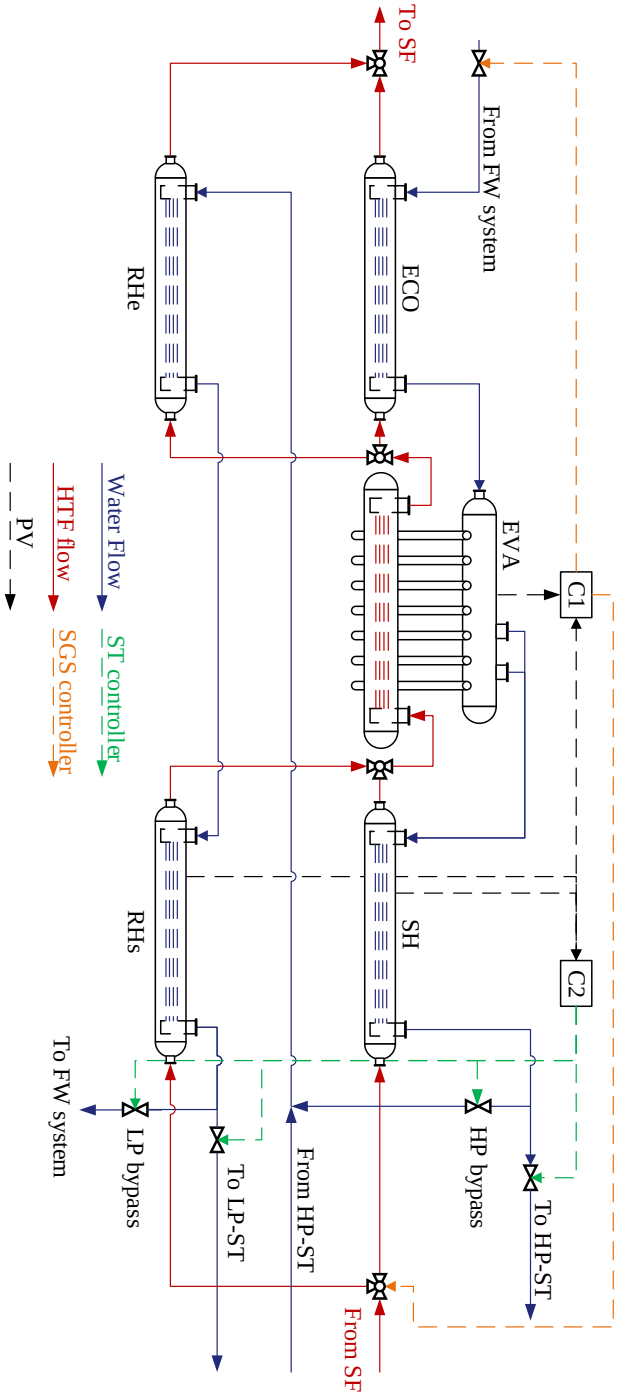

Figure 5.9: Steam generator system heat exchanger configuration.

5.3.2.4 Stress evaluation in materials

The resulting total stress in the heat exchangers materials derives from the addition of both thermal and tensile stresses as summarised by Equation 5.23 [94]. The pressure induced stress occurring in the junctions depends on a concentration factor α_{M} which is computed according to the EN 12952-3 and depends on the ratio of the diameter to the thickness of the components forming the junction. D and t represent the average diameter and thickness of the geometry considered. The thermal stresses depend on the thermal concentration factor (α_{T}) which is calculated according to the working fluid phase (vapour or liquid) and the diameter ratio of the main components. T_{i} represents the internal fluid temperature, while T_{m} represents the mean integral metal temperature.

The header metal temperature profile is computed according to Fourier's law (governs heat conduction) and necessary boundary and initial conditions as expressed in Equation 5.24. The two Robin boundary conditions are defined by imposing to heat fluxes at the outer (o) and at the inner (i) radius coordinate, in which h is the heat transfer coefficient. The inner and outer heat transfer coefficients are computed using the Gnielinski correlation [106] and the Churchill correlation [106] for forced convection against cylinders, respectively. This definition of boundary equations is set to account for the non-negligible heat resistance experienced by the fluid, especially at part-load conditions, as the heat transfer coefficient can become very low (below 200 $\mathrm{W/m^2K}$) for low mass flow rates. Considering the steam drum, the inner boundary condition is defined differently by fixing the inner metal temperature equal to the water temperature (Dirichlet boundary condition) as suggested by Kim et al. [153]. The outer heat transfer coefficient is computed using the Churchill correlation for natural convection against horizontal cylinders [151].

$$\sigma = \sigma^P + \sigma^T = \alpha_{\mathrm{M}} \frac{D}{2t} \cdot p + \alpha_{\mathrm{T}} \frac{E\beta}{1-\nu} (T_{\mathrm{m}} - T_{\mathrm{i}}) \tag{5.23}$$

$$\begin{cases} \dfrac{1}{\alpha}\dfrac{\partial T}{\partial t} = \dfrac{1}{r}\dfrac{\partial}{\partial r}\left(r\dfrac{\partial T}{\partial r}\right) \\ T(r,0) = T_0 \\ -\lambda \left.\dfrac{\partial T}{\partial t}\right|_{r=r_i} = h_i(T_i - T(r_i,t)) \\ -\lambda \left.\dfrac{\partial T}{\partial t}\right|_{r=r_o} = h_o(T(r_o,t) - T_o) \end{cases} \tag{5.24}$$

With regards to the EN 12952-3, the maximum and minimum allowable stresses are set in order to protect the magnetite layer on the metal wall of the components. The former was set to be calculated 200 MPa above the pressure stress at the nominal operating condition, while the latter was set to be 600 MPa below the pressure stress at the nominal operating condition.

5.3.2.5 Dynamic model validation

A validation was carried out to estimate the accuracy of the dynamic model both in transient and steady-state nominal conditions. The latter was performed by comparing the main thermodynamic parameters (steam mass flow rate, pressure and temperature, HTF outlet temperature) at nominal load with the data of an existing power plant. The transient validation was performed by comparing the model results with the operational data for a day in March 2014 between 8.15 and 18.15.

The following six parameters were the available measured data for the validation: superheater steam outlet temperature and pressure, steam mass flow rate, feedwater mass flow rate, re-heater steam outlet temperature and HTF outlet temperature. These parameters also represent the main output of the SGS model. The inputs to the model are the HTF inlet mass flow rate and temperature, economizer water inlet temperature and re-heater water inlet mass flow-rate, pressure and temperature. In order to quantify the validation accuracy the indicators presented in Equation 4.22, 4.23 and 4.24.

5.3.3 Results

5.3.3.1 Model validation

Table 5.11 illustrates the result of the validation for steady-state operation at nominal load. The maximum deviation is found for the superheater degree of superheat (2.8 %) which is mainly attributed to the underestimation of the steam mass flow rate by 0.79 %. All the other parameters present a deviation below 1 %, indicating that the model is accurate at steady state nominal load.

The transient validation step was carried out by considering the required inputs of the operational data of the power plant for a day in March 2014 between 8.15 and 18.15 as depicted Figure 5.10. The total HTF inlet mass flow rate, the split between the superheater and re-heater and inlet temperature are presented in Figure 5.10a and Figure 5.10b, respectively. The economizer water inlet temperature and re-heater steam inlet temperatures and pressure are illustrated in Figure 5.10c. Figure 5.11 illustrates the results of the transient validation, with Figures 5.11a, 5.11b and 5.11c presenting the temperatures of the superheater and re-heater outlet steam and HTF, respectively.

The superheater and HTF outlet temperatures are properly represented with the latter overestimated by 1.4 % on average between 2.5 h and 7.5 h from the start of the simulation. This is related to the underestimation of the steam mass flow rate, see Figure 5.11e. The re-heat steam outlet temperature is accurately represented after 2.5 hours from the start of the simulation, whereas it is overestimated before this time. This is attributed to the placement of the temperature sensor as it is positioned after the spray attemperator before the LP-ST inlet, while the model provides the results

Table 5.11: Model validation results for steady-state operation at nominal load.

Parameter	Units	Model	Data	Deviation
SH degree of superheat	[°C]	73.40	71.40	2.80%
RH degree of superheat	[°C]	207.01	206.61	0.19%
SGS HTF outlet ΔT	[°C]	92.33	92.30	0.03%
FW mass flow rate	[kg/s]	36.60	36.89	-0.79%
EVA steam outlet mass flow rate	[kg/s]	36.60	36.89	-0.79%
SH steam outlet pressure	[bar]	103.96	104.00	-0.04%

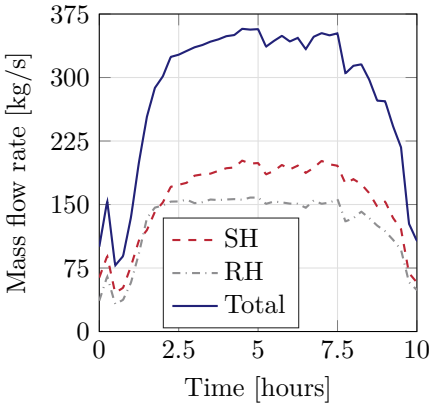

(a) HTF mass flow rate.

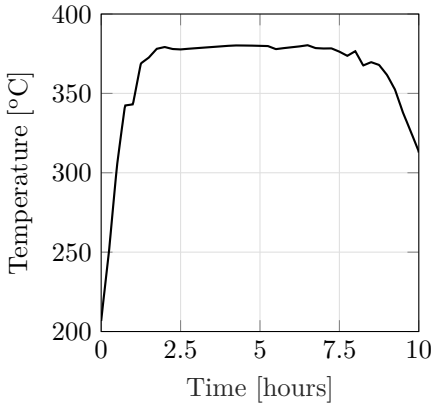

(b) HTF temperature.

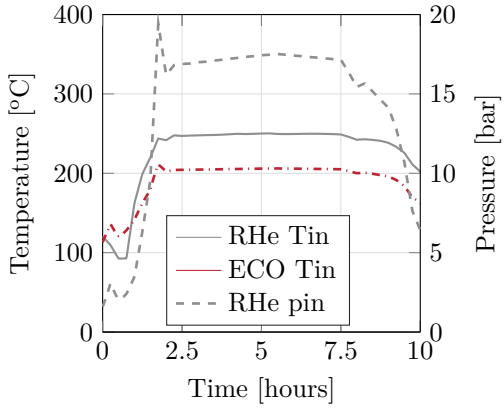

(c) Economizer water inlet temperature and re-heater steam inlet temperature and pressure.

Figure 5.10: Power plant operational data. Inputs for the validation of the dynamic model.

from the SGS outlet. The difference between the model and data results can be linked to the thermo-mechanical constraints of the steam turbine during the start-up, as lower steam temperatures are acceptable during this procedure. This observation is also supported by the good agreement in the HTF outlet temperature estimation, as lower RH outlet steam temperature would have resulted in higher HTF outlet temperature values.

Considering the water mass flow rate validation, the feedwater estimation predicts fewer fluctuations than presented in the plant data. This can be attributed to the noise issues occurring in the process variable signal and common difficulties in measuring the water density and drum level [154]. Both aspects are not taken into account in the model. If between the 1 h and 5 h simulation time, the feedwater mass flow rate is overestimated, the steam mass flow rate and pressure are underestimated as a higher mass flow rate of subcooled water, hence with low enthalpy content, enters the steam drum.

All of these considerations are summarized and quantified in Table 5.12 where the three indicators explained in section 4.3.2.2 are presented. The highest IRE and NRMSE are found for the RHs steam outlet temperature and FW mass flow rate. All the six parameters considered present a relative integral and instantaneous deviations below 10 % indicating that the dynamic model captures the characteristics of the thermodynamic parameters of the plant adequately and with sufficient accuracy for the purposes of the present thesis work.

Table 5.12: Model validation results for transient operation.

Parameter	Units	IRE [%]	RMSE [As the quantity considered]	NRMSE [%]
SH steam outlet T	[°C]	0.54	2.37	1.43
RH steam outlet T	[°C]	3.36	18.98	7.65
SGS HTF outlet T	[°C]	0.83	3.85	3.80
FW water $\dot{m}$	[kg/s]	5.29	2.78	8.14
EVA steam outlet $\dot{m}$	[kg/s]	-2.80	2.06	6.54
SH steam outlet p	[bar]	-1.33	3.77	4.84

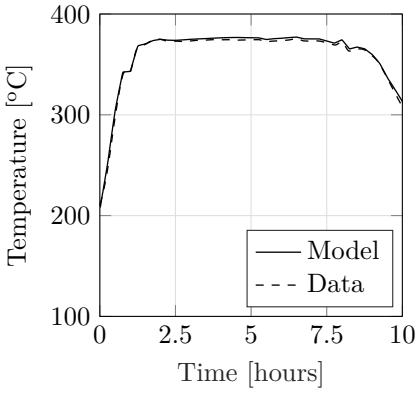

(a) Superheater steam outlet.

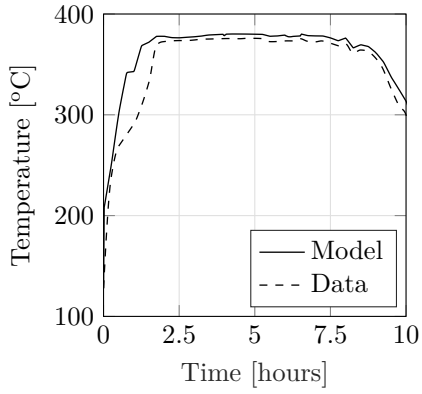

(b) Re-heater steam outlet.

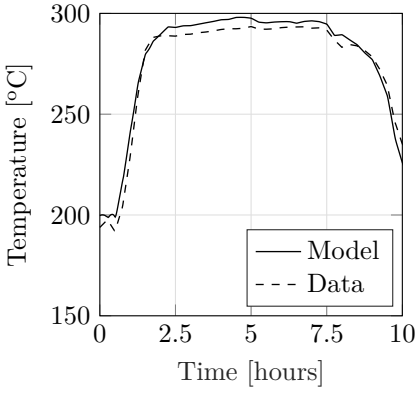

(c) HTF outlet.

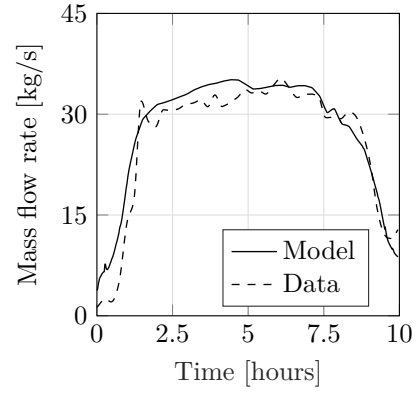

(d) Feedwater.

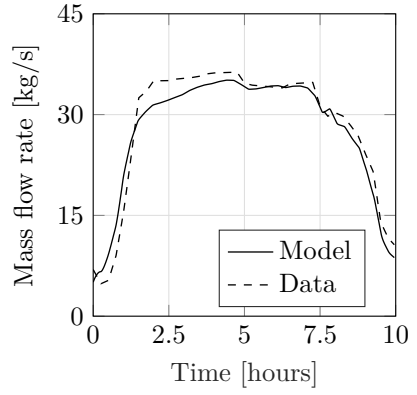

(e) Superheater outlet.

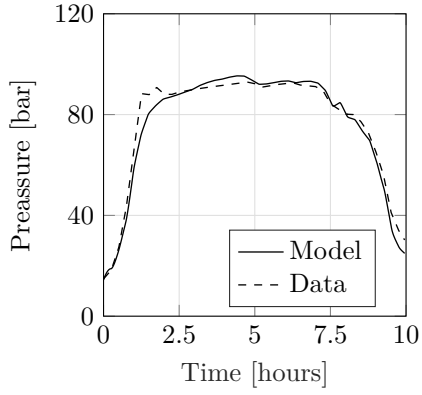

(f) Superheater outlet.

Figure 5.11: Model validation results for transient operation. Comparison with power plant operational data.

5.3.3.2 Design optimization

The optimization was carried out as previously presented in Section 5.2.3.2, with the objective of minimizing the associated PEC and total water side pressure drop and equivalent constraints. Once the multi-objective optimization results were obtained, the design points belonging to the Pareto front were used to evaluate the LCOE of the PTPP considered and ensure that the total stress values at the sensible junctions were between the allowable limits. Figure 5.12 illustrates the multi-objective optimization results for the SGS design.

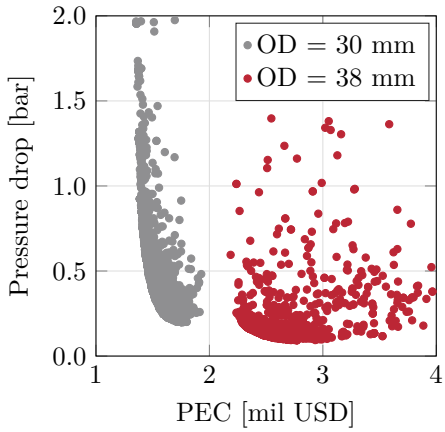

Figure 5.12: Multi-objective optimization results.

The figure indicates that the optimal solutions converged to diameters of 30 mm and 38 mm for high and low water pressure drops, respectively. Similarly as presented in the previous section (see Section 5.2.3.2), the other two available diameter choices (25 mm and 50 mm) were excluded by the optimization routine, since these diameters are associated with low maximum allowable heating rates. In order to select the most suitable design in the Pareto front, the optimal designs were evaluated with respect to the power plant LCOE, and maximum stresses ($\sigma_{\max}$) and stress variations ($\Delta\sigma = \sigma_{\max} - \sigma_{\min}$) during the start-up phase. (High $\Delta\sigma$ causes lower expected lifetime according to the LCF calculations [95], therefore it is preferable to choose the geometrical configurations which would lead to lower stress variations, leading then to higher lifetime). Figures 5.13a and 5.13b depict the normalized $\sigma_{\max}$ and $\Delta\sigma$ for both the inlet and outlet header of the superheater. The results of the stresses in the drum are not presented in the figure as they are almost constant throughout the different SGS designs. This is because the optimizer converged to a single optimal drum/downcomer

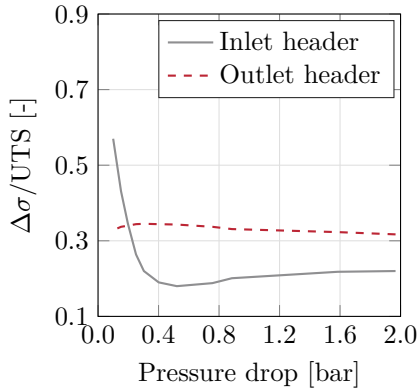

(a) Headers maximum stress difference

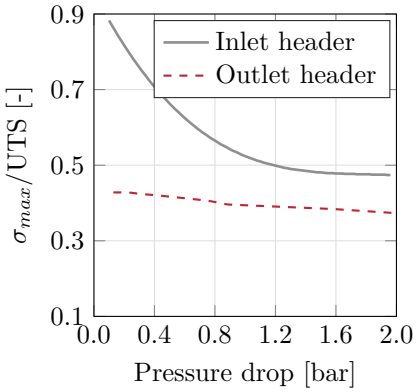

(b) Headers maximum stress

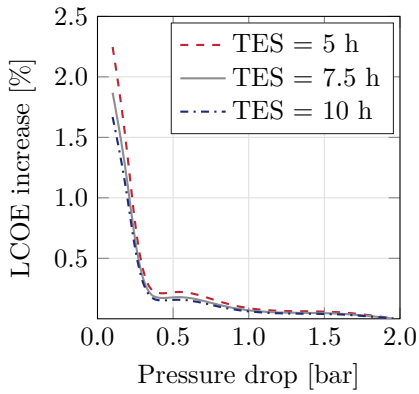

(c) Power plant LCOE increase

Figure 5.13: Optimization results.

configuration, therefore not affecting the stress results for different optimal designs. The impact of the different designs on the power plant LCOE is shown in Figure 5.13c. These are presented in terms of relative increase as compared to the design which results in the lowest LCOE.

The results shown in Figure 5.13 indicate that the design which presents the highest total water pressure drop presents the lowest LCOE. Furthermore, such a design presents the lowest maximum stress for both headers and low stress range. These findings justify the selection of the highest pressure drop solution as the optimal design for the power plant considered. Lower LCOEs are obtained for

higher pressure drops. The reason is that lower parasitic consumption associated with lower pressure drops do not compensate for the higher associated PEC and slower dynamic response of the SGS (the lower the pressure drop is, the higher the SGS total metal mass and volume are due to lower heat transfer coefficients).

The analysis of the stress state allows for excluding specific designs from a technical standpoint. Configurations which would result in pressure drop lower than 0.4 bar would result in high $\Delta\sigma$ and maximum stresses and therefore are not ideal. Even though in the case considered the economic analysis suggests high pressure drop designs anyway, it might happen that in case of different economic conditions lower pressure drop is desirable. Therefore the stress analysis might exclude such designs.

Figure 5.13c presents also results for different thermal energy storage sizes. The results suggest that the higher the storage size is, the lower the impact of SGS design is on the LCOE. This effect increases with decreasing SGS pressure drop. For the lowest pressure drop, the difference in the LCOE percentage increase varies by up to 0.5 % (absolute terms) among the three different storage sizes. However, the difference in LCOE among the storage sizes decreases as the pressure drop increases.

Table 5.13 presents the performance and geometry data of the optimal SGS design (the one corresponding to the maximum pressure drop on the water side). Additional results concerning the thermodynamic states and heat loads may be found in Appendix, in Table A.8 and Table A.9. A high number of tube layers and tube for each layer minimize the pressure drop on the SH, which comprises 66 % of the total water pressure drop. The evaporator constitutes the highest cost, comprising 44 % of the steam generator system total cost.

Table 5.13: Performance and geometry data of the optimal SGS design.

Parameter	Units	ECO	EVA (†)		SH	RHe	RHs
Shell diameter	[mm]	1429	1359	1654	1436	2018	1993
Shell length	[mm]	9.25	10.7	7.68	7.69	10.13	7.71
Shell thickness	[mm]	16	59	77	18	21	23
Number of shells	[-]	1	2	1	1	1	1
Tube outer diameter	[mm]	30	30		30	30	30
Tube thickness	[mm]	3.1	4		3.1	3.1	3.1
Tube layers	[-]	21	20		38	35	37
Tube per layers	[-]	6	3		8	15	15
Tube coils	[-]	39	3		27	7	7
Header diameter	[mm]	191.1	341.5		254.8	550.9	495.2
Header thickness	[mm]	18.0	35.2		24.0	17.0	15.0
Tube side average flow velocity	[m/s]	0.95	3.17		12.02	22.44	22.31
Shell side average flow velocity	[m/s]	1.14	-		1.28	0.55	0.49
Tube side heat transfer coefficient	[W/(m^2 K)]	7781.9	5192.6		3477.8	779.2	632.7
Shell side heat transfer coefficient	[W/(m^2 K)]	2355.9	21964.8		2329.4	1511.6	1301.8
Overall heat transfer coefficient	[W/(m^2 K)]	1514.4	3349.4		1155.2	425.0	352.8
Oil side pressure drop	[bar]	0.435	1.085		0.389	0.046	0.214
Water side pressure drop	[bar]	0.189	0.016		1.331	0.214	0.219
Purchased equipment cost	[mil USD]	0.260	0.597		0.211	0.109	0.177

(†) The shell parameters refer to the heat exchangers (left) and steam drum (right).

5.3.3.3 Transient performance results for the start-up procedure

Results for the start-up procedure are presented in Figure 5.14. Figure 5.14a and 5.14b illustrate the results for the water side, considering superheater and re-heater temperatures and evaporator and re-heater pressures and steam mass flow rate (for one SGS train out of the two available), respectively. Figure 5.14c presents the required HTF temperature and mass flow rate in order to satisfy the heating rate constraints. Each figure denotes the three start-up procedure phases with vertical dash-dotted lines and the correspondent numbers according to Figure 5.8.

The results in this section are related to the optimal design for the highest pressure drop point (1.96 bar) as explained in section 5.3.3.2. The average heating rates for the evaporator and superheater were kept at 8.5 K/min and 15 K/min as they represent the minimum value each design solution can reach (see Table 5.4). The HTF temperature starts to rise according to the allowable superheater heating rates after 1.4 minutes (see Figure 5.8, phase 1). When the outlet steam temperature reaches the minimum allowable temperature for the steam turbine, the power block start-up procedure can initiate (time = 5 minutes), and the turbine begins the roll-up and synchronization phase (see Figure 5.8, phase 2). During this phase, the steam mass flow rate is bypassed until the synchronization is terminated (at time = 13 minutes). Next, the HTF mass flow rate starts to rise according to Figure 5.14c and the flow rate slope increases as the pressure increases due to higher allowable heating rates (see Figure 5.8, phase 3). After 27.6 minutes, the start-up procedure is terminated and the SGS reaches nominal values.

These results are in line with the start-up procedure presented in Ref. [84]. The authors obtained a steam generator start-up procedure lasting for around 33 minutes. The difference between the results in this section and the ones presented in Ref. [84] is attributed to a slower SH. This causes the phase 1 to last around 10 minutes as opposed to the 5 minutes obtained with the presented design. Lower heating rate constraints (8 K/min) were also used by Gonzalez-Gomez et al. [155], resulting in 15 minutes for phase 1. An optimized SH from the dynamic operation perspective would then reduce the SGS start-up procedure by 15.2 % or by 27 % as compared to Ref. [84] and Ref. [155], respectively.

Figure 5.15 illustrates the stress results, which are normalized with respect to the correspondent ultimate tensile strength (UTS). Figure 5.15 also indicates the start-up phases numbers according to Figure 5.8 with vertical dash-dotted lines. Figures 5.15a, 5.15b, and 5.15c depict the results for the superheater inlet header, outlet header and steam drum junctions, respectively. The results

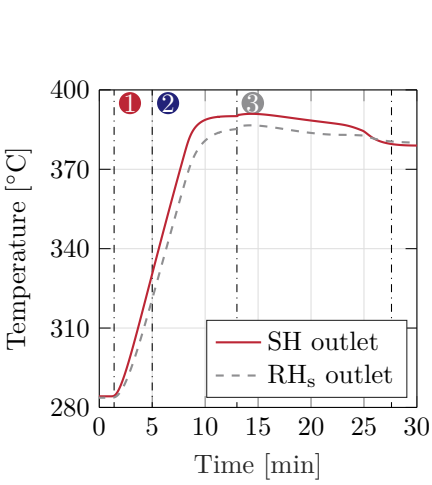

(a) Steam temperatures

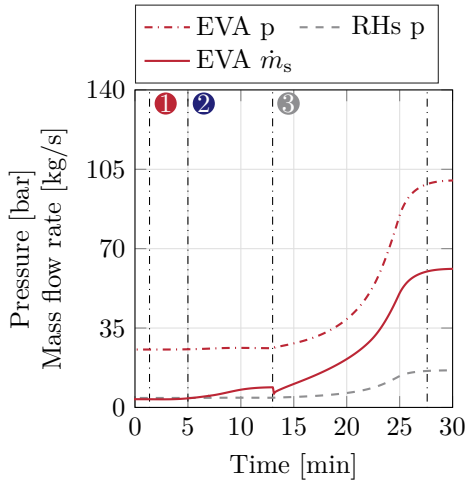

(b) Steam pressure and mass flow rates

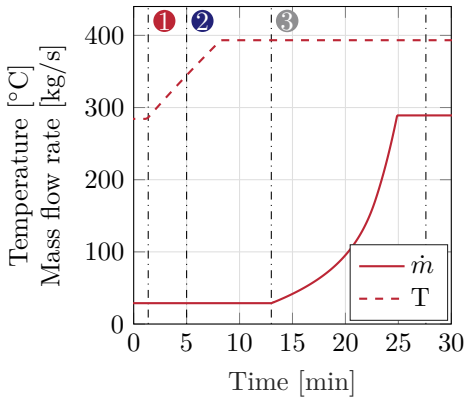

(c) HTF temperature and mass flow rate

Figure 5.14: Transient performance results for the start-up procedure.

suggest that the inlet header is more exposed to stresses than the other manifold. This is related to higher temperature differences between the hot and cold fluid than those of the outlet header. The thermal and pressure stress of the outlet header is mainly increasing during phases 2 and 3 of the start-up procedure. An increase is observed during phase 1 and at the beginning of phase 2 for the outlet header. This component experiences higher differences between the maximum and minimum values of the total stress. This is explained by the lower

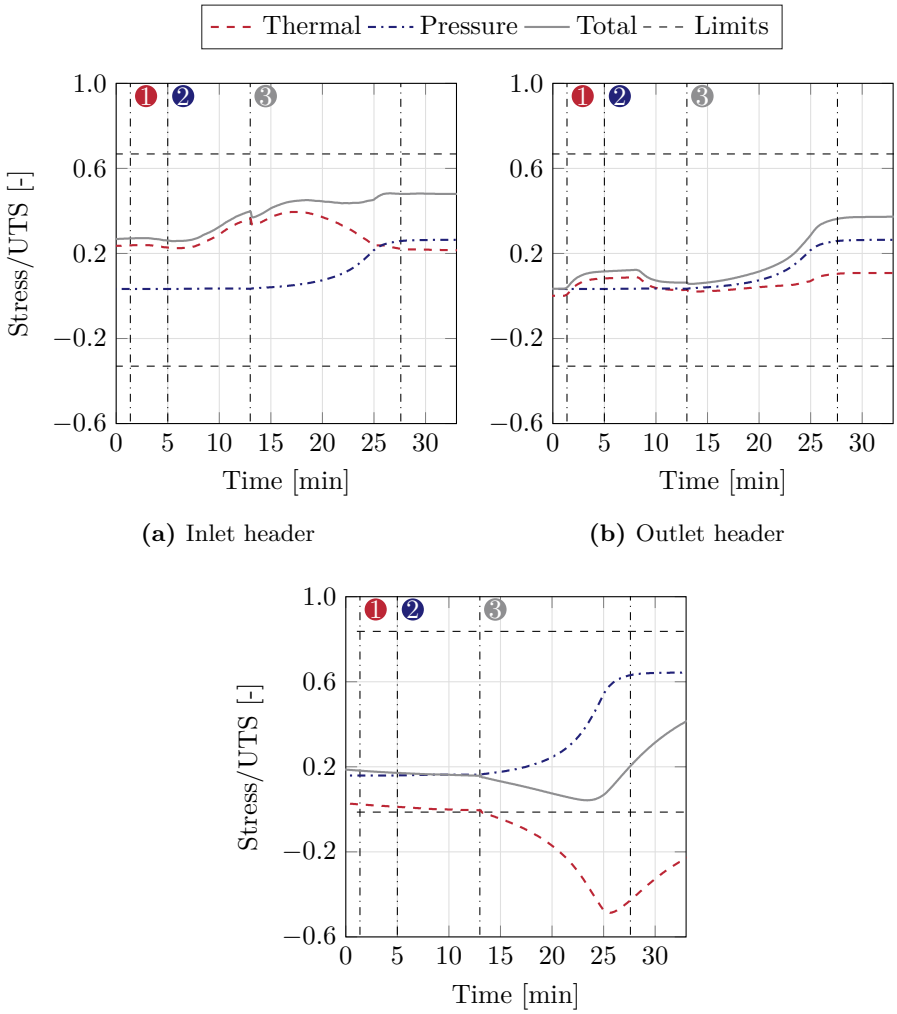

(a) Inlet header

(b) Outlet header

(c) Steam drum

Figure 5.15: Stress results during the start-up procedure

temperature difference between the hot and cold fluid, which implies lower stress state at the beginning of the start-up procedure.

Gonzalez-Gomez et al. [155] presented the analysis of stress transient response during a start-up procedure of steam generator for parabolic trough power

plants. The authors assumed a fixed heating rate constraint and calculated the stress development. However, they obtained stress exceeding the limits for the super-heater components, suggesting the importance of including LCF constraints during the design phase to properly optimize the start-up procedure. In their case, the steam drum presented stress between the allowable limits set by the EN 12952-3.

The steam drum has a larger wall thickness due to its larger diameter than those of the headers. This is why the steam drum/downcomer junction experiences the highest thermal stresses (in absolute terms) and highest stress gradients occurring in phase 3. In all cases, the total stress is within the allowable limits as all the components are designed to guarantee a 25 years lifetime according to the EN 12952-3 norm. However, the different optimized designs will experience different stress profiles, as the allowable heating rates will vary among the design points.

5.4 Discussion and summary

A tool to design and simulate the transient response of header and coil steam generator was developed and validated. The design procedure not only took into consideration thermodynamic requirements and cost estimation but it also considered the low-cycle fatigue constraints during the optimization of the geometrical parameters. The dynamic model considered the transient response during start-up procedures and the thermo-mechanical stress evolution. All these considerations were integrated into evaluating the optimal design configuration for a parabolic trough power plant with thermal energy storage. The analysis indicates that considering low-cycle fatigue constraints during the design phase might increase the associated cost but it is justifiable due to the increase in electricity production and related revenues. More details are summarized in the following sections.

5.4.1 Design accounting for low-cycle fatigue requirements

A design tool was developed and validated to define the sizing of the heat exchangers comprising a header and coil steam generator system for concentrating solar power applications. The models incorporated the area calculations based on heat transfer coefficients, sizing of the main components such as shells, tubes and headers and estimation of low-cycle fatigue requirements in terms of maximum allowable heating rates for the most sensible components. A cost estimation model was integrated to allow for a multi-objective optimization to minimize both pressure drops and purchased equipment cost.

The validation results suggest that the model is accurate with an overestimation of the total heat exchanger area by 2.5 % compared to equivalent components installed in existing power plants, while the total weight was underestimated by 3.6 %. The low-cycle fatigue norms were also implemented with a deviation in evaporator maximum allowable heating rate of -1.9 % compared to that of the existing power plant.

The optimization of the design indicated that considering the low-cycle fatigue analysis in the design routine of the steam generator systems can significantly change the design of the heat exchangers. If both evaporator and superheater maximum heating rate constraints are limited, only two tube outer diameter choices (38 mm, 50 mm) give solutions. In the case of a 1 bare total water pressure drop, the cost of an optimal heat exchanger could increase by 0.75 mil

USD (42 % purchased equipment cost increase). Nonetheless, considering the potential increase in electricity production and associated revenues, the increase in the steam generator system cost can be justifiable. The optimization results also suggest that a lower heat transfer fluid total pressure drop constraint implies high purchased equipment costs. Specifically, for the 1 bar water side pressure drop design, lowering the heat transfer fluid pressure drop from 2.0 bar to 1.5 bar would imply a purchased equipment cost increase of 13 %.

5.4.2 Design accounting for dynamic performance requirements

A more integrated approach was then defined to include the transient response evaluation of such designs and apply it to a general case with a parabolic trough power plant integrated with thermal energy storage. It included both the thermo-mechanical stress calculation of the superheater headers and steam drum/downcomer junctions and the impact of the different optimal steam generator system on the economic feasibility of the power plant in terms of levelised cost of electricity evaluation. This allowed to couple the multi-objective optimization design with the dynamic performance indicators and impact on the techno-economic indicators.

The transient models were validated against real operating data of an existing power plant which employs header and coil steam generators. The results indicate that the transient model is accurate at steady-state nominal load conditions with a maximum deviation of +2.8 % for the degree of superheat at the outlet of the superheater. In transient conditions the highest NRMSE is found for the feedwater mass flow rate and re-heater steam outlet temperature, accounting for 8.1 % and 7.7 %, respectively. The other considered parameters presented NRMSE below 7 %.

By considering both low-cycle fatigue and transient requirements, the multi-objective optimization results indicate that a 30 mm tube outer diameter is the optimal solution for the case considered, as lower parasitic consumption in case of higher tube diameters would not compensate the increase in cost and slower dynamic response of the steam generator system. By considering thermal stress sensitivity of the components, the results indicate that high pressure drop solutions are preferred as they minimize stress difference and absolute value during the start-up phase. Specifically, the highest pressure drop solution can be chosen as the optimal point as it presents the lowest associated levelised cost of electricity.

This design would result in a steam generator system total start-up time of

27.6 minutes with all the considered stress safely between the limits imposed by the norms. The inlet superheater header experiences higher thermal stresses as compared to its outlet counterpart, while the steam drum experiences the highest total stress and stress differences.

Chapter 6

Conclusions

The thesis is concluded with an overview and final remarks on the CSP plant performance evaluation considering thermo-mechanical limitations and the design of the steam generator system. Some suggestions for future research are also presented

6.1 Modelling and results

The thesis work has two main objectives. From a system perspective, the main objective is to investigate the impact of the responsiveness of the steam generator system on the parabolic trough power plant performance and how an improvement in this sense could allow for more operating flexibility throughout the year. From a component perspective, the second main objective is to first define a method which incorporated the previous findings to properly design the heat exchangers of the steam generators and secondly evaluate their transient response during the start-up procedure.

The main findings regarding the system level analysis are summarized in the following list.

- Parabolic trough power plant models were developed and validated accounting for thermo-mechanical transient limitations.
  - A first model is developed to simulate the performance of a traditional parabolic trough power plant layout with integrated thermal energy storage, similar to Andasol. The model is validated against the data

available of an existing power plant with deviations ranging between +0.5 % to -8.9 % depending on the reference considered.

  - A second model is developed to simulate the performance of a gas boosted parabolic trough power plant. The validation results in a maximum relative deviation of +4.3 % for gross electric energy production.

- The impact of the heating rate constraints on the performance of parabolic trough power plants is evaluated for two different operating strategies, namely peak-load and solar-driven.

  - An optimal range of 7-10 K/min is obtained to maximize the electric output of the power plant.
  - It is important to keep the pressure overnight at the minimum allowable turbine inlet pressure as it allows the most efficient start-up procedure.
  - In case of peak-load operating strategy the prospect of improvement in total net electricity output results in 1.5 %.
  - If the solar-driven operation is considered, the maximum potential would be around 0.41 %, as the solar field becomes the limiting component during the start-up procedure.

- The benefit of more responsive steam generators is investigated from an operating strategy flexibility perspective. This is done by minimizing the fuel consumption and maximizing the electric energy production of a gas boosted parabolic trough power plant during two different seasons, namely spring and winter.

  - If minimum fuel consumption is the desired objective low values would result to be optimal. An opposite conclusion is reached if maximum electricity production is desirable.
  - In the case of minimization of fuel consumption to electric energy production ratio, high evaporator heating rates are desirable for both seasons, resulting in optimal values of 5.7 K/min and 6 K/min for the winter and spring case, respectively.

The main findings regarding the component level analysis are summarized in the following list.

- A design tool is developed and validated in order to size each heat exchanger comprising the steam generator system and include the low-cycle fatigue constraints in the procedure. Optimal designs are

obtained by minimizing the purchase equipment cost and water pressure drop.

  - The model overestimates the area by 2.5 % and underestimates the total weight by 3.6 % and maximum allowable evaporator heating rates by 1.9 % as compared to the data of an existing power plant.
  - In case of a requirement of 1 bar total water pressure drop, the optimal heat exchanger would cost 42 % more than in the case without thermo-mechanical constraints. However, considering the increase in revenue due to a higher electricity production would make the design still affordable.

- The design method is further expanded to consider the transient response performance of the steam generator system, its sensitivity to thermal stresses and the impact on the power plant economic feasibility.
  - The transient model is validated with a maximum of 8.14 % deviation for the feedwater mass flow rate.
  - The optimization results indicate that the highest pressure drop design point is the most feasible solution when considering the sensitivity to stresses and the impact on the economic feasibility of the power plant.

On the whole, the results from this thesis indicate that even though the steam generator is a small component of the concentrating solar power plant from the economic perspective, its optimal operation and design is crucial to the improvement of the feasibility of such power plants. The methods presented in the thesis could be used as a general guideline during the sizing of such components in order to account for system requirements and limitations and optimize for transient operation.

6.2 Recommendations for further research

The current analysis may be furthered by including a similar study for the solar tower power plants. As they operate at different turbine inlet temperature, it may be worth to investigate the impact of the heating rate constraints on their technical and economic feasibility. Having molten salt as heat transfer fluid would also require different design choices due to the risk of freezing of the salt at a much higher temperature.

Another point of improvement may be the definition of new norms to account for low cycle fatigue and design of pressure vessel components specifically for a highly transient power plant. In the specific, the ASME norms are quite conservative with regards to thickness calculations as they are aimed at components which work at steady-state. This directly impacts the responsiveness of components such as the steam generator.

A more detailed finite element method may be used to estimate thermo-mechanical stresses and together with a detailed low-cycle fatigue analysis used to evaluate new heating rate constraints.

The focus of this thesis work was not on the detailed heat transfer modelling of the components. A sensitivity study on the heat transfer correlations as well more detailed characterization could improve the accuracy of both the dynamic and design models.

More advanced controllers, such as model predictive controllers, may be used instead to improve the response of the steam generator system with the aim of decreasing start-up times and associated stresses.

References

[1] European Commission. Europe leads the global clean energy transition: Commission welcomes ambitious agreement on further renewable energy development in the EU. http://europa.eu/rapid/press-release-STATEMENT-18-4155-en.html . [accessed: 23/08/2018].

[2] Norden. Nordic Energy Technology Perspectives 2016. Technical report, Nordic energy research, Paris, France, 2016.

[3] IEA. Renewables 2017 - Analysis and forecast to 2022. Technical report, International Energy Agency, Brussels, Belgium, 2017.

[4] P. Gonçalves V. Sampaio and Mario O. Aguirre González. Photovoltaic solar energy: Conceptual framework. *Renewable and Sustainable Energy Reviews*, 74:590 – 601, 2017.

[5] M. Tasbirul Islam, N. Huda, A.B. Abdullah, and R. Saidur. A comprehensive review of state-of-the-art concentrating solar power (csp) technologies: Current status and research trends. *Renewable and Sustainable Energy Reviews*, 91:987 – 1018, 2018.

[6] E. Du, N. Zhang, B. Hodge, C. Kang, B. Kroposki, and Q. Xia. Economic justification of concentrating solar power in high renewable energy penetrated power systems. *Applied Energy*, 222:649 – 661, 2018.

[7] International Energy Agency. Technology Roadmap, Solar Thermal Electricity. Technical report, IEA, Paris, France, 2014.

[8] IRENA. Roadmap for a renewable energy future. Technical report, International Renewable Energy Agency, Brussels, Belgium, 2016.

[9] G. Frisari and J. Feas. The Role of Public Finance in CSP - How Spain created a world-leading industry then shattered investor confidence. Technical report, Climate Policy Initiative, Brussels, Belgium, 2016.

[10] S. Pool and J. Dos Passos Coggin. Fulfilling the Promise of Concentrating Solar Power - Low-Cost Incentives Can Spur Innovation in the Solar Market. Technical report, Centre for American Progress, USA, 2013.

[11] Global Infrastructure Hub. Noor power plant. https://www.gihub.org/resources/showcase-projects/noor-ouarzazate-i-concentrated-solar-power-plant/. [accessed: 23/08/2018].

[12] D. Proctor. Dubai solar park. https://www.powermag.com/dubai-awards-contract-for-phase-4-of-massive-solar-park/. [accessed: 23/08/2018].

[13] World Energy Council. World Energy Resources: Solar 2016. Technical report, London, England, 2016.

[14] Groupe Reaction Inc. CSP Parabolic Trough Report : Cost , Performance and Key Trends. Technical report, CSP Today, London, England, 2014.

[15] Estela, Greenpeace, and Solarpaces. Solar Thermal Electricity - Global Outlook 2016. Technical report, Brussels, Belgium, 2016.

[16] T. R. Mancini, J. A. Gary, G. J. Kolb, and C. Ho. Power Tower Technology Roadmap and cost reduction plan. Sandia Report. Technical Report Sandia Report, April, Sandia, Sandia National Laboratories. Albuquerque, New Mexico, 2011.

[17] L. L. Vant-Hull. *Central tower concentrating solar power (CSP) systems.* Woodhead Publishing Limited, Houston, Texas, 2012.

[18] A. Almasabi, A. Alobaidli, and T. J. Zhang. Transient characterization of multiple parabolic trough collector loops in a 100 MW CSP plant for solar energy harvesting. In *Energy Procedia*, volume 69, pages 24–33. Elsevier B.V., 2015.

[19] D. Blanco, A. Luis, and I. Garc. Performance model for parabolic trough solar thermal power plants with thermal storage : Comparison to operating plant data. *Solar Energy*, 85:2443–2460, 2011.

[20] L. S. Conrado, A. Rodriguez-pulido, and G. Calderón. Thermal performance of parabolic trough solar collectors. *Renewable and Sustainable Energy Reviews*, 67:1345–1359, 2017.

[21] N. Luo, G. Yu, H. J. Hou, and Y. P. Yang. Dynamic modeling and simulation of parabolic trough solar system. In *SolarPACES 2014*, volume 69, pages 1344–1348, 2015.

[22] W. Abed, K. Al-maliki, F. Alobaid, V. Kez, and B. Epple. Modelling and dynamic simulation of a parabolic trough power plant. *Journal of Process Control*, 39:123–138, 2016.

[23] R. M. Montañés, J. Windahl, J. Pålsson, and M. Thern. Dynamic modeling of a parabolic trough solar thermal power plant with thermal storage using modelica. *Heat Transfer Engineering*, 39(3):277–292, 2018.

[24] T. E. Boukelia, M. S. Mecibah, B. N. Kumar, and K. S. Reddy. Investigation of solar parabolic trough power plants with and without integrated TES (thermal energy storage) and FBS (fuel backup system) using thermic oil and solar salt. *Energy*, 88:292–303, 2015.

[25] T. E. Boukelia, O. Arslan, and M. S. Mecibah. Potential assessment of a parabolic trough solar thermal power plant considering hourly analysis : ANN-based approach. *Renewable Energy*, 105:324–333, 2017.

[26] STEAG. Ebsilon professional. [accessed: 03/03/2018].

[27] M. Biencinto, L. González, and L. Valenzuela. A quasi-dynamic simulation model for direct steam generation in parabolic troughs using TRNSYS. *Applied Energy*, 161:133–142, 2016.

[28] M. Biencinto, L. González, E. Zarza, L. E. Díez, and J. Muñoz-antón. Performance model and annual yield comparison of parabolic-trough solar thermal power plants with either nitrogen or synthetic oil as heat transfer fluid. *Energy Conversion and Management*, 87:238–249, 2014.

[29] J. Bonilla and L. Jose. Parabolic-trough solar thermal power plant simulation scheme , multi-objective genetic algorithm calibration and validation. *Solar Energy*, 86:531–540, 2012.

[30] S. Al-Hanaei, S. Al-Shomali, and M. Abutayeh. Performance Model of Shams I Solar Power Plant. *Heat Transfer Engineering*, 37(17):1445–1454, 2016.

[31] NREL. System Advisor Model (SAM) Case Study: Andasol. Technical report, NREL, Aldeire, Spain, 2013.

[32] N. Blair, M. Mehos, C. Christensen, and C. Cameron. Modeling Photovoltaic and Concentrating Solar Power Trough Performance , Cost , and Financing with the Solar Advisor Model. In *SOLAR 2008 - American Solar Energy Society (ASES)*, pages 1–7, 2008.

[33] P. Gilman, National Renewable Energy Laboratory, and Sandia National Laboratories. Solar advisor model user guide for version 2.0. Technical Report. Technical Report August, National Renewable Energy Laboratory, (NREL), Cole Boulevard, Colorado, 2008.

[34] H. Price. A Parabolic Trough Solar Power Plant Simulation Model. In *ASME. International Solar Energy Conference*, number January, pages 665–673, 2003.

[35] M. C. Stoddard, S. E. Faas, C. J. Chiang, and J. Dirks. SOLERGY - A Computer Code for Calculating the Annual Energy from Central Receiver Power Plants. Sandia Report. Technical Report May, Sandia, Sandia National Laboratories. Albuquerque, New Mexico, 1987.

[36] J. Spelling. *Hybrid Solar Gas-Turbine Power Plants - A Thermoeconomic Analysis*. PhD thesis, Royal Institute of Technology, (KTH), Stockholm, Sweden, 2013.

[37] M. Topel, R. Guédez, and B. Laumert. Impact of Increasing Steam Turbine Flexibility on the Annual Performance of a Direct Steam Generation Tower Power Plant. *Energy Procedia*, 69(0):1171–1180, 2015.

[38] M. Topel, Å. Nilsson, M. Jöcker, and B. Laumert. Investigation Into the Thermal Limitations of Steam Turbines During Start-Up Operation. *Journal of Engineering for Gas Turbines and Power*, 140(1):012603, 2017.

[39] M. Topel and B. Laumert. Improving concentrating solar power plant performance by increasing steam turbine flexibility at start-up. *Solar Energy*, 165:10 – 18, 2018.

[40] L. Pelagotti, K. Sørensen, T. Condra, T. Joseph, and A. Franco. Modelling of a Coil Steam Generator for CSP applications. In *Proceedings of the 55th International Conference on Simulation and Modelling*, 2014.

[41] P. Á. González-Gómez, F. Petrakopoulou, J.. Briongos, and D. Santana. Steam generator design for solar towers using solar salt as heat transfer fluid. In *AIP Conference Proceedings*, volume 1850, 0300, pages 1–8, 2017.

[42] P.A. González-Gómez, F. Petrakopoulou, J.V. Briongos, and D. Santana. Cost-based design optimization of the heat exchangers in a parabolic trough power plant. *Energy*, 123:314–325, 2017.

[43] P. Á. González-Gómez, J. Gómez-Hernández, J. Briongos, and D. Santana. Thermo-economic optimization of molten salt steam generators. *Energy Conversion and Management* ·, 146(August):228–243, 2017.

[44] P. A. Gonzalez-Gomez, J. Gomez-Hernandez, J. V. Briongos, and D. Santana. Fatigue analysis of the steam generator of a parabolic trough solar power plant. *Energy*, 155:565–577, 2018.

[45] P. Dzierwa and J. Taler. Optimum Heating of Pressure Vessels With Holes. *Journal of Pressure Vessel Technology*, 137(1):011202, 2014.

[46] P. Dzierwa, D. Taler, M. Trojan, and J. Taler. Evaporator Heating with Optimum Fluid Temperature Changes. *Procedia Engineering*, 157:29–37, 2016.

[47] J. Taler, B. Weglowski, D. Taler, T. Sobota, P. Dzierwa, M. Trojan, P. Madejski, and M. Pilarczyk. Determination of start-up curves for a boiler with natural circulation based on the analysis of stress distribution in critical pressure components. *Energy*, 92:153–159, 2015.

[48] Babcock and Wilcox Company. *Steam: its generation and use*. Kessinger Publishing, 2005.

[49] B. Elmegaard. *Simulation of Boiler Dynamics*. PhD thesis, 1999.

[50] K. Sørensen. *Dynamic Boiler Performance*. PhD thesis, 2004.

[51] Mª. D. Durán, M. Valdés, A. Rovira, and E. Rincón. A methodology for the geometric design of heat recovery steam generators applying genetic algorithms. *Applied Thermal Engineering*, 52(1):77–83, 2013.

[52] F. Alessandro and N. Giannini. A general method for the optimum design of heat recovery steam generators. *Energy*, 31(15):3342–3361, 2006.

[53] P. Wildi-Tremblay and L. Gosselin. Minimizing shell-and-tube heat exchanger cost with genetic algorithms and considering maintenance. *International journal of energy research*, 31(31):135–147, 2007.

[54] R. Guedez, M. Topel, F. Ferragut, I. Callaba, and C. D. Perez-segarra. A Methodology for Determining Optimum Solar Tower Plant Configurations and Operating Strategies to Maximize Profits Based on Hourly Electricity Market Prices and Tariffs. *Solar Energy Engineering*, 138(April 2016):1–12, 2017.

[55] MATLAB. *version 9.1.0.4 (R2016b)*. The MathWorks Inc., Natick, Massachusetts, 2016.

[56] University of Wisconsin Madison. Solar Energy Laboratory. TRNSYS, a transient simulation program. Technical report, 1975.

[57] M. Dempsey. Dymola for multi-engineering modelling and simulation. In *2006 IEEE Vehicle Power and Propulsion Conference*, pages 1–6, Sept 2006.

[58] National Institute for Standard and Technology. NIST REFPROP 9.1. 2017. [Online] https://www.nist.gov/srd/refprop. [accessed: 03/03/2018].

[59] J. D. Hamilton. Historical oil shocks. Technical report, National Bureau of Economic Research, 2011.

[60] D. A. Baharoon, H. A. Rahman, W. Z. W. Omar, and S. Obaid Fadhl. Historical development of concentrating solar power technologies to generate clean electricity efficiently - a review. *Renewable and Sustainable Energy Reviews*, 41:996–1027, 2015.

[61] CSP Plaza. 2018: The Year Sees Explosive Expansion of CSP Capacity Globally, New Installed CSP Capacity Expected to Exceed 1GW. http://en.cspplaza.com/2018-the-year-sees-explosive-expansion-of-csp-capacity-globally-new-installed-csp-capacity-expected-to-exceed-1gw/. [accessed: 24/08/2018].

[62] J. A. Duffie and W. A. Beckman. *Solar Engineering of Thermal Processes*. John Wiley and Sons, 2013.

[63] M. J. Montes, A. Abanades, J. M. Martinez-Val, and M. Valdes. Solar multiple optimization for a solar-only thermal power plant, using oil as heat transfer fluid in the parabolic trough collectors. *Solar Energy*, 83(12):2165–2176, 2009.

[64] E. Zarza Moya. Parabolic-trough concentrating solar power (CSP) systems. In *Concentrating Solar Power Technology*, pages 197–239. Woodhead publishing, Cambridge, UK, 2012.

[65] A. Fernández-García, E. Zarza, L. Valenzuela, and M. Pérez. Parabolic-trough solar collectors and their applications. *Renewable and Sustainable Energy Reviews*, 14(7):1695 – 1721, 2010.

[66] D. Kearney, U. Herrmann, P. Nava, B. Kelly, R. Mahoney, J. Pacheco, R. Cable, N. Potrovitza, D. Blake, and H. Price. Assessment of a molten salt heat transfer fluid in a parabolic trough solar field. *Journal of solar energy engineering*, 125(2):170–176, 2003.

[67] DLR. Parabolic trough solar power plants. https://www.dlr.de/media/en/desktopdefault.aspx/tabid-4987/8424-read-20582/. [accessed: 24/08/2018].

[68] D. R. Mills. Linear fresnel reflector (lfr) technology. In *Concentrating Solar Power Technology*, pages 153–196. Elsevier, 2012.

[69] Novatec solar. Liddell in Australia. http://www.novatecsolar.com/80-1-Liddell.html. [accessed: 24/08/2018].

[70] G. Zhu, T. Wendelin, M. J. Wagner, and C. Kutscher. History, current state, and future of linear fresnel concentrating solar collectors. *Solar Energy*, 103:639–652, 2014.

[71] T. Mancini, P. Heller, B. Butler, B. Osborn, W. Schiel, V. Goldberg, R. Buck, R. D., C. Andraka, and J. Moreno. Dish-stirling systems: An overview of development and status. *Journal of Solar Energy Engineering*, 125(2):135–151, 2003.

[72] DLR. Dish-Stirling system. https://www.dlr.de/media/en-desktopdefault.aspx/tabid-4987/8424-read-20584/. [accessed: 24/08/2018].

[73] O. Behar, A. Khellaf, and K. Mohammedi. A review of studies on central receiver solar thermal power plants. *Renewable and sustainable energy reviews*, 23:12–39, 2013.

[74] Torresol. Gemasolar. http://torresolenergy.com/gemasolar/. [accessed: 24/08/2018].

[75] A. Gil, M. Medrano, I. Martorell, A. Lázaro, P. Dolado, B. Zalba, and L. Cabeza. State of the art on high temperature thermal energy storage for power generation. part 1concepts, materials and modellization. *Renewable and Sustainable Energy Reviews*, 14(1):31–55, 2010.

[76] S. Kalaiselvam and R. Parameshwaran. *Thermal energy storage technologies for sustainability: systems design, assessment and applications*. Elsevier, 2014.

[77] M. Medrano, A. Gil, I. Martorell, X. Potau, and L. Cabeza. State of the art on high-temperature thermal energy storage for power generation. part 2 case studies. *Renewable and Sustainable Energy Reviews*, 14(1):56–72, 2010.

[78] S. Kuravi, J. Trahan, D. Y. Goswami, M. M Rahman, and E. K. Stefanakos. Thermal energy storage technologies and systems for concentrating solar power plants. *Progress in Energy and Combustion Science*, 39(4):285–319, 2013.

[79] M. Abbas, H. Aburideh, Z. Belgroun, Z. Tigrine, and N. K. Merzouk. Comparative study of two configurations of solar tower power for electricity generation in algeria. *Energy Procedia*, 62:337–345, 2014.

[80] W. D. Steinmann. Thermal energy storage systems for concentrating solar power (csp) technology. In *Advances in Thermal Energy Storage Systems*, pages 511–531. Elsevier, 2015.

[81] O. Behar, A. Khellaf, and K. Mohammedi. A review of studies on central receiver solar thermal power plants. *Renewable and sustainable energy reviews*, 23:12–39, 2013.

[82] F. Ferrara, A. Gimelli, and A. Luongo. Small-scale concentrated solar power (csp) plant: Orcs comparison for different organic fluids. *Energy Procedia*, 45:217–226, 2014.

[83] J. Macknick, R. Newmark, G. Heath, and K. Hallett. Operational water consumption and withdrawal factors for electricity generating technologies: a review of existing literature. *Environmental Research Letters*, 7(4):045802, 2012.

[84] H. Schenk, J. Dersch, T. Hirsch, and T. Polklas. Transient simulation of the power block in a parabolic trough power plant. In *Proceedings of the 11th International Modelica Conference, Versailles, France, September 21-23, 2015*, number 118, pages 605–614. Linköping University Electronic Press, 2015.

[85] M. Topel. *Improving concentrating solar power plant performance through steam turbine flexibility.* PhD thesis, KTH Royal Institute of Technology, Stockholm, Sweden, 2017.

[86] S. Basu and A. Debnath. *Power plant instrumentation and control handbook: a guide to thermal power plants.* Academic Press, 2014.

[87] F. Lippke. Simulation of the Part-Load Behavior of a 30 Mwe SEGS Plant. Report. Technical report, Sandia National Laboratories. Albuquerque, New Mexico, 1995.

[88] K. Vignarooban, X. Xu, A. Arvay, K. Hsu, and A. Kannan. Heat transfer fluids for concentrating solar power systems–a review. *Applied Energy*, 146:383–396, 2015.

[89] T. Henrion, K. Ponweiser, D. Band, and T. Telgen. Dynamic simulation of a solar power plant steam generation system. *Simulation Modelling Practice and Theory*, 33:2–17, 2013.

[90] R. K. Shah and D. P. Sekulic. *Fundamentals of heat exchanger design.* John Wiley & Sons, 2003.

[91] R. W. Serth and T. G. Lestina. 10 - reboilers. In R. W. Serth and T. G. Lestina, editors, *Process Heat Transfer (Second Edition)*, pages 361 – 430. Academic Press, Boston, second edition edition, 2014.

[92] J. M. Gere and B. Goodno. Mechanics of materials (cengage learning, toronto, 2009). *Chap*, 9:618, 2009.

[93] American society of mechanical engineer. *ASME Boiler and Pressure Vessel Code: Section VIII - Division 2.* New York, New York, 2015.

[94] CEN. Water-tube boilers and auxiliary installations - Part 3: Design and calculation for pressure parts of the boiler. Technical report, European Committee for Standardization, Brussels, Belgium, 2012.

[95] Y. Murakami and K.J. Miller. What is fatigue damage? a view point from the observation of low cycle fatigue process. *International Journal of Fatigue*, 27(8):991 – 1005, 2005. Cumulative Fatigue Damage Conference - University of Seville 2003.

[96] M. Brown. Boiler drum level control controlling swell and shrink. *part one, Control System Design, SA Instrumentation and Control*, pages 1–2, 2011.

[97] G. Darie, H. Petcu, G. Negreanu, and V. Gherghina. Sliding pressure operation of large conventional steam power units. In *Proceedings of the 5th IASME/WSEAS International Conference on Heat Transfer, Thermal Engineering and Environment, August*, pages 25–27, 2007.

[98] D. Ferruzza, M. Topel, I. Basaran, B. Laumert, and F. Haglind. Start-Up Performance of Parabolic Trough Concentrating Solar Power Plants. In *AIP Conference Proceedings 1850*, volume 1850, 1600, pages 1–9, 2017.

[99] D. Ferruzza, M. Topel, B. Laumert, and F. Haglind. Impact of steam generator start-up limitations on the performance of a parabolic trough solar power plant. *Solar Energy*, 169:255–263, 2018.

[100] D. Ferruzza, M. R. Kærn, and F. Haglind. Design of header and coil steam generator for concentrating solar power applications accounting for low-cycle fatigue requirements. *Applied Energy*, 236(February 2019):793–803, 2018.

[101] R. Guédez. *A Techno-Economic Framework for the Analysis of Concentrating Solar Power Plants with Storage*. PhD thesis, Royal Institute of Technology, (KTH), Stockholm, Sweden, 2016.

[102] Thermoflow. Thermoflex Modular Program for Thermal Power Systems. www.thermoflow.com. [accessed: 22/11/2017].

[103] G. Leyland and D. Favrat. *Multi-objective optimization applied to industrial energy problems*. PhD thesis, École Polytechnique Féderale de Lausanne, (EPFL), Lausanne, 2002.

[104] V. Dudley. SEGS LS-2 Solar Collector. Test Results. Technical report, Sandia National Laboratories, Sandia National Laboratories. Albuquerque, New Mexico, 1994.

[105] DLR. A TRNSYS Model Library for Solar Thermal Electric Components (STEC). Technical Report November, 2006.

[106] T. Bergman, A. Lavine, F. Incropera, and D. Dewitt. *Fundamentals of heat and mass transfer*. John Wiley and sons, Jefferson city, Missouri, 7th edition, 2011.

[107] S. Pelster, D. Favrat, and M. R. Von Spakovsky. The thermoeconomic and environomic modeling and optimization of the synthesis, design, and operation of combined cycles with advanced options. *Journal of engineering for gas turbines and power*, 123(4):717–726, 2001.

[108] D. Cooke. Modeling of off-design multistage turbine pressures by stodolas ellipse. In *Energy Incorporated PEPSE Users Group Meeting, Richmond, VA, Nov*, pages 2–3, 1983.

[109] I. Basaran. A comprehensive study of the imposed limitations on concentrating solar power plant start-up speeds. msc. thesis, 2015.

[110] J. W. Price. Thermal shock cracking: design and assessment guidelines. *Journal of Pressure Vessel Technology*, 129(1):125–132, 2007.

[111] Aalborg CSP. http://www.aalborgcsp.com/quickmenu/brochures/. [accessed: 2017-08-03].

[112] NREL. System advisor model (sam) case study: Andasol-1. Technical report, Golden, Colorado, USA, 2011.

[113] NREL. Concentrating Solar Power Projects - Andasol. http://www.nrel.gov/csp/solarpaces/project-detail.cfm/projectID=4. [accessed: 05/09/2018].

[114] Solar Millennium AG. The parabolic trough power plants Andasol 1 to 3. Technical report, Erlangen, Germany, 2008.

[115] A. Alobaidli, B. Sanz, K. Behnke, T. Witt, D. Viereck, and M. Schwarz. Shams 1 - Design and operational experiences of the 100MW - 540řC CSP plant in Abu Dhabi. In *AIP Conference Proceedings*, volume 1850, 0200, pages 1–10, 2017.

[116] ASHRAE Handbook. HVAC systems and equipment. *American Society of Heating, Refrigerating, and Air Conditioning Engineers, Atlanta, GA*, pages 1–10, 2000.

[117] Solutia. Therminol VP-1, Vapour phase, Liquid phase, Heat transfer fluid, year = 2014, address = saint louis, missouri, usa. Technical report.

[118] T. Vogel, G. Oeljeklaus, K. Görner, J. Dersch, and T. Polklas. Hybridization of parabolic trough power plants with natural gas. *Energy Procedia*, 49:1238–1247, 2014.

[119] J. Taler, P. Dzierwa, D. Taler, and P. Harchut. Optimization of the boiler start-up taking into account thermal stresses. *Energy*, 92:160–170, 2015.

[120] D. Ferruzza, M. R. Kærn, and F. Haglind. Design of header and coil steam generator for concentrating solar power applications accounting for dynamic performance requirements. *(Under internal review).*, 2019.

[121] NREL. System Advisor Model (SAM) Case Study: Andasol. Technical report, NREL, Aldeire, Spain, 2013.

[122] D. Anarratore. *Handbook for heat exchangers and tube banks design.* Springer, Milano, Italy, 2010.

[123] A. Žukauskas. Heat transfer from tubes in crossflow. *Advances in Heat Transfer*, 8:93–160, 1972.

[124] K. Stephan and M. Abdelsalam. Heat-transfer correlations for natural convection boiling. *International Journal of Heat and Mass Transfer*, 23(1):73–87, 1980.

[125] I.E. Idelchik. *Handbook of hydraulic resistance. Coefficients of Local Resistance and of Friction.* National Science Foundation, Jerusalem, Israel, 1986.

[126] V. Ganapathy. Understanding boiler circulation. *Chemical Engineering*, 120(10):52–56, 2013.

[127] D. Anarratore. *Steam generators. Description and design.* Springer, Milano, Italy, 2008.

[128] S. Meinke. Modellierung thermischer kraftwerke vor dem hintergrund steigender dynamikanforderungen aufgrund zunehmender windenergie- und photovoltaikeinspeisung. msc. thesis., 2012.

[129] E. Andersson. Development of a dynamic model for start-up optimization of coal-fired power plants. msc. thesis, 2012.

[130] G. P. Purohit. Estimating costs of shell-and-tube heat exchangers. *Chemical Engineering*, (90):56–67, 1983.

[131] Capital professional services. https://inflationdata.com/. [accessed: 01/03/2018].

[132] J. D. Seader, W. D. Seider, and D. R. Lewin. *Product and Process Design Principles: Synthesis, Analysis and Evaluation.* Wiley, USA, 2004.

[133] MEPS International. http://worldsteelprices.com/. [accessed: 01/03/2018].

[134] G. Towler and R. Sinnott. Heat-Transfer Equipment. In *Chemical Engineering Design*, pages 1047–1205. Oxford, England, 2013.

[135] D. Q. Kern. *Process Heat Transfer.* McGraw-Hill, Singapore, 1965.

[136] W. A. Khan, M. M. Yovanovich, and J. R. Culham. Optimal design of tube banks in crossflow using entropy generation minimization method. *Journal of thermophysiscs and heat transfer*, 21(2):372–378, 2007.

[137] C. Merritt. *Process Steam Systems: A Practical Guide for Operators, Maintainers, and Designers.* John Wiley & Sons, New Jersey, 2015.

[138] J. W. Palen. Shell and tube reboilers. In *Heat exchanger design handbook.* Begell House, London, England, 2002.

[139] S.G. Kandlikar. A theoretical model to predict pool boiling critical heat flux incorporating effects of contact angle and orientation. *ASME Journal of Heat Transfer*, 123(6):1071–1079, 2001.

[140] Y. S. Kim. A proposed correlation for critical flow rate of water flow. *Nuclear Engineering and Technology*, 47(1):135–138, 2015.

[141] New energy update. http://analysis.newenergyupdate.com/csp-today/acwa-power-scales-tower-trough-design-set-record-low-csp-price. [accessed: 02/07/2018].

[142] F. Casella and A. Leva. Object-oriented modelling amp;amp;amp; simulation of power plants with modelica. In *Proceedings of the 44th IEEE Conference on Decision and Control*, pages 7597–7602, Dec 2005.

[143] J. Bonilla, L.J. Yebra, and S. Dormido. Chattering in dynamic mathematical two-phase flow models. *Applied Mathematical Modelling*, 36(5):2067 – 2081, 2012.

[144] J. Bonilla, L. J. Yebra, and S. Dormido. Mean densities in dynamic mathematical two-phase flow models. *Computer Modeling in Engineering and Sciences (CMES)*, 67(1):13, 2010.

[145] S. Patankar. *Numerical heat transfer and fluid flow.* Series on Computational Methods in Mechanics and Thermal Science. Hemisphere Publishing Corporation (CRC Press, Taylor & Francis Group), 1980.

[146] L. R. Petzold. A description of DASSL: a differential/algebraic system solver. In *Scientific computing (Montreal, Quebec, 1982)*, pages 65–68. IMACS, New Brunswick, NJ, 1983.

[147] A. Benato, M. R. Kærn, L. Pierobon, A. Stoppato, and F. Haglind. Analysis of hot spots in boilers of organic rankine cycle units during transient operation. *Applied Energy*, 151:119–131, 2015.

[148] S.G. Kandlikar. Heat transfer characteristics in partial boiling, fully developed boiling and significant void flow regions of subcooled flow boiling. *Journal of Heat Transfer*, 120:395–401, 1998.

[149] D. R. Nørhave. Development of a dynamic model for a steam generator for concentrated solar power applications. bachelor thesis, 2017.

[150] K. J. Åström and R. D. Bell. Drum-boiler dynamics. *Automatica*, 36(3):363–378, 2000.

[151] S. W. Churchill and H. S. Chu. Correlating equations for laminar and turbulent free convection from a horizontal cylinder. *International journal of heat and mass transfer*, 18(9):1049–1053, 1975.

[152] J. G. Ziegler and N. B. Nichols. Optimum settings for automatic controllers. *trans. ASME*, 64(11), 1942.

[153] T. S. Kim, D. K. Lee, and S. T. Ro. Analysis of thermal stress evolution in the steam drum during start-up of a heat recovery steam generator. *Applied Thermal Engineering*, 20(11):977–992, 2000.

[154] S. K. Chakrabory, N. Manna, and S. Dey. Importance of tree-elements boiler drum level control its installation in power plant. *International Journal of Instrumentation and Control Systems*, 4(2):1–12, 2014.

[155] P. Á. González Gómez. *Design and dynamic analysis of steam generators for concentrating solar power plants.* PhD thesis, 2017.

Appendix A

Additional results

A.1 Gas-boosted parabolic trough power plant model

The following section presents a list of additional results for the gas boosted PTPP model (see Chapter 4.3.2).

- Figure A.1 and Figure A.2 present the graphical results for the validation, considering spring weather data.
- Figure A.3 illustrates the optimization results and Pareto front when the spring weather data is considered

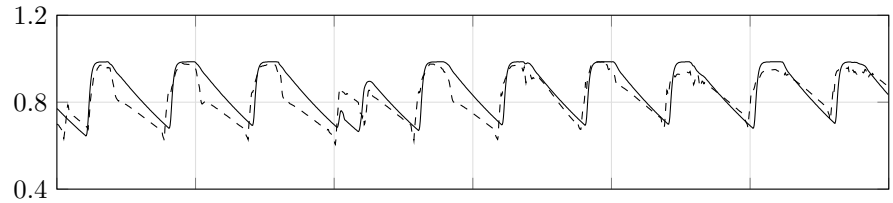

(a) Normalized turbine inlet steam temperature [-]

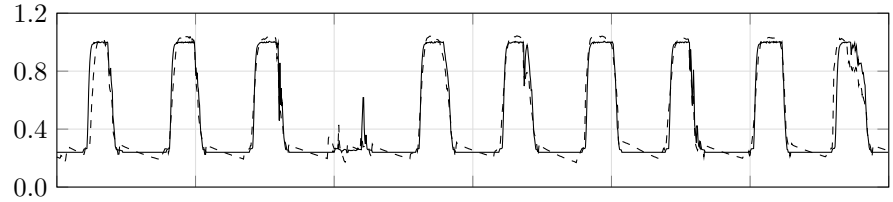

(b) Normalized evaporator inlet pressure [-]

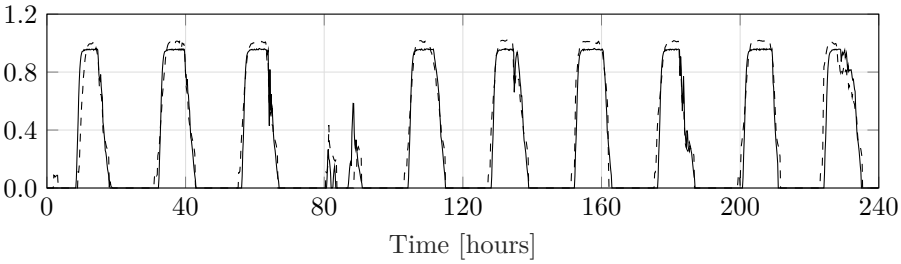

(c) Normalized turbine inlet steam mass flow rate [-]

Figure A.1: Validation for the spring case. Water related results

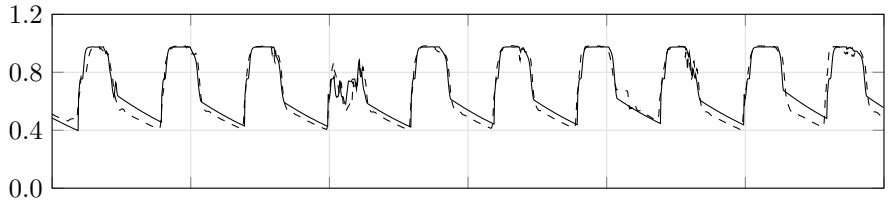

(a) Normalized solar field HTF outlet temperature [-].

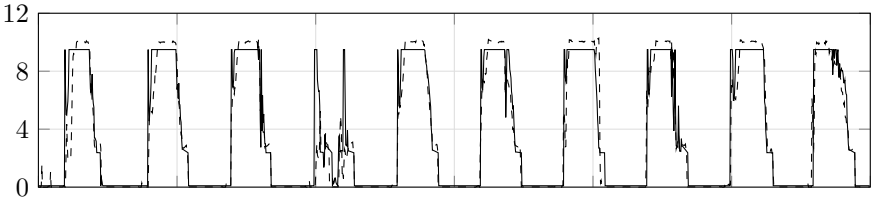

(b) Normalized solar field HTF mass flow rate [-].

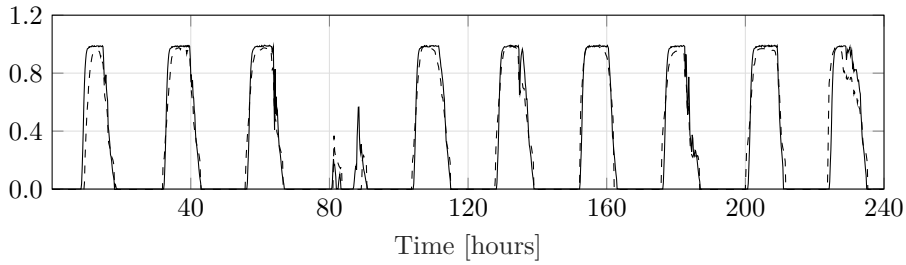

(c) Normalized electric gross power [-].

Figure A.2: Validation for the spring case. Solar field related and electric gross power results.

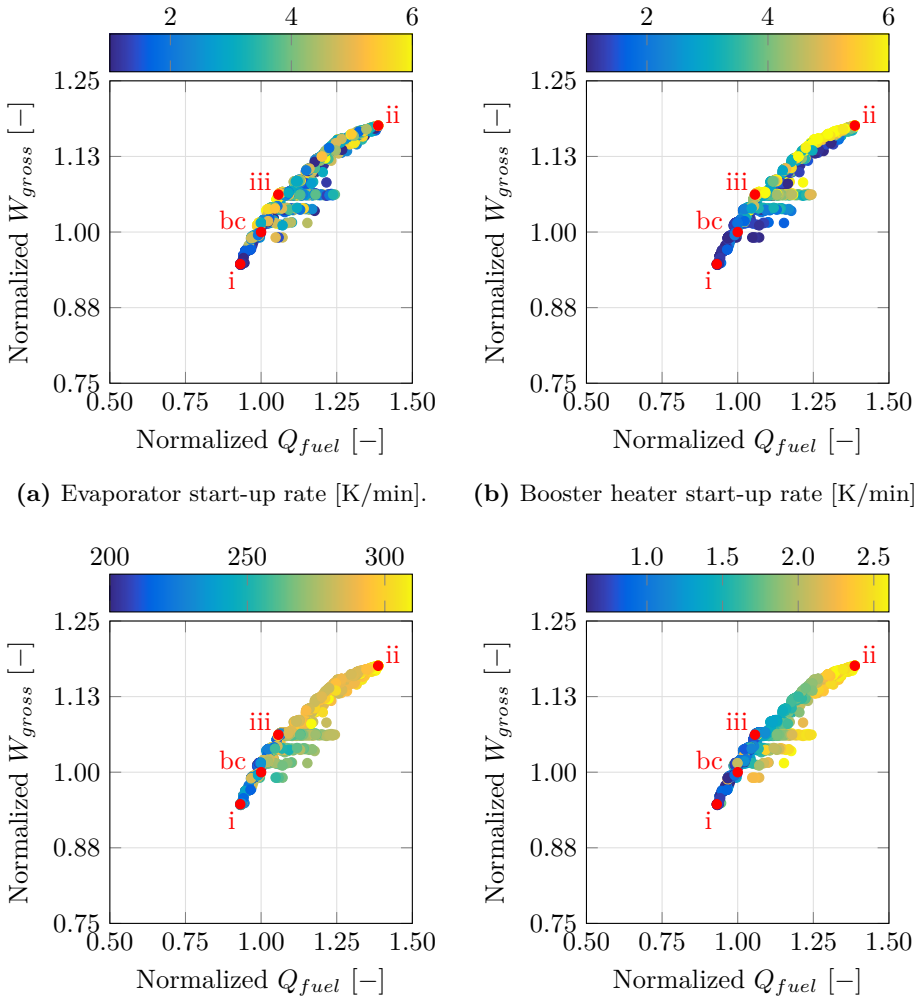

(a) Evaporator start-up rate [K/min].

(b) Booster heater start-up rate [K/min].

(c) HTF heater temperature [°C].

(d) HTF heater operating time [h].

Figure A.3: Optimization results for the spring case considering the different decision variables.

A.2 Power plant designs

The following section presents additional results regarding the design of the power plants presented in the thesis as follows.

- Table A.1 and Table A.2 present the additional results regarding the power plant and SGS presented in Chapter 4.2.
- Table A.3 and Table A.4 present the additional results regarding the power plant and SGS presented in Chapter 4.3.
- Table A.5 present the additional results regarding the power plant presented in Chapter 5.3.

Table A.1: Overview of the thermodynamic results of the Rankine cycle for the power plant presented in Chapter 4.2.

	$\dot{m}$ [kg/s]	h [kJ/kg]	p [bar]	T [°C]
HP-ST inlet	56.4	3026.3	100.0	377.6
HP outlet	56.4	2853.6	40.5	265.9
LP-ST inlet	47.6	3207.1	16.5	378.9
LP-ST outlet	37.6	2418.3	16.5	378.9
ACC outlet	44.8	173.3	0.08	41.4
LP pump outlet	44.8	181.6	13.0	43.4
HP pump outlet	56.4	747.5	115.0	176.4

Table A.2: Overview of the thermodynamic results of the SGS for the power plant presented in Chapter 4.2.

		$\dot{m}$ [kg/s]	h [kJ/kg]	p [bar]	T [°C]	$\dot{Q}$ [MW] (1)
Water	ECO inlet	56.4	1066.4	115.0	245.9	
	ECO outlet	56.4	1383.0	105.0	308.0	22.0
	EVA outlet	56.4	2718.1	105.0	314.4	78.9
	SH outllet	56.4	3026.3	100.0	377.6	18.9
	RH inlet	47.6	2705.4	17.1	204.1	
	RH outlet	47.6	3207.1	16.5	378.9	21.34
HTF	SGS inlet	621.3	765.7	15.0	393.3	
	SH inlet	261.8	765.7	15.0	393.3	
	SH outlet	261.8	699.3	15.0	367.3	
	EVA inlet	621.3	699.3	15.0	367.3	
	EVA outlet	621.3	582.2	15.0	319.4	
	ECO outlet	621.3	549.3	15.0	305.4	
	RH inlet	359.5	765.7	15.0	393.3	
	RH outlet	359.5	699.3	15.0	367.3	

(1) $\dot{Q}$ is the thermal power between the row considered and the previous one. (i.e. 1 →2 ECO, 2→3 EVA, 3→4 SH, 5→6 RH)

Table A.3: Overview of the thermodynamic results of the Rankine cycle for the power plant presented in Chapter 4.3.

	$\dot{m}$ [kg/s]	h [kJ/kg]	p [bar]	T [°C]
HP-ST inlet	123.3	3475.0	100.0	540.0
HP outlet	123.3	3129.2	23.7	349.8
LP-ST inlet	109.8	2877.1	6.6	213.7
LP-ST outlet	90.9	2476.8	0.15	54.0
ACC outlet	99.6	226.0	0.15	54.0
LP pump outlet	99.6	234.3	3.7	56.0
HP pump outlet	123.3	672.7	105.3	159.4

Table A.4: Overview of the thermodynamic results of the SGS for the power plant presented in Chapter 4.3.

		$\dot{m}$ [kg/s]	h [kJ/kg]	p [bar]	T [°C]	$\dot{Q}$ [MW] (1)
Water	ECO inlet	123.3	931.1	104.5	217.2	
	ECO outlet	123.3	1383.0	103.0	308.0	60.3
	EVA outlet	123.3	2723.9	102.0	312.3	160.6
	SH outlet	123.3	3013.0	101.0	380.0	36.6
	BH outlet	123.3	3475.0	100.0	540.0	56.6
HTF	SH inlet	1086.9	820.3	15.0	393.0	
	EVA inlet	1086.9	787.1	15.0	381.5	
	ECO inlet	1086.9	639.4	15.0	325.0	
	ECO outlet	1086.9	583.8	15.0	302.0	

(1) $\dot{Q}$ is the thermal power between the row considered and the previous one. (i.e. 1→2 ECO, 2→3 EVA, 3→4 SH, 4→5 BH)

Table A.5: Main nominal thermodynamic states of the Rankine cycle as presented in Chapter 5.3.

	$\dot{m}$ [kg/s]	h [kJ/kg]	p [bar]	T [°C]
HP-ST inlet	61.1	3026.3	100.0	377.6
HP outlet	61.1	2853.3	40.5	265.8
LP-ST inlet	51.7	3206.7	16.7	378.9
LP-ST outlet	40.8	2418.0	16.7	378.9
ACC outlet	48.7	173.3	0.08	41.4
LP pump outlet	48.7	181.6	13.0	43.4
HP pump outlet	61.1	747.5	101.2	176.4

A.3 Steam generator design model

The following section presents additional results regarding the design of the steam generator system. Figure A.4 presents the layout of the two-re-heater SGS and the numbering of the correspondent thermodynamic points.

- Table A.6 and Table A.7 present the additional results regarding the design presented in Chapter 5.2.
- Table A.8 and Table A.9 present the additional results regarding the design presented in Chapter 5.3.

Table A.9 presents a list of additional results for the optimal SGS design as presented in Table 5.13.

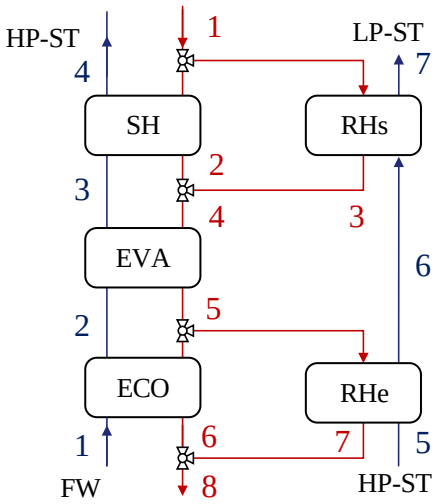

Figure A.4: Reference points for the thermodynamic states of the two-re-heater SGS. Red and blue colours refer to the HTF and water states, respectively.

Table A.6: Thermodynamic states of the SGS designed according to Table 5.8

		$\dot{m}$ [kg/s]	h [kJ/kg]	p [bar]	T [°C]
Water	1	73.8	1118.6	105.17	256.8
	2	73.8	1377.9	105.13	306.1
	3	73.8	2715.9	105.10	313.9
	4	73.8	3041.0	104.00	385.3
	5	57.3	2798.5	20.25	213.0
	6	57.3	3042.5	20.10	308.2
	7	57.3	3218.4	20.06	386.5
HTF	1	350.4	765.2	15.00	393.3
	2	350.4	696.7	14.67	366.5
	3	381.1	738.7	14.95	383.0
	4	731.4	718.6	14.67	375.2
	5	731.4	583.7	13.98	320.2
	6	350.4	529.1	13.79	296.9
	7	381.1	547.0	13.93	304.6
	8	731.4	538.4	13.79	300.9

Table A.7: Overview of additional design results for case presented in Table 5.8.

	Unit	Rhe	RHs	EVA	SUP	ECO
$\dot{Q}$	[kW]	13978	10079	98702	23981	19124
ΔT_{LMTD}	[°C]	39.1	28.4	24.2	23.6	24.9
$A_{(\text{oil side})}$	[m^2]	940.2	966.2	1283.8	1106.6	665.2
U	[W/(m^{2}K)]	379.9	367.1	3180.1	916.7	1155.5

Table A.8: Thermodynamic states of the SGS designed according to Table 5.13

		$\dot{m}$ [kg/s]	h [kJ/kg]	p [bar]	T [°C]
Water	1	61.0	1066.4	101.51	245.9
	2	61.0	1377.8	101.35	306.0
	3	61.0	2723.0	101.33	311.0
	4	61.0	3025.1	100.00	377.6
	5	51.6	2794.3	16.90	204.0
	6	51.6	3001.0	16.78	286.0
	7	51.6	3207.6	16.76	378.9
HTF	1	294.87	765.19	15.00	393.30
	2	294.87	702.71	14.61	368.9
	3	283.30	727.56	14.96	378.7
	4	578.17	714.89	14.61	373.7
	5	578.17	572.99	13.92	315.7
	6	294.87	508.58	13.48	287.9
	7	283.30	535.36	13.87	299.6
	8	578.17	521.70	13.48	293.7

Table A.9: Overview of additional design results for case presented in Table 5.13.

	Unit	Rhe	RHs	EVA	SUP	ECO
$\dot{Q}$	[kW]	10660	10660	82042	18422	18993
ΔT_{LMTD}	[°C]	56.4	42.1	22.4	32.3	22.0
$A_{(\text{oil side})}$	[m^2]	444.9	718.5	1094.7	493.3	569.0
U	[W/(m^{2}K)]	425.0	352.8	3349.4	1155.2	1514.4

Appendix B

Additional parameters

B.1 CSP models parameters

The following section present a list of tables summarizing additional parameters for the CSP models (see Chapter 4). Table B.1 presents the presents all the necessary parameters to size the solar field and HTF loop.

Table B.1: Solar field design parameters for the parabolic trough power plant models.

Parameters	Units	Chapter 4.2.2	Chapter 4.3.2
Reference day	[-]	173 - 12.00	173 - 12.00
Reference DNI	[W/m^2]	700	528
Reference T_{amb}	[°C]	22.8	43
f_{track}	[-]	0.99	0.99
f_{clean}	[-]	0.97	0.97
ρ_{col}	[-]	0.935	0.97
F_{col}	[m]	1.71	1.71
W_{col}	[m]	5.77	5.76
A_{col}	[m^2]	817.5	849.2
L_{col}	[m]	148.5	147.4
L_{spa}	[m]	15	17.3
$n_{\text{sca,loop}}$	[-]	4	4
A_{pt}	[-]	74.08	74.08
B_{pt}	[-]	-0.0047851	-0.0047851
C_{pt}	[-]	7.44	7.44
D_{pt}	[-]	-5.58399 $\cdot 10^{-05}$	-5.58399 $\cdot 10^{-05}$
a (IAM)	[-]	5.25 $\cdot 10^{-04}$	5.25 $\cdot 10^{-04}$
b (IAM)	[-]	2.86 $\cdot 10^{-05}$	2.86 $\cdot 10^{-05}$

B.2 SGS model parameters

The following section presents a list of tables summarizing additional parameters or material selection for the SGS model (see Chapter 5).

- Table B.2 presents the material selection for the design of the SGS. The carbon steel type selection is based on the ASME BPVC.
- Table B.3 presents the formulation of each coefficient for the PEC estimation of heat exchanger according to Purohit et al. [130].

Table B.2: Material selection for the main components of the heat exchangers (Selected according to Refs. [41, 93]).

Component	Material
Tube	SA-210-A
Header	SA-106-B
Shell	SA-516-Gr. 70
Pipe	SA-106-B
Steam drum	SA-516-Gr. 70

Table B.3: Purohit method for calculating heat exchanger costs (Ref. [130])

Parameters	Unit	Formulation or value
a	[-]	1.00
p	[-]	$0.75 \cdot {S_\mathrm{t}}^2 \cdot \left(\frac{a}{OD}\right)$
f	[-]	1.05
r	[-]	1.00
b	[USD/m^2]	$p \cdot f \cdot r \cdot \frac{6.6}{1 - e^{\left(\frac{7 - ID}{27}\right)}}$
c_L	[-]	$(1 - L/20) \cdot (1.5 - 0.002083 \cdot (ID_\mathrm{shell} - 15)(1 - L/20))$
c_NTP	[-]	$(NTP - 1)/100$
$c_\mathrm{p,shell}$	[-]	$(p_\mathrm{shell}/150 - 1) \cdot (0.07 + 0.0016 \cdot (ID_\mathrm{shell} - 12))$
$c_\mathrm{p,tube}$	[-]	$(p_\mathrm{tube}/150 - 1) \cdot (0.035 + 0.00056 \cdot (ID_\mathrm{shell} - 12))$

Appendix C

Articles

The following section presents the papers previously mentioned in the Publications section. Journal paper 4 is not presented as it is still under review and the draft is being improved. Only the papers on which the thesis is based upon are hereby presented:

- Page 154: Ferruzza, D., Topel, M., Laumert, B., Haglind, F. (2018). Impact of steam generator start-up limitations on the performance of a parabolic trough solar power plant. Solar Energy, 169, 255-263.
- Page 163: Ferruzza, D., Topel, M., Laumert, B., Haglind, F. (2018). Optimal start-up operating strategies for gas-boosted parabolic trough solar power plants. Solar Energy, 176, 589-603.
- Page 179: Ferruzza, D., Kærn, M.R., Haglind, F. (2018). Design of header and coil steam generators for concentrating solar power applications accounting for low-cycle fatigue requirements. Applied Energy, in press.
- Page 191: Ferruzza, D., Topel, M., Basaran, I., Laumert, B., Haglind, F. (2017). Start-up performance of parabolic trough concentrating solar power plants. In AIP Conference Proceedings (Vol. 1850, No. 1, p. 160008). AIP Publishing.

Solar Energy 169 (2018) 255–263

Contents lists available at ScienceDirect

Solar Energy

journal homepage: www.elsevier.com/locate/solener

Impact of steam generator start-up limitations on the performance of a parabolic trough solar power plant

Davide Ferruzza[a,*], Monika Topel[b], Björn Laumert[b], Fredrik Haglind[a]

[a] Department of Mechanical Engineering, Technical University of Denmark, Nils Koppels Allé, Building 403, 2800 Kongens Lyngby, Denmark
[b] Department of Energy Technology, KTH Royal Institute of Technology, 100 44 Stockholm, Sweden

ARTICLE INFO

Keywords:
Solar energy
Concentrating solar power
Parabolic trough power plant
Steam generator
Steam turbine
Start-up

ABSTRACT

Concentrating solar power plants are an attractive option in the renewable energy generation market. The possibility of integrating relatively cheap forms of energy storage makes them a desirable solution when power generation must be readily available at any time of the day. Solar power plants typically start-up and shut down every day, so in order to maximize their profitability, it is necessary to increase their flexibility in transient operation and to initiate power generation as rapidly as possible. Two of the key components are the steam generator and steam turbine and the rates at which they can reach operational speed are limited by thermo-mechanical constraints. This paper presents an analysis of the effects of the thermal stress limitations of the steam generator and steam turbine on the power plant start-up, and quantifies their impact on the economy of the system. A dynamic model of a parabolic trough power plant was developed and integrated with a logic controller to identify start-up limitations, and subsequently the dynamic model was integrated in a techno-economic tool previously developed by the authors. The plant was analysed under two different operating strategies, namely solar-driven and peak-load. The results indicate that for steam generator hot start-ups, a 1.5% increase in peak-load electricity production would be achieved by doubling the maximum allowable heating rate of the evaporator. No useful increase would be achieved by increasing the rates beyond a limit of 7–8 K/min, as the turbine would then be the main limiting component during start-up. Similar conclusions can be drawn for the solar-driven case, for which the solar field and the energy source availability would pose the major constraint when starting up the steam generator system.

1. Introduction

Concentrated solar power plants (CSPPs) are becoming more common in the renewable energy market. This trend is expected to rise in the upcoming years due to their key capability of being integrated with relatively cheap thermal energy storage (International Energy Agency, 2014). This feature makes it possible to decouple the energy generation from the solar input, making the power they can generate available at any time (Guedez et al., 2017). However, despite this characteristic feature, CSPPs are not currently designed for continuous operation, therefore they still experience daily start-ups and shut-downs. In order to maximize their performance from both technical and economical standpoints, increasing the flexibility of their dynamic performance is an important aspect which must be addressed (Topel et al., 2017). The rate at which a power plant can start up is limited by thermo-mechanical constraints, which may increase the time to reach the nominal load of the power plant. The receiver, the steam turbine and the steam generator system (SGS) are usually the most limiting components in this regard. While the receiver (Samanes and Garcia-Barberena, 2014) and steam turbine (Topel et al., 2017) have been examined in the literature, the steam generator has not been the focus of many studies .

Many CSPPs in use today have steam generators which were typically designed as conventional heat exchangers, not optimised for transient applications (Vant-Hull, 2012). As the industry mainly used designs from conventional power plants, their SGS responded inefficiently to sudden changes in incident solar radiation and equally poorly to repeated morning start-ups. This can cause failures in the component due to excessive thermal stresses, which may compromise the economic viability of the power plants. Although the industry is interested in optimising SGS designs for CSPPs (Pelagotti et al., 2014), there is little information on optimal heating rate requirements. In order to maximize the flexibility (i.e. to increase the responsiveness of the power plant to a change in the power load or in insolation), and both the peak and the baseline rate of electric power production, it is essential that all the components are able to start as quickly as possible

* Corresponding author.
E-mail address: daferr@mek.dtu.dk (D. Ferruzza).

https://doi.org/10.1016/j.solener.2018.05.010
Received 22 January 2018; Received in revised form 16 April 2018; Accepted 3 May 2018
Available online 06 May 2018
0038-092X/

Nomenclature

ACC	air cooled condenser
CSPP	concentrating solar power plant
CT	cold tank
D	deaerator
ECO	economizer
EVA	evaporator
HP	high pressure
HT	hot tank
HTF	heat transfer fluid
HX	heat exchanger
IHX	indirect heat exchanger
LCF	low cycle fatigue
LP	low pressure
PB	power block
PI	proportional-integral
PTPP	parabolic trough power plant
RH	re-heater
SF	solar field
SGS	steam generator system
SH	super-heater
SM	solar multiple
ST	steam turbine
TES	thermal energy storage

Symbols

ITD	inlet temperature difference [°C]
$\dot{m}$	mass flow [kg/s]
p	pressure [bar]
T	temperature [°C]
t	time [s]
v_T	allowable ramp-up rate/heating rate [K/min]

Subscripts

f	fluid
max	maximum
min	minimum

and enable the CSPPs to quickly start harvesting the incoming solar radiation. On the other hand, there might be limiting factors for one component, which might reduce the required heating rate for another. For example, if the receiver or solar field are the limiting factors, there is no need for the SGS to be able to start up at a faster rate than that of the solar field (Ferruzza et al., 2017).

The SGS and steam turbine both start up at a rate that is governed by the need to limit thermal stresses and low-cycle fatigue (LCF) (Pelagotti et al., 2014; Topel et al., 2017). Thick-walled components, material properties and temperature gradients are the limiting factors. In the case of the steam generator, the main constraining factors are the maximum allowable stresses in thick walled components such as the steam drum, super-heater headers and T or Y junctions in the steam pipelines (Dzierwa and Taler, 2014; Taler et al., 2015). Typically, the limiting component is the evaporator drum, which is designed as a large diameter high pressure vessel, which must consequently have thick walls. The start-up procedure of the component is intended to reach nominal conditions for temperature, pressure and mass flow rates as rapidly as possible. In the case of the steam turbine, the shaft seal and blading clearances determine the maximum allowable thermal expansion of the components, while the shaft thickness is the limiting factor for thermal stress. As a general rule, the starting procedure of a steam turbine can be considered to have three different phases: pre start-up heating, rolling up and loading up. During this procedure, the key parameter which limits the heating rate is the difference in temperature between the incoming steam and the metal of the turbine. In order to avoid excessive thermal stresses in this component it is desirable to keep the temperature difference as low as possible (Spelling et al., 2012).

In previous studies, much attention is given to the thermal stress that limits the maximum heating rates of these components, but little information is available about their impact on the performance of the overall power plant. For instance, González-Gómez et al. (2017) analysed the thermo-mechanical stress in the case of SGS for solar applications, but the study was performed at component level, without considering the impact of such limitations on the performance of the power plant. The author also focused on design and cost-based optimization of such components without considering the system perspective.

The abovementioned studies considered the limitation regarding either the steam generator or the turbine, without addressing the interaction between the two (Dzierwa et al., 2016; Dzierwa and Taler, 2014; Taler et al., 2015). It is of crucial importance to evaluate how much different constraints on the start-up procedures of CSPPs affect their electric power production and whether significant differences occur under different conditions. This information will indicate where to improve the operation of the power plant and the design specifications for the components, from a thermo-mechanical point of view. Lastly, the operational strategy of the power plant determines the number of start-ups and their typology (hot, warm or cold start-ups) (Guedez et al., 2017; Spelling et al., 2012). For instance, if a CSPP operates purely in solar-driven without fuel back-up, its start-up would mainly occur in the morning when the sun is still rising. On the other hand, if a power plant is designed to work in peak load during a particular time of the day (e.g. during evening hours, when the price of electricity is higher), the start-up would occur when solar radiation or heat from the storage are readily available. From a start-up perspective (in the absence of back-up fuels), this would mean different availability of heat input, hence different start-up constraints.

The dynamic performance of parabolic trough power plants has been analysed previously (Almasabi et al., 2015; Blanco et al., 2011; Conrado et al., 2017; Luo et al., 2015), although the models proposed deal only with validation of the detailed component modelling of the solar field. Blanco et al. (2011) presented a model of a parabolic trough power plant (PTPP) and validated it against experimental data, but in this case the model of the power block was developed with a simplified correlation. Another approach was presented by Abed et al. (2016), in which a detailed dynamic model in APROS (Advanced Process Simulation Software) was validated against the operational data of Andasol II. The focus of the study was to develop a detailed control strategy of the power plant by means of PI (Proportional-Integral) controllers. The model presented did not focus on yearly performance but on daily control. None of these studies considered start-up constraints due to thermo-mechanical limitations. In previous works such constraints were usually analysed from a component perspective. For instance, Pelagotti et al. (2014) described in detail a dynamic model of a steam generator, and carried out a low-cycle fatigue analysis. The authors predicted the impact on the annual electricity production of PTPPs. Their calculations did not take into account start-up schedules of steam turbines or rates of heat availability, nor yearly performance evaluation of such power plants. A previous work by the authors (Topel et al., 2015) considered the impact of the start-up rate of the steam turbine for solar tower direct steam generation; however, in this work the start-up constraints of the steam turbine were not coupled with SGS constraints.

This paper presents an analysis of the effects of the thermal stress limitations of the steam generator and steam turbine on the power plant

start-up, and quantifies their impact on the economy of the system. The study was performed for both solar-driven and peak-load conditions to emphasize on how different constraints on starting up a steam generator have different impacts on the electric power production and depend on how the plant is operated (Guedez et al., 2017). The paper also considers how differently sized solar fields (in terms of solar multiple) affect the impact of the steam turbine and steam generator constraints from an operational perspective.

In Section 2 the paper presents the approach used for modelling the power plant. Secondly, it summarizes the main limitation for the start-up of the steam generator and turbine and how such constraints were implemented in the control logic for the overall model. In Section 3, it presents the evaluation of the impact of the constraints of the steam generator on the electric power production both in peak-load and solar-driven together with a discussion on the results. Lastly Section 4 outlines the conclusions and final remarks.

2. Methods

Modelling was performed in DYESOPT, an in-house tool developed at KTH, Royal Institute of Technology, Stockholm, which was developed for techno-economic modelling of CSP plants (Guedez et al., 2017). The tool has been validated against Thermoflex, a commercially available software for power plant performance estimation (Thermoflow, 2014), demonstrating a relative deviation between the results of two software below 10% in the case considered. As may be seen in Fig. 1, the tool allows for both steady-state design and dynamic simulation, and can make techno-economic calculations for different assumed locations for the plant. The overall approach, as shown in Fig. 1, can be linked to a multi-objective optimizer (Guedez et al., 2017).

The model of the PTPP was implemented in the tool and validated as described in Ferruzza et al. (2017). The author implemented the parabolic trough sizing methodology and the TRNSYS model in DYESOPT and validated against data available in literature with a maximum error of −8.9% (Ferruzza et al., 2017). The model was further developed by including different operating strategies and the option of including an air-cooled condenser (ACC). The consideration of ACCs is of topical interest, as many plants that are currently under development or in the tender phase will be placed in desert areas. Having no direct access to cooling water mandates the use of ACC in which the condensation of steam is achieved solely by air cooling and parasitic electrical power consumption (Moore et al., 2013). The ACC model was previously validated by Guedez et al. (2017).

2.1. Steam generator start-up limitations

The start-up procedure for a steam generator consists of bringing temperature, pressure and mass flow rate to nominal values in each component of the system. As noted above, the rate at which this can be done is highly dependent on thermo-mechanical limitations that are determined by their materials and geometry. Previous studies have shown that the main limiting components during an SGS start-up are the evaporator and super-heater, hence these two were considered in detail in the present study (Basaran, 2015; Taler et al., 2015). Another constraint which must be addressed is the occurrence of thermal shocks that might occur if the HTF temperature is higher than the metal temperature by more than a critical amount, as the material could then experience cracking and ultimately failure (Price, 2017). A limit on the maximum allowable temperature difference is usually implemented in the control logic of the start-up operation. Even though the minimum and maximum heating rates $v_{T\min}$ and $v_{T\max}$ for the required pressure can be determined according to the norm DIN EN 12952-3 (CEN, 2012), the goal of the present study is to determine the optimal range of values from a system perspective. The heating rates used to calculate the permitted fluid temperature change were obtained using the following equation (Taler et al., 2015):

$$\frac{dT_f}{dt} = \frac{p_{\max} v_{T\min} - p_{\min} v_{T\max}}{p_{\max} - p_{\min}} + \frac{v_{T\max} - v_{T\min}}{p_{\max} - p_{\min}} p(T_f) \quad (1)$$

These equations express the rate at which the fluid temperature (T_f)

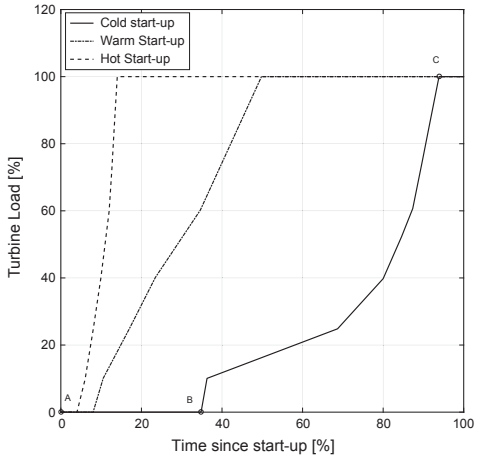

Fig. 2. Cold, warm and hot steam turbine start-ups (Adapted from Topel et al. (2015)).

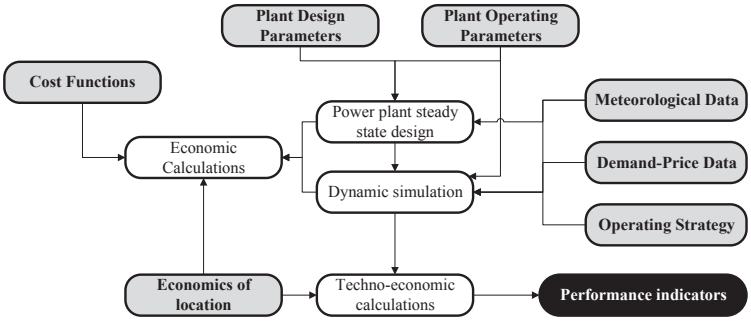

Fig. 1. DYESOPT workflow diagram.

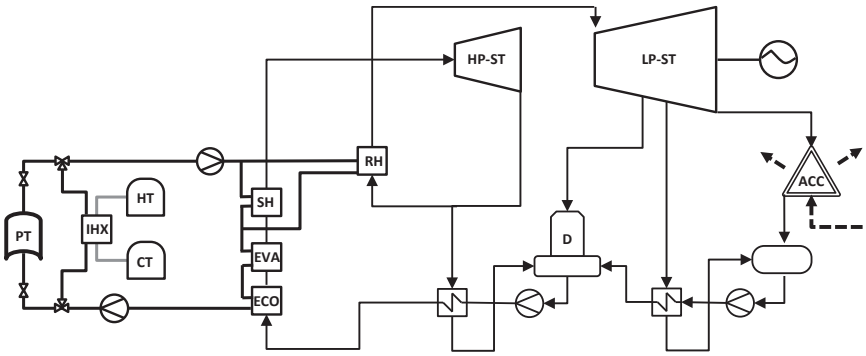

Fig. 3. Layout of the considered parabolic trough power plant integrated with indirect thermal energy storage and air cooled condenser.

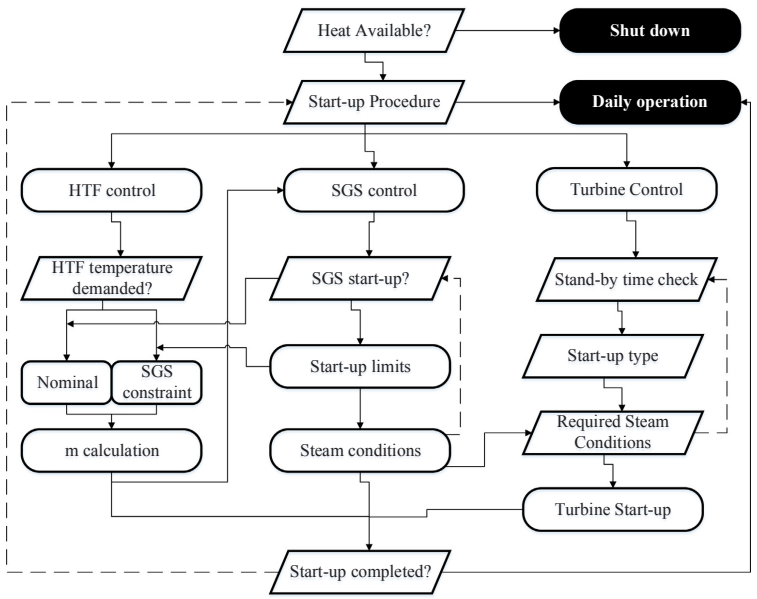

Fig. 4. Control logic for the power plant during start-ups.

Table 1
Summary of operation modes.

Operation mode name	Condition
Solar-driven	Whenever radiation or TES are available
Peak-load	Only between 15 and 21 if heat input is available

can change depending on the pressure of the fluid (minimum (p_{min}) and maximum (p_{max})) and the minimum and maximum heating rates which are dependent on the geometry, material properties and operating temperature and pressure. In an evaporator, the water is at saturation point so the pressure and temperature are related. As a consequence, the temperature of the fluid will be dependent on the pressure, and Eq. (1) can be solved using a Runge-Kutta method, assuming $T_f(\ t{=}\ 0) = T_0$. In the case of the super-heater, the fluid is not at saturation conditions, the pressure is a function of time and determined by the evaporator conditions.

Simulations were carried out for different constraints on the evaporator and the super-heater. As discussed by the authors in Ferruzza et al. (2015), an optimal heating rate constraint can be found for the super-heater by assuming that it is 1.8 times higher than the evaporator limit. However, simulations were also carried out using a 1.1 multiplier, to demonstrate the impact of this value and show how sensitive the results are to this design parameter. Two main start-up schedules can be identified for the evaporator. In the case of an evaporator with a drum configuration (natural or forced circulation), the minimum allowable pressure of the steam turbine can be maintained overnight. Such a start-up routine will be termed a hot start-up. However, when this is not possible (absence of steam drum or pressure vessel), the pressure would not be maintained overnight and the evaporator would have to start up

Table 2
Summary of design parameters.

Operation mode name	Units	Peakload case	Solar-driven case
SM	[–]	1.1	1.5–3
Gross power	[MW]	55	55
TES capacity	[h]	5	10
Inlet HP/LP pressure	[bar]	100/16.7	100/16.7
Nominal condensing pressure	[bar]	0.06	0.06
SF HTF maximum temperature	[°C]	393	393
Nominal turbine inlet temperature	[°C]	378	378

Table 3
Summary of the respective parameters for the four different cases analysed.

Case name	Case 1 a/b	Case 2 a/b	Case 3 a/b	Case 4 a/b
Average evaporator heating rate [K/min]	3–12	3–12	3–12	3–12
Super-heater heating rate multiplier [K/min]	1.1/1.8	1.1/1.8	1.1/1.8	1.1/1.8
Start pressure [bar]	35	1	35	1
Thermal shock Δ T [K]	63	63	63	63
Operation strategy	Peakload	Peakload	Solar-driven	Solar-driven

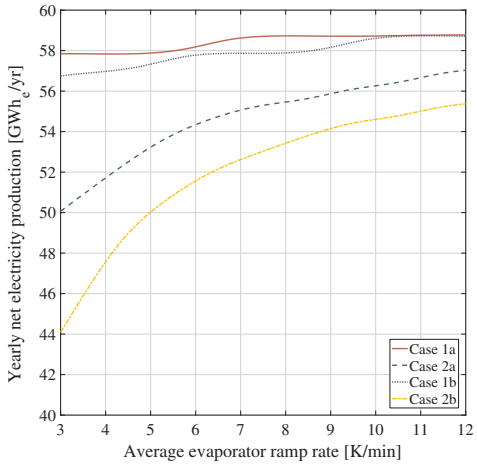

Fig. 5. Impact of the evaporator heating rate constraints on the net electricity production for a peak-load operating strategy.

from ambient pressure conditions. This will be termed a cold start-up. In order to study how different heating rate routines will affect the start-up of the power plant, both hot and cold start-ups were included, making the assumption that the overnight heat losses from the steam drum will be negligible. Observations from existing power plants indicate that the overnight heat losses from the steam drum may be neglected due to the large mass of water containing a high thermal inertia and experiencing a limited temperature drop.

2.2. Steam turbine start-up schedule

As for the SGS, the steam turbine start-up procedure is limited by the permissible temperature difference between the metal surface and the steam. Different start-up schedules are defined by the manufacturer based on the initial temperature of the turbine metal (or stand still time). The start-ups procedures are classified as cold, warm or hot. A hot start-up would take only 8–10% of the time it takes for a cold start-up, while a warm start-up would take 45–50% of that of a cold start-up (Topel et al., 2015). Fig. 2 illustrates the three different start-up curves. The start-up procedure involves two phase which are denoted for the cold case as the A-B and B-C lines which represent the rolling up and loading up of the turbine, respectively (Topel et al., 2015).

The start-up schedules were kept constant in order to focus mostly on the impact of the steam generator on the overall performance of the power plant. The minimum allowable pressure was kept at 35 bar (as by requirement of the steam turbine) and the rate at which pressure, mass flow rate and temperature could rise were determined following the paper by Schenk et al. (2015). During the running-up the mass flow rate is kept at 5% of the nominal value, while during the loading up the mass flow rate increases with a rate determined directly by the steam turbine start-up routine depending on the metal temperature at which the procedure begins. The different hot, warm and cold start-up curves presented in Fig. 2 were introduced in the model, depending on the metal temperature (Topel et al., 2015).

2.3. Power plant modelling

The plant layout considered in the paper is shown in Fig. 3. The thick lines represent the HTF loop, which is heated up by the parabolic trough (PT) mirrors, and either fed directly to the steam generator (comprising an economizer (ECO), evaporator (EVA), super-heater (SH) and re-heater (RH)) or to heat-up, through the indirect heat exchanger (IHX), the salts from the cold tank (CT) which are then pumped to the hot tank (HT). The other cycle represents a conventional Rankine-reheat cycle with high pressure (HP) and low pressure (LP) steam turbines (ST) an air-cooled condenser (ACC) and a deaerator (D).The power plant was designed for the location of Seville, Spain, with a power output of 55 MWe gross, according to Guedez et al. (2017) for the power block, Gilman et al. (2008) for the HTF cycle Lippke (1995) and Dudley (1994) for the solar field. Firstly, the Rankine cycle was designed for the chosen gross power, determining its efficiency and thermal input requirement. The size of the solar field was determined accordingly and scaled considering the solar multiple (SM). Lastly, the thermal energy storage (TES) mass was calculated to ensure the amount of hours desired to satisfy the thermal demand of the power block. The design methodology was implemented in Matlab, while the yearly performance dynamic model was developed in TRNSYS (University of Wisconsin Madison, 1975) in order to be implemented in DYESOPT.

The dynamic model of the power plant was integrated with a controller, which ran the start-up procedure and applied the constraints to the steam generator and turbine. The logic of the controller is shown in Fig. 4. A similar strategy was applied when the power plant was operating either in solar-driven or peak-load. In solar-driven, the start-up will occur in the morning as soon as the solar heat is available. In this case, both the thermal shock and the thermal stresses (in the form of heating rates) are calculated and a required HTF temperature is sent to the solar field. Afterwards, the steam temperature and pressure rise accordingly, until the minimum allowable condition for superheated steam is reached. At this point the steam turbine can start according to the start-up procedure. Similarly, for peak-load operation, the heating rate constraints are calculated, from which a HTF temperature is obtained. However, as the plant operates at specific times of the day, an optimal design is supposed to ensure that there is heat available to be extracted from either the solar field or the thermal storage hot tank. If the thermal storage is used, the oil temperature can be regulated by adjusting the salt mass flow rate. If HTF temperatures higher than the allowable SGS HTF temperature occur, an attemperator may be used to reduce the temperature of the thermal oil or the HTF may be mixed (if possible) with oil at a lower temperature, either from the solar field loop or the SGS return line. One of the key differences between the two operation modes is the fact that at peak-load the heat is readily

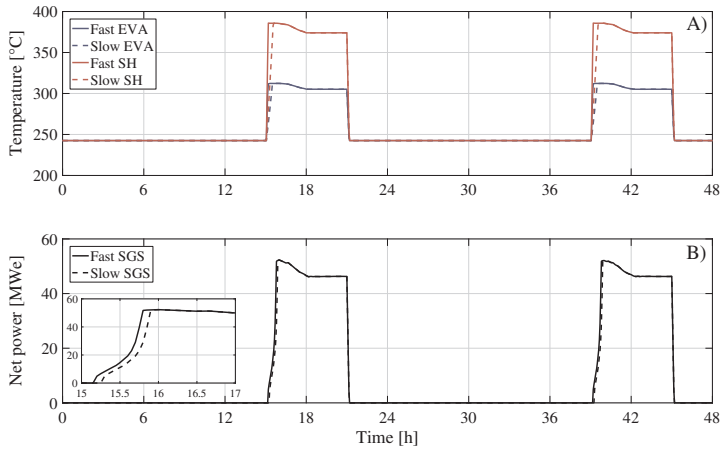

Fig. 6. Comparison of a two-day performance between a slow and a fast evaporator during a hot start-up for a peak-load operating strategy case. A) Evaporator and super-heater temperatures, B) Net power output.

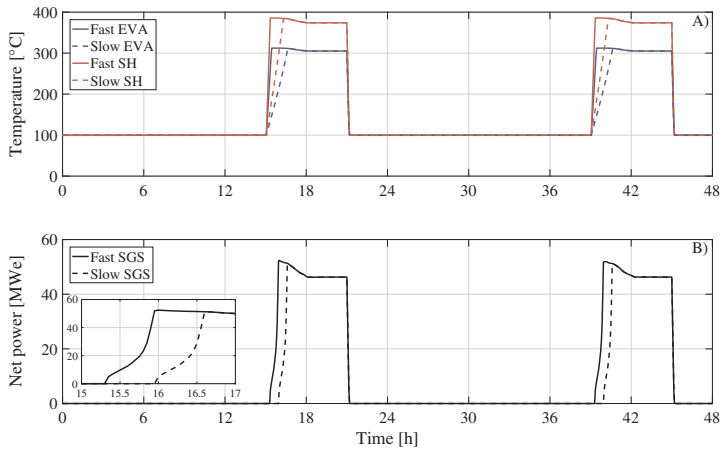

Fig. 7. Comparison of a two-day performance between a slow and a fast evaporator during a cold start-up for a peak-load operating strategy case. (A) Evaporator and super-heater temperatures, (B) Net power output.

available for the SGS and its constraints are the limiting factors, while in solar-driven operation mode, the heat availability is dependent on the position of the sun and the size of the solar field.

Once both the turbine and the steam generator have reached nominal operating conditions, the start-up procedure is finished and the power plant enters daily operation. Part-load operation is taken into account according to DLR (2006), if nominal heat input is not reached at the steam generator. The strategy depicted in Fig. 4 is applicable in both peak-load and solar-driven operation mode. Table 1 summarizes the conditions for the two operational modes following Guedez et al. (2017).

The main design parameters and thermal performance indicators are listed in Table 2. It summarizes both the parameters which were considered fixed and the ones that were allowed to vary for the purpose of the analysis. The PTPP designed according to Table 2 served as a basis for an analysis of the impact of the constraints. The SM and TES size for the peak-load case were chosen following Guedez et al. (2017). In the solar-driven case the SM was varied to account for the impact of the solar field size while the TES was kept at 10 h as this was a size that would still require warm turbine start-ups while allowing the plant to operate in the evening even in winter periods. The 15–21 time operation was chosen according to Guedez et al. (2017). However, in Guedez et al. (2017) the price of electricity in the suggested location was higher than zero even between 5 and 17. The study considered only peak price hours, in order to remove the influence of the solar field on the SGS. This means that the heat provided to the steam generator comes directly either only from the TES or from the combination of the TES and SF, in case it cannot come directly from the solar input. If the DNI is high enough the PT has already gone through its start-up phase and could potentially provide nominal heat input to the steam generator. This makes it possible to focus on how the constraints of the evaporator and super-heater affect the performance of the power plant if electricity

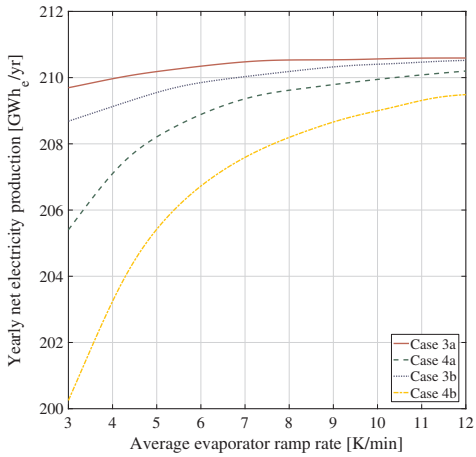

Fig. 8. Impact of the evaporator ramp rate on the net electricity production for a solar-driven operating strategy case, considering a solar multiple equal to 2.

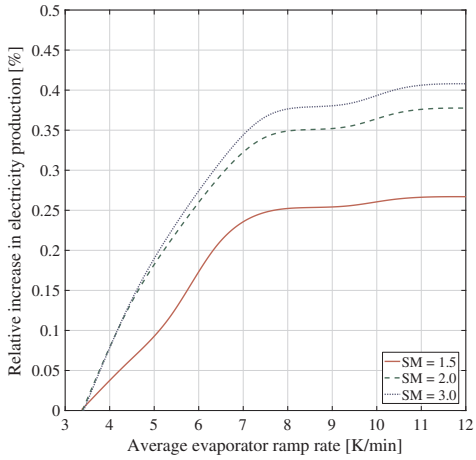

Fig. 9. Sensitivity to the solar field size on the impact of the evaporator ramp rate constraints for a solar-driven operating strategy case.

production was postponed to a particular time of the day.

3. Results and discussion

The impact of the start-up constraints was investigated and the performance of the power plant under different limitations is presented in this section. Both peak-load and solar-driven operation were analysed. For both of these modes, the start-up constraint of the steam generator was analysed for the cases shown in Table 3.

The lower threshold for evaporator constraints was chosen as a reference, representing a slow start-up of the SGS system (Pelagotti et al., 2014). This constraint can be considered as representative of a steam generator system based on a kettle-reboiler type evaporator (González-Gómez et al., 2017). The higher threshold was chosen as a potential improvement compared with the designs of header and coil geometrical configurations already available in industry (Aalborg CSP, 2015). The cases are also considering different start-up strategies for the steam generator. If a hot start-up is available (Case 1 and Case 3 respectively), it means that the minimum allowable pressure of the turbine is kept at the steam drum. In the case of a cold start-up (Case 2 and Case 4 respectively), the pressure starts from ambient conditions.

3.1. Peak-load case

Fig. 5 shows the results of the impact of the SGS heating rate constraints on the yearly electricity production for the cases presented in Table 3. The graph indicates that for a hot start-up, the potential improvement in Case 1 is 1.54% (0.9 GWhe) for Case 1a. For cold start-ups of the evaporator, the potential increases to 12.5% (6.3 GWhe). Higher impacts were found for Cases 1b and 2b, when lower SH heating rate multipliers were chosen, the potential for improvement being as high as 3.6% and 25%. In the first cases, the evaporator was the main limiting factor during the start-up, while in the latter the limitations imposed on the super-heater delayed the initial phase of the turbine start-up, making the impact of the procedure more significant in terms of electricity production. These findings demonstrate the importance of a properly designed and operated super-heater while starting up the SGS. The results of Case 1a suggest that for hot evaporator start-ups it is possible to identify an optimal range of heating rate constraints around 7–8 K/min. Beyond this threshold, no significant increase in power production was observed, making it unnecessary to go above this design point. This is mainly due to the fact that even though the SH could reach its nominal operating condition at faster rates, the turbine would still have to be operated so as to respect its thermal limitations. This underlines how significant it is to consider both components when optimising the total system design to respect thermo-mechanical constraints. If a faster start-up rate was achievable for the steam turbine, then higher start-up constraints would be required for the steam generator. For a cold start-up of an evaporator, higher start-up rates would always imply greater electricity production for both a slow and a fast super-heater. In fact, the pressure that could be maintained overnight was well below the minimum allowable pressure for the steam turbine, requiring that SGS covers a larger temperature gradient, in turn postponing the beginning of the steam turbine start-up.

Fig. 6a and b shows respectively the steam temperature during a two day period and the net electricity output for case 1a. The two different lines refer to a slow (3 K/min) and a fast (12 K/min) SGS configuration. Fig. 7a and b shows the same variables but for case 2a. The results illustrated in Fig. 5 may better understood by looking at Figs. 6 and 7. In the first two, it may be seen that even if the evaporator start-up rate is 4 times higher than in the slow case, the impact on the net power output is barely noticeable (a close up is shown in the left part of the graph). This means that every day the beginning of the steam turbine start-up procedure is delayed by 6 min. In case 2, on the other hand, if the steam pressure is not maintained overnight, the delay is more significant and observable. In this case the steam turbine would experience a delay of as much as 30 min, making the SGS a bottleneck for the start-up procedure. These considerations indicate that the presence of a pressure vessel (in the form of a steam drum in this case) is important, to make the start-up procedure as effective as possible.

3.2. Solar-driven case

Fig. 8 illustrates an analysis similar to the one described in Section 3.1 but for a solar-driven operational strategy. The reference case adopted was for a SM equal to 2, being a representative value for existing power plant configurations like Andasol (Ferruzza et al., 2017). Following a similar consideration as before, if only hot evaporator start-ups are considered, the results indicate that the potential for improvement of the net electricity production is as low as 0.27% (0.56 GWhe), while for cold start-ups, this impact increases to a maximum of 2.3%. As

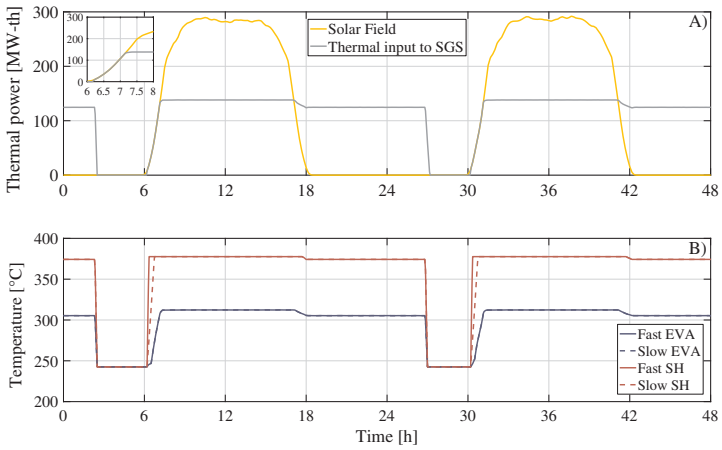

Fig. 10. Comparison of a two-day performance between a slow and a fast evaporator during a hot start-up for a solar-driven operating strategy case. (A) Thermal power at solar field and input to the steam generator system, (B) Evaporator and Super-heater temperatures.

in the previous case, if the super heater is not operated or designed optimally, the maximum potential improvement is 4.65% for cold start-ups.

Fig. 9 illustrates the relative increase in electricity production for different Solar Multiple (SM) cases. The figure suggests that the impact of the start-up constraints on the steam generator is considerably affected by the size of the solar field. It may be seen that by doubling the size of the solar field from a SM of 1.5–3.0, the relative increase can be improved from a maximum of 0.28%–0.41%. However, the impact is not very important in the economy of the power plant. Fig. 10 illustrates the development of the solar field thermal output and thermal input to the SGS and may suggest some reasons for this low improvement. The close-up in the figure shows that in the morning, the heat input to the SGS follows the same trend as the solar field output, as no storage is available. This means that to reach the nominal operating condition of thermal output takes roughly 1 h.

The pressure at the SGS follows a similar trend, as it is proportional to the heat input to the evaporator. Hence the start-up at the evaporator is no longer limited by its thermo-mechanical constraints but more by the heat available from the solar field. This is directly shown in the lower part of Fig. 10. It may be seen that in both the slow and fast cases, the temperature at the evaporator (and therefore the pressure, as it is at saturation point), are not two separate lines but they overlap. The only limiting component from a thermo-mechanical standpoint is therefore the super-heater, resulting in only negligible differences in power production. In these cases the steam reaches the minimum allowable conditions at a later stage, delaying the start-up of the turbine.

4. Conclusions

A detailed analysis was used to illustrate the impact of the SGS constraints during the start-up procedure of a PTPP. To achieve this, an existing detailed model of a PTPP that had previously been developed by the authors was extended to allow the simulation of two different operating strategies, namely peak-load and solar-driven operation. The model was also extended by the addition of an air-cooled condenser. A simulation tool was used to apply the start-up constraints of both the steam generator and the turbine. The model was integrated with an existing tool for the dynamic performance evaluation of power plants (DYESOPT).

The results suggest that for peak-load operation, by changing the constraints of the steam generator from 3 K/min to 12 K/min, the potential improvement in total net electricity output is 1.5%. It was shown that being able to maintain the minimum allowable turbine pressure overnight would be highly beneficial as it makes it possible to start the steam turbine in the most efficient way. The optimal range of maximum allowable heating rate for the evaporator was found to be about 7–8 K/min, designing a component with higher constraints would provide no benefit for the economy of the power plant. For solar-driven operation, the results indicate that for a solar field design with a SM equal to 2, the potential improvement of electricity production is as low as 0.27%. This figure might increase if the SF is further oversized, but only to 0.41%. The main limiting factor during start-ups is the amount of heat available in the solar field. As the solar field can only provide nominal operating power to the SGS after 1 h, the pressure at the evaporator cannot achieve its nominal value before that time, so the heating rate will be slower than the maximum limits in most start-up procedures. As a general conclusion, the results indicate that raising the maximum allowable evaporator constraints would not proportionally increase the yield of the power plant, as their effect is limited, either by other constraints at the steam turbine or at the solar field. It is therefore clear that the interaction among the three components is crucial when optimising the thermo-mechanical design of an SGS.

References

Abed, W., Al-maliki, K., Alobaid, F., Kez, V., Epple, B., 2016. Modelling and dynamic simulation of a parabolic trough power plant. J. Process Control 39, 123–138. http://dx.doi.org/10.1016/j.jprocont.2016.01.002.

Almasabi, A., Alobaidli, A., Zhang, T.J., 2015. Transient characterization of multiple parabolic trough collector loops in a 100 MW CSP plant for solar energy harvesting. Energy Procedia 69, 24–33. http://dx.doi.org/10.1016/j.egypro.2015.03.004.

Basaran, I., 2015. A comprehensive study of the imposed limitations on concentrating solar power plant start-up speeds. MSc, Thesis. Royal Institute of Technology (KTH), Stockholm.

Blanco, D., Luis, A., Garcı, I.L., 2011. Performance model for parabolic trough solar thermal power plants with thermal storage: Comparison to operating plant data. Sol. Energy 85, 2443–2460. http://dx.doi.org/10.1016/j.solener.2011.07.002.

CEN, 2012. Water-tube boilers and auxiliary installations - Part 3: Design and calculation for pressure parts of the boiler. Brussels.

Conrado, L.S., Rodriguez-pulido, A., Calderón, G., 2017. Thermal performance of parabolic trough solar collectors. Renew. Sustain. Energy Rev. 67, 1345–1359. http://dx.doi.org/10.1016/j.rser.2016.09.071.

DLR, 2006. A TRNSYS Model Library for Solar Thermal Electric Components (STEC), Reference manual.

Dudley, V., 1994. SEGS LS-2 Solar Collector. Test Results. Sandia National Laboratories, Albuquerque, New Mexico.

Dzierwa, P., Taler, D., Trojan, M., Taler, J., 2016. Evaporator heating with optimum fluid temperature changes. Procedia Eng. 157, 29–37. http://dx.doi.org/10.1016/j.proeng.2016.08.334.

Dzierwa, P., Taler, J., 2014. Optimum heating of pressure vessels with holes. J. Press. Vessel Technol. 137, 11202. http://dx.doi.org/10.1115/1.4027584.

Ferruzza, D., Topel, M., Basaran, I., Laumert, B., Haglind, F., 2017. Start-up performance of parabolic trough concentrating solar power plants. AIP Conf. Proc. 1850, 1–9. http://dx.doi.org/10.1063/1.4984542.

Gilman, P., Laboratory, N.R.E., Laboratories, S.N., 2008. Solar advisor model user guide for version 2.0. Technical Report.

González-Gómez, P.Á., Gómez-Hernández, J., Briongos, J.V., Santana, D., 2017a. Thermo-economic optimization of molten salt steam generators. Energy Convers. Manage. 146, 228–243. http://dx.doi.org/10.1016/j.enconman.2017.05.027.

González-Gómez, P.Á., Petrakopoulou, F., Briongos, J.V., Santana, D., 2017b. Steam generator design for solar towers using solar salt as heat transfer fluid. AIP Conf. Proc. 1–8. http://dx.doi.org/10.1063/1.4984363.

Guedez, R., Topel, M., Ferragut, F., Callaba, I., Perez-segarra, C.D., 2017. A methodology for determining optimum solar tower plant configurations and operating strategies to maximize profits based on hourly electricity market prices and tariffs. Sol. Energy Eng. 138, 1–12. http://dx.doi.org/10.1115/1.4032244.

International Energy Agency, 2014. Technology Roadmap. Solar Thermal Electricity, Paris.

Lippke, F., 1995. Simulation of the Part-Load Behavior of a 30 Mwe SEGS Plant. Sandia National Laboratories, Albuquerque, New Mexico Report.

Luo, N., Yu, G., Hou, H.J., Yang, Y.P., 2015. Dynamic modeling and simulation of parabolic trough solar system. SolarPACES 2014, 1344–1348. http://dx.doi.org/10.1016/j.egypro.2015.03.137.

Moore, J., Grimes, R., O'Donovan, A., Walsh, E., 2013. Design and testing of a novel air-cooled condenser for concentrated solar power plants. Energy Procedia 49, 1439–1449. http://dx.doi.org/10.1016/j.egypro.2014.03.153.

Pelagotti, L., Sørensen, K., Condra, T.J., Joseph, T., Franco, A., 2014. Modelling of a coil steam generator for CSP applications. In: Proceedings of the 55th International Conference on Simulation and Modelling.

Price, J.W.H., 2017. Thermal shock cracking: design and assessment guidelines thermal shock cracking: design and assessment guidelines. J. Press. Vessel Technol. 129, 125–132. http://dx.doi.org/10.1115/1.2389029.

Samanes, J., Garcia-barberena, J., 2014. A model for the transient performance simulation of solar cavity receivers. Sol. Energy 110, 789–806. http://dx.doi.org/10.1016/j.solener.2014.10.015.

Schenk, H., Dersch, J., Hirsch, T., Polklas, T., 2015. Transient simulation of the power block in a parabolic trough power plant. In: Proc. 11 Int. Model. Conf., pp. 605–614. doi: http://dx.doi.org/10.3384/ecp15118605.

Spelling, J., Jöcker, M., Martin, A., 2012. Annual performance improvement for solar steam turbines through the use of temperature-maintaining modifications. Sol. Energy 86, 496–504. http://dx.doi.org/10.1016/j.solener.2011.10.023.

Taler, J., Węglowski, B., Taler, D., Sobota, T., Dzierwa, P., Trojan, M., Madejski, P., Pilarczyk, M., 2015. Determination of start-up curves for a boiler with natural circulation based on the analysis of stress distribution in critical pressure components. Energy 92, 153–159. http://dx.doi.org/10.1016/j.energy.2015.03.086.

Thermoflow, 2014. Thermoflex Modular Program for Thermal Power Sys- tems [WWW Document]. URL www.thermoflow.com (accessed 11.22.17).

Topel, M., Genrup, M., Jöcker, M., Spelling, J., Laumert, B., 2017. Operational improvements for startup time reduction in solar steam turbines. Sol. Energy Eng. 137, 1–8. http://dx.doi.org/10.1115/1.4028661.

Topel, M., Guédez, R., Laumert, B., 2015. Impact of increasing steam turbine flexibility on the annual performance of a direct steam generation tower power plant. Energy Procedia 69, 1171–1180. http://dx.doi.org/10.1016/j.egypro.2015.03.196.

University of Wisconsin Madison. Solar Energy Laboratory., 1975. TRNSYS, a transient simulation program. Madison, Wis. : The Laboratory, 1975.

Vant-Hull, L.L., 2012. Central Tower Concentrating Solar Power (CSP) Systems, Concentrating Solar Power Technology: Principles, Developments and Applications. Woodhead Publishing Limited, Houston https://doi.org/10.1016/B978-1-84569-769-3.50008-X.

Aalborg CSP, 2015. Aalborg CSP Steam Generator. URL http://www.aalborgcsp.com/quickmenu/brochures/ (Accessed 8.3.17).

Solar Energy 176 (2018) 589–603

Contents lists available at ScienceDirect

Solar Energy

journal homepage: www.elsevier.com/locate/solener

Optimal start-up operating strategies for gas-boosted parabolic trough solar power plants

Davide Ferruzza[a,*], Monika Topel[b], Björn Laumert[b], Fredrik Haglind[a]

[a] Department of Mechanical Engineering, Technical University of Denmark, Nils Koppels Allé, Building 403, 2800 Kongens Lyngby, Denmark
[b] Department of Energy Technology, KTH Royal Institute of Technology, Sweden

ARTICLE INFO

Keywords:
Solar energy
Concentrating solar power
Parabolic trough power plant
Steam generator
Steam turbine
Start-up
Hybridization
Operation strategy
Flexibility
Optimization

ABSTRACT

Concentrating solar power plants are taking an increasing share in the renewable energy generation market. Parabolic trough is one of such technologies and the most commercially mature. However, this technology still suffers from technical challenges that need to be addressed. As these power plants experience daily start-up procedures, the optimal performance in transient operation needs to be considered. This paper presents a performance based modelling tool for a gas-boosted parabolic trough power plant. The objective of the paper is to define an optimal operational strategy of the power plant start-up procedure with the aim of minimizing its fuel consumption while at the same time maximizing its electric energy output, taking into account all the thermo-mechanical constraints involved in the procedure. Heating rate constraints of the steam generator and the booster heater, and the steam turbine start-up schedule were considered. The simulation model was developed based on a power plant located near Abu Dhabi, and was validated against real operational data with a maximum integral relative deviation of 4.3% for gross electric energy production. A multi-objective optimization was performed for a typical operating week during winter and spring weather conditions. The results suggest that in order to minimize the fuel consumption and at the same time maximize the electric energy production, an evaporator heating rate of 6 K/min is an optimal value both for winter and spring conditions.

1. Introduction

The concentrating solar power (CSP) technology shows an increasing trend in capacity installations around the globe. One of the key reasons for this, is the possibility to integrate such technology with relatively cheap ways of storing thermal energy, hence allowing it to decouple the electric energy production from the solar input (International Energy Agency, 2014). Parabolic trough power plants (PTPPs) are the most mature and economically viable plants among the CSP technologies. They account for 85% of the current capacity installed (Groupe Reaction Inc., 2014; Khetarpal, 2016) and 80% considering the power plants currently planned to be installed (Estela et al., 2016). However, they still face problems both at technical and economic levels. From a technical stand-point, the intrinsic fluctuating nature of the solar irradiation causes operating challenges such as daily start-up procedures and frequent variations in loads, which some components of the plant are not fully designed to endure. From an economic perspective, CSP technologies are still not fully competitive with respect to traditional technologies such as gas or coal power plants. A way to improve the operating flexibility and the economic feasibility of PTPPs is to optimize the power block operation by maximizing its flexibility towards fluctuating loads and cyclic daily start-up procedures (Mancini et al., 2011). By doing so, it is possible to harvest as quickly as possible the solar irradiation, hence maximizing its electric energy production and profitability.

One of the key aspects to improve the technical performance of CSP plants is to increase the rate at which the plant can load-up in order to harness the solar energy quickly. On the other hand, in order to preserve the lifetime of certain components, the ramp-up rate is limited by thermo-mechanical constraints (Ferruzza et al., 2017). With regards to the power block this is especially true for the steam generator system (SGS) and the steam turbine (Ferruzza et al., 2017). For the former, the heating rate at which it can experience a temperature increase is limited by the thermo-mechanical stresses on the thick walled components and junctions such as the steam drum, super-heater headers and T or Y junctions in the steam pipelines (Dzierwa et al., 2016; Dzierwa and Taler, 2014; Taler et al., 2015b). Generally, the component limiting the ramp-up rate in the evaporator is the steam drum, which is designed as a high-pressure vessel, with a large diameter and consequently thick walls. The start-up procedure of the component is intended to reach as

* Corresponding author.
E-mail address: daferr@mek.dtu.dk (D. Ferruzza).

https://doi.org/10.1016/j.solener.2018.10.059
Received 4 September 2018; Received in revised form 9 October 2018; Accepted 19 October 2018

Nomenclature

ACC	air cooled condenser
BH	booster heater
CSPP	concentrating solar power plant
CT	cold tank
D	deaerator
DNI	direct normal irradiation
DSG	direct steam generator
ECO	economizer
EVA	evaporator
HT	hot tank
HTF	heat transfer fluid
HTFH	heat transfer fluid heater
HX	heat exchanger
LCOE	levelised cost of electricity
PB	power block
PSA	Plataforma Solar de Almería
PT	parabolic trough
PI	proportionate integrative
PTPP	parabolic trough power plant
RD	ramp delay
SAM	system model advisor
SD	synchronization delay
SF	solar field
SGS	steam generator system
SH	super-heater
SM	solar multiple

Symbols

A	area [m^2]
m	mass flow [kg/s]
p	pressure [bar]
Q	thermal energy [GWh]
T	temperature [°C]
t	time [s]
U	overall heat transfer coefficient [$W/(m^2 K)$]
v_T	allowable ramp-up rate/heating rate [K/min]
W	electric energy [GWh]

Subscripts

f	fluid
max	maximum
min	minimum

rapidly as possible nominal conditions for mass flow rates, pressure and temperature. In the case of the steam turbine, the shaft thickness is the main limiting aspect regarding thermal stresses. Therefore, in order to avoid excessive thermal stresses it is desirable to keep the temperature difference between the steam and the turbine metal as low as possible (Topel et al., 2015a, 2015b, 2017).

In order to achieve maximum responsiveness of the power plant towards a change in power load or insolation it is essential that all the components are able to start quickly thus enabling the CSP plants to start harvesting the incoming solar energy as soon as possible. However, there might be limiting factors for one component, which might reduce the required heating rate for another. For example, if the receiver or solar field are the limiting factors, there is no need for the SGS to be able to start up at a faster rate than that of the solar field. From a yearly perspective and optimization point of view, it might happen that a lower constraint is actually needed either for the steam turbine or the SGS. On the other hand, having for instance components like the SGS exceeding such optimal point might allow for more flexibility in the operational strategies of the power plant.

Considering previous work available in literature, research has been performed on modelling and evaluation of the performance of PTPPs with both oil and molten salts as heat transfer fluid, with and without gas-fired backup. For instance, Boukelia et al. (2017, 2015) investigated this by modelling specifically the power block in Ebsilon professional (STEAG, 2012) and evaluated the optimal levelised cost of electricity (LCOE) by means of artificial neural network algorithms implemented in Matlab. This, however, was done without considering detailed start-up constraints or different operating strategies. Biencinto et al. (2016) performed modelling of PTPPs both with nitrogen and Therminol-VP as heat transfer fluids. The model of the solar field was validated in detail against real plant data, while the overall model was compared with SAM (System advisor model) (Biencinto et al., 2014). In this case, the model was used to compare the annual yield of the two configurations. Bonilla and Jose (2012) modelled a direct solar steam generator PTPP using object-oriented modelling and calibrated it by comparing the model results with plant data from CIEMAT-PSA (Centro de Investigaciones Energéticas, Medioambientales y Tecnológicas – Plataforma Solar de Almería) by means of genetic algorithm based multi-objective optimization. The model focused mainly on the solar field detailed modelling and not on the overall power plant. Blanco et al. (2011) developed a model in the Wolfram mathematical software and compared the results to available power plant data. In this case, the power block was not modelled in detail, but used thermal efficiency correlations as function of the thermal input. Another example can be found in the work performed by Al-Hanaei et al. (2016), in which the authors developed a model of the Shams I power plant. The model did not consider the details of the power block and a validation was not presented in the paper. Detailed models can be also found in the research works presented by Sun et al. (2015) and Li et al. (2017b, 2017a, 2017c), in which the authors developed a multi-dimensional model to address optical, hydraulic and thermo-elastic issues during the operation of a direct steam generator (DSG) parabolic trough collector. Even though the authors addressed the thermo-elastic problems and monitoring, they did not integrate the findings in the definition of an optimal start-up strategy.

In general, it may be claimed that many simulation tools are available to perform CSP plants design and performance evaluations. System Model Advisor (SAM) from NREL (National Renewable Energy Laboratories, USA) (Blair et al., 2008; Gilman et al., 2008; Price, 2003), Greenius (Dersch et al., 2011) from DLR (Deutschen Zentrums für Luft- und Raumfahrt) and Solergy from Sandia National laboratories (Stoddard et al., 1987) are commonly known tools in the CSP community. However, papers including detailed comparisons of simulation results with operational data of existing power plants are scarce. Concerning the start-up limitations, studies have been performed at component level. As for steam turbines, Topel et al. (2015a, 2015b, 2017) studied the thermo-mechanical limitations on steam turbines due to thermal stresses and start-up procedures. Concerning the steam generator system, González-Gómez et al. (2017a, 2017b) analysed such constraints for the heat exchangers and employed dynamic models for the stress evaluation. At system performance level, Topel et al. (2015a, 2015b) and Spelling et al. (2012) considered the impact of increasing the turbine flexibility with regards to the power plant performance. In a previous study, the authors of this paper analysed the mutual interdependencies between the turbine and steam generator and the impact of their constraints on a parabolic trough power plant performance (Ferruzza et al., 2017). However, no previous study addressed the optimization of the start-up operational strategy of a parabolic trough solar power plant considering thermo-mechanical constraints related to the steam generator, heat exchangers and steam turbine. Specifically,

there are no studies available in literature that aim at lowering the fuel consumption of such plants by optimizing the start-up operating strategy.

In this paper, a hybridized PTPP with a gas-fired booster located near Abu Dhabi is considered. The plant is also integrated with an additional heat transfer fluid heaters. The objective of the paper is to define an optimal operational start-up strategy of the power plant start-up procedure with the aim of minimizing its fuel consumption while at the same time maximizing its electric energy output, taking into account all the thermo-mechanical constraints involved in the procedure. This was done by taking into consideration the evaporator and booster heater heating rate constraints to verify how a dynamic performance oriented design for such components could lead to a higher flexibility from an operational standpoint. The optimal range for these constraints in order to satisfy the aforementioned objective were determined. The numerical model was thoroughly validated considering the steady state and transient performances using two sets of operational data of a power plant located near Abu Dhabi.

In Section 2 the paper presents the methods used to model the plant and validate it against operational data. It summarizes the constraints taken into account in the start-up strategy and dynamic operation and the implementation of the operation of the power plant in the control logic. Lastly, it presents the multi-objective optimization routine implemented. Section 3 presents the results of the validation, and afterwards the results and discussion of the multi-objective optimization performed for two different weather conditions. Section 4 outlines the conclusions and final remarks.

2. Methods

The modelling of the PTPP was carried out in DYESOPT, a tool able to perform power plant steady state nominal design, performance evaluation and techno-economic calculations. The tool has been previously developed and validated at KTH, Royal Institute of Technology, Stockholm (Guédez, 2016; Spelling, 2013). Fig. 1 illustrates the logic flow of information and calculations within the tool, where the grey and black boxes represent the inputs and outputs of the model respectively. In order to perform the power plant design, meteorological data and an operating strategy are the required inputs together with price data if economic calculations are required. The results of the design serve for the time-dependent performance evaluation, which is carried in TRNSYS (University of Wisconsin Madison, 1975). Lastly, the results are post-processed in Matlab to obtain the required performance indicators. If these involve economic indicators, cost functions and economics of the plant location are taken into consideration. The whole procedure can be coupled with a multi-objective optimizer.

The steady state design and modelling of the power plant were developed and added to the tool. The sizing was performed in Matlab, while the dynamic modelling was performed in TRNSYS, and it was integrated with a control strategy to take into account the heating rate constraints during the start-up procedure. More details are provided in the following sections. DYESOPT incorporates a modified version of a queueing multi-objective optimizer (QMOO) based on a genetic algorithm developed at the Industrial Energy Systems Laboratory in Lausanne (Leyland and Favrat, 2002). Fig. 1 shows the flow of information required for an optimization study. At the start of the optimization, it is possible to set conflicting objectives with regards to whether to maximize or minimize their quantities. Both design parameters and operation parameters can be set to allow for variation within the limits chosen for the study. The algorithm performs then as many iterations as needed to finalize the optimization and obtain an optimal trade-off curve or Pareto front.

2.1. Heat exchangers heating rate constraints

The details of the steam generator, heat transfer fluid heater and booster heater constraints are explained in the current section. As noted above, the rate at which each of them can start-up or heat-up is limited by material and geometrical constraints. As for the SGS start-up, previous studies (Basaran, 2015; Taler et al., 2015b) have shown that the main limiting components in this regard are the super-heater and the evaporator, hence these two were considered in detail in the current work. From a system perspective, the limit on the maximum allowable temperature difference for the heat exchangers is implemented in a

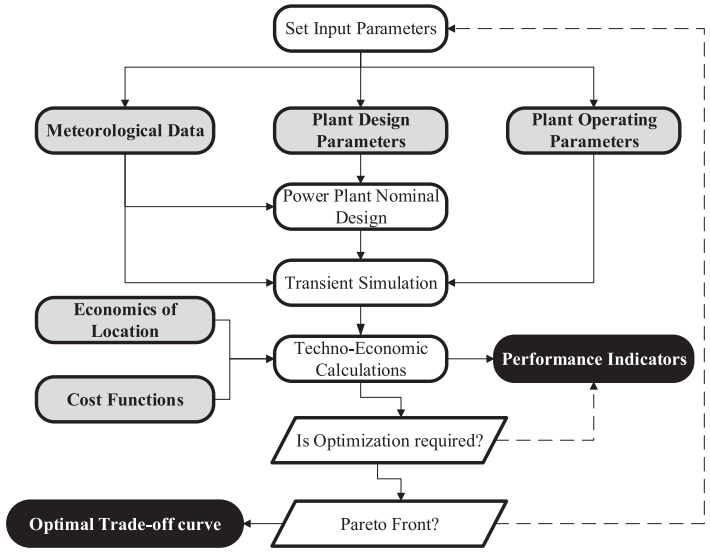

Fig. 1. DYESOPT workflow diagram. Solid lines represent a YES logic while dashed lines represent a NO logic.

control logic for the morning start-up procedures and daily transients. The minimum and maximum heating rates may be calculated based on the geometrical configuration and material specifications according to the norm DIN EN 12952-3 (CEN, 2012). However, the objective of this paper is to determine the optimal range of constraints from a system perspective, specifically tailored for start-up strategies. Such heating rates can be used to calculate the permitted fluid temperature change using the following equations (Taler et al., 2015b):

$$\frac{dT_f}{dt} = \frac{p_{max} v_{T_{min}} - p_{min} v_{T_{max}}}{p_{max} - p_{min}} + \frac{v_{T_{max}} - v_{T_{min}}}{p_{max} - p_{min}} p(T_f) \quad (1)$$

These equations express the rate at which the fluid temperature (T_f) can change depending on the pressure of the fluid (minimum (p_{min}) and maximum (p_{max})) and the minimum and maximum heating rates ($v_{T_{min}}$and $v_{T_{max}}$) which are dependent on the geometry, material properties and operating temperature and pressure. In an evaporator, the water is at saturation point so the pressure and temperature are related. As a consequence, the temperature of the fluid will be dependent on the pressure, and Eq. (1) can be solved using a Runge-Kutta method, assuming $T_f(t = 0) = T_0$. In the case of the super-heater, the fluid is not at saturation conditions, the pressure is a function of time and determined by the evaporator conditions. The same considerations are applicable to both the HTF heater and the booster heater. In these cases as the two fluids considered (oil and super-heated steam) are not at saturation point.

2.2. Steam turbine start-up schedule

In order to capture a thorough start-up operation of the power plant, the TRNSYS model was implemented with a control strategy for the start-up of the steam turbine. The rate at which this component can increase its load is determined by the metal temperature at the beginning of the procedure. The warmer the turbine, the faster a start-up procedure will be. The turbine metal cool-down was modelled according to a lumped capacitance method (Bergman et al., 2011). Depending on the metal temperature, the appropriate start-up schedule curve was chosen in order to minimize the difference between the steam and metal temperatures. Once these are selected, the appropriate synchronization delay (SD) and the time for the turbine to reach full load (or ramp delay (RD)) are defined. Depending on the metal temperature, the start-ups can be generally classified as hot, warm and cold. A hot start-up typically takes only 8–10% of the time it takes for a cold start-up, while a warm start-up requires between 45 and 50% of the time it takes for a cold start-up. Fig. 2 illustrates the three main different start-up curves implemented in the transient model, with the A-B and B-C lines representing the synchronization delay and ramp delay, respectively for the cold case (Topel et al., 2015a, 2015b). Fig. 3 illustrates the turbine start parameters such as pressure and temperature for a typical start-up schedule of the considered turbine.

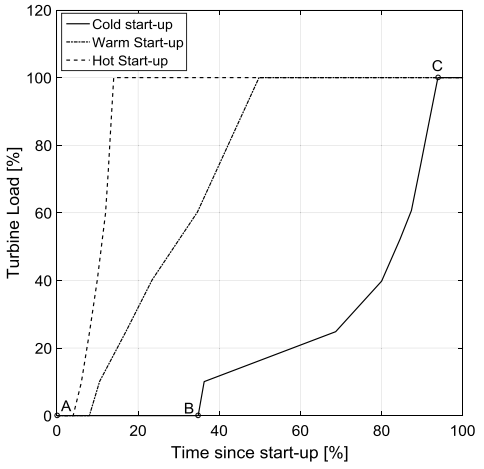

Fig. 2. Cold, warm and hot steam turbine start-ups (adapted from Topel et al., 2015a, 2015b).

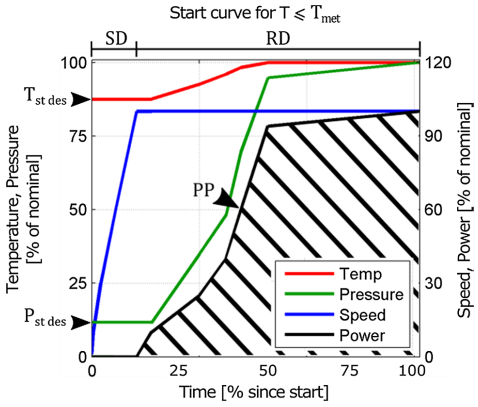

Fig. 3. Turbine start parameters within a start-up schedule (Topel et al., 2015a, 2015b).

2.3. Power plant modelling

Fig. 4 illustrates the power plant layout considered. The schematic layout of the plant is based on the configuration of a power plant located near Abu Dhabi (Alobaidli et al., 2017). The thick lines represent the heat transfer fluid loop. The oil is heated up by the parabolic trough (PT) collectors and pumped to the steam generator system, which comprises a super-heater (SH), an evaporator (EVA) and an economizer (ECO). In the morning when there is not high direct normal irradiation (DNI) a gas-fired heat transfer fluid heater (HTFH) can be turned on to raise the temperature of the recirculating oil to the desired set point. The other cycle represents a conventional regenerative Rankine cycle with the only exception of the booster heater (BH). The super-heater outlet steam temperature is raised to the turbine inlet temperature (TIT) by the booster heater. The power block layout comprises a steam turbine (ST) with extractions to a deaerator (D) and closed feed-water heaters. The outlet steam from the turbine is condensed by an air-cooled condenser (ACC). The main design parameters of the power plant are summarized in Table 1.

The equations of the zero-dimensional physical models governing the components are based on the STEC library (DLR, 2006) for the power block. The inertia and response time of the components was taken into account by means of a lumped capacitance method (Bergman et al., 2011; DLR, 2006). The heat exchanger off-design models are based on scaling functions of the UA (overall heat transfer coefficient times area) value, which depends on the ratio of the actual cold side mass flow rate to that at the nominal point, while the turbine off-design performance was modelled according to the Stodola equations. The parabolic trough solar field was modelled taking into account optical efficiencies depending on the position of the sun, geometry of the collectors and weather conditions as well as thermal losses due to piping and expansion vessels (Dudley, 1994; Gilman et al., 2008; Lippke, 1995). The booster heater model is based on an efficiency map which

depends on the steam inlet temperature according to the ASHRAE handbook (ASHRAE, 2000). Properties of the HTF were computed by linear interpolation in a data sheet from the oil manufacturer (Solutia, 2014).

The transient model of the plant was implemented with a logic controller to take into account the morning start-up strategies and hybridization with the HTF heater as well as the heating constraints for the abovementioned components. A summary of the morning start-up strategy is presented in Fig. 5. Fig. 6 presents a summary of the operating modes during the start-up. In the morning (as indicated by (1) in Fig. 5) the main factors to account for, are the time at which the HTF heater is set to operate and when the PT can actually start to operate. These are choices usually set by the plant operator. In presence of DNI, the latter is allowed to operate after a certain time constraint, and more importantly, if the wind is below the maximum allowable threshold. Before that, the fluid is heated up by the HTFH (OM1). The start time of the HTFH is a variable which can be set in the plant operating parameters (see Fig. 1). Once the HTF is heated up and reaches the minimum allowable temperature (as indicated by (2) in Fig. 5) for the SGS, the HTF mass flow rate is calculated and the start-up procedure takes place (OM2). The oil temperature is raised according to the SGS heating-rate constraints. Lastly, the needed flow rate is pumped to the SGS. The same can happen if the DNI is high enough to start the solar field. In this case, the HTFH is turned off and the procedure is carried on in a solar only mode (OM3).

The steam coming from the SGS is heated up by the booster heater, which as well needs to comply with thermal stress constraints. In the meanwhile, the metal temperature of the steam turbine is checked, and if the steam has allowable conditions, the turbine start-up can begin, according to the corresponding start-up curve, which is dependent on the metal temperature. The steam temperature and pressure are raised according to the heating constraints and the mass flow rate is kept at a constant value during the rolling up phase (5% of the nominal value (Schenk et al., 2015)) before the steam turbine can actually start to load up. The water mass flow rate raises and the nominal values can be reached (OM4) (as indicated by (3) in Fig. 5). Once the procedure is terminated the plant enters into daily operation, taking into account both steady state performance and part-load performance when the DNI is not high enough according to DLR (2006). During the daily transient operation a similar procedure is performed, always checking the governing thermal stress constraints.

2.4. Multi-objective optimization

The performance of the power plant can be measured by means of different indicators. For instance, when considering maximizing the electric energy generation of the considered power plant it is an intrinsic consequence to increase the fuel consumption. However, if the other objective is to minimize the fuel consumption, these two objectives will be in conflict. Hence, no single optimum solution exists but instead, for a given fuel consumption, a maximum electric energy production can be found, thus obtaining a trade-off of best operating designs considering fuel consumption and energy production. The optimization results can be used to choose an optimal start-up strategy for a particular requirement (Leyland and Favrat, 2002; Spelling, 2013). The objectives of the optimization were to minimize the fuel thermal energy consumption (Q_{fuel}) and maximize the electric gross energy production (W_{gross}). The decision variables chosen for the optimization studies are summarized in Table 2.

The optimization was performed for two seasons, winter and spring weather conditions, illustrating the operational flexibility of the plant throughout the year. The two periods chosen correspond to the data available for validation in order to show how the operation of the plant can be improved with the proposed operating strategies. Using two different sets of weather conditions allows to see how the optimal operation strategy changes throughout the seasons considered. The minimum and maximum values of the decision variables were chosen to allow the possibility of radically different operating strategies. Having a higher pre-heating temperature would put less strain on the steam generator as it would need to cover a lower temperature difference to reach the nominal condition, which may result in lower optimal heating rates. Minimum and maximum heating rate constraint values were

Table 1
Design parameters of the power plant (Alobaidli et al., 2017; Vogel et al., 2014).

Start-up parameter	Units	Value
Location	[–]	Abu Dhabi
Solar multiple	[–]	1
Gross power	[MWe]	124
Power block nominal efficiency	[–]	0.35
Solar field aperture	[m^2]	627,840
Solar field nominal efficiency	[–]	0.75
Parabolic trough collector type	[–]	Astro
Solar field outlet temperature	[°C]	393
Steam generator steam outlet temperature	[°C]	380
Turbine inlet pressure	[bar]	100
Condensation pressure	[bar]	0.17
Turbine inlet temperature	[°C]	540
Nominal condensing pressure	[bar]	0.13
Operating strategy	[–]	Solar-driven

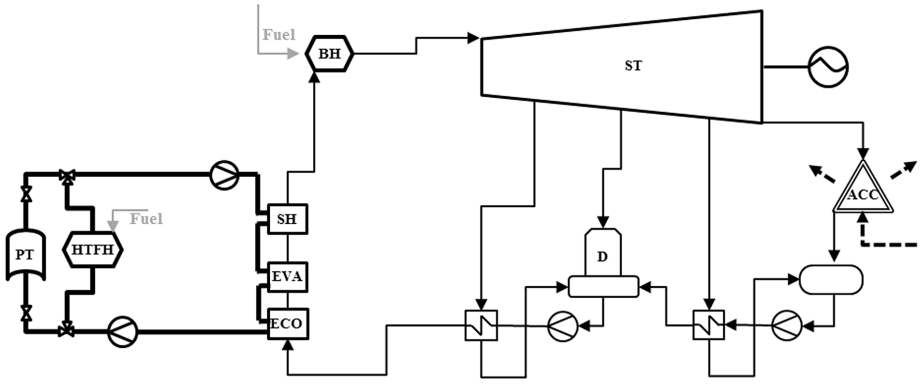

Fig. 4. Layout of the considered parabolic trough power plant integrated with an oil heater and a booster heater (Alobaidli et al., 2017; Vogel et al., 2014).

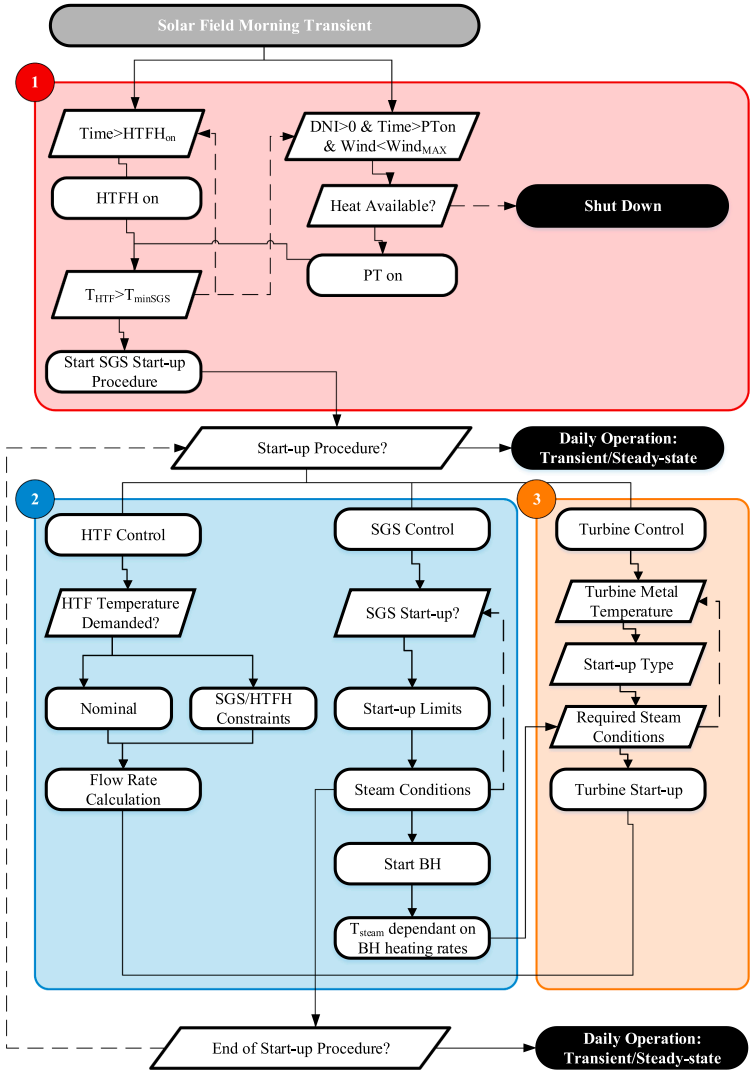

Fig. 5. Morning start-up strategy control logic. Solid lines represent a YES logic while dashed lines represent a NO logic. ().
Adapted from Al-Hanaei et al., 2016; Ferruzza et al., 2018; Schenk et al., 2015

chosen as reference, and potential improvements were selected to reflect the best technologies commercially available. The ramp rate range of 3 K/min to 9 K/min represents a practically achievable range for commercially available steam generators (Aalborg CSP, 2015; Taler et al., 2015a). An intermediate value of 6 K/min was chosen as the maximum value for the decision variables considered.

2.5. Validation

In order to check the reliability and accuracy of the developed model, a validation was carried out both for the steady-state design and for the transient performance evaluation. The steady state validation was performed by comparing the sizing of all power plant components in DYESOPT in terms of rated thermal load and mass flow rates with the available data of the power plant in Abu Dhabi. After the model was implemented in TRNSYS, the transient performance was validated against operational data of the power plant. It was tested against available data sets of 16th – 28th February and 6th – 16th May, representing winter and spring weather conditions, respectively.

As the purpose of the model is to represent properly the power plant electric power production, the following six main parameters were chosen for the validation: Turbine inlet temperature (TIT), evaporator

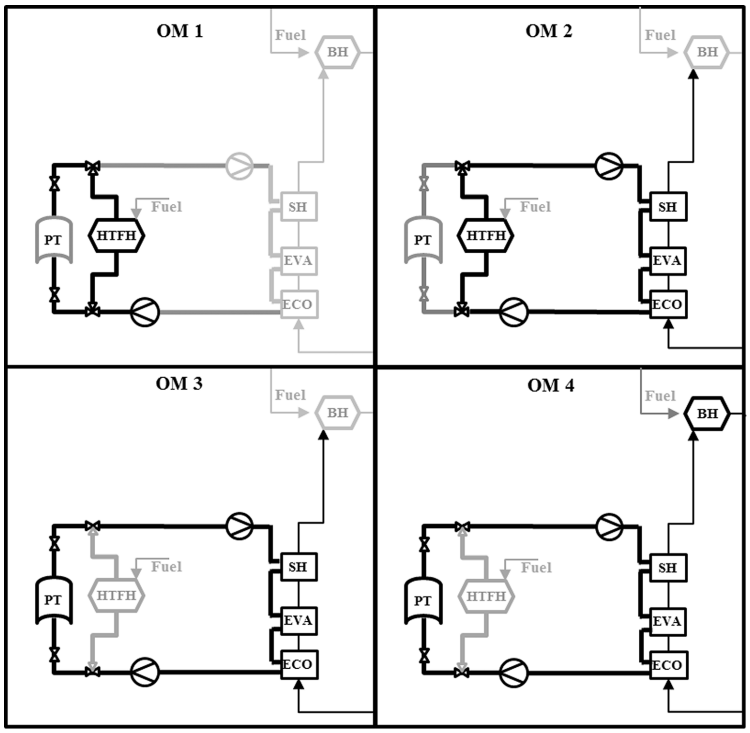

Fig. 6. Operating modes (OM) during the start-up of the steam generator.

Table 2
Decision variables and constraints (Almasabi et al., 2015; Moya, 2012).

Parameter	Unit	Minimum value	Maximum Value
EVA heating rate	[K/min]	1	6
BH heating rate	[K/min]	1	6
HTFH operating time	[h]	0	2.5
HTFH T	[°C]	200	310

Table 3
Results of the validation of the main parameters (normalized values).

	Model	Data	Relative deviation
Steam generator nominal thermal load	207.3%	207.5%	−0.12%
Booster heater nominal thermal load	45.6%	47.0%	−2.90%
Condenser nominal thermal load	152.9%	153.4%	−0.36%
Power block net electric power output	89.4%	89.1%	+0.39%
Parasitic consumption	10.6%	11.2%	−5.13%
Solar + fuel to electricity efficiency	28.34%	28.57%	−0.81%

Table 4
Results of the validation of mass flow rates (normalized values).

	Model	Data	Relative deviation
SGS HTF mass flow rate	869.66%	931.67%	−6.66%
SGS steam mass flow rate	98.62%	100.00%	−1.38%
BH exhaust gas mass flow rate	20.92%	21.38%	−2.13%
Condenser water mass flow rate	72.71%	72.67%	+0.06%

steam inlet pressure, steam mass flow rate, HTF outlet temperature at the SF, HTF mass flow rate and gross electric power. In order to quantify the reliability and accuracy of the model the following indicators were used (Blanco et al., 2011):

Integral relative error:

$$IRE = \frac{(\int_0^{time}(y_{model} - y_{data})dt)}{(\int_0^{time}(y_{data})dt)} \quad (2)$$

Root Mean Square Error:

$$RMSE = \left(\frac{\sum(y_{model} - y_{data})^2}{N}\right)^{\frac{1}{2}} \quad (3)$$

Normalized RMSE:

$$NRMSE = \frac{RMSE}{y_{max} - y_{min}} \quad (4)$$

The Integral Relative Error (IRE) gives an overall measure throughout the simulation time considered of the accuracy of the model. It quantifies the deviation of the integral result over the time period considered between the model results and the available data. For example, if the gross power is considered, it will give an estimation of the error of the electric energy produced throughout the time considered. The Root Mean Square Error (RMSE) and normalized RMSE (NRMSE) give a measure of the instantaneous accuracy of the model both in absolute and relative terms. The y values refer to the model and data sets for a certain number of available data points (N).

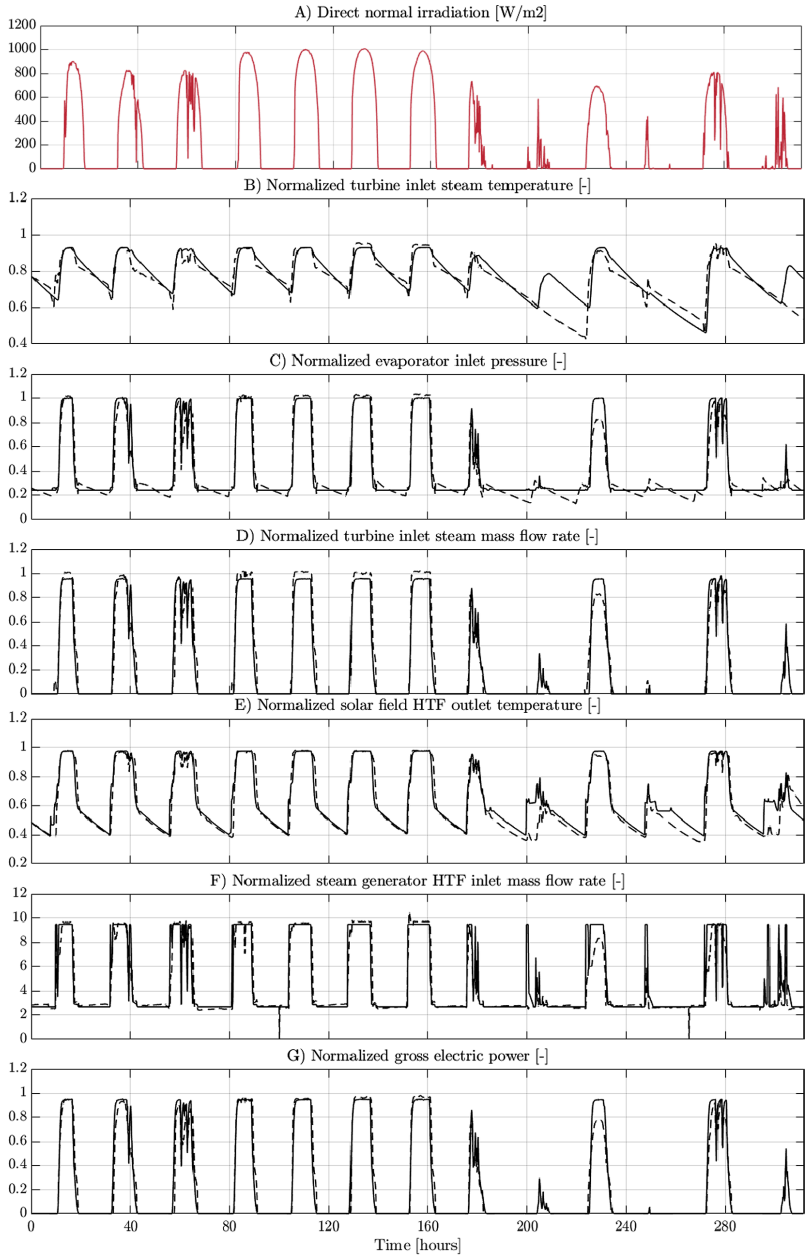

Fig. 7. Validation for the winter case; (A) DNI for the case considered (input), (B) Normalized turbine inlet temperature, (C) Normalized evaporator inlet water pressure, (D) Normalized steam mass flow rate, (E) Normalized solar field HTF outlet temperature, (F) Normalized SGS HTF mass flow rate, (G) Normalized gross electric power. The solid and dotted lines represent the result of the model and operational data, respectively.

Table 5
Validation results for the winter case.

Parameter	IRE [%]	RMSE [% of nominal reference values]	NRMSE [%]
TIT	2.25	7.35	9.66
P_{inEVA}	2.11	7.74	8.49
FR_{steam}	−2.57	8.56	8.34
T_{HTF}	3.19	7.62	12.00
FR_{HTF}	3.86	119.49	11.39
Gross power	2.37	8.45	8.60

3. Results and discussion

3.1. Validation of the model

This section presents the validation both for steady state at design point/nominal load and for the dynamic performance. Tables 3 and 4 present the result of the validation of the main parameters and mass flow rates, respectively, at steady state nominal load. As the values are confidential, the validation is presented in terms of normalized parameters. The mass flow rates and power were normalized with the nominal values of steam mass flow rate and gross power (see Table 1, Section 2.3).

The maximum deviation is found for the HTF mass flow rate at the inlet of the SGS (−6.7%) which is attributed to the approximations made in the property calculations of the HTF (see Section 2.3). As the steam mass flow rate nominal value was used as normalization parameter for all the mass flow rate results, the HTF related results are higher than 100%. This means that the required HTF mass flow rate is higher than the nominal turbine inlet mass flow rate. Lower deviations are found in the validation of the main parameters with a maximum error in absolute term of −5.1% for the parasitic consumption. This deviation can be directly related to the lower nominal mass flow rate of the HTF which is required by the SGS in the model and which would affect the parasitic consumption of the solar field. Based on the results shown in the tables, it may be concluded that the plant sizing model provides reasonable results, which are sufficiently accurate in the context of the paper.

The model was also validated for transient operation; Fig. 7 illustrates the validation of the model for the data available between 16th and 28th of February, showing the common input for both the model and the operational data as summarized by Table 5. Temperature and pressure values were normalized with nominal turbine inlet temperature and pressure. The figure illustrates that the model is able to predict properly the trends of the main thermodynamic points and relative mass flow rates as well as produced electric power. The major deviations for each quantity, which may be observed in Fig. 7, may be noticed at the end of the day (between 17.00 and 19.00), as (due to the high inertia of the parabolic trough solar field) the mass flow of the HTF is recirculated through the PT even though there is no DNI. This is done to exploit the remaining thermal inertia of the SF; however, the model is not able to fully capture this possibility. Another major deviation for each quantity may be observed on day 9. In this case, the DNI is low but high enough to allow the operation of the solar field according to the constraints set in the model. However, the plant was not operated in that day, due to a decision of the operator. A similar consideration may be applied to the last day of the simulation.

Table 5 summarizes the relative error indicators as presented in Section 2.5 and the RMSE values are normalized to the nominal reference values. The table illustrates that as an overall result (as integral over the days of the simulation) the model is accurate in predicting the performance of the power plant, with a maximum relative error of 3.9% for the flow rate of the HTF at the inlet of the SGS. Even though at nominal point the HTF mass flow is underestimated as noted in Table 4, the integral area is overestimated. This is mainly related to the days in which the power plant was not operated. The gross energy production validation resulted in 2.4% overestimation as compared to the operational data. Higher relative errors may be observed for the instantaneous validation. In this case the NRMSE goes up to +12% for the HTF outlet temperature and +8.6% for the gross electric power. Also in this case this can be related to a different operational decision of the operator.

In order to test further the validity of the model, its performance has been validated against the available operation data for the period 6–16 May in which a less irregular DNI was measured (even though with lower values), being a representative case for the spring. The time variant results are shown in Fig. 8 and Table 6 for the error estimation. Similar considerations as those of the winter case can be drawn for the spring case from Fig. 9 and Table 6, resulting in deviations of similar magnitudes. However, in the spring case the gross electric power production is overestimated to a higher extent (+4.3%), primarily because of day 4 when the plant was not operated due to a planned outage, whereas the model allowed for electric power production. In this case, the highest error is observed for the flow rate, both for the integral and instantaneous errors due to the same reasons as those of the winter validation.

Moreover, a validation of the time delay until reaching experimental power output was carried out. Table 7 illustrates the results for such validation on a daily basis for both weather conditions. An average value of the absolute term of the deviations is also presented. It may be noticed that a significant deviation is observed for day 10 in the winter case. This is mainly due to lower HTF mass flow rates caused by additional defocusing set by the plant operator, which is not reflected in the model. This is also why lower values are observable in Fig. 7. Days 9, 11 and 13 were excluded from the winter related calculations as in those days the plant was not operated. The same reasoning applies for day 4 in the spring data set. Excluding these outliers, the highest deviation (+11.1%) in rising time is observed for day 7 for winter conditions, which is illustrated in Fig. 9 B. The lowest deviation is obtained in day 4 (−0.46%) and the corresponding daily validation is depicted in Fig. 9 A. Higher deviations (in absolute terms) are observed for the spring case with values up to −15.6% in the case of day 8 (represented in Fig. 9 D). A lower value, −8.7%, is observed for day 7 (represented in Fig. 9 C). These deviations are mainly due to a more conservative approach employed by the operator in starting up the power plant during these periods. As an overall result, the absolute average deviation on the rise time is 7.9% and 11.8% for winter and spring weather conditions, respectively.

The last step of the validation consists in comparing the estimated results of the model for the daily gross energy production with the equivalent operational data. Fig. 9 illustrates such comparison in percentage form (the data were normalized against the maximum integral value obtained from the operational data sets). Fig. 9 A and B refer respectively to the winter and spring weather conditions. The dots represent the operational data points, while the dashed lines represent ± 10% and ± 5% deviation in the winter and spring case, respectively. For the spring case the results indicate that 80% of the values are within a 5% deviation while the two worst days are overestimated. In the winter weather conditions, the deviation slopes raise to ± 10% and in this case 85% of the points are within this margin. The other two points correspond to day 9 and 13 when the plant did not operate. In case of day 11 (on the (0,0) coordinate in Fig. 10 A) both the plant and the model predicts little to no electricity output and that is why even though the plant did not operate, no major discrepancies are observed.

These observations support the aforementioned considerations on how the model differs more significantly only when the plant decision makers decided to change the normal operating routines. Overall, the results of Fig. 10 suggest that the model is more accurate from an integral perspective in spring conditions as the deviations are essentially lower. On the other hand, the errors for the winter case compensate for each other making the IRE lower in this case. In conclusion, the results

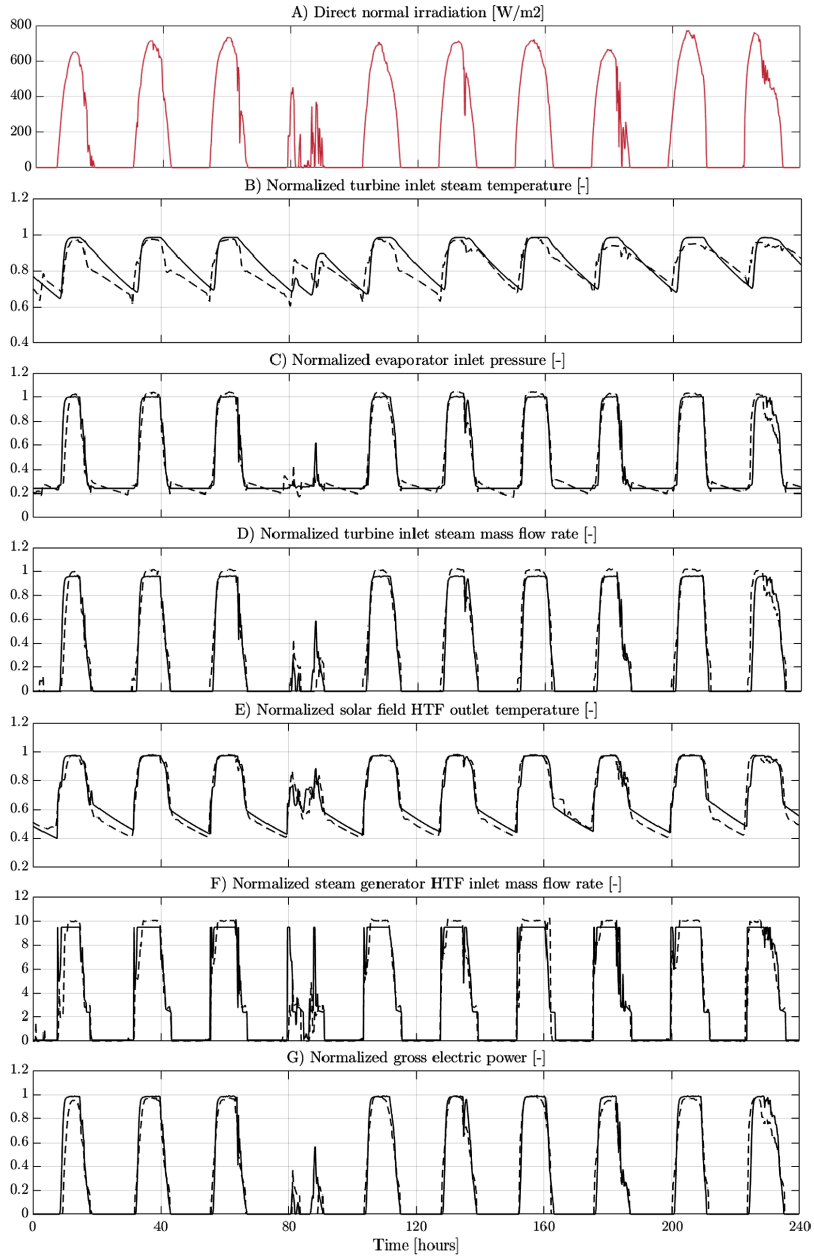

Fig. 8. Validation for the spring case; (A) DNI for the case considered (input), (B) Normalized turbine inlet temperature, (C) Normalized evaporator inlet water pressure, (D) Normalized steam mass flow rate, (E) Normalized solar field HTF outlet temperature, (F) Normalized SGS HTF mass flow rate, (G) Normalized gross electric power. The solid and dotted lines represent the result of the model and operational data, respectively.

Table 6
Validation results for the spring case.

Parameter	IRE [%]	RMSE [% of nominal reference values]	NRMSE [%]
TIT	2.97	6.41	7.71
P_{inEVA}	1.02	7.98	9.12
FR_{steam}	−4.12	9.93	9.72
T_{HTF}	1.67	5.63	8.28
FR_{HTF}	4.76	139.17	13.54
Gross Power	4.32	10.23	10.32

of the validation indicate that the model is able to predict the dynamic behavior of a gas-boosted parabolic trough solar power plant with reasonable accuracy, which is sufficient for the purpose of the study.

3.2. Optimization of the start-up strategy

This section summarizes the results obtained for the optimization studies both for the winter and spring weather conditions. Fig. 11 illustrates the results of the optimization for the winter case; the normalized objective variables (normalized with respect to the base case) are shown on the x-y-axes with one of the four decision variables (see Table 3) in each figure.

Fig. 11 highlights four different points, respectively:

i. Minimum fuel consumption
ii. Maximum electricity production
iii. Trade-off between the two objectives in the form of minimizing the fuel to electricity ratio $\frac{Qfuel}{Wgross}$.

bc. Base Case (bc): Case used for the validation of the model.

Their operational parameters and results are summarized in Table 8.

Table 7
Deviation results for rise time for gross power.

	Deviation on rise time	
Day	Winter	Spring
1	−6.8%	−13.2%
2	−13.2%	−11.9%
3	−10.2%	−11.7%
4	−0.5%	–
5	5.3%	−10.3%
6	5.0%	−8.8%
7	11.1%	−8.7%
8	10.0%	−15.6%
9	–	−15.4%
10	−25.9%	−10.5%
11	–	
12	−9.1%	
13	–	
Average (absolute value)	7.9%	11.8%

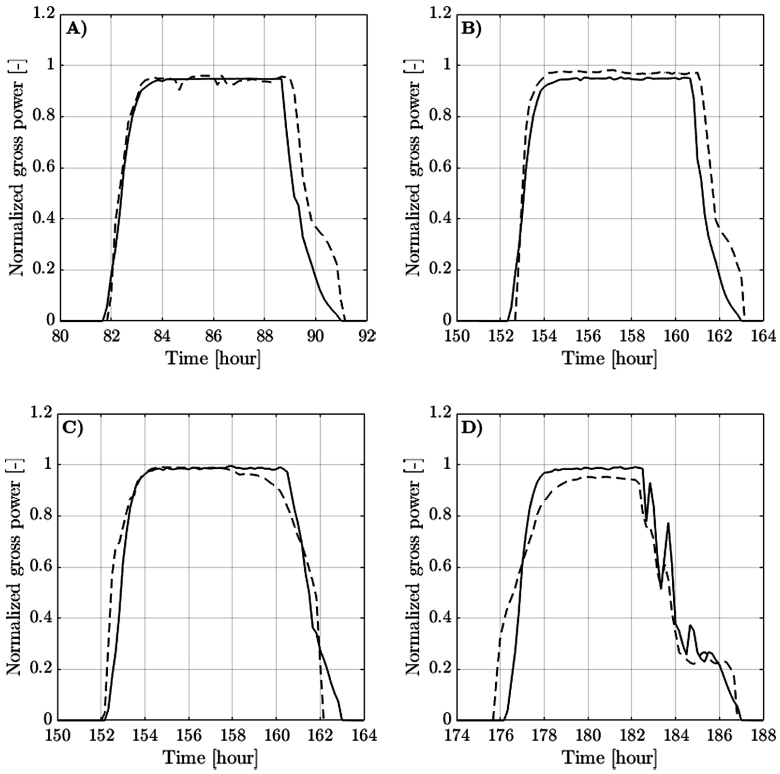

Fig. 9. Close-ups on the transient daily validation results for the winter and spring data resulting in lowest (A, C) and highest deviations (B, D), respectively. The solid and dotted lines represent the result of the model and operational data, respectively.

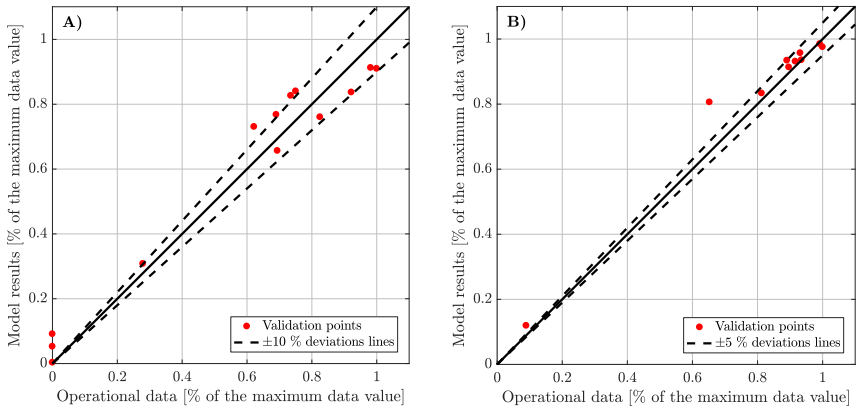

Fig. 10. Comparison of the model results in terms of daily electric energy production for the days available in the data sets; (A) February, (B) May.

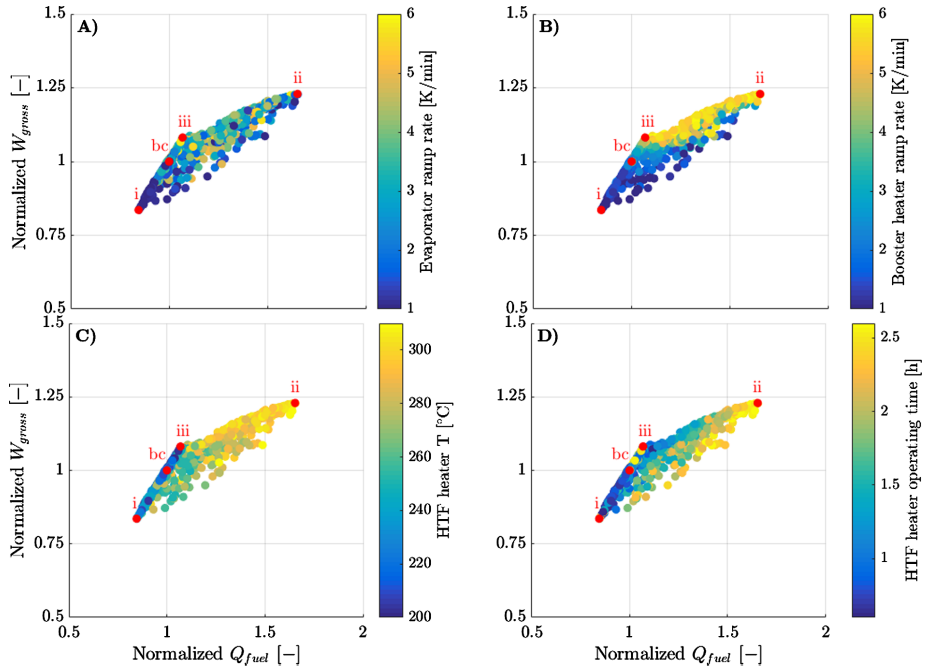

Fig. 11. Optimization results for the winter case considering the different decision variables. Values normalized towards the base case results. (A) Evaporator start-up rate constraints. (B) Booster heater start-up rate. (C) HTF heat Temperature. (D) HTF heater operating time.

In general, the results shown in Fig. 11 demonstrate that it is not possible to define a single optimal point for the start-up constraints both for the evaporator and the booster heater. However, it is possible to identify a range values maximizing the performance of the plant. For the evaporator, a range between 2.5 and 4.5 K/min can be selected, including 47% of the points in Fig. 11, and an optimal value of 5.7 K/min is obtained in order to have a high electricity production without at the same time increasing significantly the fuel consumption. In case (iii), having a sufficiently high start-up constraint both for the evaporator and the super-heater allows for setting the temperature of the HTF heater to a low value of 200 °C, minimizing significantly the fuel consumption. Case (ii) shows that in order to maximize the electricity production, not only it is necessary to have a higher set point for the HTF heater temperature (with the maximum operating time), but also it is required to have higher start-up constraints. This mainly relates to the operating choices, which would allow for more electric production by increasing significantly the fuel consumption. Table 8 and Fig. 11 also indicate that the base case (bc) has a slightly higher

Table 8
winter case optimization results.

Cases	EVA v [K/min]	BH v [K/min]	HTFH time [h]	HTFH T [°C]	Normalized W_{gross} [–]	Normalized Q_{fuel} [–]
bc	1	4	2.5	310	1	1
i	1	1	1.58	238	0.836	0.845
ii	4.4	5.2	2.6	310	1.229	1.654
iii	5.7	5.6	2.4	200	1.077	1.067

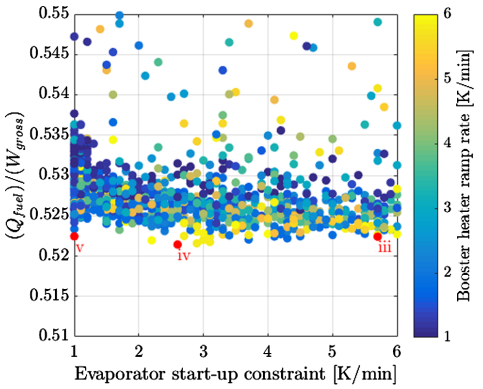

Fig. 12. Analysis of evaporator constraints on the Fuel/Electricity ratio – close-up on the optimal ratio Q_{fuel}/W_{gross}.

Table 9
Optimal efficiency points comparison.

Cases	EVA v [K/min]	BH v [K/min]	HTFH time [h]	HTFH T [°C]	Normalized W_{gross} [–]	Normalized Q_{fuel} [–]
iii	5.7	5.6	2.43	200	1.077	1.067
iv	2.6	6.0	2.12	220	1.082	1.069
v	1	1.8	0.9	242	0.932	0.921

fuel/electricity ratio than the optimal cases (i.e. cases close to point (iii)). By employing the start-up strategy depicted in case (iii) it is possible to lower the fuel/electricity ratio by 1.5% and increase the electricity production by 7.7%, compared with the base case.

These results indicate that it is not always necessary to have a SGS designed with high thermo-mechanical constraints. However, having such possibility can further increase the operational flexibility of the power plant. In this regard an analysis of the fuel efficient solution is performed. Fig. 12 illustrates a close-up on case (iii), showing the fuel/electricity ratio as a function of the evaporator heating rate constraint. On the z-axis color bar the booster heater heating rate constraints is shown. Table 9 summarizes the decision variables and objective functions of case (iii) and case (iv) and (v).

These cases give very similar results, but employ different operating strategies. The results shown in Table 9 and Fig. 12 suggest that it is possible to obtain a slightly higher (0.45%) gross electricity production at the cost of increasing (by 0.22%) the fuel consumption. However in this case, even though lower constraints on the evaporator might be obtained, it would be required to increase the set-point temperature of the HTFH and increasing the constraint of the booster heater. It is then preferable to choose option (iii), as the heater would only be used to pre-heat the oil to a maximum temperature of 200 °C. In case it is not possible to employ a steam generator, which allows for such constraints as its design might not allow for it, it is still possible to operate of the power plant in the optimal region at the cost of employing the HTF heater for more time and at a higher temperature. In terms of fuel to electricity ratio, a similar result can be obtained, see case (v), which represents a limit case for a very slow evaporator in terms of heating rates. However, if the heating rates of the evaporator are constrained to the lower limit, in order to have a similar fuel to electricity ratio (0.522) a much lower (−13.5%) electric energy production is achieved.

The results of the multi-objective optimization for the spring season are summarized in Fig. 13; the aforementioned four cases are also indicated in the figure. The base case is again below the Pareto front, meaning a non-optimal operating point. The detailed results of the different cases are presented in Table 10.

In the spring case, higher optimal values (towards the upper boundary of the constraints) are obtained for the evaporator heating rates, especially for case (iii). As the heater is operated at a lower temperature, it is necessary to increase the start-up speed of the steam generator. Compared to the base case (bc), in case (iii), by increasing the fuel consumption (+5.6%) it is possible to increase the electricity production by 6.2%, decreasing the fuel to energy ratio. The results indicate that if the fuel consumption is set as a constraint, a higher electricity production (+1.9%) can be achieved by increasing the heating rates to the maximum limits and at the same time decreasing the HTF heater utilization.

One of the main differences between Fig. 11 and Fig. 13 is the narrower range of solutions for the spring case. This can be directly linked to the lower fluctuations in the DNI and therefore a lower impact of the constraints on the electricity production, explaining why a lower value of the maximum heating rate constraint is obtained for case (ii). This would mean that having components designed for higher heating rates would enable a larger degree of flexibility in operating the power plant. In conclusion, the results suggest that there are no clear range of optimal values for the heating rates of the evaporator and booster heater. However, by being able to operate them at a faster rate it is possible to reduce the operating time of the HTF heater and maximize the electricity to fuel ratio.

4. Conclusions

A detailed model was used to find the optimal start-up operational strategy of a gas-boosted parabolic trough power plant. The model was developed in DYESOPT – a techno-economic tool for dynamic performance evaluation of power plants. The power block part of the model was developed accounting for the heating rate constraints of the steam generator system, booster heater and the steam turbine start-up control strategy. The model was validated both at steady-state and dynamic operating conditions, and subsequently used to optimize the start-up strategy by minimizing the fuel consumption and maximizing the electric energy production by means of a genetic algorithm based multi-objective optimizer. Both the validation and optimization were performed for two different time series corresponding to a winter and a spring case, respectively.

The results of the validation indicate that the model is able to predict with a reasonable accuracy the behavior of a gas-boosted parabolic trough solar power plant, both at steady state and dynamic operating conditions. The validation at steady-state condition shows a maximum relative error of −6.7% for the SGS HTF mass flow rate and −5.1% for the total electric parasitic consumption. For dynamic operating conditions, the validation results in a maximum NRMSE of +13.5% for the solar field HTF mass flow rate, 11.8% on gross power rise time and a maximum integral relative error of +4.3% for gross electric energy production in the case of the spring case. Considering the daily electric energy production, the validation indicates that 85% of the values are within a ± 10% confidence range.

The result of the multi-objective optimization indicates that it is not possible to define a range of optimal heating rates for evaporator

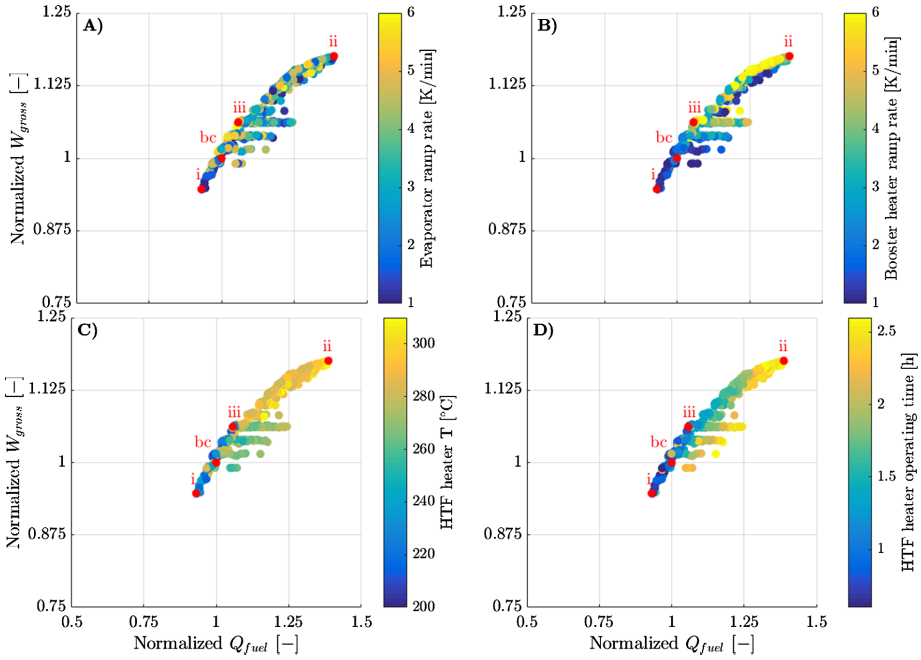

Fig. 13. Optimization results for the spring case considering the different decision variables. Values normalized towards the base case results. (A) Evaporator start-up rate constraints. (B) Booster heater start-up rate. (C) HTF heat temperature. (D) HTF heater operating time.

Table 10
spring case optimization results.

Cases	EVA v [K/min]	BH v [K/min]	HTFH time [h]	HTFH T [°C]	Normalized W_{gross} [−]	Normalized Q_{fuel} [−]
bc	1.00	1.00	2.5	310.00	1	1
i	1	1	0.62	263	0.947	0.930
ii	4.3	4.3	1.83	281	1.134	1.211
iii	6	6	0.78	290	1.062	1.057

constraints. However, different optimal start-up strategies can be identified. If minimum fuel consumption is desirable, the heating rates would result optimal around the lower threshold of 1 K/min together with low utilization of the heat transfer fluid heater. An opposite conclusion can be drawn if maximum electric production is desirable, resulting in a higher utilization of the heat transfer fluid heater both in terms of higher set point temperature and in time of activation. If however the operating strategy is to maximize the plant performance with regards to the electricity production to fuel consumption ratio, higher evaporator heating rates are desirable, namely, 5.7 K/min and 6 K/min for the winter and spring cases, respectively. These values are representative for steam generators that are commercially available. As a general conclusion, it can be stated that even though an optimal value for the operation of the power plant can be lower than the maximum constraints stated by the manufacturer, it may be desirable to design the evaporator for higher constraints, enabling more flexibility regarding operating strategies. It is therefore clear that it is critical to take into consideration the heating rates constraints when finding the optimal start-up strategies of CSP plants.

References

Aalborg CSP, 2015. Aalborg CSP Steam Generator. URL http://www.aalborgcsp.com/quickmenu/brochures/ (accessed 8.3.17).

Al-Hanaei, S., Al-Shomali, S., Abutayeh, M., 2016. Performance model of shams I solar power plant. Heat Transf. Eng. 37, 1445–1454. https://doi.org/10.1080/01457632.2016.1142312.

Almasabi, A., Alobaidli, A., Zhang, T.J., 2015. Transient characterization of multiple parabolic trough collector loops in a 100 MW CSP plant for solar energy harvesting. Energy Procedia 24–33. https://doi.org/10.1016/j.egypro.2015.03.004.

Alobaidli, A., Sanz, B., Behnke, K., Witt, T., Viereck, D., Schwarz, M.A., 2017. Shams 1 – Design and operational experiences of the 100MW – 540°C CSP plant in Abu Dhabi. AIP Conf. Proc. 1–10. https://doi.org/10.1063/1.4984325.

ASHRAE, 2000. Ashrae handbook HVAC Systems and Equipment, I-P Editio. ed. Tullie Circle, N.E., Atlanta, GA.

Basaran, I., 2015. A comprehensive study of the imposed limitations on concentrating solar power plant start-up speeds. MSc Thesis. Royal Institute of Technology (KTH), Stockholm.

Bergman, T., Lavine, A., Incropera, F., Dewitt, D., 2011. Fundamentals of Heat and Mass Transfer, 7th ed. John Wiley and sons.

Biencinto, M., González, L., Valenzuela, L., 2016. A quasi-dynamic simulation model for direct steam generation in parabolic troughs using TRNSYS. Appl. Energy 161, 133–142. https://doi.org/10.1016/j.apenergy.2015.10.001.

Biencinto, M., González, L., Zarza, E., Díez, L.E., Muñoz-antón, J., 2014. Performance model and annual yield comparison of parabolic-trough solar thermal power plants with either nitrogen or synthetic oil as heat transfer fluid. Energy Convers. Manag. 87, 238–249. https://doi.org/10.1016/j.enconman.2014.07.017.

Blair, N., Mehos, M., Christensen, C., Cameron, C., 2008. Modeling photovoltaic and concentrating solar power trough performance, cost, and financing with the solar advisor model. SOLAR 2008 - American Solar Energy Society (ASES) 1–7.

Blanco, D., Luis, A., Garcı, I.L., 2011. Performance model for parabolic trough solar thermal power plants with thermal storage : comparison to operating plant data. Sol. Energy 85, 2443–2460. https://doi.org/10.1016/j.solener.2011.07.002.

Bonilla, J., Jose, L., 2012. Parabolic-trough solar thermal power plant simulation scheme, multi-objective genetic algorithm calibration and validation. Sol. Energy 86, 531–540. https://doi.org/10.1016/j.solener.2011.10.025.

Boukelia, T.E., Arslan, O., Mecibah, M.S., 2017. Potential assessment of a parabolic trough solar thermal power plant considering hourly analysis: ANN-based approach. Renew. Energy 105, 324–333. https://doi.org/10.1016/j.renene.2016.12.081.

Boukelia, T.E., Mecibah, M.S., Kumar, B.N., Reddy, K.S., 2015. Investigation of solar

parabolic trough power plants with and without integrated TES (thermal energy storage) and FBS (fuel backup system) using thermic oil and solar salt. Energy 88, 292–303. https://doi.org/10.1016/j.energy.2015.05.038.
CEN, 2012. Water-tube boilers and auxiliary installations – Part 3: Design and calculation for pressure parts of the boiler. Brussels.
Dersch, J., Schwarzbözl, P., Richert, T., 2011. Annual yield analysis of solar tower power plants with GREENIUS. J. Sol. Energy Eng. 133, 031017. https://doi.org/10.1115/1.4004355.
DLR, 2006. A TRNSYS Model Library for Solar Thermal Electric Components (STEC), Reference manual.
Dudley, V., 1994. SEGS LS-2 Solar Collector. Test Results. Sandia National Laboratories, Albuquerque, New Mexico.
Dzierwa, P., Taler, D., Trojan, M., Taler, J., 2016. Evaporator heating with optimum fluid temperature changes. Procedia Eng. 157, 29–37. https://doi.org/10.1016/j.proeng.2016.08.334.
Dzierwa, P., Taler, J., 2014. Optimum heating of pressure vessels with holes. J. Press. Vessel Technol. 137, 011202. https://doi.org/10.1115/1.4027584.
Estela, Greenpeace, Solarpaces, 2016. Solar Thermal Electricity – Global Outlook 2016.
Ferruzza, D., Topel, M., Basaran, I., Laumert, B., Haglind, F., 2017. Start-up performance of parabolic trough concentrating solar power plants. AIP Conf. Proc. 1850, 1–9. https://doi.org/10.1063/1.4984542.
Ferruzza, D., Topel, M., Laumert, B., Haglind, F., 2018. Impact of steam generator start-up limitations on the performance of a parabolic trough solar power plant. Sol. Energy 169. https://doi.org/10.1016/j.solener.2018.05.010.
Gilman, P., Laboratory, N.R.E., Laboratories, S.N., 2008. Solar advisor model user guide for version 2.0. Technical Report.
González-Gómez, P.A., Petrakopoulou, F., Briongos, J.V., Santana, D., 2017a. Cost-based design optimization of the heat exchangers in a parabolic trough power plant. Energy 123, 314–325. https://doi.org/10.1016/j.energy.2017.02.002.
González-Gómez, P.Á., Petrakopoulou, F., Briongos, J.V., Santana, D., 2017b. Steam generator design for solar towers using solar salt as heat transfer fluid. AIP Conf. Proc. 1–8. https://doi.org/10.1063/1.4984363.
Groupe Reaction Inc., 2014. CSP Parabolic Trough Report: Cost, Performance and Key Trends. London.
Guédez, R., 2016. A Techno-Economic Framework for the Analysis of Concentrating Solar Power Plants with Storage. Ph.D. Thesis. Royal Institute of Technology, (KTH), Stockholm.
International Energy Agency, 2014. Technology Roadmap, Solar Thermal Electricity. Paris.
Khetarpal, D., 2016. World Energy Resources: Solar 2016, World Energy Council.
Leyland, G.B., Favrat, D., 2002. Multi-objective optimization applied to industrial energy problems. Ph.D. Thesis. Mech. Eng. École Polytechnique Féderale de Lausanne, (EPFL), Lausanne. doi: 10.5075/epfl-thesis-2572.
Li, L., Li, Y., Sun, J., 2017a. Prospective fully-coupled multi-level analytical methodology for concentrated solar power plants: applications. Appl. Therm. Eng. 118, 159–170. https://doi.org/10.1016/j.applthermaleng.2017.02.094.
Li, L., Sun, J., Li, Y., 2017b. Prospective fully-coupled multi-level analytical methodology for concentrated solar power plants: general modelling. Appl. Therm. Eng. 118, 171–187. https://doi.org/10.1016/j.applthermaleng.2017.02.086.
Li, L., Sun, J., Li, Y., 2017c. Thermal load and bending analysis of heat collection element of direct-steam-generation parabolic-trough solar power plant. Appl. Therm. Eng. 127, 1530–1542. https://doi.org/10.1016/j.applthermaleng.2017.08.129.
Lippke, F., 1995. Simulation of the Part-Load Behavior of a 30 Mwe SEGS Plant. Report. Sandia National Laboratories, Albuquerque, New Mexico.
Mancini, T.R., Gary, J.A., Kolb, G.J., Ho, C.K., 2011. Power Tower Technology Roadmap and cost reduction plan. Sandia Report. Sandia National Laboratories. Albuquerque, New Mexico. doi: 10.2172/1011644.
Moya, E.Z., 2012. Parabolic-trough concentrating solar power (CSP) systems. In: Concentrating Solar Power Technology. Woodhead publishing, Cambridge, UK. pp. 197–239. doi: 10.1533/9780857096173.2.197.
Price, H., 2003. A Parabolic Trough Solar Power Plant Simulation Model. In: ASME. International Solar Energy Conference. pp. 665–673. doi: 10.1115/ISEC2003-44241.
Schenk, H., Dersch, J., Hirsch, T., Polklas, T., 2015. Transient Simulation of the Power Block in a Parabolic Trough Power Plant. In: Proc. 11 Int. Model. Conf. 605–614. doi: 10.3384/ecp15118605.
Solutia, 2014. Therminol VP-1, Solutia.
Spelling, J., 2013. Hybrid Solar Gas-Turbine Power Plants – A Thermoeconomic Analysis. PhD Thesis. Royal Institute of Technology (KTH), Stockholm.
Spelling, J., Jöcker, M., Martin, A., 2012. Annual performance improvement for solar steam turbines through the use of temperature-maintaining modifications. Sol. Energy 86, 496–504. https://doi.org/10.1016/j.solener.2011.10.023.
STEAG, 2012. Ebsilon professional [WWW Document]. URL https://www.steag-systemtechnologies.com/sst-home.html (accessed 12.1.17).
Stoddard, M.C., Faas, S.E., Chiang, C.J., Dirks, J.a., 1987. SOLERGY – A computer code for calculating the annual energy from central receiver power plants. Sandia Report. Sandia National Laboratories, Albuquerque, New Mexico.
Sun, J., Liu, Q., Hong, H., 2015. Numerical study of parabolic-trough direct steam generation loop in recirculation mode: characteristics, performance and general operation strategy. Energy Convers. Manag. 96, 287–302. https://doi.org/10.1016/j.enconman.2015.02.080.
Taler, J., Dzierwa, P., Taler, D., Harchut, P., 2015a. Optimization of the boiler start-up taking into account thermal stresses. Energy 92, 160–170. https://doi.org/10.1016/j.energy.2015.03.095.
Taler, J., Weglowski, B., Taler, D., Sobota, T., Dzierwa, P., Trojan, M., Madejski, P., Pilarczyk, M., 2015b. Determination of start-up curves for a boiler with natural circulation based on the analysis of stress distribution in critical pressure components. Energy 92, 153–159. https://doi.org/10.1016/j.energy.2015.03.086.
Topel, M., Guédez, R., Laumert, B., 2015a. Impact of increasing steam turbine flexibility on the annual performance of a direct steam generation tower power plant. Energy Procedia 69, 1171–1180. https://doi.org/10.1016/j.egypro.2015.03.196.
Topel, M., Jöcker, M., Paul, S., Laumert, B., 2015b. Differential expansion sensitivity studies during steam turbine startup. J. Eng. Gas Turbines Power 138, 062102. https://doi.org/10.1115/1.4031643.
Topel, M., Nilsson, Å., Jöcker, M., Laumert, B., 2017. Investigation into the thermal limitations of steam turbines during start-up operation. J. Eng. Gas Turbines Power 140, 012603. https://doi.org/10.1115/1.4037664.
University of Wisconsin Madison. Solar Energy Laboratory, 1975. TRNSYS, a transient simulation program. Madison, Wis.: The Laboratory, 1975.
Vogel, T., Oeljeklaus, G., Görner, K., Dersch, J., Polklas, T., 2014. Hybridization of parabolic trough power plants with natural gas. Energy Procedia 49, 1238–1247. https://doi.org/10.1016/j.egypro.2014.03.133.

Applied Energy 236 (2019) 793–803

Contents lists available at ScienceDirect

Applied Energy

journal homepage: www.elsevier.com/locate/apenergy

Design of header and coil steam generators for concentrating solar power applications accounting for low-cycle fatigue requirements

Davide Ferruzza*, Martin Ryhl Kærn, Fredrik Haglind

Department of Mechanical Engineering, Technical University of Denmark, 2800 Kongens Lyngby, Denmark

HIGHLIGHTS

- The heating rates of steam generators are limited by thermo-mechanical constraints.
- Traditionally the design of steam generators does not account for low-cycle fatigue.
- The method accounting for low cycle fatigue constraints is presented.
- The results are compared to those obtained without heating rate constraints.
- Heating rates constraints considerably affect the optimal design results.

ARTICLE INFO

Keywords:
Concentrating solar power
Parabolic trough power plants
Steam generator
Heat exchanger design
Heating rates

ABSTRACT

Concentrating solar power plants are experiencing an increasing share in the renewable energy generation market. Among them, parabolic trough plants are the most commercially mature technology. These plants still experience many challenges, one of which is the cyclic daily start-up and shut-down procedures. These pose new challenges to industrially mature components like the steam generator system, as frequent load changes might decrease their lifetime considerably due to cyclic thermo-mechanical stress loads. In this context, the header and coil design is a promising configuration to minimize the stresses.

This paper presents a method to design the header and coil heat exchangers of the steam generator, taking into account low-cycle fatigue requirements, by defining minimum allowable heating rates for the evaporator and superheater. Optimal designs were obtained by minimizing the total water pressure drops and purchase equipment costs. A comparison with a sizing routine without accounting for low-cycle fatigue constraints was also conducted.

The model was validated against the component data of a 55 MWe power plant, with a maximum deviation on the total area estimation of +2.5%. The results suggest that including the heating rate constraints in the design routine substantially affects the optimal design configuration, with a 41% cost increase for a 1 bar pressure drop. The optimal design for maximizing the lifetime of the components uses tube outer diameters of 38 mm and 50 mm and a low number of tubes per layer (4–10) for the superheater.

1. Introduction

Today's growing attention towards renewable energy sources is posing an increasing demand for flexibility towards electricity generation. Concentrating solar power (CSP) plants are experiencing a developing interest in this context. Specifically, the possibility of integrating CSP technology with relatively cheap ways of storing thermal energy allows decoupling the electricity output from the solar input, making these plants suitable for alternating electricity grid loads [1]. Even though an interesting technology, CSP plants are still not fully competitive with respect to fossil-fuel based technologies. From a technical perspective, the fluctuating and stochastic nature of solar radiation causes operating challenges such as frequent variations in load and daily start-up and shut-down procedures. A way to overcome these challenges is to improve the operating performance by maximizing the flexibility of the components given fluctuating loads. By doing so it is possible to utilize solar irradiation as effectively as possible, thereby maximizing the electrical energy production and profitability [2]. On the other hand, in order to preserve the lifetime of certain components, the maximum gradient of temperature (heating

* Corresponding author.
E-mail address: daferr@mek.dtu.dk (D. Ferruzza).

https://doi.org/10.1016/j.apenergy.2018.12.030
Received 10 July 2018; Received in revised form 16 November 2018; Accepted 6 December 2018
Available online 13 December 2018

Nomenclature

Abbreviations

BPVC	boiler pressure vessel code
CSP	concentrating solar power
D	deaerator
ECO	economizer
EVA	evaporator
HP	high pressure
HPI	historical price index
HTRI	Heat Transfer Research, Inc.
LP	low pressure
PTPP	parabolic trough power plant
RH	re-heater
SGS	steam generator system
SH	superheater
ST	steam Turbine
TEMA	tubular exchangers manufacturers association

Subscripts

b	bend
dc	downcomer
dp	driving pressure
e	parallel to the economizer
fm	friction and momentum
hx	heat exchanger
i	inside
m	mechanical
o	outside
r	riser
s	parallel to the superheater
s	shell
T	thermal
tl	tube layer
txl	tube for each layer

Symbols

α	stress concentration factor [–]
β	thermal expansion coefficient [K^{-1}]
λ	thermal conductivity [W/(mK)]
ν	Poisson ratio [–]
ω	outer to inner diameter ratio [–]
Φ_w	non-dimensional geometrical coefficient [–]
ρ	density [kg/m^3]
σ	stress [Pa]
θ	tube coil angle of bend [rad]
f	heat exchanger specific cost front head correction factor [–]
f_D	Darcy's friction factor [–]
p_{OD}	heat exchanger specific cost outer diameter correction factor [–]
r	heat exchanger specific cost rear head correction factor [–]
S_l	longitudinal pitch [m]
S_t	transversal pitch [m]
ν_T	heating rate [K/min]
A	area [m^2]
b	heat exchanger specific cost [USD/m^2]
c	heat exchanger specific cost correction factor [–]
E	Young's modulus [Pa]
F	LMTD correction factor [–]
h	heat transfer coefficient [W/m^2 K]
ID	internal diameter [m]
L	length [m]
OD	outer diameter [m]
p	pressure [bar]
PEC	purchase equipment cost [USD]
S	maximum allowable stress [Pa]
T	temperature [°C]
t	thickness [m]
U	overall heat transfer coefficient [W/m^2 K]
u	velocity [m/s]
y	safety coefficient [–]

rate) is limited by thermo-mechanical constraints.

Parabolic trough power plants (PTPP) represent the most technically and economically mature technology among CSP plants. They account for around 80% of both the currently installed and planned to be constructed power plants [3–5]. In such power plants, the conventional fossil-fuel fired boiler is replaced by a series of parabolic mirror lenses to concentrate direct beam solar radiation onto the receiver tubes to produce useful high temperature heat. This can be used to produce electricity by a Rankine cycle. The main link between the solar field and the power block is the steam generator system (SGS). It consists of a train of heat exchangers which transfer the useful high temperature heat from a heat transfer fluid (HTF) to the water coming from the condensing line of the Rankine cycle. The temperature of the liquid water is raised until it reaches superheated steam conditions at the inlet of the turbine [4].

Generally the SGS, together with the steam turbines, poses limitations with regards to the rate of the power block start-up [6]. High temperature gradients induce high thermal stresses and therefore limit the lifetime of such components. Specifically the maximum heating rates at which the SGS can experience a temperature increase is limited by the thermo-mechanical stresses on the thick-walled components and junctions, such as, the steam drum, superheater headers and T or Y junctions in the steam pipelines [7–9]. The main limiting component is usually the evaporator steam drum, which is designed as a high pressure vessel with a large diameter, hence consisting of thick walls. Regarding the most conventional single phase heat exchangers, the heating rates are limited by the stresses in the thick tube plates [10]. The maximum heating rates are calculated based on low-cycle fatigue (LCF) theories, by minimizing the resulting stress from a cyclic load and keeping it below a safety threshold to guarantee the required lifetime [11]. It is of common practice in the industry to do so by using the European norm EN 12952-3, which illustrates all the steps to calculate minimum and maximum allowable heating rates [12].

Many CSP plants currently in operation, have SGSs which were designed as conventional heat exchangers, not optimized for transient operation [13]. One of the possible configurations that can be used to overcome such problems is the header and coil design. In contrast to what happens in kettle reboiler type evaporators or TEMA (Tubular exchangers manufacturers association) heat exchangers, the coil type heat exchanger does not have thick tube plates. The heat transfer fluid (HTF) flows are distributed to the tube bank via a circular manifold (header). The round shape of the header results in lower thickness requirements for pressure resistance, and therefore, there are low thermal stresses which are proportional to the square of the thickness [14]. A similar reasoning can be applied to the single phase heat exchangers, such as the economizer (ECO), re-heaters (RH) and superheaters (SH). Also in this case the typical TEMA F or H heat exchangers are characterized by thick tube plates which reduce their transient response.

There is an increasing interest for the design and analysis of steam generator systems. For instance, Mercati et al. [15] developed a method to design a SGS for a system which aimed at producing both superheated steam and hydrogen. The authors also evaluated the impact of

the steam generator performance on the energy conversion system behavior. Many of the previous works on steam generator investigations are related to nuclear applications. For instance, Liu et al. [16] and Chen et al. [17] investigated a natural circulation SGS for pressurized water reactors by means of optimization algorithms. Recently, due the increasing interest for renewable energy sources, there has been an increasing focus on the design of steam generator systems for CSP applications. For instance, an exergonomic analysis was carried out by Gomez-Hernandez et al. [18] to design SGSs for solar tower power plants. Similarly, Lin et al. [19] presented a design procedure and design guidelines for direct steam generation solar tower power plants. The focus towards CSP applications has meant also more interest in the transient performance of such components. The transient performance of SGSs was investigated by Gonzalez-Gomez et al. [20] for solar tower power plants and by Gonzalez-Gomez et al. [21] for PTPP applications, while Mertens et al. [22] compared the transient response during a fast start-up procedure between a natural circulation and a once-through steam generator. In general, the design of each of the SGS components is a key aspect when analysing the steam generator system.

The design of the heat exchangers used in the energy system is characterized by two steps, the heat transfer area estimation and pressure drop calculations coupled with a cost analysis. One of the most common methods to size the shell and tube heat exchangers is the Delaware method for shell-side calculations, which takes into account the different fluid flow paths in the complex shell geometry [23]. Another available method in literature is the Stream Analysis method, which is also implemented in the commercially available software HTRI (Heat Transfer Research, Inc.) [24]. However, if the shell geometry is not too complex, the method proposed by Kern [25] can be used to obtain a good approximation of the area requirements. Considering tube banks, the method summarized by Anarratore et al. [26] can be applied to modify the logarithmic mean temperature based on the tube configurations. Regarding the cost estimation, both simplified [27] and more detailed methods are available. Concerning the latter, Purohit [28] proposed a method to estimate the cost of the heat exchangers not only based on the area requirements, but also on many other factors such as operating pressure, tube configurations and shell sizes.

In literature, different sizing methodologies are applied to different cases. For instance, Duran et al. [29] applied a genetic algorithm to optimize the geometric design of heat recovery steam generators (HRSG). However, the focus was only on the geometrical design and not on the economic analysis. A similar approach is presented by Franco et al. [30], and in this case a two-step optimization approach is presented, by firstly minimizing pressure drops and secondly minimizing the dimension of the heat exchangers. As for the associated cost, for instance, Wildi-Tremblay and Gosselin [31] used a genetic algorithm to minimize both investment and operational costs. Gonzalez-Gomez et al. [32] applied a cost-based optimization methodology to find a trade-off between levelized cost of electricity and investment costs for the SGS specifically for parabolic trough power plant applications.

A general conclusion is that many design methodologies are available and applied in literature, but none so far have taken into consideration the LCF limitations during the design phase. In previous works, the LCF constraints were evaluated as a performance check afterwards by calculating what is the maximum allowable heating rate for a specific given design. For instance, Pelagotti et al. [14] analyzed the lifetime of the header and coil steam generator for a given design. A more detailed approach was performed by Gonzalez-Gomez et al. [10] who estimated the lifetime of the heat exchangers according to the ASME boiler pressure vessel code (BPVC) div. II for a given geometry and assumed heating rates. However, as concluded in a previous work by the authors [6], it is essential to include the heating rates in the design procedure. Increasing the evaporator heating rates from 3 K/min to 7–10 K/min leads to an increase in the electricity production between 1.5% and 5% for a peak-load case.

The objective of this paper is to present a method to design the SGS

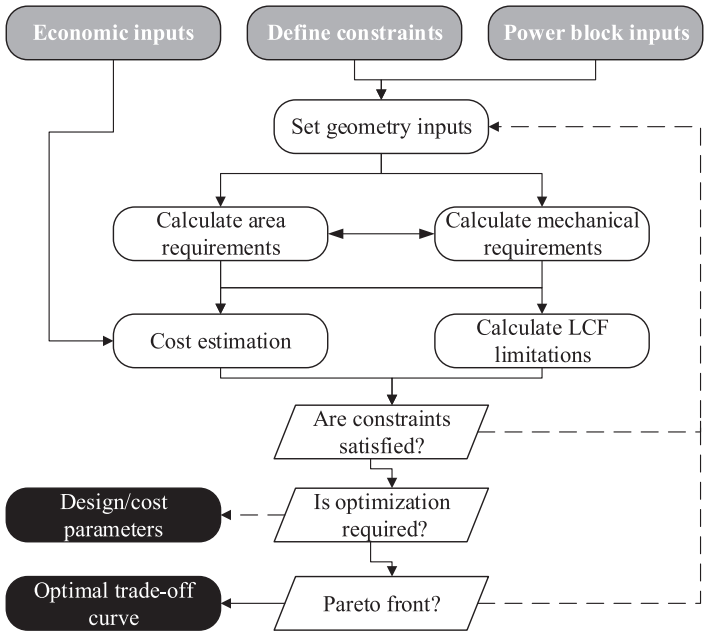

Fig. 1. SGS design method workflow. Solid lines represent a YES flow while dashed lines represent a NO flow.

taking into account LCF constraints for concentrating solar power applications. The significance of the results is demonstrated by comparing the results with those of a design which was obtained without considering the LCF constraints.

The thermodynamic and economic calculations were coupled in a multi-objective optimization framework aiming at minimizing both pressure drops and purchase equipment costs (PEC) and considering LCF constraints as obtained from Ref. [6]. The header and coil design was chosen as it is a promising solution for CSP applications. The numerical models were validated with data provided by a manufacturer of a 55 MWe PTPP without storage. In order to show the relevance for a practical application, the proposed design method was applied to the requirements of the mentioned power plant. This is the first paper presenting a method for incorporating the low-cycle fatigue requirements in the design procedure of steam generator systems.

Section 2 below presents the methods used to calculate the required heat transfer parameters and pressure drops as well as the cost estimation and LCF heating rate calculations. Section 2 also contains the multi-objective optimization method and required constraints in order to obtain feasible solutions. Section 3 presents and discusses these findings of the validation and multi-objective optimization performed for two different cases in order to compare the results with the results obtained for the case without accounting for LCF constraints. Section 4 outlines the conclusions and final remarks.

2. Methods

Fig. 1 illustrates the main steps that are required for the design routine. The grey and black boxes represent the inputs and outputs of the model, respectively.

In order to perform the SGS design, power block data and operating constraints are the required inputs, together with price data if economic calculations are to be done. The results of the design serve for the LCF analysis according to the norm EN12952-3 [12]. If the constraints are not met, the geometry inputs are changed until the requirements are satisfied.

If the geometrical configuration is already known, the tool can proceed with the design routine. Otherwise, the tool allows for coupling with a multi-objective optimizer available in the Matlab toolbox [33]. At the start of the optimization, it is possible to set conflicting objectives with regards to whether to maximize or minimize their quantities. Both design parameters and operation parameters can be set to allow for variations within the limits chosen for the study. The algorithm performs then as many iterations as needed to finalize the optimization and obtain an optimal trade-off curve or Pareto front [34].

2.1. Case study

The power plant of the case study is based on a PTPP similar to the Andasol 1, located near Sevilla [35]. The main difference is the absence of the thermal energy storage and the arrangement of the re-heaters, as in this case the RH is split into two heat exchangers parallel to the economizer (RHe) and the superheater (RHs). The twofold split of the re-heater allows for lower temperature gradients on the tubes, thus resulting in lower thermal stresses [36]. Fig. 2 illustrates a diagram of the reference power plant and the arrangement of the heat exchangers in the system.

The red lines represent the HTF (Therminol-VP1) loop, which is heated up by the parabolic trough (PT) mirrors and fed directly to the steam generator system. The blue line cycle represents a regenerative Rankine-reheat cycle with high pressure (HP) and low pressure (LP) steam turbines (ST), a condenser and a deaerator (D). The main inputs required for defining the boundary conditions of the SGS are summarized in Table 1.

The SGS consists of two parallel trains which comprise a SH, ECO, EVA and two RHs [32]. The heat transfer fluid flows on the shell-side in the single phase heat exchangers. In the evaporator the heat transfer fluid flows in the tube-side, while the heat transfer is characterized by pool boiling on the shell-side. The water flows in the tubes for all the other heat exchangers. The blue and red lines represent, respectively, the water and heat transfer fluid flows. The HTF flows through the SGS to supply the thermal energy to increase the temperature of the inlet subcooled water to the desired turbine inlet temperature. The low pressure steam, coming from the extraction, is heated up in the two re-heaters to the desired re-heat turbine inlet temperature.

To reduce both the dimensions of the HTF header and the EVA shell,

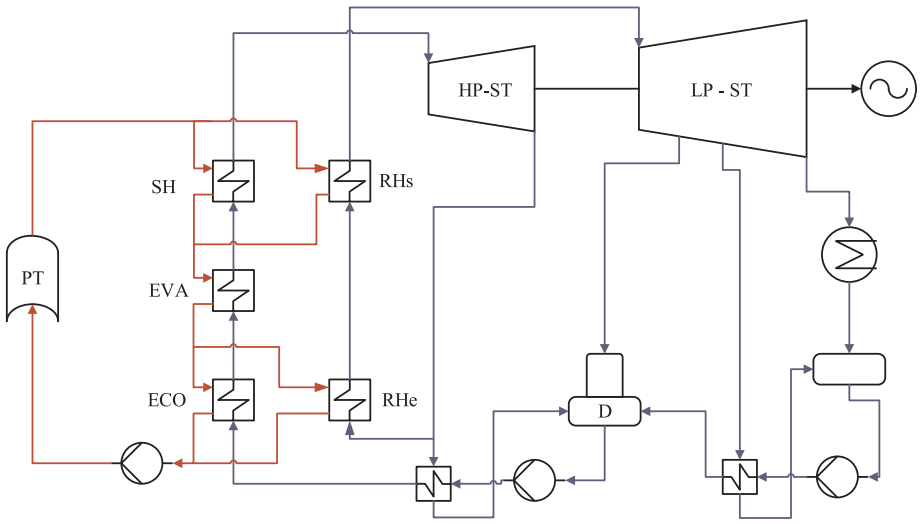

Fig. 2. Parabolic trough power plant layout.

Table 1
Power block boundary conditions.

Parameters	Units	Value
Turbine inlet temperature	[°C]	385.34
Turbine inlet pressure	[bar]	104
Reheat outlet temperature	[°C]	386.46
Inlet pressure at reheat	[bar]	20.25
Inlet temperature at reheat	[°C]	213
Feedwater temperature	[°C]	256.8
HTF inlet temperature	[°C]	393.3
HTF inlet pressure	[bar]	15
Heat load requirement	[MW]	166.2

the heat exchanger was split in two. The EVA is characterized by a natural circulation arrangement between the steam drum and the heat exchangers. Fig. 3 illustrates the geometrical configuration of the evaporator under consideration. Fig. 4 shows the single phase heat exchanger geometry, which was approximated as parallel tube banks as illustrated in Fig. 5, where S_l, S_t, N_{tl} represent the tube longitudinal and transversal pitch and the number of tube layers, respectively. The tubes are fixed in horizontal positions in order to avoid vibration and bending in the transversal direction.

2.2. Heat transfer and pressure drops in the heat exchangers

Once the heat duty of the heat exchangers and their boundary conditions are obtained, the mean logarithmic temperature difference (LMTD) is calculated according to Eq. (1) and depends on the inlet (i) and outlet (o) temperature (T) of the cold and hot streams. F is a correction factor which depends on the flow configuration. Anarratore et al. [26] suggested, however, that if the number of tube coils is higher than 6, the flow configuration can be assumed to be a counter-current; therefore F becomes 1. The area (A), defined in Eq. (3), is calculated by using the overall heat transfer coefficient (U) as defined in Eq. (2).

$$\Delta T_{LMTD} = F \cdot \frac{(T_{i,hot} - T_{o,cold}) - (T_{o,hot} - T_{i,cold})}{(\ln((T_{i,hot} - T_{o,cold})/(T_{o,hot} - T_{i,cold})))} \quad (1)$$

$$Q = U \cdot A \cdot \Delta T_{LMTD} \quad (2)$$

$$A_o = N_{tl} \cdot N_{txl} \, (pi \cdot OD \cdot L_{tube}) \quad (3)$$

$$\frac{1}{U_o} = \frac{r_o}{r_i \cdot h_i} + \frac{1}{h_o} + \frac{r_o \cdot ln\left(\frac{r_o}{r_i}\right)}{\lambda_w} \quad (4)$$

The area depends on the number of tubes for each layer (txl) and tube layers, as well as on the single tube length (L). The U value, as expressed in Eq. (4), depends on the heat transfer coefficients h of both shell and tube sides, the internal and the outer radius (r), as well as on the thermal resistance posed by the tubes which depends on the wall (w) thermal conductivity (λ). In the case of the single phase heat exchangers, the tube (water) and the shell (HTF) side heat transfer coefficient were calculated using the Gnielinski [37] and Zukauskas [38] correlations, respectively. In the case of the evaporator, the pool boiling heat transfer coefficient was determined using the Stephan-Abdelsalam correlation [39]. The convective effects on the evaporator water side heat transfer coefficient was considered negligible due to the low water velocities involved (lower than 0.1 m/s). This assumption is also supported by the fact that the heat transfer performance is governed primarily by the heat transfer coefficient on the oil side. Furthermore, the fouling factors were considered negligible. In fact, the manufacturer of such steam generator design guarantees no fouling [36].

Pressure drops on the shell-side were estimated according to the Zukauskas correlation, which takes into account the effective fluid area flow inside the tube layer and is dependent on the number of tube layers the fluid needs to cross [38].

The resulting tube pressure drop can be expressed as the sum of the friction loss on the equivalent length which also takes into account the bend radius and the resulting pressure drop due to the change of direction, normally expressed in terms of a bend-loss coefficient k_b. This coefficient depends on the curvature ratio and the bend angle and is obtained according to Idelchik et al. [40]. Eq. (5) presents the calculation of the pressure drop where ρ and u are the density and the velocity of the fluid, and θ and R_b are the angle and the radius of the bend. Lastly, f_D is the Darcy friction factor which was calculated according to the Colebrook equation for the turbulent regime and to the Poiseuille equation for the laminar regime [37].

$$\Delta P_f = \frac{1}{2} f_D \rho u^2 \left(\frac{\theta R_b + L_{tube}}{ID} \right) + \frac{1}{2} k_b \rho u^2 \quad (5)$$

The driving pressure of the natural circulation mechanism results from the difference in density between the two-phase mixture in the

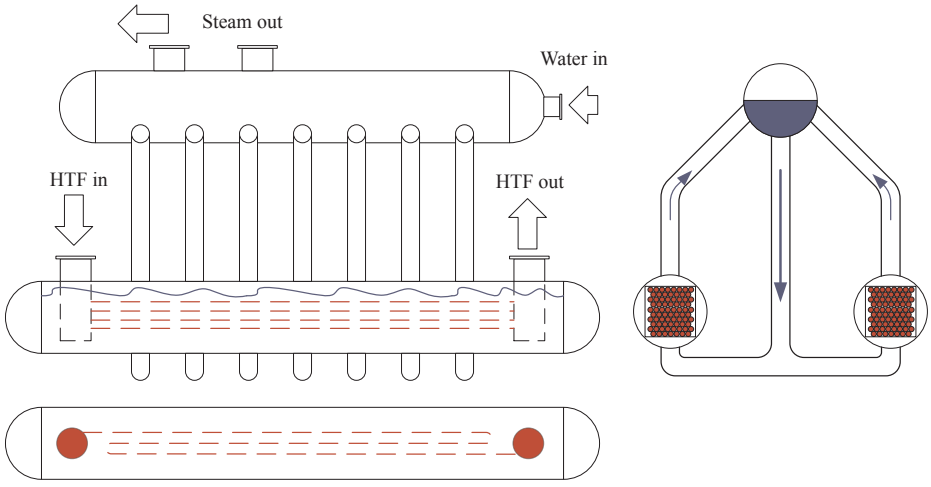

Fig. 3. Header and coil shell recirculation evaporator.

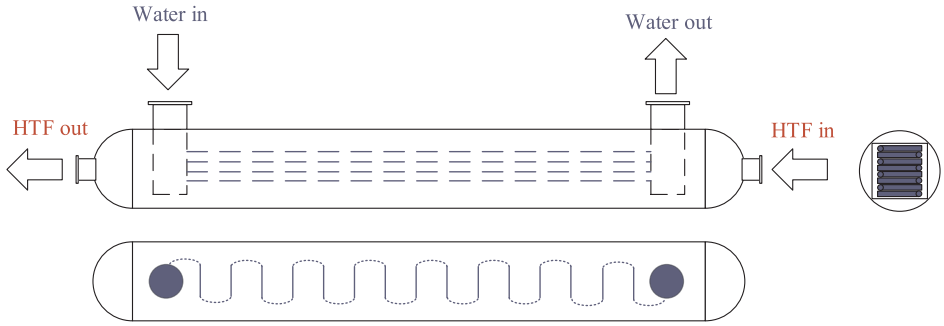

Fig. 4. Header and coil shell single phase heat exchanger geometry.

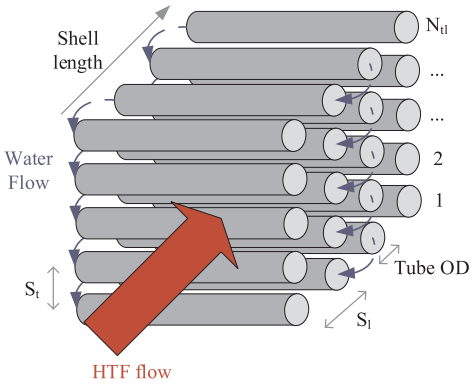

Fig. 5. Tube bundle geometry approximation.

riser and the downcomer tubes [41]. For a given circulation ratio (CR) the resulting tube height (H) is obtained when the driving pressure (dp) equals the frictional and momentum (fm) pressure losses in the natural circulation circuit (downcomer (dc), riser (r) and heat exchangers (hx)). This was calculated according to Eqs. (6) and (7). Each pressure drop term is calculated according to Anarratore et al. [42].

$$\Delta P_{dp} = g\rho_{dc}H_{dc} - g(\rho_{hx}H_{hx} + \rho_r H_r) \tag{6}$$

$$\Delta P_{fm} = \Delta P_{dc} + \Delta P_r + \Delta P_{hx} + \Delta P_{nozzles} + \Delta P_b \tag{7}$$

2.3. Mechanical and geometrical design

The ASME boiler pressure vessel code (BPVC) provides the norms and regulations for calculating the thickness of the shell, headers and tubes in the heat exchangers, which are made of carbon steel material [43].

The shell diameter of each heat exchanger depends on the geometry of the tube bundle, meaning the number of tube layers and the number of coils of the proposed design. In order to minimize the space required by the shell, the length of each coil was calculated to have a square geometry which can be placed inside the shell with a low space waste. Therefore, the internal diameter was determined based on the tube-side geometry, and subsequently the thickness of the shell was calculated according to the BPVC sec. VIII using Eq. (8). The thickness t is dependent on the maximum allowable stress (S) of the chosen material at design temperature, design pressure p (in barg) and a safety coefficient y. The equation takes into account a tolerance for allowable corrosion (C) which usually depends on the material and on the fluid as well as on the requirements of the power plant operator.

$$t_{Shell} = \frac{p \cdot ID/2}{S - (1 - y)p} + C \tag{8}$$

A similar approach was adapted for each pipe (like the headers and risers/downcomers) and tube that are included in the geometry of each heat exchanger. The header diameter was calculated in order to align each tube equidistantly in each layer of the tube bundle geometry. Then the thickness was calculated according to Eq. (9), which depends on the outer diameter (OD) of the pipes. Eq. (10) refers to the tube thickness calculation.

$$t_{Tubes} = \frac{p \cdot OD}{2S + p} + 0.005 \cdot OD + C \tag{9}$$

$$t_{Pipes} = \frac{p \cdot OD}{2S + 2y \cdot p} + C \tag{10}$$

In the case of the evaporator heat exchangers, the tube thickness was not calculated directly, as the highest pressure is on the shell and not on the tube side. For externally loaded tubes, the calculation procedure starts by assuming a tube length and thickness, followed by a calculation of the maximum allowable pressure. The iteration stops when this value is higher than or equal to the design pressure considered.

The steam drum volume depends on the operating pressure and on the steam load required by the evaporator. The steam volume chamber was determined according to charts that illustrate the minimum and maximum steam volumes as a function of the operating pressure according to Anarratore et al. [42]. These charts were digitized and the data were obtained using linear interpolation during the optimization. The volume was determined to ensure that the maximum vapor velocity that allows gravitational settling of entrained liquid is not exceeded [42]. Considering that usually the water level corresponds to the center line of the drum, the drum volume becomes twice as large as the required steam drum chamber. According to industrial experience, the internal drum diameter was set to a minimum value of 1.5 m in order to allow for the correct placement of the separating devices and space requirement for internal inspection.

2.4. Heating rate calculations

The maximum allowable heating rates (v_T) were determined according to the European standard EN 12952-3, in order to keep the resulting stress in the singularities (i.e. junction between downcomer and steam drum or header and tubes) below the allowable stress (σ_a) determined from a LCF diagram for a given number of cycles corresponding to the chosen lifetime of the component [12]. The norm can

be applied to both steam drum/downcomer [7] and header/tubes junctions [44,45]. Eq. (11) summarizes the concept and illustrates how the resulting total stress is a sum of the thermal stress and tensile stress. They depend on thermal and mechanical stress concentration factors, respectively (α), which were calculated according to the norm. E, β, and ν are the Young's modulus, thermal expansion coefficient and Poisson's ratio, respectively. The main non-dimensional parameter is Φ_w which depends on the outer to inner diameter ratio ω according to Eq. (12).

$$\left|\alpha_m(p-p_0)\frac{ID+t}{t}+\alpha_T\cdot c\cdot\rho\frac{E\cdot\beta}{1-\nu}\frac{v_T t^2}{\lambda}\Phi_w\right|\leqslant|\sigma_a| \tag{11}$$

$$\Phi_w=\frac{1}{8}\frac{(\omega^2-1)(3\omega^2-1)-4\omega^4\cdot ln\omega}{(\omega^2-1)(\omega-1)^2} \tag{12}$$

The norm provides the allowable rates at the corresponding minimum and maximum pressure p_1 and p_2 in the specified start-up cycle. Once the two values are determined, the heating rate can be calculated at each intermediate pressure by means of linear interpolation according to Eq. (13). In the case of two-phase conditions, the pressure p(t) becomes a function of the fluid temperature T_f; therefore, the equation was solved using a fourth-order Runge-Kutta method [46]. Otherwise, the pressure is a function of time and the equation can be directly solved [7]. The minimum and maximum heating rates do not, however, illustrate the overall start-up process as v_T changes during the start-up phase. In order to capture the overall responsiveness of the start-up procedure, an average heating rate was defined according to Eq. (14). The heating rates were also calculated for a specific start-up cycle, which was obtained from the results of a parabolic trough model, previously developed by the authors [6]. The chosen lifetime equals 25 years, with 346 starts in a year of which there were 91 hot, 234 warm and 21 cold starts which would respectively correspond to a starting pressure of 26 bar, 16 bar and 1 bar, respectively.

$$\frac{dT_f}{dt}=\frac{p_2\cdot v_{T1}-p_1\cdot v_{T2}}{p_2-p_1}+\frac{v_{T2}-v_{T1}}{p_2-p_1}\cdot p(t) \tag{13}$$

$$v_{T\,average}=\frac{1}{t_{end}-t_{start}}\cdot\int_{t_{start}}^{t_{end}}\frac{dT_f}{dt}\,dt \tag{14}$$

2.5. Cost estimation

The cost estimation of the whole SGS was carried out following the method presented by Purohit et al. [28]. The method is based on estimating the cost of a baseline exchanger according to Eq. (15), where p_{OD}, f and r are cost multipliers for the outer diameter, front and rear head types, respectively. The total heat exchange cost was then determined as a function of the heat exchange area according to Eq. (17), where N_s represents the number of shells and $c_{i,j}$ represent a number of correction factors which take into account design pressure, length of the tubes and material selection. The cost of the steam drum was estimated as a function of the drum metal mass [47] and carbon steel prices according to Ref. [48]. Lastly, the total investment cost was adjusted to 2017 as a reference year according to the historical price index (*HPI*) reported in Ref. [49].

$$b=\left(\frac{6.6}{1-e^{\left(\frac{7-ID}{27}\right)}}\right)\cdot p_{OD}\cdot f\cdot r \tag{15}$$

$$PEC_{hx}=b\cdot\left(1+\sum_{i=1}^{n}c_i\right)\cdot A\cdot N_s \tag{16}$$

$$PEC_{SGS}=\frac{HPI_{2017}}{HPI_{1983}}\cdot\sum_{j=1}^{n_{hx}}\left(b_j\cdot\left(1+\sum_{i=1}^{n}c_{i,j}\right)\cdot A_j\cdot N_{s,j}\right) \tag{17}$$

2.6. Optimization and constraints

Apart from the investment cost, another important parameter to consider during a heat exchanger feasibility study is the pressure drop of both fluids. The lower the pressure drop, the higher the heat exchanger area required as lower heat transfer coefficients are obtained. Therefore, investment cost and pressure drops are conflicting parameters. Moreover, from a system perspective, higher mass flow rates from the HTF side would imply higher parasitic consumptions and therefore lower profitability of the power plant. Lastly, if the CSP plant includes TES systems, lower outlet HTF temperatures would allow for a lower cost on the thermal energy storage. Gonzalez-Gomez et al. [32] included all these considerations in their cost analysis; however, as the focus of this paper is to look into the details of just the SGS, only the minimization of the pressure drop and PEC was considered. Secondly, it is common practice in industry to ask the manufacturer of SGSs for a system of heat exchangers for certain fixed power plant specifications and maximum allowable pressure drop. Hence having a trade-off curve between pressure drop and PEC, would allow to choose the most cost-effective design for a set of power plant constraints.

The optimization was carried out with the genetic algorithm multi-objective optimization toolbox available in Matlab by varying the parameters as presented in Table 2. It was decided to choose the same tube outer diameter for each heat exchanger, to favor an economy of scale. The diameter was chosen to be a discrete variable, with the possibility to choose from four different commonly available tube outer diameters according to Coulson et al. [50]. The four choices (referred to as index in Table 3) were 25 mm, 30 mm, 38 mm and 50 mm, respectively, with lower diameters excluded from the optimization since these designs gave rise to high pressure drops (above 10 bar). The tube pitch values were chosen to be fixed to the lowest value allowable by not drastically increasing the pressure drops. This resulted in a tube pitch ratio (distance/diameter) of 1.25 and a staggered alignment to allow for the lowest shell diameters, higher heat transfer coefficient and easy mechanical cleaning [25,51]. These choices are also in agreement with the results presented by Gonzalez-Gomez et al. [32].

In order to allow the optimization algorithm to obtain feasible designs, constraints were set according to Table 3. The minimum and maximum tube side velocities were set in order to reduce possible fouling and avoid excessive corrosion, respectively [50]. The maximum steam flow velocities, which are dependent on operational pressure, were set according to the steam velocity diagram presented by Merritt et al. [52].

The constraints also took into consideration the minimum heating rates for each component (header/tube junction for single phase heat exchangers and drum/downcomer junction for the evaporator). As the evaporator is the main limiting component for the SGS, a minimum heating rate was chosen according to a previous work by the authors [6]. This value was chosen to maximize the electric power output of the

Table 2
Optimization decision variables.

Variables	Unit	Lower boundary	Upper boundary
Tube outer diameter index	[–]	1	4
RHe number of layers	[–]	20	40
RHs number of layers	[–]	20	40
EVA number of layers	[–]	20	40
SUP number of layers	[–]	20	40
ECO number of layers	[–]	20	40
Rhe number of tubes per layer	[–]	3	15
RHs number of tubes per layer	[–]	3	15
EVA number of tubes per layer	[–]	3	15
SUP number of tubes per layer	[–]	3	15
ECO number of tubes per layer	[–]	3	15
Riser outer diameter	[mm]	200	300
Number of risers	[–]	5	15

Table 3
Optimization constraints.

Parameter	Unit	Value
Tube minimum velocity	[m/s]	0.5
Tube maximum velocity	[m/s]	4
Shell minimum velocity	[m/s]	0.2
Shell maximum velocity	[m/s]	1.5
Steam maximum velocity	[m/s]	25
Oil maximum pressure drop	[bar]	2
Evaporator minimum heating rate	[K/min]	8.5
Super-heater minimum heating rate	[K/min]	15
Minimum drum internal diameter	[mm]	1500

power plant. All the other components were checked to have a lifetime higher than or equal to 25 years. The optimization was carried out for the following two cases:

1. No LCF constraints
2. LCF constraints, with minimum heating rate for both the evaporator and superheater

Other constraints, which specifically apply only to the evaporator, were related to limiting the maximum heat flux for the tube bundle to avoid film boiling [53,54] and assuring that the critical flow G_c in the water-steam mixture is not reached. This was estimated according to Eq. (18), in which the reference (ref) properties were calculated at the upstream stagnation point (steam drum) and c_f is a choking correction factor [55].

$$G_c = \sqrt{2 \cdot [p_{ref} - c_f \cdot p_{sat} \cdot (T_{ref})] \cdot \rho_{l,ref}} \quad (18)$$

3. Results and discussion

3.1. Model validation

A steady state validation was performed by comparing the most significant outputs of the model with data of the SGS of an existing 55 MWe parabolic trough power plant employing a header and coil steam generator. Table 4 summarizes the validation of the key parameters of the design routine. As the detailed geometrical design of the components considered for evaluating the accuracy of the model is confidential, only the main results are presented here. The total area required by each heat exchanger is in line with the plant data with a deviation of +2.5%, meaning that the model is able to predict the heat transfer coefficients with a reasonable degree of accuracy. This is also reflected in a deviation below 1% for the total HTF temperature drop. The small deviations in outlet velocities of water and HTF indicate that the pressure drops on each fluid side are estimated with good accuracy.

The Purohit method used for the SGS cost estimation was developed specifically for the TEMA configuration, but in the case of the header and coil geometry, its applicability was demonstrated by comparing its results with cost figures provided by the boiler manufacturer. For the different sizes provided, the relative deviations between the results of the cost model and the manufacturer data were below 2%, justifying the use of the method also for the header and coil geometry. Furthermore, the results shown in Table 4 indicate that even though the area is overestimated, the weight experiences an opposite trend. This can be explained by the fact that the thicknesses of the components are underestimated with an average of 2.9%. This is related to the fact that a manufacturer would choose a tube with the closest dimensions in terms of thickness and diameter among those available on the market. In conclusion, the results of the validation suggest that the models provide sufficiently accurate results for the purpose of the work presented in this paper.

3.2. Optimization results

The multi-objective optimization results are presented in Fig. 6. Fig. 6a presents a comparison of the results when excluding (Case 1) and including the LCF constraints (Case 2), see Section 2.6. Fig. 6b presents the optimization results with the HTF total pressure drop as color. If the main thermodynamic constraints are considered (Case 1), the 25 mm outer diameter solution is excluded as the pressure drop and velocity constraints (HTF/water) are not met. Therefore, only the other three diameters of 30 mm, 38 mm and 50 mm (from left to right) are feasible tube diameter options. If the LCF constraints are considered with a required minimum heating rate for the evaporator (Case 2), the 30 mm outer diameter is excluded for two reasons. In the case of a low tube number (towards the lower limit), the pressure drop on the SH side would increase significantly, meaning a higher steam pressure requirement at the drum, if the turbine inlet pressure is considered to be constant. This would require higher thicknesses on both the drum and downcomer tubes, increasing thermal stresses and lowering the maximum allowable heating rates. If the superheater tube number would be increased, the header diameter would need to be increased. This would mean higher thickness requirements; therefore, the superheater header would experience higher thermal stresses and hence the LCF constraints would not be satisfied at the superheater tube/header junction. In order to include the 30 mm outer diameter solution the evaporator heating rate constraint would need to be lowered to 6 K/min, hence making the design not optimal from a system perspective.

If a tube diameter of 50 mm for all the heat exchangers is considered, for the same pressure drop the design would change with an associated increase in PEC. For instance, for 0.1 bar pressure drop this would result in a 7.6% increase in the PEC. This is due to the fact that in order to keep low pressure drops as well as meeting the LCF constraints, more layers would be required resulting in higher shell diameters. This would in turn increase the cost for the superheater.

Fig. 6a also illustrates that in order to obtain a desired pressure drop, the design could drastically change if the LCF constraints are considered during the design procedure. For instance, if a 1 bar pressure drop is required, the PEC would increase by around 0.75 million USD, while increasing the LCF constraint from 6.2 K/min (Case 1) to 9.1 K/min (Case 2). Even though this figure corresponds to a 42% increase in capital cost of the SGS, it is justifiable if the economy of the whole power plant is taken into consideration.

According to a previous work of the authors [6], an evaporator ν_T increase from 6.2 K/min to 8.5 K/min would imply an increase in electricity production which would range between 0.84% and 3.31%, with the highest value in the case the superheater is optimally designed and operated considering the heating rate perspective. In a 25-year lifetime of the plant, and even assuming the lowest bid for CSP power production of 94.5 USD/MWh [56], this could result in an increase in revenues of between 1.17 million USD and 4.7 million USD. If there were different designs where only low heating rate constraints (3 K/min) were employed, the, these figures could rise to 2.1 million USD and 7.1 million USD, respectively.

The optimal geometrical parameters for Case 2 for different

Table 4
Validation results.

Parameters	Units	Model	Plant data	Deviation
Total area required (HTF side)	[m^2]	2755	2688	2.50%
HTF SGS temperature drop	[K]	92.40	91.70	0.76%
Pressure drop (HTF side)	[bar]	1.663	1.640	1.40%
Pressure drop (Water side)	[bar]	1.850	1.852	−0.11%
Velocity SH steam outlet	[m/s]	10.81	10.95	−1.32%
Velocity ECO HTF outlet	[m/s]	0.912	0.900	1.33%
EVA maximum heating rate	[K/min]	8.830	9.000	−1.89%
Total weight	[ton]	231.8	240.4	−3.59%

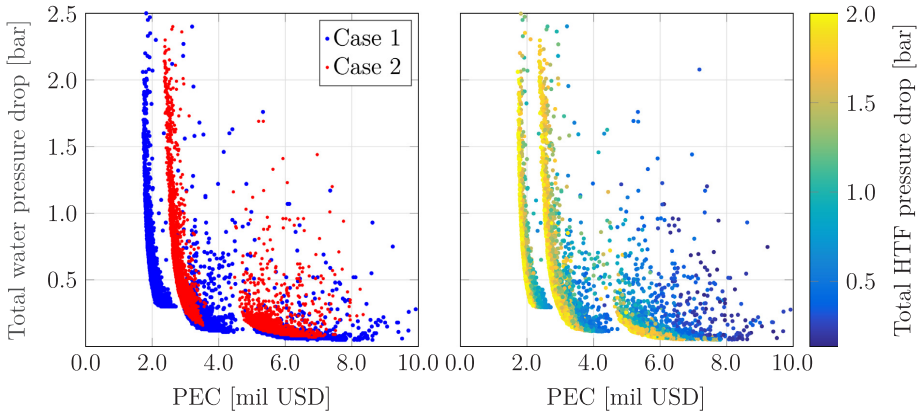

(a) Comparison between the two cases (b) HTF total pressure drop

Fig. 6. Optimization results.

conditions are presented in Table 5. It lists the arithmetic mean average, relative standard deviation (RSD) around the mean, and minimum and maximum values of the optimized variables at the Pareto front. In order to give an indication of feasible designs for different pressure drops, the table is split between pressure drops higher and lower than 1 bar for the solution corresponding to a tube outer diameter of 38 mm. A third column is presented for the 50 mm solution, which corresponds to pressure drops lower than 0.225 bar.

A low RSD and small difference between minimum and maximum values mean that the corresponding variable does not vary significantly within the optimal configuration. The EVA, ECO, SH number of layers and EVA tubes per layer present the lowest RSD for pressure drops higher than 1 bar. Similar conclusions can be drawn for designs which would result in lower pressure drops. The results presented for the number of tube layers for the superheater support the aforementioned discussion regarding the necessity to increase such parameter in cases where low pressure drops are required. The third column shows that in this case, an increase by 28% is necessary to satisfy this condition.

It may also be noticed that the riser configuration (outer diameter and numbers) presents a low RSD. Low number of risers would imply higher pressure drops, therefore larger height values for both downcomers and risers. Larger diameters would imply lower velocities and hence lower pressure drops, but higher required thicknesses. The results presented in the three columns can be interpreted as the optimal configuration, considering the trade-off between the number of tubes and diameter to minimize thickness and height and hence the associated cost. The differences among the three columns are due to the different operating pressure at the evaporator (due to higher pressure drops at the superheater), thus leading to different optimal configurations.

The difference in optimal diameter for the high pressure drop designs is the most evident change between the two cases. Table 6 presents a comparison in terms of relative change in the number of tubes among the optimal designs for the pressure drop ranges as presented in Table 5. The average values for the whole Pareto front are presented in an additional column. Each column presents the relative variation of tube numbers in Case 2 as compared to Case 1. The variation stems from either an increase in number of tube layers or number of tubes for each layer. The main trend is an overall increase in number of tubes for each heat exchanger. The superheater presents the highest relative increase in number of tubes both for the high pressure drop designs and as an average considering the whole pressure drop range. By lowering the water pressure drop, the economizer presents the highest increase. In this case, in order to lower further the water side pressure drop and at the same time keep high maximum allowable heating rates, the economizer pressure drop is decreased by increasing its number of tubes in equal proportion between number of layers and number of tubes for

Table 5
Optimization results for Case 2. Minimum, mean, maximum and relative standard deviation of the optimized variables. The values are acquired from the Pareto front in Fig. 6a.

Variables	Units	Higher than 1 bar				Between 0.225 and 1 bar				Lower or equal to 0.225 bar			
		min	mean	max	RSD	min	mean	max	RSD	min	mean	max	RSD
Tube outer diameter	[mm]	38	38	38	0%	38	38	38	0%	50	50	50	0%
RHe number of layers	[–]	28	29	30	3%	28	32	39	10%	27	34	38	9%
RHs number of layers	[–]	31	34	36	5%	34	35	35	1%	28	34	40	8%
EVA number of layers	[–]	29	30	33	4%	21	23	29	7%	20	20	22	3%
SH number of layers	[–]	20	22	24	6%	21	25	29	6%	25	32	39	13%
ECO number of layers	[–]	21	23	26	6%	21	22	29	6%	20	21	29	9%
RHe number of tubes per layer	[–]	7	8	10	14%	8	11	13	10%	14	15	15	3%
RHs number of tubes per layer	[–]	7	8	9	11%	8	11	15	18%	14	15	15	3%
EVA number of tubes per layer	[–]	4	4	4	0%	4	5	5	4%	3	3	5	21%
SH number of tubes per layer	[–]	4	6	7	18%	7	10	11	10%	8	8	11	12%
ECO number of tubes per layer	[–]	5	6	7	12%	5	6	8	13%	6	7	8	9%
Riser outer diameter	[mm]	253	280	296	5%	261	293	300	3%	294	298	300	1%
Number of risers	[–]	5	6	7	10%	5	6	8	9%	5	6	8	8%

Table 6
Comparison of designs of the two optimization cases (Case 2 compared with Case 1) in terms of relative change in the number of tubes for each heat exchanger.

Component	p > 1 bar	0.225 bar < p ⩽ 1 bar	p ⩽ 0.225 bar	Average
RHe	145.0%	134.1%	105.6%	128.2%
RHs	141.5%	132.8%	110.4%	127.9%
EVA	105.0%	134.8%	127.6%	122.1%
SH	154.8%	145.0%	125.6%	141.8%
ECO	121.8%	156.1%	131.7%	136.5%

each layer. Both Fig. 6a and Table 6 suggest that by including LCF constraints during the design phase, different optimal designs are obtained in the whole cost range, with the cheaper designs being the most affected.

Table 7 illustrates the results of the optimized geometry for a 1 bar pressure drop on the water side. The header diameter results support the aforementioned observations concerning the number of tubes. Low numbers are preferred in the high pressure heat exchangers, while large header diameters are preferred on the re-heater train side. The two most expensive components are the evaporator and superheater, accounting for 34% and 27%, respectively, of the overall PEC. That is also why the optimizer tends to provide a low number of tubes and high heat transfer coefficients for these components. On the other hand, the re-heaters are less sensitive both from a heating rate and an area/cost perspective, accounting for 14% and 12% of the overall PEC. That is why in Table 5, the re-heater parameters experience high variations in the optimal solutions.

In order to minimize the PEC, the HTF total pressure drop converges to the maximum allowable value of 2 bar. That is, if this value decreases, higher costs would be obtained; see Fig. 6b. This is mainly due to the fact that, in order to decrease the shell-side velocity, a lower number of coils would be needed, meaning a higher number of tubes. In turn this would cause low water side velocities, hence an increased heat exchanger area requirement. This would mean that for a water-side 1 bar pressure drop, decreasing the HTF pressure drop from 2.0 to 1.5 bar would result in a PEC increase of 13%.

It needs to be stressed that the results presented in this section are governed by the power plant design specifications. Therefore, if a CSP plant is optimized while employing the method presented in this paper for the SGS design, different optimal SGS designs other than the ones presented here may be obtained, depending on the size of the solar field and thermal energy storage. However, the method presented in this paper can be used to provide guidelines on how to design the SGS for a given set of design specifications and be applied during the pre-design phase of CSP plants to obtain the most suitable design.

The results presented in the paper are specific to the parabolic trough power plants. Even though these plants are the most commercially mature, solar tower plants are experiencing an increasing trend in interest [57]. The methods presented in the paper could be applied in a similar way to solar tower power plants. The main difference would derive from the presence of molten salt as the heat transfer fluid and the associated risk of freezing at relatively high temperature [58]. This would require a different design of the evaporator as the molten salt would be required on the shell-side in order to minimize the freezing risk and facilitate maintenance. Another difference would be the operating temperature. Typically, solar tower plants operate at around 565 °C. Having a higher temperature would require different materials and impose different stress cycles, hence the impact of the LCF constraints is expected to be more pronounced.

4. Conclusions

A design tool was developed to size all the heat exchangers of a steam generator system for concentrating solar power applications. The models included the area calculations based on heat transfer coefficients, and sizing of the main components, such as tubes, headers and shells. For the first time a sizing routine was presented including the evaluation of low-cycle fatigue requirements, in terms of maximum allowable heating rates for the most significant components, and its significance was demonstrated by comparison of the results with a design for which thermo-mechanical constraints were not considered. The sizing was also coupled with a cost estimation model. This allows coupling the thermo-mechanical and economic aspect to integrate the model in a genetic algorithm based multi-objective optimization to minimize both pressure drops and purchase equipment cost.

The results of the validation indicate that models provide accurate results, resulting in an overestimation of the total heat exchanger area by 2.5% compared to components installed in existing power plants. The total weight was underestimated by 3.6%. Lastly, the low-cycle fatigue norms were implemented with a resulting deviation in an evaporator heating rate calculation of −1.9% compared to that of the existing power plant.

The results of the multi-objective optimization indicate that

Table 7
Result design for 1 bar pressure drop on water side.

Parameter	Units	ECO	EVA (†)		SH	RHe	RHs
Shell diameter	[mm]	1636	1465	1658	1709	2246	2599
Shell length	[mm]	9.3	13.2	8.95	15.03	16.54	17.1
Shell thickness	[mm]	18	65	79	20	23	29
Number of shells	[–]	1	2	1	1	1	1
Tube outer diameter	[mm]	38	38		38	38	38
Tube thickness	[mm]	3.8	4.8		3.8	3.8	3.8
Tube layers	[–]	22	29		23	30	34
Tube per layers	[–]	6	4		7	9	9
Tube coils	[–]	23	3		34	10	12
Header diameter	[mm]	380.6	216.4		465.9	560.5	489.2
Header thickness	[mm]	27.0	22.6		37.0	19.0	16.0
Tube side average flow velocity	[m/s]	0.52	3.39		6.50	18.48	17.82
Shell side average flow velocity	[m/s]	1.01	–		1.04	0.59	0.52
Tube side heat transfer coefficient	[W/(m^2 K)]	4567.0	5311.0		2024.3	735.5	578.3
Shell side heat transfer coefficient	[W/(m^2 K)]	1993.1	23472.7		1866.1	1441.3	1218.1
Overall heat transfer coefficient	[W/(m^2 K)]	1155.2	3245.6		1155.2	402.7	325.4
Oil side pressure drop	[bar]	0.289	1.133		0.445	0.078	0.294
Water side pressure drop	[bar]	0.031	0.017		0.472	0.294	0.206
Purchase equipment cost	[mil USD]	0.350	0.850		0.690	0.290	0.350
v_T average	[K/min]	68.7	9.1		31.7	246.1	153.7

(†) The shell parameters refer to the heat exchangers (on the left) and steam drum (on the right).

integrating the low-cycle fatigue analysis in the design routine of steam generator systems can change significantly the design of the heat exchangers. If both the superheater and the evaporator minimum heating rate constraints are considered, only two tube outer diameter choices (38 mm, 50 mm) give optimal solutions. If 1 bar water-side pressure drop is a requirement from a power plant owner, the cost of an optimal heat exchanger could potentially increase by 0.75 million USD (42% purchase equipment cost increase). However, considering that high heating rates could lead to an increase in electricity production, the increase in steam generator system cost can be justifiable. The optimization results also suggest that a lower heat transfer fluid total pressure drop constraint implies high purchase equipment costs. Specifically, for the 1 bar water-side pressure drop design, lowering the heat transfer fluid pressure drop from 2.0 bar to 1.5 bar would imply a purchase equipment cost increase of 13%.

The results presented in this work are specifically tailored for one power plant design in order to keep the focus of the work only on the component design. Integrating this methodology in a more general system level optimization may lead to different optimal steam generator configurations depending on the power plant specifications, such as thermal energy storage, solar field size and parasitic consumption.

References

[1] International Energy Agency. Technology roadmap, solar thermal electricity. Technical report. Paris (France): IEA; 2014.
[2] Mancini Thomas R, Gary Jesse A, Kolb Gregory J, Kuofei Ho Clifford. Power tower technology roadmap and cost reduction plan. Sandia report. Technical report Sandia report. Albuquerque (New Mexico): Sandia, Sandia National Laboratories; 2011.
[3] World Energy Council. World energy resources: solar 2016. Technical report. London, England; 2016.
[4] Groupe Reaction Inc. CSP parabolic trough report: cost, performance and key trends. Technical report. London (England): CSP Today; 2014.
[5] Estela, Greenpeace, and Solarpaces. Solar thermal electricity - global outlook 2016. Technical report. Brussels, Belgium; 2016.
[6] Ferruzza D, Topel M, Laumert B, Haglind F. Impact of steam generator start-up limitations on the performance of a parabolic trough solar power plant. Sol Energy 2018;169:255–63.
[7] Dzierwa Piotr, Taler Jan. Optimum heating of pressure vessels with holes. J Press Vessel Technol 2014;137(1):011202.
[8] Dzierwa Piotr, Taler Dawid, Trojan Marcin, Taler Jan. Evaporator heating with optimum fluid temperature changes. Procedia Eng 2016;157:29–37.
[9] Taler Jan, Weglowski Bohdan, Taler Dawid, Sobota Tomasz, Dzierwa Piotr, Trojan Marcin, et al. Determination of start-up curves for a boiler with natural circulation based on the analysis of stress distribution in critical pressure components. Energy 2015;92:153–9.
[10] Gonzalez-Gomez PA, Gomez-Hernandez J, Briongos JV, Santana D. Fatigue analysis of the steam generator of a parabolic trough solar power plant. Energy 2018;155:565–77.
[11] Duda Piotr, Rzasa Dariusz. Numerical method for determining the allowable medium temperature during the heating operation of a thick-walled boiler element in a supercritical steam power plant. Int J Energy Res 2012;36(6):703–9.
[12] CEN. Water-tube boilers and auxiliary installations - Part 3: design and calculation for pressure parts of the boiler. Technical report. Brussels (Belgium): European Committee for Standardization; 2012.
[13] Vant-Hull LL. Central tower concentrating solar power (CSP) systems. Houston (Texas): Woodhead Publishing Limited; 2012.
[14] Pelagotti Leonardo, Sørensen Kim, Condra Thomas J, Joseph Thomas, Franco Alessandro. Modelling of a coil steam generator for CSP applications. In: Proceedings of the 55th international conference on simulation and modelling; 2014.
[15] Mercati Stefano, Milani Massimo, Montorsi Luca, Paltrinieri Fabrizio. Design of the steam generator in an energy conversion system based on the aluminum combustion with water. Appl Energy 2012;97:686–94. Energy Solutions for a Sustainable World - Proceedings of the Third International Conference on Applied Energy, May 16-18, 2011 - Perugia, Italy.
[16] Liu Chengyang, Yan Changqi, Wang Jianjun. Optimal design of vertical natural circulation steam generator. Nucl Eng Des 2012;252:167–78.
[17] Chen Lei, Yan Changqi, Wang Jianjun. Multi-objective optimal design of vertical natural circulation steam generator. Prog Nucl Energy 2013;68:79–88.
[18] Gómez-Hernández J, González-Gómez PA, Briongos JV, Santana D. Influence of the steam generator on the exergetic and exergoeconomic analysis of solar tower plants. Energy 2018;145:313–28.
[19] Lin Meng, Reinhold Jan, Monnerie Nathalie, Haussener Sophia. Modeling and design guidelines for direct steam generation solar receivers. Appl Energy 2018;216:761–76.
[20] González-Gómez PA, Gómez-Hernández J, Briongos JV, Santana D. Transient thermo-mechanical analysis of steam generators for solar tower plants. Appl Energy 2018;212:1051–68.
[21] González-Gómez PA, Gómez-Hernández J, Ferruzza D, Haglind F, Santana D. Dynamic performance and stress analysis of the steam generator of parabolic trough solar power plants. Appl Therm Eng 2019;147:804–18.
[22] Mertens Nicolas, Alobaid Falah, Starkloff Ralf, Epple Bernd, Kim Hyun-Gee. Comparative investigation of drum-type and once-through heat recovery steam generator during start-up. Appl Energy 2015;144:250–60.
[23] Serna M, Jiménez Arturo. A compact formulation of the Bell-Delaware method for heat exchanger design and optimization. Chem Eng Res Des 2005;83(5 A):539–50.
[24] Serth Robert W, Lestina Thomas G. The stream analysis method. 2nd ed. Boston (Massachusetts): Academic Press; 2014.
[25] Kern DQ. Process heat transfer. Singapore: McGraw-Hill; 1965.
[26] Anarratore Donatello. Handbook for heat exchangers and tube banks design. Milano (Italy): Springer; 2010.
[27] Hall SG, Ahmad S, Smith R. Capital cost targets for heat exchanger networks comprising mixed materials of construction, pressure ratings and exchanger types. Comput Chem Eng 1990;14(3):319–35.
[28] Purohit GP. Estimating costs of shell-and-tube heat exchangers. Chem Eng 1983(90):56–67.
[29] Dolores Durán Ma, Valdés Manuel, Rovira Antonio, Rincón E. A methodology for the geometric design of heat recovery steam generators applying genetic algorithms. Appl Therm Eng 2013;52(1):77–83.
[30] Franco Alessandro, Giannini Nicola. A general method for the optimum design of heat recovery steam generators. Energy 2006;31(15):3342–61.
[31] Wildi-Tremblay Philippe, Gosselin Louis. Minimizing shell-and-tube heat exchanger cost with genetic algorithms and considering maintenance. Int J Energy Res 2007;31(31):135–47.
[32] González-Gómez PA, Petrakopoulou F, Briongos JV, Santana D. Cost-based design optimization of the heat exchangers in a parabolic trough power plant. Energy 2017;123:314–25.
[33] MATLAB, version 9.1.0.4 (R2016b). The Natick (Massachusetts): MathWorks Inc.; 2016.
[34] Basil Leyland Geoffrey, Favrat Daniel. Multi-objective optimization applied to industrial energy problems [Ph.D. thesis]. Lausanne: École Polytechnique Féderale de Lausanne (EPFL); 2002.
[35] NREL. System advisor model (SAM) case study: andasol. Technical report. Aldeire (Spain): NREL; 2013.
[36] Aalborg CSP. http://www.aalborgcsp.com/quickmenu/brochures/ [accessed: 2017-08-03].
[37] Bergman Theodore, Lavine Adrienne, Incropera Frank, Dewitt David. Fundamentals of heat and mass transfer. 7th ed. Jefferson city (Missouri): John Wiley and Sons; 2011.
[38] Žukauskas A. Heat transfer from tubes in crossflow. Adv Heat Transfer 1972;8:93–160.
[39] Stephan K, Abdelsalam M. Heat-transfer correlations for natural convection boiling. Int J Heat Mass Transfer 1980;23(1):73–87.
[40] Idelchik IE. Hanbook of hydraulic resistance. Coefficients of local resistance and of friction. Jerusalem (Israel): National Science Foundation; 1986.
[41] Ganapathy V. Understanding boiler circulation. Chem Eng 2013;120(10):52–6.
[42] Anarratore Donatello. Steam generators. Description and design. Milano (Italy): Springer; 2008.
[43] American society of mechanical engineer. ASME Boiler and Pressure Vessel Code: Section VIII - Division 2, New York, New York; 2015.
[44] Hübel Moritz, Meinke Sebastian, Andrén Marcus T, Wedding Christoffer, Nocke Jürgen, Gierow Conrad, et al. Modelling and simulation of a coal-fired power plant for start-up optimisation. Appl Energy 2017;208:319–31.
[45] Meinke Sebastian. Modellierung thermischer kraftwerke vor dem hintergrund steigender dynamikanforderungen aufgrund zunehmender windenergie- und photovoltaikeinspeisung [M.Sc. thesis]; 2012.
[46] Butcher JC, Wanner G. Runge-Kutta methods: some historical notes. Appl Numer Math 1996;22(1):113–51 Special Issue Celebrating the Centenary of Runge-Kutta Methods.
[47] Seader JD, Seider Warren D, Lewin Daniel R. Product and process design principles: synthesis, analysis and evaluation. USA: Wiley; 2004.
[48] MEPS International. http://worldsteelprices.com/ [accessed: 01/03/2018].
[49] Capital professional services. https://inflationdata.com/ [accessed: 01/03/2018].
[50] Towler Gavin, Sinnott Ray. Heat-transfer equipment. In: Chemical engineering design. Oxford, England; 2013. p. 1047–1205.
[51] Khan Waqar Ahmed, Yovanovich MM, Culham JR. Optimal design of tube banks in crossflow using entropy generation minimization method. J Thermophys Heat Transfer 2007;21(2):372–8.
[52] Merritt Carey. Process steam systems: a practical guide for operators, maintainers, and designers. New Jersey: John Wiley & Sons; 2015.
[53] Palen JW. Shell and tube reboilers. In: Heat exchanger design handbook. Begell House, London, England; 2002.
[54] Kandlikar SG. A theoretical model to predict pool boiling critical heat flux incorporating effects of contact angle and orientation. ASME J Heat Transfer 2001;123(6):1071–9.
[55] Kim Yeon Sik. A proposed correlation for critical flow rate of water flow. Nucl Eng Technol 2015;47(1):135–8.
[56] New energy update. http://analysis.newenergyupdate.com/csp-today/acwa-power-scales-tower-trough-design-set-record-low-csp-price [accessed: 02/07/2018].
[57] Islam Md Tasbirul, Huda Nazmul, Abdullah AB, Saidur R. A comprehensive review of state-of-the-art concentrating solar power (csp) technologies: current status and research trends. Renew Sustain Energy Rev 2018;91:987–1018.
[58] Vignarooban K, Xu Xinhai, Arvay A, Hsu Keng, Kannan AM. Heat transfer fluids for concentrating solar power systems—a review. Appl Energy 2015;146:383–96.

Start-Up Performance of Parabolic Trough Concentrating Solar Power Plants

Davide Ferruzza[1,a)], Monika Topel[2,b)], Ibrahim Basaran[2)], Björn Laumert[2)], Fredrik Haglind[1)]

[1]*Department of Mechanical Engineering, DTU, Technical University of Denmark, 2800, Kgs. Lyngby, Denmark*
[2]*Department of Energy Technology, KTH Royal Institute of Technology, 100 44, Stockholm, Sweden*

[a)]Corresponding author: daferr@mek.dtu.dk
[b)]monika.topel@energy.kth.se

Abstract. Concentrating solar power plants, even though they can be integrated with thermal energy storage, are still subjected to cyclic start-up and shut-downs. As a consequence, in order to maximize their profitability and performance, the flexibility with respect to transient operations is essential. In this regard, two of the key components identified are the steam generation system and steam turbine. In general it is desirable to have fast ramp-up rates during the start-up of a power plant. However ramp-up rates are limited by, among other things, thermal stresses, which if high enough can compromise the life of the components. Moreover, from an operability perspective it might not be optimal to have designs for the highest heating rates, as there may be other components limiting the power plant start-up. Therefore, it is important to look at the interaction between the steam turbine and steam generator to determine the optimal ramp rates. This paper presents a methodology to account for thermal stresses limitations during the power plant start up, aiming at identifying which components limit the ramp rates. A detailed dynamic model of a parabolic trough power plant was developed and integrated with a control strategy to account for the start-up limitations of both the turbine and steam generator. The models have been introduced in an existing techno-economic tool developed by the authors (DYESOPT). The results indicated that for each application, an optimal heating rates range can be identified. For the specific case presented in the paper, an optimal range of 7-10 K/min of evaporator heating rate can result in a 1.7-2.1% increase in electricity production compared to a slower component (4 K/min).

INTRODUCTION

Concentrated solar power plants (CSPP) are foreseen to increase their share in the electricity production due to their ability to decouple the energy generation from the solar input. Although the majority of these plants are integrated with thermal energy storage (TES), they are still subject to daily start-ups and shut-downs [1]. Hence, in order to maximise the profitability of CSPPs it is essential that they are flexible with respect to transient operation. In this context, the most important components to study are the receiver, the turbine and the steam generator. The two former have been given attention in the research and studies on their dynamic performances have been conducted previously [2] [3], while the latter has not been the focus on any previous study, even though it represents a critical component, by being the connection link between the power block (PB) and the solar field (SF).

In current CSPPs, the steam generators have been designed as typical heat exchangers, and not as boilers suited specifically for CSP applications, requiring fast response times and high temperature ramp rates. Steam generators in CSP applications were firstly designed without focusing on the dynamic performance [4], as the industry mainly applied design of the components suited for conventional power generation practices. This has resulted in plants with start-up delays and a poor capacity to handle sudden changes in incident solar radiation or load demand, which in turn may cause failures in the steam generator due to excessive thermal stresses and deteriorate the economic viability of the plant. Currently, there is a tendency towards the development of steam generators tailored for CSPPs,

SolarPACES 2016
AIP Conf. Proc. 1850, 160008-1–160008-9; doi: 10.1063/1.4984542
Published by AIP Publishing. 978-0-7354-1522-5/$30.00

though there is still a lack of knowledge regarding the optimal ramp-up rate requirements. From the annual performance and competitiveness perspectives of a CSPP, it is desirable that both the turbine and the steam generator are able to start quickly, enabling the power plant to harvest the sun energy as soon as it becomes available. However, there may be limiting factors for the ramp-up time for one component, making it unnecessary to have a shorter ramp-up time for another. If, for example, the start-up rate of the turbine is the limiting factor, there is no need to design a boiler with a faster start-up rate than that of the turbine.

The objective of the paper is to identify which are the components that limit the start-up times for CSPPs during various operating conditions and evaluate their impact on the annual performance of the plant. In particular, the paper focuses on Parabolic Trough Power Plants (PTPP). Recent studies [5, 6], have focused their attention on the single component (i.e. turbine or steam generator), while in the work presented, both start-ups are considered, and their impact on the annual electricity production is evaluated. Firstly, the paper presents a brief description of the start-up limitations of the components. Secondly, in the methods section, the modelling of the PTPP and the operating strategy including the start-up are explained. Lastly, in the results section, the start-up performance of turbine and steam generator is analyzed together with the impact on the electricity production of the PTPP.

Nomenclature

Abbreviations

CSPP	Concentrated Solar Power Plant	**ST**	Steam Turbine
CT	Cold tank	**TES**	Thermal Energy Storage
D	Dearator	**WCC**	Wet cooled condenser
ECO	Economizer		
EVA	Evaporator	**Subscripts**	
HP	High pressure	**f**	Fluid
HT	Hot tank	**Max**	Maximum
HTF	Heat Transfer Fluid	**Min**	Minimum
HX	Heat Exchanger	**nom**	Nominal
LP	Low pressure		
OPEX	Operation Expenditure	**Symbols**	**Units**
PB	Power block	**ITD**	[°C] Inlet Temperature Difference
PTPP	Parabolic Trough Power Plant	**m**	[kg/s]
REF	Reference case	**p**	[bar] Pressure
RH	Re-heater	**T**	[°C] Temperature
SF	Solar field	**t**	[s] Time
SGS	Steam Generator System	$\mathbf{v_T}$	[k/min] Allowable ramp-up rate/heating rate
SH	Super-heater		

Steam Turbine and Steam Generator Start-up Description

The speed, at which both the steam generator system (SGS) and the steam turbine (ST) can start, is limited by constraints related to thermal stresses and low cycle fatigue. In both cases, these are related to thickness of components, material properties and temperature gradients [5] [6]. In the case of a steam turbine, the shaft seal and blading clearances define the allowable thermal expansion of the components. Typically, the starting up of a steam turbine can be divided in three phases: pre-start heating, running up and loading up. During the start-up the key parameter that limits the running and loading up speed is the difference in temperature between the incoming steam and turbine metal. Therefore, it is beneficial to keep these two temperatures as close as possible to avoid elevated thermal stresses in the component. As a consequence, the warmer the turbine material is before the start-up, the faster the start-up can be [5]. Manufacturers provide turbine loading curves governed by the metal temperature, to keep the stress within the allowable limits. Depending on the initial temperature of the turbine, (or on the turbine stand still time), the start-ups can be classified as hot, warm or cold. A hot start-up would take 8-10% of time of a full cold start-up while a warm start-up would range up to 45-50% [2].

In the case of steam generators, the main limiting factor for fast boiler start-ups are the maximum allowable stresses in the thick walled components such as headers of super-heaters, evaporator drum and T or Y junctions in the steam pipelines. The governing limiting component is the evaporator steam drum, as typically, it is designed as a high diameter vessel to withstand high pressures, and therefore large material thicknesses are required [6]. The start-up procedure in this case, is to reach the set points for steam temperature, pressure and mass flow rates as fast and as efficient as possible. Previous studies have pointed out that the main limiting components during the start-up, are either the evaporator or the super-heater [6] [7].Therefore these two will be considered in detail for the study.

METHODS

The study was carried out using DYESOPT, an in-house numerical tool developed at KTH, Royal Institute of Technology, Sweden, [2], allowing location-tailored, techno-economic performance evaluations integrated with multi-objective optimization of power plants. An annual performance analysis was carried out. As a first step, the start-up performance of the SGS and turbine was analyzed. The allowable start-up rates were included in the software by considering the allowable stresses on the most sensible parts of the steam generator (i.e. the steam drum and headers) [7] [8]. The allowable temperature gradients obtained for the thick-walled metal parts were used to determine the appropriate fluid temperature and pressure start up conditions [9]. Metal temperatures and start-up schedules provided by the manufacturer for the turbine were considered [2]. Secondly, the parabolic trough power plant (PTPP) was modeled by looking at its steady state design and dynamic performance. Lastly, the annual performance of such plant was analyzed, focusing on the start-up of the two components. This was considered by introducing in the model a control strategy, which accounted for the ramp-rates limitations. Based on this analysis, the optimal range of start-up rates of the components was determined.

Start-up Limitations for Turbine and Steam Generator

The start-up limitations of both components were considered by looking at the turbine loading curves for the different start-ups and by calculating the allowable fluid temperature change in the SGS components (EVA and SH).

Figure 1 illustrates the different start-up curves, in particular the A-B and B-C lines represents respectively the running up and loading up of the turbine [10]. The study analyzed different turbine ramp-up speeds, as well as the possibility to always ramp with a hot start-up. The latter requires that temperature maintaining modifications like electrically powered heat blankets or high speed barring are employed [5].

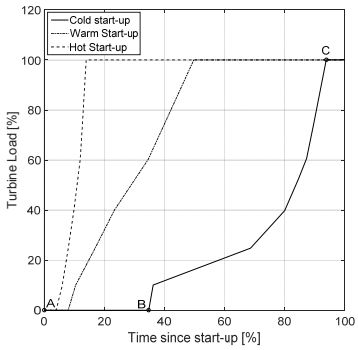

FIGURE 1: Turbine loading curves versus the percentage in time since start-up procedure has begun [10]

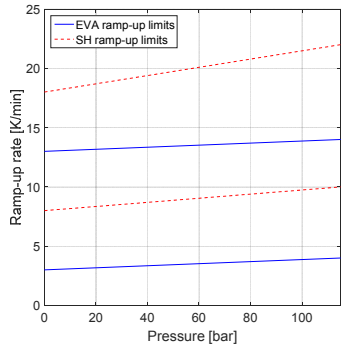

FIGURE 2: Assumed evaporator and super-heater ramp-up limits considered – For both components, the upper limit refers to a very fast case, while the lower limit refers to a slow case

Figure 2 presents different heating rates for both the super-heater and the evaporator. In both cases the upper and lower curves represent respectively the highest and lowest ramp-up rates that will be used in the yearly simulations of the power plant. The heating rates v_{Tmin} and v_{Tmax} respectively for the minimum and maximum allowable

pressures can be determined according to the norm DIN EN 12952-3 [8]. In the case of this paper, the geometry of the components was not considered, instead an optimal ramp up rate from a system perspective was determined. The heating rates are used to calculate the allowable fluid temperature change using the following two equations [6]:

$$\frac{dT_f}{dt} = \frac{p_{max}\, v_{T_{min}} - p_{min}\ v_{T_{max}}}{p_{max} - p_{min}} + \frac{v_{T_{max}} - v_{T_{min}}}{p_{max} - p_{min}}\, p(T_f) \quad (1)$$

$$\frac{dT_f}{dt} = \frac{p_{max}\, v_{T_{min}} - p_{min}\ v_{T_{max}}}{p_{max} - p_{min}} + \frac{v_{T_{max}} - v_{T_{min}}}{p_{max} - p_{min}}\, p(t) \quad (2)$$

In the case of the evaporator, the water is at saturation point and therefore the pressure and temperature will be related. As a consequence, the temperature of the fluid will be dependent on the pressure and equation (2) can be solved with a Runge-Kutta method, assuming $T_f(t = 0) = T_0$ [6]. In the case of SH the fluid is not at saturation conditions and the pressure is a function of time determined by the evaporator conditions.

Parabolic Trough Power Plant Modeling and Design

The analysis of the annual performance and of the impact of the start-up performance was carried for PTPP. The layout of the power plant analyzed for the paper is shown in **Fig. 3.** The PTPP considered is integrated with an indirect TES system and a Wet Cooled Condenser (WCC). The power plant has been designed for the location of Seville, with a power output of 55 MWe gross. The design has been carried following ref. [11] for PB, ref. [12] for the HTF cycle and ref. [13] and ref. [14] for SF. The dynamic modeling was implemented in TRNSYS, as DYESOPT allows the coupling of steady state design in Matlab and the aforementioned software [5, 11].

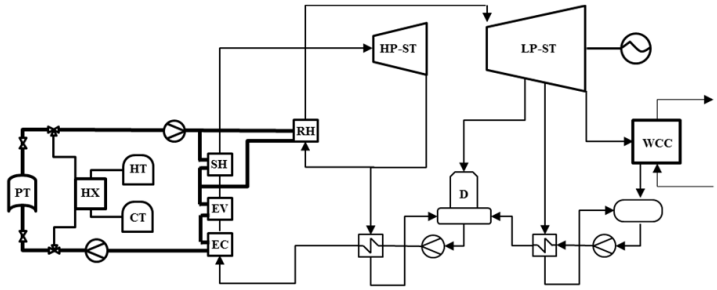

FIGURE 3: Layout of the considered parabolic trough power plant integrated with thermal energy storage and wet cooled condenser [13]

The main design parameters and thermal performance indicators are listed in **Table 1** and **Table 2**. **Table 2** also presents a comparison of the main performance indicators obtained with a similar PTPP model (SAM) [15].

The comparison with the data of the reference model [15] indicate that the largest deviation occurs for the yearly electricity production, and in this case the model predicts a value 8.9% lower than that of the reference model. However when considering comparison with ref. [16] and ref. [17] , the deviation ranges between +0.5% and -3.7%. Moreover in the reference model, the PTPP is integrated with an auxiliary burner to improve the production of electricity during start-ups or sudden losses in available thermal power [15] , which was not implemented in the model developed by the authors. These comparisons suggest that the models give results with sufficient accuracy for the purpose of the current paper. The power plant considered, will serve as a basis for further analysis of the start-up performance.

TABLE 1. Main design parameters for the analyzed PTPP

Main Design Parameters	Units	Value
SM	[-]	1.75
Gross Power Output	[MW_e]	55
TES Capacity	[h]	7.5
Inlet HP/LP-ST pressure	[bar]	100/16.5
SF Maximum outlet temperature	[°C]	393.3
Nominal WCC ITD	[°C]	11
# of HP/LP ST extractions	[-]	2/3
Operating strategy	[-]	Baseload

TABLE 2. Main performance indicators for the validation of the PTPP model

Performance indicators	Model results	Reference	Relative Error
Net Power Output [MWe]	49.97	49.90 [17]	+0.14%
PTPP annual average efficiency [%]	15.27	15.00 [17]	+1.8 %
Yearly electricity production [GWh]	158.9	158/165/174.5 [16] [17] [15]	+0.5%/-3.7%/ -8.9%
SF land area [hectares]	202.2	200 [17]	+1.1%

Control Strategy for Optimal Start-up

In order to implement their start-up performance, the control strategy, presented in **Fig. 4,** was implemented in the dynamic model of the power plant in TRNSYS. It comprises the strategy for turbine operation developed by the authors [7], and the operational strategy for steam generator in case of a heat transfer fluid (HTF).

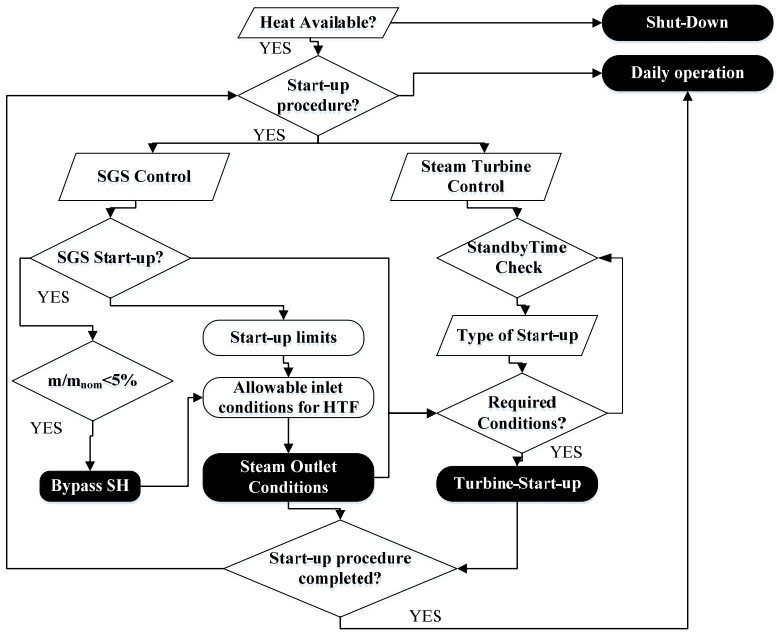

FIGURE 4: Control strategy logic diagram for start-up considering the interactions between steam generator and turbine

When the HTF is supplied to the evaporator, the system starts to produce steam, however the valves at the outlet of the drum are kept close until a certain amount of mass flow rate can be produced (5% of the nominal mass flow rate). This is to avoid overheating of the SH tubes. When the steam reaches acceptable conditions for the turbine (minimum pressure and temperature or degree of superheat), the control valves are opened and the turbine starts to run up, while pressure and temperature of the steam are increasing. Each type of turbine start-up has different acceptable conditions. For instance, a hot start-up would require higher steam inlet temperature than a warm or cold case. This is related to the fact that a hot start-up would imply a higher turbine metal temperature, therefore the acceptable steam temperature is higher to keep the difference between the two temperatures as low as possible and minimize the thermal stresses. After each shut down, the steam drum is able to keep the lowest admissible pressure of the turbine; therefore, aside from losses (which in this case are considered negligible), each consequent start-up will not begin from ambient pressure, but from the value set by the characteristics of the turbine. This always happens, unless a maintenance occurs, requiring start-up from ambient pressure and temperature.

During each start-up (either at the beginning of the day or due to sudden heat unavailability), the controller checks for turbine stand time and water conditions in the steam drum. This determines the type of turbine start-up (cold, warm or hot) and the allowable heating rate for the pressure reached at the evaporator. This signal is translated into the allowable oil inlet conditions (enthalpy, temperature and mass flow rate), according to heat availability from the SF and TES and the temperature reached by the oil. The outlet conditions from the super-heater are checked to determine whether the turbine can accept the steam in order to proceed for the start-up. Once both components reach their nominal operating points, the start-up procedure is completed.

RESULTS

Figure 5 presents the result of a start-up of the two components for the different cases presented in **Table 3**. The different cases are chosen to understand under which conditions, a start-up might be delayed. These are considered not only by looking at different SGS configuration (Cases a, b, c, d) but also at faster turbine (assuming a 20% faster than the reference case) (Cases 1, 2, 3, 4), to look if in any case the SH is not able to provide the nominal conditions when the turbine reaches full load. The figures illustrate temperature (for SH and EVA) and pressure (for EVA) evolution in time (represented in percentage in respect to the total simulation time) together with the turbine load.

TABLE 3. Summary of different start-up cases considering evaporator, super-heater and steam turbine ramp rates

	SH ramp-rates	EVA ramp-rates	Turbine ramping mode
Case a	Fast	Fast	For each case:
Case b	Slow	Fast	1) Warm start-up
Case c	Fast	Slow	2) 20% faster than the Warm start-up
Case d	Slow	Slow	3) Hot start-up
			4) 20% faster than the Hot start-up

The figures indicate that for cases a and b the SGS is able to provide the nominal conditions of steam when the turbine reaches full load, no matter what start-up mode is employed for the ST. However, it may be noted that a slow SH as in case b would postpone the start-up of the turbine as it is not able to provide sufficient degree of superheat to the outlet steam. On the other hand, for a too fast ramp-up of the SH at the beginning of the process as in case a, the SH would be constrained by the limitations of the EVA and consequently be ramped-up at a lower rate.

The comparison of case a and c suggests that a slower EVA could result in 2-18% lower start-up time, depending on the turbine conditions. However, cases b and d result in little differences (<0.5%), as the SH in case b is acting as the bottleneck of the entire start-up procedure, and reaching allowable turbine inlet conditions at the same time as in case d. These considerations suggest that the SH and the EVA should be optimally ramped up together and a fast SH is generally advisable. In the particular case of the PTPP under study, an optimal SH heating rate 179% higher than the EVA is found. In this way both components would reach the nominal point at the same time. Even if the design of the SH would allow higher ramp rates, operating at a slower rate would determine a lower associated fatigue and a longer durability of the component.

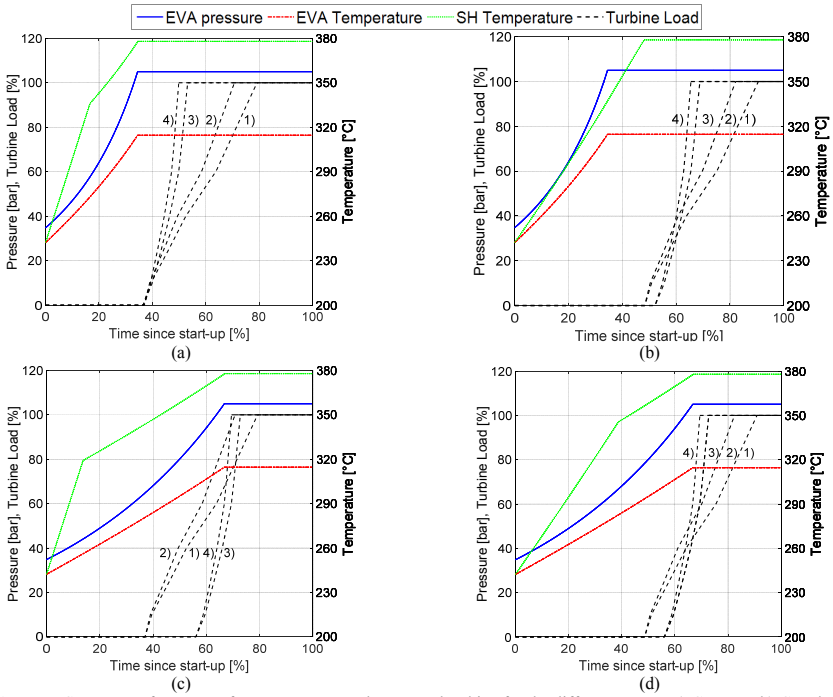

FIGURE 5. Start-up performance of evaporator, super-heater and turbine for the different cases – a) Case a – b) Case b – c) Case c – d) Case d

In order to assess the impact of the different ramp-rates on the yearly energy production of the PTPP, three different cases were compared with a reference case. The variation for EVA and SH ramp limits is illustrated in **Fig. 2**, while the turbine cases refer to **Table 3**. **Figure 6** presents the result of the analysis. Each point in **Fig. 6** represents the results of the annual dynamic simulation, deriving from different combinations of ramp rate design of the three components considered. The upper and lower curves represent the limits due to the different cases considered in the study, while the gray area represents all possible combinations in between. The key parameter chosen to be presented was the evaporator ramp-rate as it is the one with the higher influence in the results

Looking at the lower limit of the graph, a decreasing trend against the EVA ramp rates may be observed. This is due to the fact that the points in the bottom part of the graph are associated with low SH ramp rates values, making the SH the bottleneck of the start-up and postponing the turbine start-up procedure (as presented in Case b). On the contrary, the upper limit is characterized by an increasing trend, because each case is associated with the relative optimal SH ramp rate. Different cases are illustrated in **Fig. 6** and summarized in **Table 4**, to show the impact of the ramp rate conditions on the electricity production.

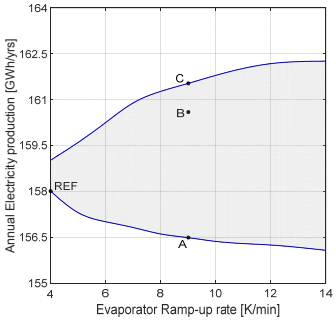

FIGURE 6: Annual electricity production considering different ramp-up rates for super-heater, evaporator and turbine

TABLE 4: Comparison of different cases for PTPP yearly performance

Case	Description	Electricity Production [GWh/yr]	Relative difference
(REF)	Slow EVA, Optimal SH, No turbine ramp modifications	158.01	0 %
(A)	Fast EVA, Slow SH, No turbine ramp modifications	156.49	-0.96 %
(B)	Fast EVA, Optimal SH, No turbine ramp modifications	160.6	+1.64 %
(C)	Fast EVA, Optimal SH, Only turbine hot start-ups	161.53	+2.23%

Each case (A, B, C) represents a possible combination of designs with a fast evaporator and compared to a slow reference case (REF), to show how a faster SGS could improve the performance of the power plant. Case A represents a non-optimal configuration shown as the bottom line of **Fig. 6**, suggesting that if the EVA and SH are not operated optimally together (or not designed properly), it would result in a nearly 1% loss in electricity production. If a fast optimally designed SGS (compared to the base case) is employed, the PTPP performance would benefit 1.64% in electricity production with a 0.59%-points potential increase if the turbine start-up improvements are considered. Note that having only hot turbine start-ups does not have a significant impact. This can be explained by looking at **Fig. 5a-b**. Even if the hot start-up is much faster, the steam temperature requirement is higher than in a warm case, postponing the actual start-up of the turbine and improving in a lower percentage the performance of the power plant than if the start-up could have occurred at the same instant as that of a warm start-up. Moreover from **Fig. 6**, it can be observed that an optimal range of start-up time for the evaporator can be identified. Indeed between 7-10 K/min the slope of the curve decreases to reach an asymptote for higher ramp-rates. This means that after this threshold, the increase in the heating rate of the component is affecting less the performance of the power plant. If, for example, a 14 K/min evaporator could be designed, it would result in a 0.46% increase (compared to case C) in electricity production, making it less worthwhile to reach for such limits.

CONCLUSIONS

A detailed methodology has been presented to show the interaction between steam turbine and steam generation system during the start-up of a PTPP. For this purpose a detailed model of a PTPP has been developed and implemented with a control strategy to account for the start-up limitations and performance of the aforementioned components. This has been validated and integrated in an existing tool for the dynamic performance evaluation of power plants (DYESOPT). The results suggested, that an optimal design and/or operating strategy accounting for both SH and EVA is crucial not to make the SGS the bottleneck of the power plant start-up. As such, for the particular application, it was found that a 179% higher start-up rate for the SH than the EVA is an optimal design/control point in order to both perform optimally the start-up procedure while affecting to a small extent the lifetime of the components. From a system perspective an optimal range of average heating rate for the evaporator has been found to lie between 7-10 K/min. With this configuration and an optimally operated super-heater, the increase in the yearly power plant energy production would result in 1.7-2.1%. However, an economic analysis comprising the OPEX related to the different SGS designs would be required to study the impact of such designs on the techno-economic indicators and profitability of PTPPs.

REFERENCES

1. CSP Today (Groupe Reaction Inc.), "CSP Solar Tower Report 2014: Cost, Performance and Thermal Storage," CSP Today, 2014.
2. M. Topel, M. Genrup, M. Jöcker and B. Laumert, "Operational improvements for startup time reduction in solar steam turbines," *Journal of Engineering for Gas Turbines and Power,* vol. 137, no. No. 4, 2015.
3. J. Samanes and J. Garcia-Barberena, "A model for the transient performance simulation of solar cavity receivers," *Solar Energy,* pp. 789-806, 2014.
4. L. L. Vant-Hull, "Central tower concentrating solar power (CSP) systems," in *Concentrating Solar Power Technology - Principles, Developments and Applications*, Woodhead Publishing Limited, 2012, pp. 240-283.
5. M. Topel, R. Guedez and B. Laumert, "Impact of increasing steam turbine flexibility on the annual performance of a direct steam generation tower power plant," in *SolarPaces*, 2014.
6. J. Taler, B. Weglowski, D. Taler, T. Sobota, P. Dzierwa, M. Trojan, P. Madejski and M. Pilarczyk, "Determination of start-up curves for a boiler with natural circulation based on the analysis of stresses distribution in critical pressure components," *Energy,* vol. 92, pp. 153-159, 2015.
7. I. Basaran, A comprensive study of the imposed limitations on concentrating solar power plant start-up speeds, Stockholm: KTH, Master Thesis, 2015.
8. European Standards, "EN 12952-3, Water tube boilers and auxiliary installations. Part 3: Design and calculation for pressure parts of the boiler;," DIN, 2011.
9. P. Dzierwa and J. Taler, "Optimum heating of pressure vessels with holes," *Journal of pressure vessel technology,* vol. 137, no. 1, p. 8, 2014.
10. J. Spelling, M. Jöcker and A. Martin, "Annual performance improvement for solar steam turbines through the use of temperature-maintaining modifications," *Solar Energy,* vol. 86, no. 1, pp. 496-504, 2012.
11. R. Guedez, M. Topel, I. Conde, F. Ferragut, I. Callaba, J. Spelling, Z. Hassar, C. D. Perez-Segarra and B. Laumert, "A methodology for determining optimum solar tower plant configurations and operating strategies to maximize profits based on hourly electricity market prices and tariffs," *Journal of Solar Engineering,* vol. 138, pp. 021006-1-11, 2016.
12. P. Gilman, N. Blair, M. Mehos, C. Christensen and S. Janzou, "Solar advisor model user guide for version 2.0," NREL, 2008.
13. F. Lippke, "Simulation of the Part-Load Behavior of a 30 Mwe SEGS Plant," Sandia National Laboratories, 1995.
14. V. A. Dudley, "SEGS LS-2 Solar Collector. Test Results," Sandia National Laboratories, 1994.
15. NREL, "System Advisor Model Case Study: Andasol-1," NREL, 2011.
16. NREL, "Concentrating Solar Power Projects - Andasol," 2013. [Online]. Available: http://www.nrel.gov/csp/solarpaces/project_detail.cfm/projectID=4. [Accessed 19 07 2016].
17. Solar Millenium AG, "The parabolic torugh power plants Andasol 1 to 3," Solar Millenium AG, 2008.
18. MAN Diesel & Turbo, "Solar Power Generation - Industrial steam turbines for CSP plants," MAN, 2011.

Concentrating solar power plants employ reflecting mirrors to concentrate the incident solar irradiation, convert it into high-temperature heat and, in a second step, into electricity. The fluctuating nature of the solar irradiation requires more operating flexibility towards the rate of responsiveness to changes in load. In particular, steam generator systems are usually designed for baseload application. However, the high thermo-mechanical stresses they experience during start-up procedures might limit the components lifetime or cause failure.

The thesis has the objectives to quantify the impact of the heating rate constraints on the economy of parabolic trough power plants and to define a method to design the steam generator system considering optimal constraints. The results from this thesis indicate that it is of significant importance to account for the steam generator thermo-mechanical limitations during its design phase. The use of suitable components could increase the electric energy production of the power plant, while at the same time allowing for operating decision flexibility throughout the year.

DTU Mechanical Engineering
Section of Thermal Energy
Technical University of Denmark

Nils Koppels Allé, Bygn. 403
DK-2800 Kgs. Lyngby
Denmark
Tlf.: +45 4525 4131
Fax: +45 4525 1961

www.mek.dtu.dk

October 2018

ISBN: 978-87-7475-556-2

DCAMM
Danish Center for Applied Mathematics and Mechanics

Nils Koppels Allé, Bld. 404
DK-2800 Kgs. Lyngby
Denmark
Phone (+45) 4525 4250
Fax (+45) 4525 1961

www.dcamm.dk

DCAMM Special Report No. S257

ISSN: 0903-1685